



**Investigation of the correlation of elastic and electronic properties  
of diamond-like carbon films**

Wilfred M. Mbiombi

A thesis submitted to the Faculty of Science, University of the Witwatersrand,  
Johannesburg, in fulfilment to the requirements for the degree of philosophy.

Johannesburg 2019

## **Declaration**

I declare that this thesis is my own unaided work. It is being submitted for the degree of Doctor of Philosophy in the University of the Witwatersrand, Johannesburg. It has not been submitted before for any degree or examination in any other University.

Signed

---

Date

---

## Abstract

Diamond - like carbon (DLC) is a unique material because of the excellent combination of properties such as high hardness, low friction coefficient and high wear resistant, electrical insulation and chemical inertness. Besides, DLC materials have tunable optical, electronic and electromechanical properties that depend largely on the ratio of  $sp^3/sp^2$  carbon bonds. In this work, the roles of the  $sp^3$ ,  $sp^2$  bonds and hydrogen content are analyzed closely on DLC films prepared using RF and DC magnetron sputtering, with and without active biasing. Diamond-like carbon thin films were prepared using a graphite target in a  $CH_4/Ar$  atmosphere by RF and DC reactive magnetron sputtering. Variable sputter powers and  $CH_4$  flow rates were used, whilst maintaining a fixed argon flow rate. As a first result, the optimum thin film growth condition comprised of 50 % of  $CH_4$ -Ar concentration for these room- temperature sputtered films, applicable to both RF and DC sputtered films were determined. The amorphous hydrogenated carbon films (RF sputtered) exhibit more diamond-like features at this composition, characterized by moderately high fraction of  $sp^3$  bonds, coupled with higher Tauc gap values, (1 - 1.5 eV). There was also a notable increase in density ( $\sim 2.5 \text{ g/cm}^3$ ) and mechanical strength ( $E \sim 51 \text{ GPa}$ ). It was evident that the mechanical and structural properties of the films depended on the degree of  $CH_4$  dilution of the Ar ambient, due to the different chemistry occurring in the plasma. As the amount of methane increased, X-ray reflectivity (XRR ) results showed structural changes from a more disordered polymer-like structure to a less disordered graphitic arrangement. In addition, at the optimum condition, the films had a higher resistivity owing to the increased proportion of  $sp^3$  bonds as evidenced by the increased presence of  $CH_n$  ( $n=1-3$ ) radicals. The accompanying observed changes of the phonon phase velocity were related to the microstructural changes of the films. It was demonstrated that the mechanical strength of the *as-deposited* films flattens out at 50 % composition, thus

necessitating either an active biasing of the substrate or annealing of the films in order to further improve the mechanical strength. The structural evolution of the DLC films as a function of the deposition conditions (such the substrate bias voltage, the pressure and power) studied using Raman and UV-Visible spectra showed that increasing substrate bias voltage leads to the reduction of the cluster size of  $sp^2$  rings, whilst increasing the  $sp^2$  chains and the  $sp^3$  bonds. These observations were confirmed by the optical performance of the coatings, characterised by transmittance, which was observed to similarly increase as the  $sp^3$  bonds increased. The results of Raman analysis suggested that the  $sp^3$  phase that is related to the disordered  $sp^2$  phase attained its maximum content at a bias voltage of - 100V on films grown on silicon. In addition, the results of electrical conductance, Fourier transform infrared (FTIR) and X-ray photoemission spectroscopy (XPS) analyses revealed that a bias voltage of -100V was more favorable to  $sp^3$  phase formation under the current experimental conditions. The FTIR results further confirmed that these films were indeed more diamond-like carbon by virtue of the presence of absorption bands such as  $sp^3$  C-H<sub>2</sub> symmetry and asymmetry (at 2850 and 2920  $cm^{-1}$ ) and  $sp^3$  C-H<sub>3</sub> asymmetry (at 2950  $cm^{-1}$ ). In addition, it was postulated that it is likely that the main reason for the observed lower elastic moduli (~ 17 GPa - 20 GPa) for DC sputtered films, compared to that of RF sputtered films (~ 47 - 62 GPa) is likely directly linked to the increase of polymeric carbon content in the DC films as evidenced by the Rayleigh velocities ranging between 1860 - 2274 m/s, characteristic of polymer-like carbon films. Thus, in this study, the direct influences of growth conditions on the DLC microstructure and also construct a correlation between electrical, mechanical properties and electronic properties of these materials have been demonstrated.

## Table of contents

<b>Declaration</b>	<b>i</b>
<b>Abstract</b>	<b>ii</b>
<b>Table of contents</b>	<b>iv</b>
<b>Acknowledgements</b>	<b>ix</b>
<b>List of Figures</b>	<b>xi</b>
<b>List of Tables</b>	<b>xxi</b>
<b>Chapter 1: Introduction</b>	<b>1</b>
1.1 Diamond like carbon .....	2
1.2 Objectives of the present study.....	5
1.3 Thesis breakdown .....	5
<b>Chapter 2: Literature Review</b>	<b>7</b>
2.1 Layout of the chapter .....	7
2.2 General Review .....	7
2.3 Deposition methods .....	9
2.3.1 Ion Beam Deposition Methods.....	10
2.3.2 Sputtering Process.....	12
2.3.3 Cathodic vacuum arc System.....	13
2.3.4 Plasma Enhanced Chemical Vapour Deposition Methods (PECVD).....	13
2.3.5 Pulsed laser deposition (PLD) process.....	16

2.4 Deposition Mechanism.....	16
2.4.1 Hydrogenated amorphous carbon (a-C: H).....	18
2.5 Nucleation and Thin film growth.....	21
2.5.1. Film nucleation and growth.....	22
2.5.2 Structural Zone Model (SZM).....	23
2.6. Atomic structure and characterisation.....	25
2.6.1. Bonding configuration.....	25
2.6.2 Raman spectroscopy of carbon based materials.....	27
2.6.3 Fourier Transform Infrared (FTIR) spectroscopy.....	30
2.6.4 Hydrogen content in disordered carbon.....	31
2.6.5 Density determination by X-ray reflectivity (XRR).....	32
2.6.6 X-ray photoemission spectroscopy (XPS).....	34
2.7 Electronic structure of disordered carbon.....	35
2.7.1 The $\sigma$ and $\pi$ states.....	35
2.7.2 Cluster model.....	35
2.7.3 Network calculations.....	36
2.7.4 Optical gap.....	37
2.8 The Doping of DLC.....	39
2.9 Electrical properties.....	40
2.10 Surface Brillouin scattering.....	41
2.10.1 Introduction.....	41
2.10.2 The Mechanisms for Brillouin Scattering.....	41

**Chapter 3: Thin Film Growth and characterisation 59**

Introduction .....59

3.1.1 Diamond like carbon thin film deposition.....59

3.1.2 Experimental procedure.....62

3.2.3 X-ray photoelectron spectroscopy and X-ray induced Auger spectroscopy.....74

3.2.4 X-ray reflectometry (XRR).....77

3.2.5 Infrared spectroscopy.....80

3.2.6 Optical emission and UV-Vis spectroscopy.....82

3.2.7 Surface Brillouin scattering.....83

**Chapter 4: Correlation of optoelectronic and mechanical properties of unbiased DLC thin films 89**

4.1 Introduction .....89

4.3 Thin film growth rate determination using X-ray reflectivity .....91

4.4 Determination of  $sp^3$  and  $sp^2$  fractions and hydrogen content by Raman spectroscopy .....94

4.4.1 Raman spectroscopy of diamond like carbon using RF magnetron sputtering.....95

4.4.2 Raman spectroscopy of DLC films grown using DC magnetron sputtering.....100

4.4.3 Raman parameters related to microstructure and optical property.....108

4.5 Vibrational mode of DLC thin films by Fourier Transform Infrared.....111

4.6 I-V Characteristics of DLC thin films .....117

4.7 X-ray photoelectron and Auger electron spectroscopy analyses.....120

4. 8 Surface Brillouin scattering on DLC thin films.....	127
4.8.1 Theoretical considerations: Phonon Dispersion curves.....	133
4.9 Conclusion.....	137

**Chapter 5: Bias enhanced nucleation and growth for improving  
DLC quality 138**

5.1 Introduction .....	138
5.2 Growth rate, thickness and density determination using X-ray reflectivity .....	140
5.3. Raman spectroscopy analysis of $sp^3$ , $sp^2$ and hydrogen- contents .....	143
5.3.1 RF magnetron sputtering with substrate bias voltage on $SiO_2$ (glass substrate).....	144
5.3.2 DLC thin films fabricated by RF magnetron on (001) Silicon at varying bias voltages..._	148
5.3.3 Structural properties of DLC films prepared by DC Magnetron sputtering on DC biased (001) Si.....	153
5.4. Electrical properties of DLC thin films .....	157
5.4.1. Current –Voltage (I-V) Characteristics.....	157
5.4.2. Current-Voltage (I-V) characteristics of DLC thin films.....	157
5.5. X-ray photoelectron and Auger electron spectroscopy .....	161
5.6 Optical spectroscopy in the visible range.....	169
5.6.1 UV-Vis transmittance of biased DLC thin films on glass.....	169
5.6.2 Fourier Transform Infrared spectroscopy of DLC films: Transmission mode.....	171
5.7 Surface Brillouin scattering.....	179
5.8 Conclusion.....	186

**Chapter 6: Conclusion and future work 188**

## **Dedication**

This work is dedicated to my wife Mathy Madangi, my children, Kerene Molangi, Tigo Mbiombi, Elada Mbiombi and Princess Mbiombi.

## Acknowledgements

My deepest gratitude goes to my supervisors, Dr. Bhekumusa Mathe and Professor Daniel Wamwangi for their guidance and support and for all the knowledge I have gained from them. Thank you very much. I am also very grateful to Professor Arthur Every for his financial support and training on the Green's function simulation. I am also deeply grateful to Dr. Rudolph Erasmus for the Raman measurements and for his vast experience and insightful discussions on several aspects of my work. Additionally his facilitation of the FTIR and XPS measurements with National Metrology Institute of South Africa, NMISA is greatly appreciated.

I am also deeply indebted to the DST/NRF Centre of Excellence in Strong Materials, the African Laser Centre, ALC, and the School of Physics for the financial support without which my work at WITS might have been so turbulent. Thank you very much.

I would like to thank and acknowledge the Head of the School of Physics, Prof Joao Rodrigues and the Director of Materials Physics Research Institute, MPRI Prof Elias Sideras-Haddad for their financial support during the final year of my PhD. Their moral and constant queries on the status of the PhD work facilitated its expedited completion. All technicians in the School of Physics are thanked for their technical support in matters related to the research infrastructure of the project as well as fostering a jovial working environment. I thank to all my office mates for their assistance and advice in writing this thesis. The organization of the references in the PhD thesis as well as surmounting the frequent teething problems entailing *ENDNOTE* software would not have been possible without the assistance of Dr Francis Otieno. He is thanked for his unreserved support. Since the commencement of this journey relationships were established and nurtured, to this end I would

also like express my sincere and deepest gratitude to my friends and fellow postgraduate students for making my stay at WITS a memorable one.

To my family, particularly my wife and children, I cannot thank you enough as you always bore the wrath of my absence with patience, dignity and understanding. Despite the long hours away from home especially during the weekends, the family remained intact and coalesced towards the greater good and goal. I'm forever indebted to you all.

Lastly, I thank God, who is a provider by his grace and mercy, makes all things possible.

## List of Figures

Figure 2.1: Ternary phase diagram of bonding in amorphous carbon-hydrogen alloys [15] .....	9
Figure 2.2: Schematics of various DLC deposition methods [29]. .....	11
Figure 2.3: Berman-Simon phase diagram for carbon [40]. .....	18
Figure 2.4: Component processes in the growth mechanism of a-C:H [59, 60]. .....	19
Figure 2.5: Process in the nucleation and growth of the films on a substrate [74]. .....	23
Figure 2.6: Typology of structure -zone [76]. .....	25
Figure 2.7: Schematic of density of state of carbon showing $\sigma$ and $\pi$ states [85]. .....	26
Figure 2.8: X-ray reflectivity pattern illustrating Kiessig oscillations of a thin film on a substrate system [104] .....	34
Figure 2.9: Kinematic condition for Brillouin scattering, Eq. (2.9). .....	43
Figure 2.10: Backscattering geometry commonly utilised for SBS measurements [135]. .....	45
Figure 2.11: Dispersion relations for (a) an aluminium layer on a fused quartz substrate and (b) an aluminium layer on zinc. and denote the substrate T and L threshold velocities respectively [140].	53
Figure 2.12: Calculated combined surface and bulk Brillouin spectra for various values of the complex dielectric constant and $\epsilon = \epsilon_1 + i\epsilon_2$ [142]. .....	55
Figure 2.13: Phase velocity dispersion curves for tungsten carbide (WC) films on a silicon substrate, calculated using optimized values of elastic constants and density for the film [146]. .....	57
Figure 3.1: Schematic diagram of RF sputter system with sputtering process [150]. .....	61
Figure 3.2: RF magnetron sputtering system and the related instruments. A– RF generator, PFG 300RF; B – gas control unit; C – vacuum chamber; D – turbo pump control unit, Turbotronik NT 150/360 VH; E – linear amplifier, Kenwood TL-922; F – fore pump; G – Compac cooling unit [151].	62

Figure 3.3 : A transition scheme for an Ar <sup>+</sup> laser. The first collision ionises the neutral argon and the next pumps it to an excited state (from the Operational Manual for the Spectra Physics 2020/2025 Ion Laser) .....	67
Figure 3.4: Schematic diagram of a gas laser [152].....	68
Figure 3.5: Schematic diagram of the Raman Spectrograph showing the beam trajectory (From the Instruction Manual for the Jobin-Yvon T64000 Raman spectrograph). .....	70
Figure 3.6: Model 4140B and supplied accessories (From manual HP 4140B pA Meter/D.C Voltage Source).....	73
Figure 3.7: Schematic diagram of the Model 4140B and supplied accessories for I-V characteristics measurements.....	74
Figure 3.8: Picture of the Thermo ESCALab 250Xi X-Ray Monochromatic Al K $\alpha$ (1486.7 eV). ....	76
Figure 3.9: D-parameter of DLC thin prepared by RF magnetron sputtering Ar/CH <sub>4</sub> :13/6. ....	77
Figure 3.10: Schematic diagram depicting the X-ray total external reflection from a film substrate system [155].....	78
Figure 3.11: IR spectrum of a-C:H films [157]. ....	81
Figure 3.12: Schematic diagram of the Varian Cary 500 spectrophotometer.....	83
Figure 3.13: A schematic diagram of the external optics used for Brillouin light scattering in the backscattering geometry [150].....	84
Figure 3.14: Selection of the single axial longitudinal mode from the intersection of the maximum of the laser gain profile and the minimum of the Etalon loss curve (From the instruction manual for the spectra-Physics Model2060/2080 Ion Laser).....	85
Figure 3.15: The reflection of a plane wave in a plane parallel plate, Fabry-Pérot [150] . ....	86
Figure 3.16: A photograph of (3+3) multipass Tandem interferometer, in which FP1 (A) and FP2 (B) are mounted in tandem on a translating stage. The detector (C) is mounted on the TFPI box and the shutter mechanism is labelled (D) [151]......	88

Figure 3.17: Translational stage of the two Fabry-Pérot, which are capable of scanning synchronously (From JRS Scientific Instruments, TFPI operator manual). .....	88
Figure 4.1: Optical emission spectroscopy of DLC film with the highest deposition rate occurs at 50 % methane and 50 % argon composition using RF magnetron sputtering. ....	91
Figure 4.2: Typical XRR scan of DLC thin films deposited on silicon with a bias substrate at -100V, for a 50 % methane and argon composition and deposition power of 200W. ....	92
Figure 4.3: The deposition rate versus methane concentration, highest deposition rate occurs at 50 % methane composition of the (argon and methane) mixture.....	93
Figure 4.4: Raman Spectra of DLC films deposited at different (Ar and CH <sub>4</sub> ) flow rate ratios using RF magnetron sputtering at 200 W.....	96
Figure 4.5: Raman Spectra of DLC films deposited at different (Ar and CH <sub>4</sub> ) flow rate ratios: (a) 3.3/13, (b) 6.5/13, (c) 13/13 and (d) 26/13 using RF sputtering at 200W.....	97
Figure 4.6: Raman spectra of DLC thin films prepared using RF magnetron sputtering .....	100
Figure 4.7: Raman Spectra of DLC films deposited at different (Ar and CH <sub>4</sub> ) flow rate ratios.....	101
Figure 4.8: The Raman spectra of DC sputtered DLC thin films grown on unbiased (001) Si.....	107
Figure 4.9: FTIR spectra for DC magnetron sputtering showing the CH <sub>2</sub> symmetric stretching peaks at ~ 2850 cm <sup>-1</sup> , characteristic of DLC films deposited at 50 at.% Ar/CH <sub>4</sub> concentrations.....	114
Figure 4.10: FTIR spectra RF magnetron sputtering showing the CH <sub>2</sub> symmetric stretching peaks at ~ 2850 cm <sup>-1</sup> , characteristic of DLC films deposited at 50 at.% Ar/CH <sub>4</sub> concentrations.....	114
Figure 4.11: FTIR spectra of absorbance of RF magnetron sputtering showing the CH <sub>2</sub> symmetric stretching peaks at ~ 2850 cm <sup>-1</sup> , characteristic of DLC films deposited at 50 at.% Ar/CH <sub>4</sub> concentrations.....	115
Figure 4.12: FTIR spectra of absorbance of DC magnetron sputtering showing the CH <sub>2</sub> symmetric stretching peaks at ~ 2850 cm <sup>-1</sup> , characteristic of DLC films deposited at 50 at.% Ar/CH <sub>4</sub> concentrations.....	116

Figure 4.13: Current-Voltage characteristics for RF sputtered films at the optimum condition of 50% methane composition. The lower conductivity is attributed to the presence of a higher $sp^3$ fraction in the films. ....	119
Figure 4.14: Current-Voltage characteristics for DC sputtered films showing increased conductivity below 50% methane composition, attributed to the presence of a higher $sp^2$ fraction in the films. .	119
Figure 4.15: XPS survey scan spectrum of DLC thin film prepared with Ar/CH <sub>4</sub> 1:1 deposited on silicon substrate at 200W, unbiased substrate.....	123
Figure 4.16: XPS survey C1s scan spectrum of DLC thin film prepared with Ar/CH <sub>4</sub> 1:1 deposited on silicon substrate at 200W, unbiased substrate.....	123
Figure 4.17: XPS survey scan spectrum of DLC thin film prepared with Ar/CH <sub>4</sub> 13:6 deposited on silicon substrate at 200W, unbiased substrate.....	124
Figure 4.18: XPS survey C1s scan spectrum of thin film prepared with Ar/CH <sub>4</sub> 13:6 deposited on silicon substrate at 200W, unbiased substrate.....	124
Figure 4.19: Auger spectra of DLC thin film prepared with Ar/CH <sub>4</sub> 1:1 deposited on silicon substrate at 200W, with D- Parameter, 13.50 eV.....	126
Figure 4.20: Auger spectra of DLC thin film prepared with Ar/CH <sub>4</sub> 13:6 deposited on silicon substrate at 200W with D- Parameter, 13.40 eV.....	126
Figure 4.21: Surface Brillouin scattering spectrum of RF sputtered films measured at 70° incidence, showing the two phonon modes, Rayleigh and Longitudinal guided modes; a) Ar (13 sccm), CH <sub>4</sub> (6.5 sccm).....	130
Figure 4.22: Surface Brillouin scattering spectrum of RF sputtered films measured at 70° incidence, showing the two phonon modes, Rayleigh and Longitudinal guided mode; b) Ar (13 sccm), CH <sub>4</sub> (13 sccm).....	131

Figure 4.23: Surface Brillouin scattering spectrum of RF sputtered films measures at 70° incidence, showing the two phonon modes, Rayleigh and Longitudinal guided mode; c) Ar (13sccm), CH <sub>4</sub> (26sccm).....	131
Figure 4.24: Dispersion plot of experimental data measured from 50 to 70° incidence, with deposition times 3, 5 and 8 minutes and the q <sub>  d</sub> was varied from 2.5 to 3.5; and velocity dispersion simulations by elastodynamic Green's function (continuous line). ....	134
Figure 5.1: Raman spectra of RF sputtered films, showing D- and G-peaks of films deposited at different bias voltage: (a) -25 V, (b) -50 V, (c) -75 V and (d) -100 V on SiO <sub>2</sub> . ....	145
Figure 5.2: DLC thin film spectra showing influence of hydrogen on background photoluminescence at varying bias voltages, from -25 V to -100 V. ....	147
Figure 5.3: Raman spectra of DLC films deposited by RF magnetron sputtering on a Si substrate biased from -25 V to -100 V. ....	149
Figure 5.4: Fitted Raman spectrum of DLC films deposited by RF magnetron sputtering with different bias substrate voltage (a) -25 V, (b) -50V, (c) -75V and (d) -100V. ....	150
Figure 5.5: Raman spectra of DC magnetron sputtered DLC films with substrate bias variations in the range -25 V to -100 V. ....	154
Figure 5.6: Raman spectra of DC magnetron sputtered DLC films with substrate bias voltage variations in the range -25 V to -100 V. ....	155
Figure 5.7: Schematic representation for hydrogen estimation in the films for DC magnetron sputtered with substrate bias varied in the range -25V to -100V. ....	156
Figure 5.8: Current-Voltage characteristics of RF magnetron sputtering for various substrate bias voltages deposited DLC thin films (from -25 V to -100 V).....	158
Figure 5.9: Current-Voltage characteristics of DC magnetron sputtering for various substrate bias voltages deposited DLC thin films (from -25 V to -100 V).....	158

Figure 5.10: XPS survey spectrum of RF magnetron sputtering of DLC deposited on silicon with a bias -75V and power 200W. ....	162
Figure 5.11: XPS survey spectrum of RF magnetron sputtering of DLC deposited on silicon bias -100 V and power 200W. ....	162
Figure 5.12: X-ray induced C KLL Auger peak of RF magnetron sputtering of DLC deposited on silicon bias -75 V and power 200W. ....	164
Figure 5.13: X-ray induced C KLL Auger peak of RF magnetron sputtering of DLC deposited on silicon bias -100 V and power 200W. ....	164
Figure 5.14: XPS survey spectrum of DC magnetron sputtering of DLC deposited on silicon bias -75V and power 200W. ....	166
Figure 5.15: XPS survey spectrum of DC magnetron sputtering of DLC deposited on silicon .....	167
Figure 5.16: X-ray induced C KLL Auger peak of RF magnetron sputtering of DLC deposited on Si at -75 V and power 200W. ....	168
Figure 5.17: X-ray induced C KLL Auger peak of RF magnetron sputtering of DLC deposited on silicon bias -100V and power 200W. ....	168
Figure 5.18: Transmittance spectrum of biased DLC thin films on glass. ....	170
Figure 5.19: The plot of $(\alpha h\nu)^{1/2}$ versus $h\nu$ for DLC thin films on glass. ....	170
Figure 5.20: Transmittance spectrum of biased DC sputtered DLC thin films. ....	172
Figure 5.21: Transmission versus wavenumber for RF magnetron sputtering in between (2800-3000 $\text{cm}^{-1}$ ) .....	173
Figure 5.22: FTIR spectrum of RF sputtered DLC films showing the $\text{CH}_2$ symmetric stretching peaks at $\sim 2850 \text{ cm}^{-1}$ . These films are deposited at -100V bias substrate. ....	175
Figure 5.23: FTIR spectrum showing the $\text{CH}_2$ symmetric stretching peaks at $\sim 2850 \text{ cm}^{-1}$ , characteristic of DLC films deposited at -75 V using RF magnetron sputtering. ....	175

Figure 5.24: FTIR spectrum showing the CH<sub>2</sub> symmetric stretching peaks at ~ 2850 cm<sup>-1</sup>, characteristic of DLC films deposited at -25 V..... 176

Figure 5.25: FTIR absorbance spectrum exhibiting the CH<sub>2</sub> symmetric stretching peaks at ~ 2850 cm<sup>-1</sup>, characteristic of DC magnetron sputtered DLC films deposited at -100 V bias voltage..... 177

Figure 5.26: FTIR spectra of absorbance of DC magnetron sputtering showing the CH<sub>2</sub> symmetric stretching peaks at ~ 2850 cm<sup>-1</sup>, characteristic of DLC films deposited at -75V..... 177

Figure 5.27: FTIR spectra of absorbance of DC magnetron sputtering showing the CH<sub>2</sub> symmetric stretching peaks at ~ 2850 cm<sup>-1</sup>, characteristic of DLC films deposited at -50V biased substrate. .. 178

Figure 5.28: Surface Brillouin scattering spectra of RF sputtered films measured at 70° incidence.181

Figure 5.29: Surface Brillouin scattering spectra of DC sputtered films measured at 70° incidence. .... 181

Figure 5.30: Dispersion curve for RF- sputtered DLC films grown on Si substrate bias at -100V.. 183

Figure 5.32 Elliptical plots to determine the best fit elastic constants and associated error estimates for RF sputtered DLC thin films grown on (001)Si at -100 V. The elastic constants have been refined to C<sub>11</sub> = 65.0 ± 5.0 GPa and C<sub>44</sub> = 25.9 ± 3.0 GPa..... 184

## List of Tables

Table 3.1: Growth conditions for RF sputtered films with biased SiO <sub>2</sub> substrate condition from -25 to -100V. ....	64
Table 3.2: Growth conditions for RF magnetron sputtered films with biased silicon substrate from -25 to -100V. ....	65
Table 3.3: DC magnetron sputtering biased silicon substrate from -25 to -100V .....	65
Table 4.1: Physical properties of DLC thin films measured using X-ray reflectivity with varied Ar/CH <sub>4</sub> ratio. ....	94
Table 4.2: DLC films deposited on unbiased substrate by (a) RF magnetron sputtering - and (b) DC magnetron sputtering - at different flow rate ratios and power (CH <sub>4</sub> = 20 sccm, Ar+ = 20 sccm). ....	95
Table 4.3: Summary of spectral features of RF sputtered films at 200W .....	98
Table 4.4: Summary of spectral features of DC sputtered films grown at fixed power of 200W, obtained after deconvolution of the D and G-peaks. ....	105
Table 4.5: Summary of spectral features obtained after deconvolution of the D and G-peaks for DC sputtered films, using different powers. ....	106
Table 4.6: Microstructure and electronic properties of RF sputtered thin films. ....	110
Table 4.7: Microstructure and electronic properties of DC sputtered thin films. ....	111
Table 4.8: C-H <sub>n</sub> bonds and hydrogen density at optimum condition of DLC films. ....	116
Table 4.9: Electrical properties of DLC prepared by RF magnetron sputtering. ....	120
Table 4.10: Electrical properties of DLC prepared by DC magnetron sputtering. ....	120
Table 4.11: Summary of the XPS results of DLC prepared by RF magnetron sputtering with.....	124
Table 4.12: Summary of the AES results and sp <sup>2</sup> fraction of DLC films. ....	126
Table 4.13: Elastic constants and related mechanical moduli of RF magnetron sputtered films .....	130
Table 5.1: Physical properties of biased DC sputtered DLC thin films on (001) Si. ....	142
Table 5.2: Physical properties of biased RF sputtered DLC thin films on (001) Si. ....	142

Table 5.3: Physical properties of RF sputtered DLC thin films on SiO <sub>2</sub> substrate. ....	142
Table 5.4: Structural parameters of RF sputtered DLC thin films deposited on biased glass substrates. .....	148
Table 5.5: DLC thin films on (001) Si substrate by RF magnetron sputtering at various substrate bias voltages.....	151
Table 5.6: Dependence of Hydrogen content in DLC films with substrate bias.....	152
Table 5.7 : Parameters of DLC thin films by Raman Spectroscopy ( $\lambda_{exc} = 514.5$ nm) .....	153
Table 5.8: Parameters of DC magnetron sputtered DLC thin films for substrate bias voltages. ....	156
Table 5.9: Electrical properties of RF sputtered DLC films at biased substrate voltage .....	160
Table 5.10: Electrical properties of DLC prepared by DC magnetron sputtering biased substrate..	160
Table 5.11: XPS data showing composition and concentration of RF magnetron sputtering of DLC deposited on silicon bias -100 V and power 200W. ....	163
Table 5.12: Summary of the AES results of DLC films prepared by RF magnetron sputtering at bias voltages of -75 and -100V.....	165
Table 5.13: XPS data on DC magnetron sputtered DLC on (001) Si at -100 V and 200W.....	167
Table 5.14: Summary of AES results of DC magnetron sputtered DLC: Si substrate biased .....	169
Table 5.15: Optical and structural properties of DLC thin films. ....	171
Table 5.16: C-H bonds and hydrogen density of RF sputtered DLC films on biased substrate. ....	178
Table 5.17: C-H bonds, hydrogen density and the ratio of sp <sup>3</sup> /sp <sup>2</sup> for DC sputtered DLC films on biased substrate.....	179
Table 5.18: Rayleigh velocities of biased RF and DC sputtered films. ....	182
Table 5.19: Elastic constants and mechanical moduli of DLC films.....	183

## Chapter 1: Introduction

**Carbon** has proven to be one of the most important chemical elements occupying the sixth position in the periodic table. On one hand it occurs in various polymorphs, ranging from crystalline carbon such as diamond, graphite, graphene all the way to disordered structures which span from amorphous carbon, fullerene to glassy carbon amongst others. The formation of these polymorphs is attributed to three hybridizations of the s and p electron wave functions, namely the  $sp^3$ ,  $sp^2$  and  $sp^1$  hybridizations of carbon [1]. The ubiquitous “diamond” is composed of 4 carbon atoms each covalently bonded through sharing of the four valence electrons. This directional bonding leads to the formation of  $sp^3$  hybridization in which the s orbital combines with all 3 p orbitals of the 2<sup>nd</sup> energy level of carbon. This leads to the formation of 4 hybrid orbitals with a tetrahedral coordination constituting 4 neighboring carbon atoms and it is this type of hybridization that forms the strong  $\sigma$ -bond.

The three valence electrons in graphite constitute the  $sp^2$  orbitals in which the s-orbital and 2 p-orbitals form three hybrid orbitals with an unchanged p-orbital. This type of hybridization leads to the formation of planar  $\sigma$ -bonds separated at  $120^\circ$ . The fourth electron  $sp^2$  lies perpendicular to the  $\pi$ -bond in the  $p_\pi$  orbital plane. This  $\pi$  orbital forms a weaker  $\pi$  bond with a delocalized  $\pi$  orbital on one or more neighboring atoms.

Lastly, the  $sp^1$  hybridization of carbon is formed by combination of each of the s and p – orbitals. This form of hybridization leads to the formation of 2 hybrid orbitals with a  $180^\circ$  separation between them. The unbound 2 p orbitals exist orthogonally to each other and to the  $sp^1$  hybrid thus enabling the formation of a triple bond for this configuration [1]. The nature and the coexistence of these hybridizations can be exploited to form materials with tunable opto-electrical

and mechanical properties. This is the basis of the Diamond like carbon films that comprise of  $sp^3$  and  $sp^2$  type bonds in varying fractions.

### **1.1 Diamond like carbon**

Diamond-like carbon (DLC) film as a form of carbon was fabricated for the first time in 1969 by Aisenberg and Chabot [1]. It is a metastable allotrope of amorphous carbon containing  $sp^2$  clusters embedded in high fractions of  $sp^3$  bonded carbon. DLC thin films have unique properties such as  $sp^3$  fraction dependent optical transmittance and electrical resistivity which coexist with superior mechanical properties. The mechanical properties include high hardness ( $\sim 20-80$  GPa), - high elastic modulus ( $\sim 200-800$  GPa), and low friction coefficient [1-7] and enable DLC thin films to be used in diverse environments and applications. The unique combination of these properties makes them very interesting as protective coatings in various applications such as;

- optical windows,
- magnetic storage disks
- cutting tools [8].

Furthermore, the tuning of the  $sp^2$  and  $sp^3$  fractions in DLC thin films has seen them utilised as strain gauges in microelectromechanical systems (MEMS). DLC's can exhibit properties similar to either diamond or graphite depending on the fraction of  $sp^3$  in the films. More recently the composition of hydrogen has been found to determine the mechanical properties of DLC thin films. The concentrations of hydrogen in the films have been posited to drive phase transitions in amorphous carbon material systems.

Thus the classification of the amorphous carbon is broad and dependent on not only on the fraction of  $sp^3$  but also on the hydrogen concentrations inherent therein. These films are classified among the amorphous carbon that can contain diamond crystallites. These materials do not qualify to be called diamond except if it is proven in three-dimensional, some micro- or nano-crystalline inclusions of all carbon forms can be found in the amorphous matrix. Diamond-like carbon films with hydrogen free content can be prepared by a variety of deposition techniques that are categorized as either physical vapor deposition (PVD) or chemical vapor deposition (CVD): These techniques include; carbon ion beam deposition, ion - assisted sputtering from graphite or by laser ablation of graphite. Diamond-like carbon films with high hydrogen content are predominantly observed in films prepared by chemical vapor deposition. The hydrogen content in this mode of film fabrication is often more than 25 at. %. Despite their extensive potential, the presence of high hydrogen content in DLC thin films may preclude their application due to inferior mechanical properties. This is evident in DLC thin films fabricated by conventional plasma enhanced chemical vapour deposition (PECVD) which often contains more hydrogen even at low temperature. The evolution of large fractions of hydrogen in these films often leads to moderate fractions of  $sp^3$  bonding, low hardness, weak adhesion, limited resistance to wear and tear and low optical transmission.

In the present work, DLC thin films have been prepared by radio frequency (RF) and direct current (DC) unbalanced reactive magnetron sputtering techniques at room temperature. Methane and argon have been employed as the precursor gases with pure graphite (99.99%) as the target. These films have been grown on (001)Si and  $SiO_2$  substrates under various ambient during growth. The ability to tune the  $sp^3/sp^2$  ratio and hydrogen fraction opens the way to improve the optical, electrical and mechanical properties of these materials and in the thesis, various methods have

been employed to measure this ratio. This tunability further enhances their application in non-volatile memory as active layers with high scalability and low power consumption devices [8]. In all the above cases, DLC thin films are incorporated as active layer in multilayer devices, thus strain control and stress relaxation play a dominant role in the performance and life span of these devices. Despite the wide range of applications, DLC thin films exhibit high compressive internal residual stress, which often leads to poor adhesion, and thus limit their commercial use. The magnetron sputtering process is one of the most useful techniques to tune adhesion energies using the structural zone model as a roadmap for microstructure control. Thus it has become the process of choice for the deposition of a wide range of industrially important coatings. In many cases, magnetron sputtered films now outperform films deposited by other PVD processes, and can offer the same functionality as much thicker films produced by other surface coatings techniques. Consequently, magnetron sputtering now makes a significant impact in application areas including hard, wear-resistant coatings, decorative coatings and coatings with specific optical or electrical properties. In this work, DLC thin films grown by RF and DC magnetron sputtering under different conditions of growth have been optimised using diverse substrate bias voltages to provide insights into the correlation between microstructure and film – substrate adhesion. The reason behind the change in the properties and the microstructure by substrate biased may be due to change of ion-energy to dissociate the methane and enhance the production of methyl ( $\text{CH}_3$ ) or CH radicals and ions with the films growth rate, an aspect that the author has sort to study in detail, correlating that with elastic moduli. It is well known that the probability of penetration increases with energy, and then at higher energies the probability of relaxation increases, giving rise to an optimum energy for densification  $\text{sp}^3$  bonding.

## **1.2 Objectives of the present study**

The study investigates the dependence of the optoelectronic and the mechanical properties of the DLC thin films based on the tunability of the ratio of  $sp^2/sp^3$  coupled with the hydrogen content, with a view to establish optimum DLC characteristics. Furthermore, the functionality and quality of the films has been modified to optimum level by biasing the substrate with DC voltage during growth.

The objectives of the present research are itemized as follows:

- (i) To investigate the optoelectronic and microstructure of DLC thin films
- (ii) To study the electrical properties
- (iii) To probe the mechanical properties using inelastic light scattering
- (iv) Establish the role of microstructure on these properties and subsequently build up a correlation between electrical, mechanical properties and electronic or microstructure properties of these samples.

## **1.3 Thesis breakdown**

The thesis is presented in a series of 6 chapters with the following outline;

Chapter 1 presents a brief introduction on the applications of Diamond like carbon thin films thus leading to the motivation of the present study. Additionally the aims and objectives of the thesis are outlined in this chapter followed lastly by the outline of the thesis.

Chapter 2 provides an overview of the theoretical background of this study.

Chapter 3 describes in detail the principles of the experimental techniques used in the growth and characterization of DLC thin films.

Chapters 4 and 5 provides the description, analysis and discussion of the results obtained from RF and DC magnetron sputtering under diverse conditions of film growth (unbiased substrate, varying CH<sub>4</sub>/Ar flow rates). In addition, the results on the properties of DLC films produced using RF and DC magnetron sputtering at various substrate bias voltages on Si and SiO<sub>2</sub> are presented and discussed in detail.

Chapter 6 provides a summary of important results and outlines the recommendations for further work.

## **Chapter 2: Literature Review**

### **2.1 Layout of the chapter**

This chapter gives an overview of the theoretical background of diamond like carbon thin films: this includes general review, deposition methods, nucleation and thin film growth, atomic structure and characterization, electronic structure, doping of diamond-like carbon thin films, electrical properties and some introductory background to Raman scattering and surface Brillouin scattering.

### **2.2 General Review**

The second part of the last century has seen an intensive research on diamond and diamond-like carbon (DLC) materials. The research has been motivated by the numerous and newly found applications of diamond following the discovery of synthetic diamond [9]. The extreme hardness of both natural and synthetic diamonds has seen them used foremost as cutting tools and as abrasive materials. Since then, the commercial interest on CVD diamond films has been driven by its potential application in electronics, coatings, optics and acoustics [10].

In 1971 Aisenberg and Chabot [11] reported the application of the ion beam method for the synthesis of thin carbonaceous films. These films were also called diamond-like carbon due to the resemblance of their properties to those of diamond. From that time, many methods have been used in the fabrication of DLC thin films [12-14]. It has been shown that, it is possible to produce DLC thin films having high hardness [11], good thermal conductivity [8, 10], low thermal expansion, low coefficient of friction and high chemical stability and resistance [18]. Furthermore, the high transparency in DLC films can be determined using Fourier based infrared technique [10]. For its physical properties, DLC thin films were considered as potential candidates for both passive and active electronics.

The term “*diamond-like*” is frequently applied to many types of non-crystalline or amorphous carbonaceous films. Generally, DLC films consist not only of amorphous carbons (a-C) but also of hydrogenated alloys (a-C:H) also known as hydrogenated amorphous carbon.

Using the ternary phase diagram of Figure 2.1, the various compositions of amorphous C:H alloys are shown on the  $sp^3 - sp^2$  axis and are generally characterised by interconnecting C-C networks [15]. Deposition techniques have been improved to generate amorphous carbon (a-Cs) with rising degrees of  $sp^3$  bonding. In this regard, deposition of thin films exhibiting ranges from  $sp^2$  bonding to somewhere towards almost complete  $sp^3$  bonding have been reported. If the fraction of  $sp^3$  bonding exceeds 70 % of the composition, the resulting carbon based film is termed as tetrahedral amorphous carbon (ta-C) and their properties differ entirely from those of a-C [16]. A range of deposition methods, such as plasma enhanced chemical vapour deposition (PECVD) [17], have been used to prepare ta-Cs. It is seen from Fig.2.1 that the fraction of  $sp^3$  bonding of carbon material is obviously not so large, whilst its hydrogen fraction occurs over a wide range. Thus, a more  $sp^3$  bonded material with less hydrogen which can be generated by high plasma density (PECVD) reactors is called hydrogenated tetrahedral amorphous carbon (ta-C:H) [18]. The properties of carbon based materials could still be improved through doping with silicon (Si), nitrogen (N), fluorine (F) and different metal atoms (Fe, Co, Ni,). The resulting materials are denoted as Si-C:H, a-C:H-N, a-C:H-F and Me-C:H. The principal structural difference between the diamond (natural or synthetic) and the diamond-like systems is the presence and the amount (sometime up to 60 %) of  $sp^3$  bonding. The relation between the amount of graphitic  $sp^2$  and aliphatic  $sp^3$  bonding is one of the most important features of DLC, which influences and determines not only the physical properties of DLC films but also their mechanical properties as well [19-23].

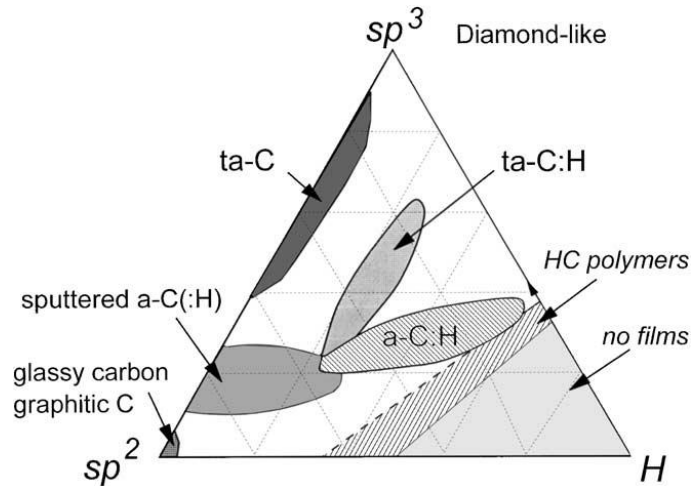


**Figure 2.1:** Ternary phase diagram of bonding in amorphous carbon-hydrogen alloys [15] .

Magnetron sputtering has developed rapidly over the last three decades to the point where it has become established as the process of choice for the deposition of wide range of industrially important coatings. The driving force behind this development has been the increased demand for high- quality functional films in diverse market sectors.

In many cases, magnetron sputtered films now perform better than other PVD processes, and can offer the same functionality as much thicker films produced by other surface coating techniques. Consequently, magnetron sputtering now makes a significant impact in application areas including hard, wear-resistant coatings, low friction coatings, corrosion-resistant coatings, decorative coatings and coatings with specific optical, or electrical properties [24], hence in this study magnetron sputtering has been used exclusively.

### 2.3 Deposition methods

A large number of processes are available [8, 25-29] for the deposition of DLC films, which rely on the lower density of  $sp^2$  relative to  $sp^3$  bonds. The application of hydrostatic pressure, impact, or some combination of these at the atomic scale can force  $sp^2$  bonded carbon atoms closer together

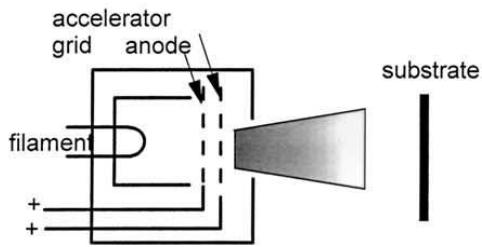
leading to the formation of the  $sp^3$  bonds. Different deposition techniques are shown schematically in figure 2.2.

### **2.3.1 Ion Beam Deposition Methods**

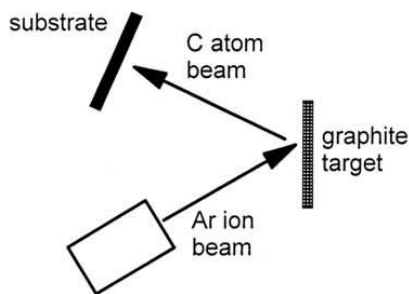
The first ever DLC was prepared using ion beam deposition. In an ion beam deposition system [Fig. 2.2(a-b)], there are two processes to produce the ion beam; in one, a hydrocarbon gas such as methane is ionised in a plasma and another one created by the sputtering of the solid target [30-32]. An ion beam is then extracted through a grid from the plasma source under a bias voltage onto a substrate. The hydrocarbon and carbon ions are directed with high speed in the high vacuum deposition chamber. The beam contains a wide flux of neutral species at a finite pressure. This may decrease the flux ratio of ions to neutrals to as low as 2-10%.

An appropriate solid phase ion source is generally a graphite target. These ions are sputtered by collision with argon ions. The carbon ions produced in this way condense onto a substrate surface leading to the deposition of the DLC film. A variation of this method is the mass selected ion beam, where the beam is passed through a magnetic field and only ions within a certain mass and energy interval are used for deposition. The disadvantage of the latter method is the very low deposition rate of order  $0.001 \text{ \AA s}^{-1}$  and the high cost and size of the apparatus.

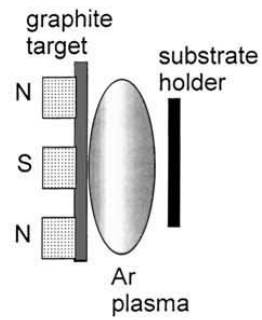
(a) Ion deposition



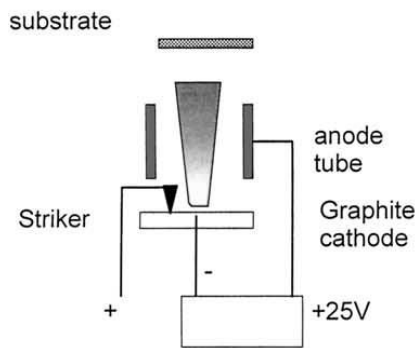
(b) Ion assisted sputtering



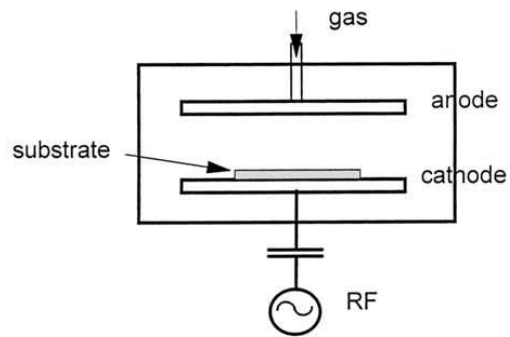
(c) Sputtering



(d) Cathodic Vacuum Arc



(e) Plasma deposition



(f) Pulsed laser deposition

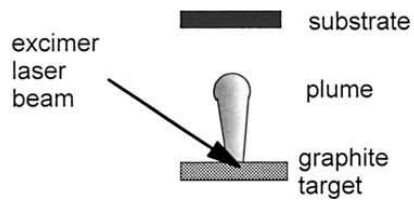


**Figure 2.2:** Schematics of various DLC deposition methods [29].

### 2.3.2 Sputtering Process

The most typical industrial process for the deposition of DLC is sputtering and the most common form use either DC or RF magnetron sputtering (Fig.2.2c), where a graphite cathode is sputtered by an Ar plasma [33]. The low sputter yield of graphite necessitates the use of magnetron sputtering to increase the deposition rate. Magnets are placed after the target to rotate and to increase the electron mean free path and subsequently enhance the degree of ionisation of the Ar gas to generate a sustainable plasma with a high ion density.

The extent of the magnetic field in the chamber can lead to either a balanced or unbalanced magnetron; unbalanced magnetrons are characterized by varying strength in the magnetic polarity of the annular magnets thus extending the net field towards the substrate. This leads to bombardment of the substrate. DC bias is used to vary the ion energy and in the selection of the sputter species. To produce a-C: H, a plasma of Ar ions and hydrogen or methane is used and for a-C:N<sub>x</sub> an argon-nitrogen plasma is used.

In another way, an ion beam of Ar sputters from the graphite target to create the carbon flux [33] and another ion beam of Ar is used to bombard the growing film, to increase the density of sp<sup>3</sup> bonding. This method is called ion beam assisted deposition (IBAD) or ion plating.

The basic sputtering process has been known for many years and many materials have been successfully deposited using this technique. However, the process is limited by low deposition rates, low ionisation efficiencies in the plasma, and high substrate heating effects. These limitations have been overcome by the development of magnetron sputtering and, more usefully, unbalanced RF magnetron sputtering [33]. This is a technique used to prepare a-C: H samples that have been used in this work. RF and DC magnetron reactive sputtering has been used in this study.

### **2.3.3 Cathodic vacuum arc System**

In this method, an arc is produced in a high vacuum from the instantaneous passage of high electrical current between two graphite electrodes (Fig. 2.2d) to generate an intense plasma with a high ion density ( $\sim 10^{13} \text{ cm}^{-3}$ ). The cathode spot creates particulates that are filtered by passing the plasma along a toroidal magnetic filter duct[34]. This is called filtered cathodic vacuum arc (FCVA). The advantages of FCVA are twofold:

- Produce a highly ionised plasma,
- Maintain high growth rates of 1 nm/s at reasonable costs.

The main drawback of the technique is the inadequate filtering of the particulates due to the instability of the cathode spot.

### **2.3.4 Plasma Enhanced Chemical Vapour Deposition Methods (PECVD)**

The RF- PECVD power is always connected to the capacitor which is coupled to the smaller electrode on which the substrate is set up, and the other electrode is connected to the earth. The RF power creates a plasma between the electrodes. As electrons move faster than the ions in the plasma, a sheath will generate near the electrodes with a high ion density. This forms a positive space charge, thus the plasma generates a positive voltage with regards to the electrodes, which balances the average electron and ion current to the wall [35]. The sheaths work just like a diode, in order that the electrodes have a DC self-bias voltage of the same value as the peak RF voltage. The RF voltage is split between the sheaths of both electrodes as in a capacitive divider, as stated by their inverse capacitance. So, DC self-bias voltage changes inversely with the electrode surface area [35]. The smaller electrode which has smaller capacitance received the wider bias voltage and consequently has negative value relative to the larger electrode. This becomes the substrate

electrode. The negative sheath voltage augments the speed of the positive ions to create the  $sp^3$  bonding on the substrate electrode. For DLC deposition, the plasma must be obtained at the lowest possible pressure, so that the Ar ion is maximised in the plasma atmosphere. However, even at 50 mTorr pressure, the ions are only roughly 10% of the film-forming flux. The ions can reduce their energy by collisions during the acceleration across the sheath. The ion energy doesn't depend anymore on the sheath voltage. It is important to use a low pressure to minimise these collisions and to maintain a narrow ion energy distribution. The sheath thickness decreases with increasing pressure [35] and the ion mean free path becomes less than the sheath thickness at low enough pressures. So, even at 50 mTorr there is still important ion collisions in the sheath, so that there is a large ion energy distribution and the mean ion energy is only about 0.4 of the sheath voltage [36-38]. As discussed, it is necessary to use lower pressure, but this is impossible for conventional PECVD as the plasma will not be deposited anymore on the substrate. The magnetic field can be applied to compress the plasma at the lower pressure and increase the electron mean free path. The use of the magnetic field increases the efficiency of ionisation, thus allowing the apparatus to work with very small pressures in the range of 0.5 mTorr. The ion mean free path overcomes the sheath thickness and the ion energy now becomes a narrow distribution [35-37]. The plasma beam source (PBS) that has a magnetic field that confines plasma so that it exits through an earthed grid. This ensures that the applied RF power to the movable electrode acquires a positive self-bias which repulses positive ions through the grid. The resulting plasma beam deposits on the substrate to form ta-C:H. At this instance the plasma beam is considered neutral [38]. The problem of the simple capacitive coupled PECVD system is that the ion current and the ion energy depend on the RF drive power. This means that the bias voltage varies with RF power and pressure, and the mean ion energy varies with the bias voltage. Generally, the magnetic field compresses the plasma to a

part of the anode area and variation of the anode position changes the bias voltage and subsequently the ion energy.

From the preceding discussion it is understood that high - density plasma sources are possible [35]. The plasma density ( $n_o$ ) and the electron temperature ( $T_e$ ) are two basic properties of the plasma. The plasma electrons have a Maxwellian energy distribution, which defines the electron temperature,  $T_e$ . The capacitive coupling at RF frequencies of 13.6 MHz, produces very little plasma and its density is very low, at most  $n_b \sim 10^9 \text{ cm}^{-3}$ . When the RF frequency increases and reaches a VHF or using an inductively coupled plasma (ICP), it improves excitation of the plasma. In another technique, known as electron cyclotron resonance (ECR) framework, microwave frequencies have been used [39, 40]. An ECR system consists of a large static axial magnetic field to make electrons vibrate at a cyclotron resonance frequency of 2.45 GHz. At this condition, the excited Ar atoms in the chamber intersects with the reactant gas, collide and transfer energy to the reactant gas. The latter, then deposits on the substrate. The best RF powered, high plasma-density is improved by electron cyclotron wave resonance (ECWR) source [39]. The ECWR source produces very high-density plasma of  $10^{12} \text{ cm}^{-3}$  or more, yet it does not control the ion energy and ion current density [39]. It has a small ion energy distribution with a width of less than 5%. The ECWR generates ta-C:H at a much higher growth rate ( $1.5 \text{ nm}\cdot\text{s}^{-1}$ ) compared to the plasma beam deposition (PBS) and gives uniform deposition over a diameter of 10 cm. It was the first industrialised, high-density PECVD source for DLC.

Generally, the properties of a-C:H depend on the precursor gas used in PECVD. Currently, benzene is chosen as a precursor with low ionisation potential due to its higher growth rate. The deposition rate rises exponentially with reducing ionisation energy [36].

### 2.3.5 Pulsed laser deposition (PLD) process

An ArF laser generates very short, high energy pulses, which can vaporise a solid target material and produce an energetic plasma plume [41-44] [45-49] which consists of ions which are directed towards the substrate. The main advantage of PLD is that it is a laboratory scale method used for deposition of many different materials ranging from large  $T_c$  superconductors to hard coatings.

### 2.4 Deposition Mechanism

As discussed earlier, DLC is dominated by the  $sp^3$  fraction obtained by a physical process, namely, ion bombardment [50]. The largest  $sp^3$  fractions are realised by carbon ions of energy ( $\sim 100$  eV).

The atomistic description of the deposition mechanism has undergone many improvements over the last century. It starts first by comparing the ion energy ranges and the efficiency for many processes of C and H ions in solid carbon [51]. Spencer *et al.* [41] suggested several mechanisms, for example, the idea that  $sp^3$  sites appear from the  $sp^3/sp^2$  ratio by a favoured sputtering of the  $sp^2$  sites. The sputtering efficiency is regarded as a function of an atom's cohesive energy, which is roughly the same for the  $sp^2$  and  $sp^3$  sites. This model has some analogue with later models such as the shock wave model; however, the shock wave is mostly used for higher ion energies and higher ion masses. Lifshitz *et al.* [19] applied Auger analysis of the depth profiles of medium energy C ions incident on Ni substrates to prove that growth was sub-surface. This method is known as sub-plantation. Lifshitz *et al.* then suggested that the  $sp^3$  sites increase by the displacement of  $sp^2$  sites. This model was improved by Moller [8], where it was shown that the preferential displacement is not a correct concept and they instead proposed a displacement threshold [8]. It was noted that the displacement threshold of graphite is slightly anisotropic.

Banhart [43] observed that the small displacement thresholds are  $sp^2$  sites. McKenzie *et al.*[9] proposed that  $sp^2$  bonded graphite occupied 50% more volume than  $sp^3$  bonded diamond. This situation appears to be amenable to the phase diagram of diamond and graphite that is shown in figure 2.3, with diamond clearly stable at higher pressures above the Berman-Simon line. It was further suggested by Davis [41] that the role of ion beam is to generate a compressive stress in the film, which shifts the film above the Berman-Simon line and thus stabilise the high pressure diamond (-like) phase. Further to this, Robertson [52-57] proposed that the sub-plantation created a metastable augment in density, which tends to cause the local bonding to change to  $sp^3$  preferential displacement, thus only sub-surface growth in a limited volume is needed to have  $sp^3$  bonding.

In the atomic range processes, generally the elastic collision of ions in materials is described by the binary collision approximation. The cross-section of the collisions decreases with the energy. When the ion energy becomes very large, the atomic radius is reduced leading to larger interstices within the lattice. At a certain energy, the ions cross an interstice and traverse the surface layer. This ion energy is denoted by the penetration threshold  $E_p$ . The minimum energy of an incoming ion necessary to lift an atom from a bonded network and create internal vacancy-interstitial pair is called the displacement threshold,  $E_d$ . The surface of the solid behaves as an attractive potential barrier of height  $E_B$ , the surface binding energy and thus the net penetration threshold for free ions is

$$E_p \sim E_d - E_B \quad (2.1)$$

For an amorphous carbon on the surface [58], if the ion energy is small, it will not be allowed to penetrate the surface, thus it will only be attached to the surface to form its lowest energy state which is the  $sp^2$  configuration. If the ion energy is larger than  $E_p$ , it has a chance to penetrate the

surface, and enter a sub-surface interstitial site. Thus increase the local density. In the latter, the configuration will be changed around that atom with regards to the new density. As it is amorphous, atomic hybridisations can become more  $sp^2$  if the density is diminished and more  $sp^3$  if the density is improved. The penetration becomes deeper into the solid, when the energy and ion range increases. A rather small fraction of ion energy is used to penetrate the surface, and another fraction of about 30% is dissipated in atom displacement. The ion must dissipate the rest of this energy ultimately as phonons (heat) [40] .

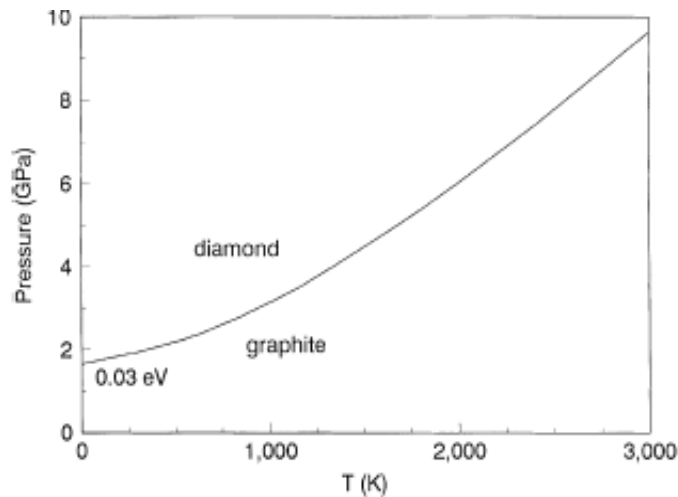


**Figure 2.3:** Berman-Simon phase diagram for carbon [40].

### 2.4.1 Hydrogenated amorphous carbon (a-C:H)

The actual deposition of a-C:H consists of many processes as shown figure 2.4. The properties of plasma deposition depend strongly on the bias voltage and hence on the ion energy of carbon, which shows that carbon ions are very important element in the deposition of a-C:H. This is not the case for ta-C as the ion flux fraction is around 10% [59, 60]. The deposition of a-C:H can be obtained using different source gases such as  $CH_4$ ,  $C_2H_4$ ,  $C_2H_2$  and  $C_6H_6$ . The film density

variation with bias voltage for each source gas can be plotted on a scale of bias voltage per C atom in the molecule. After this, the maxima in density are found at the same energy [61]. This shows that the action of the ions is still through the sub-plantation. It means the energy of molecular ions incident at the film surface will be divided into atomic ions and the energy will be spread uniformly, hence each atomic ion will sub-plant independently at that energy. A complete model of a-C:H can be described by the consideration of the neutral species and dehydrogenation [3, 6, 62-72], this is a chemical process that also benefits from sub-plantation. The plasma deposition can be summarised as consisting of three stages, namely;

- the reactions in plasma (dissociation, ionisation, etc.)
- the plasma-surface interaction
- the sub-surface reactions in the film.

The plasma reactions are conducted by the energetic electrons which are defined by the electron energy distribution (EED). These are only important in the case of high-density plasmas, since the mass spectra of the dissociation pattern of CH<sub>4</sub>, C<sub>2</sub>H<sub>4</sub> and C<sub>2</sub>H<sub>2</sub> at different pressures shows that un-dissociated source gas molecules are still the majority in the plasma [73].

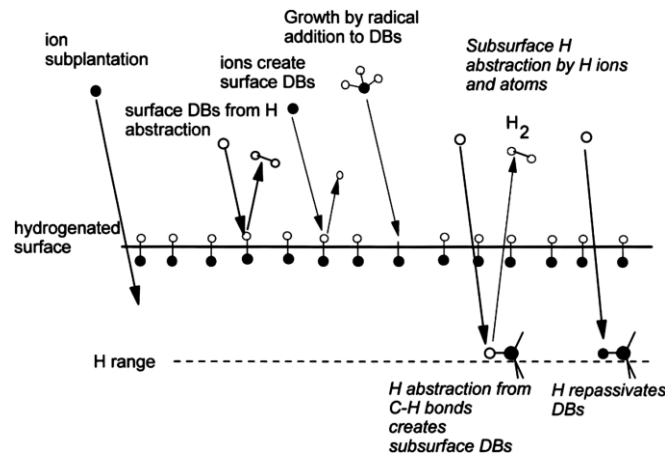


**Figure 2.4:** Component processes in the growth mechanism of a-C:H [59, 60].

The plasma species which impact onto the substrate compose primarily of ions, neutrals and a large amount of atomic hydrogen 'H'. It is thus expected that the neutral species participate in the growth as the mass deposition rate overcomes the rate due to ions alone. The first effect, namely the increase in growth rate is observed when the temperature increases. This effect has been attributed to the weak adsorption of the neutrals on the surface at low temperatures and also by the neutral species desorption at higher temperatures [62, 63]. The input of each neutral species to the growth rate is a function of their sticking coefficient. The a-C:H surface is generally covered with C-H bonds, thus it is chemically inert. Di-radicals and other unsaturated species can be introduced straight into surface C-C or C-H bonds, thus these species are very active in the film as their sticking coefficients are strong and tend to 1. On the contrary, methane has very low sticking coefficients ( $10^{-4}$ ) and the effect is thus significantly minimised. The mono-radicals have a moderate smooth effect. They cannot be introduced directly into a bond; they can only interact with the film if there is an existing dangling bond on the surface. They will be enjoined to the bond to form a C-C bond. The dangling bonds have to be created by displacement of an H from a surface C-H bond. Generally, this can be induced by an ion moving an H atom from the bond, or by an H atom abstracting H from the bond, or by another radical such as  $\text{CH}_3$  abstracting H from the C-H bond. Measurement have shown that atomic H' is the most efficient species for abstraction (30 times faster than  $\text{CH}_3$ ) [71]. The  $\text{CH}_3$  adds to this dangling bond. So, the effective sticking coefficient of  $\text{CH}_3$  is small, but it becomes strong in the presence of atomic hydrogen [70, 71]. For neutral hydrocarbon species, the effect is not strong and they can only react at the surface. H atoms are too small and can only penetrate about 2 nm into the film [88]. There, they are able to remove again H from C-H bonds and form sub-surface dangling bonds and  $\text{H}_2$  molecules. Some of these dangling bonds will be re-saturated by incident atomic H. Carbon and hydrocarbon ions can cause

sub-plantation and are capable to go deeper into the film. In addition, the more important role of ions in a-C:H is to remove H from C-H bonds. This H can then abstract other H' to form H<sub>2</sub> molecules, and be removed from the film. This is the principal method which causes the H fraction of PECVD a-C:H to decrease with increasing bias voltage. Some of the atomic H' does not recombine, but finds dangling bonds to re-saturate [6]. As hydrogen ion mass is small, they do not strongly interact with C atoms. So, H<sup>+</sup> ions have the longest range and reach highest depth into the film [73]. They experience the same reactions as atomic H', but to a greater depth. Therefore, von Keudell [73] concluded that a-C:H films have three characteristic depths:

- the surface itself which is controlled by hydrocarbon and hydrogen species reactions
- an upper 2 nm in which chemistry is controlled by reactions of atomic H',
- larger ion energy dependent depths for which reactions are controlled by H<sup>+</sup> ions.

## **2.5 Nucleation and Thin film growth**

The deposition of the films of various materials such as metals, ceramics and plastics onto a substrate can be achieved through different deposition techniques. Basically deposition techniques are categorized in a large sense as physical vapour deposition and chemical vapour deposition processes. The PVD processes include: vacuum evaporation, pulsed laser deposition (PLD), molecular beam epitaxy (MBE) and sputtering. In this study RF and DC magnetron sputtering were used to fabricate thin films using the concepts of the Thornton model. Sputter deposition methods are used to generate and maintain a desired plasma and to establish a bias or electric field for the acceleration of ions to the electrode or target being bombarded. The ad-atoms are later deposited as thin films on the substrate. Several processes occur upon bombardment of the target by Ar<sup>+</sup> and hydrocarbons [74].

### **2.5.1. Film nucleation and growth**

Thin solid films are generally prepared from the vapour phase on a substrate by a process consisting of nucleation and growth of individual islands (or clusters). A short summary of the ensuing processes is illustrated in fig 2.5. At the initial stage; small nuclei are formed from individual atoms or molecules. Then, as time progresses, these islands coalesce and form a continuous film. The enhanced coalescence increases the thickness of the film [74]. The morphology and structure of the thin film depends on the size, shape, the coverage /area density, packing fractions of the substrate and growth rate of the individual islands. Atoms originating from the glow discharge are adsorbed on the surface. The incident rate at which the atoms strike the substrate surface is mostly dependent on the deposition parameters. The diffusion of the adsorbed atoms is dependent on the surface temperature and substrate bias voltage. Adsorbed atoms either re-evaporate or form clusters which consequently develop into large clusters. Generally, clusters greater than a critical size is thermodynamically stable (critical nucleus) and therefore proceed to form thin films. Single atoms may diffuse across the substrate to be part of the stable clusters, or else they may impinge directly on the grown clusters and become incorporated in the clusters [74].

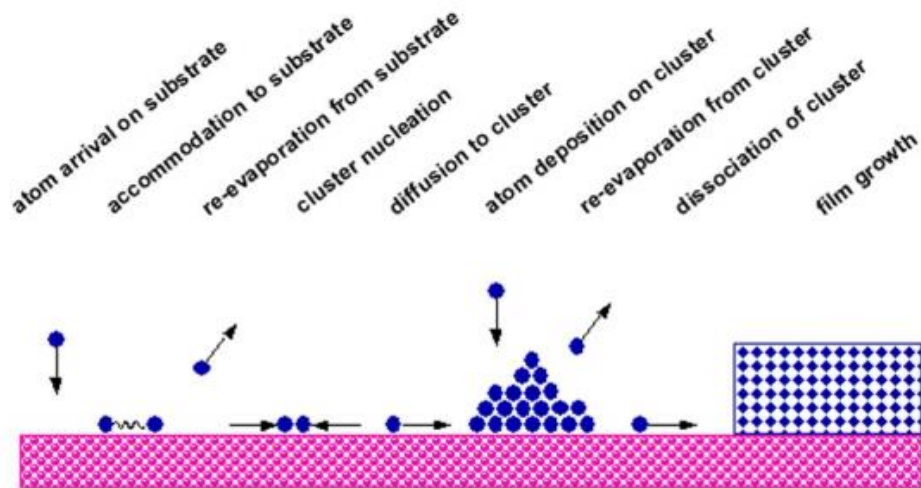


**Figure 2.5:** Process in the nucleation and growth of the films on a substrate [74].

### 2.5.2 Structural Zone Model (SZM)

The mobility of the ad-atoms during growth is dependent on the energy given to the atoms and this has an effect on the microstructure of the film. The energy given to an atom can be supplied by several different mechanisms namely;

- Thermal effect (substrate temperature),
- Ion bombardment
- Chemical reactions at the substrate.

Thin films produced by these mechanisms conform to the zone classifications of the structural zone model. Irrespective of the type of material, the SZM is appropriate to illustrate the nature of the morphology and microstructure of the films as a function of the ad-atom species or energy.

The parameters that are used in this model for determining the microstructure of the films are:

- substrate temperature,
- working gas pressure,

- bias voltage applied to the target and substrate, and its polarity
- thermal characteristics of the target.

This model is based on the substrate temperature ( $T_s$ ) which affects predominantly the film surface structure through ad atom mobility, based on the ratio of substrate and melting temperature of the target material ( $\frac{T_s}{T_m}$ ). The film microstructure is thus divided into 3 main structural zones with the following boundary temperatures;

$T_1 = 0.3 T_m$  and  $T_2 = 0.5 T_m$ . At low temperature ( $T < T_1$ , zone 1), the surface diffusion of ad-atoms is negligible. This leads to the formation of columnar structures. Films produced at higher temperatures ( $T_1 < T < T_2$ , zone 2) show large columns. In this case the surface diffusion of ad-atoms is enough to engender surface crystallizations of the film. The films deposited at ( $T > T_2$ , zone 3) result in big grains with flat and faceted faces as shown in figure 2.6. An increase in temperature produces a similar effect on the adsorption and mobility of the atoms. Equivalent to the temperature effect is the substrate bias voltage which determines the energy of the ion dissipated in the film in the form of heat. This will influence the size of the grains and thus affect the mechanical properties of thin films by increasing the deformation of the lattice or grain size. This causes high residual stress and low adherence between the substrate and the films. The nucleation and growth of thin films are entirely dependent on the thermodynamics and kinetics of the deposition and the substrate surface interaction between the substrate material and the ad-atoms [75].

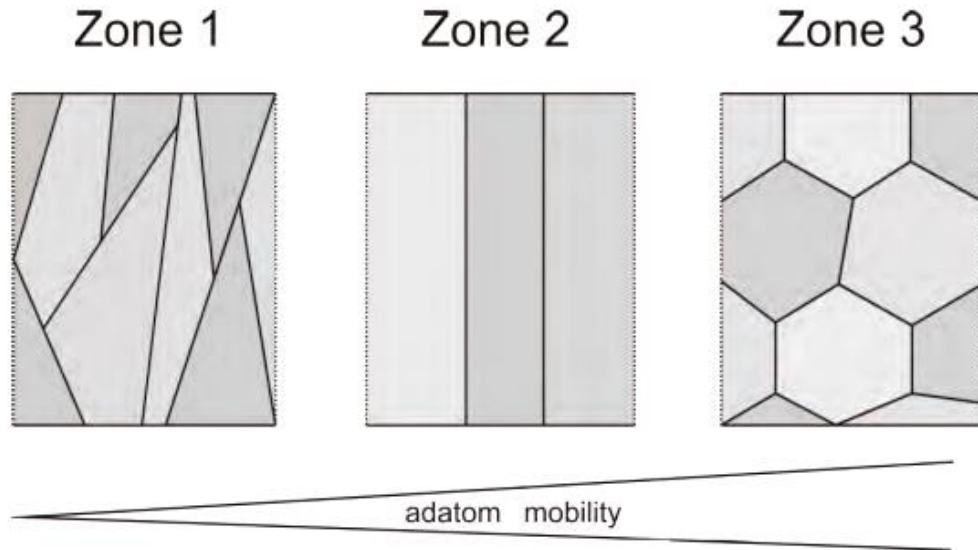


**Figure 2.6:** Typology of structure -zone [76].

## 2.6. Atomic structure and characterisation

### 2.6.1. Bonding configuration

Carbon has three types of hybridisation,  $sp^3$ ,  $sp^2$  and  $sp^1$  as discussed in the section 1.1. There are carbons with four  $sp^3$  orbitals due to the directional covalent bonding. They consist of strong  $\sigma$  bonds, which form with the adjacent atoms. Other carbon atoms have three  $sp^2$  orbitals which form the  $\sigma$  bonds while the fourth orbital forms the  $\pi$  bond with one or more neighbouring  $\pi$  orbital. The  $sp^1$  configuration constitutes of two  $\sigma$  bonds along the  $\pm x$ - axis and two  $p_\pi$  bonds formed in the y and z planes. All the C-C and C-H bonds in the valence bands form filled  $\sigma$  states, however in the conduction band the  $\pi^*$  states are empty. The valence and conduction bands are separated by a large  $\pi$ - $\pi^*$  gap [77] as seen for diamond. On the other hand, the  $\pi$  bonds of  $sp^2$  and  $sp^1$  sites are occupied by  $\pi$  and empty  $\pi^*$  states, which are separated by very small  $\pi$ - $\pi^*$  gap [78, 79] as shown in Fig. 2.7. The simple model of atomic structure is based on the properties of  $\sigma$  and  $\pi$  bonds [80, 81]. Generally, it has been observed that with a very strong  $\pi$  bonding energy, the  $sp^2$

sites will form  $\pi$  bonded clusters within a  $sp^3$  bonded matrix. Therefore, the cluster size is inversely proportional to Tauc gap. However, this model does not give a good estimation of cluster size [82, 83], nevertheless it is useful for the characterisation of the structure in amorphous carbon [84]. Jacob and Moller [6] were the first to use a ternary phase diagram of the carbon-hydrogen (C-H) system. Their model established two important parameters that determine the structure and properties of DLC, namely, the fraction of  $sp^3$  bonded carbon sites and the hydrogen content. The ordering of  $sp^2$  sites is a third important parameter, principally for the electronic properties of DLCs.

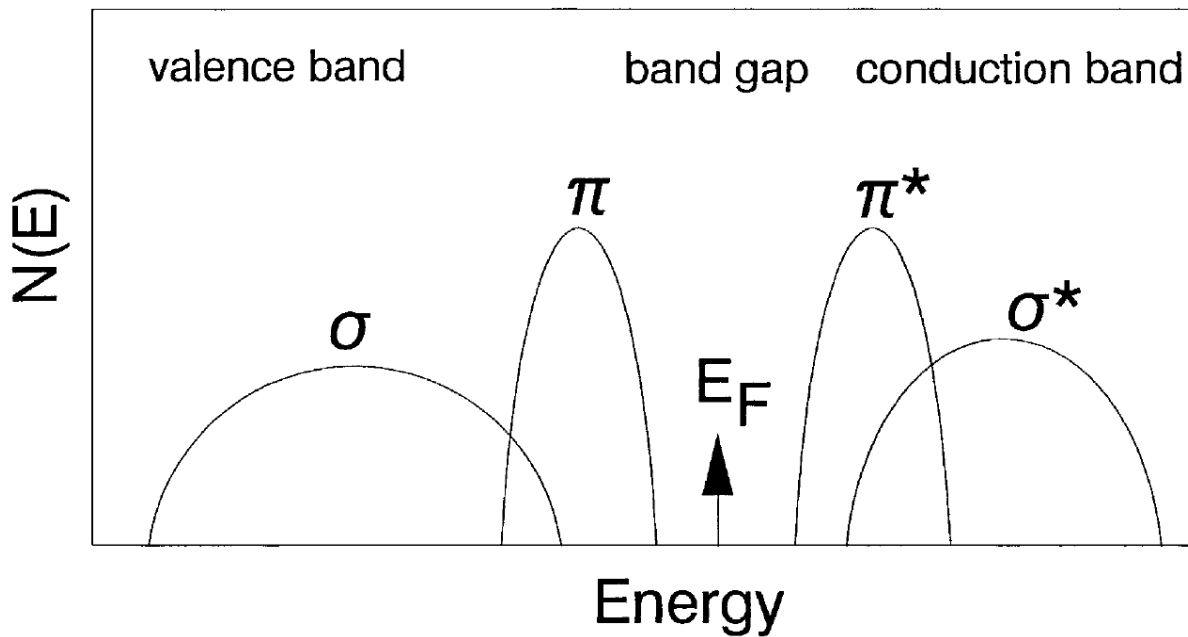


**Figure 2.7:** Schematic of density of state of carbon showing  $\sigma$  and  $\pi$  states [85].

In addition, there are many other methods of characterisation used to determine the structure parameters, such as Raman spectroscopy, Fourier Transform Infrared (FTIR), X-ray diffraction, Nuclear Magnetic Resonance and X-ray reflectivity. These will all be used as complimentary techniques.

## 2.6.2 Raman spectroscopy of carbon based materials

When monochromatic light is incident on an atom or a molecule, most of the radiation will be transmitted, some will be absorbed, while a very small fraction will be scattered by the molecules in directions different from that of the incoming radiation. About 0.01 - 0.1 % of the radiation will be elastically scattered, that is, no energy will be lost and the frequency of the incident and scattered radiation will be the same. This type of scattering is also called Rayleigh or Classical scattering, which is of no interest in Raman spectroscopy.

A minute fraction ( $10^{-6} - 10^{-4}$ ) of the scattered radiation will be in-elastically scattered. The inelastic scattering of light by matter was theoretically predicted in 1923 and the first experimental observation was made by C.V. Raman in 1928 [86]. Raman discovered that the visible wavelength of a minute fraction of the radiation scattered by certain molecules differs from that of the incident radiation and thus the shift in wavelength depends on the chemical structure of the molecule responsible for the scattering. The effect, known as the Raman effect, was due to the interaction of the photons of incoming light with the vibrations and rotations of the molecules [86, 87].

Raman spectroscopy is the most commonly used technique for structural characterisation of carbon based materials, such as diamond [73, 77], graphite, DLCs and carbon nanotubes [78]. It is a non-destructive and non-invasive technique. The Raman spectrum of diamond consists of a single Raman active mode,  $T_{2g}$  at  $\sim 1332 \text{ cm}^{-1}$ . Single crystal graphite on the other hand consists of a zone centre Raman active mode at  $\sim 1580 \text{ cm}^{-1}$ . This mode is of the  $E_{2g}$  symmetry and it has been labelled as the G band. Disordered graphite however displays two modes, the first mode at  $\sim 1350 \text{ cm}^{-1}$  which has been assigned to the zone centre mode of  $A_{1g}$  symmetry and this occurs at K- point phonons [88] and it is labelled D for disorder. In addition, the second mode known as the G peak

occurs between 1580 and 1600  $\text{cm}^{-1}$ . It is surprising that all the Raman spectra of most disordered carbons is dominated by the D and G modes, even when there are no clustering graphite [89]. These Raman parameters are very important in the derivation of the structural information of DLCs.

A very small part of the light is scattered in-elastically. It is this scattering which gives information about energy levels of the sample. The light of an incident photon ( $\omega$ ,  $k$ ) is scattered by the change in polarizability  $\xi$  due to a lattice vibration. This change in polarizability causes the inelastic scattering of photon ( $\omega'$ ,  $k'$ ) known as Raman scattering. The polarisation can happen when the electronic ground state is excited by incident photon into a virtual level at energy  $E$  or into real levels at  $E$ . The latter case is denoted resonant Raman scattering [88]. The  $\pi$  states lie at energies lower than the  $\sigma^*\pi^*$  states and therefore are much more polarisable [90]. Thus Raman cross-section of  $sp^2$  is larger than that of  $sp^3$  sites [91-93]. The G mode consists of the stretching vibration of any pair of  $sp^2$  sites, whether in chains or in rings [94]. The D mode is the breathing mode of  $sp^2$  sites. Mapelli *et al.* [87] proposed a model in which the force field is based on the  $\pi$  bond clusters and the polarizability. The model further postulates the short-range field as the source of the long-range force. Thus the polarizability of  $\pi$  states will be also long-ranged, and this gives the modes quite large effective charges. In addition, the long-range polarizability intensifies both the G and D modes which are the bond stretching modes. Further, the D mode is intensified more as it is the breathing mode of the six-fold rings. This makes the D mode the double resonance [95]. All these factors increase G and D breathing modes and eliminate the modes of other symmetries. The intensity of D mode varies with the nature of the atomic order. Tuinstra and Koenig [78] proposed that the ratio of D and G peak intensity,  $I_D/I_G$ , is inversely proportional to the cluster size in the form;

$$\frac{I_D}{I_G} = \frac{C(\lambda)}{L_a} \quad (2.1)$$

Where  $C(\lambda)$  is a wavelength-dependent constant ( is equal to 0.0055 for 514.5nm) and  $L_a$  is the cluster diameter or in-plane correlation length.

Equation (2.1) gives the dependence of the intensity ratios with the number of rings at the border of the clusters and it is only valid for  $L_a$  values  $> 2$  nm. Lower cluster sizes have been observed to satisfy the following relationship for the intensity ratios of the D and G bands as shown [80];

$$\frac{I(D)}{I(G)} = C(\lambda)L_a^2 \quad (2.2)$$

The intensity ratio decreases when the number of rings per cluster decreases and the fraction of chain groups increase. For DLC, the grain size is generally below 2 nm, this means the eqn. (2.2) is valid.

In conventional PECVD deposited a-C:H, the  $sp^3$  content increases with increasing H content. The role of H in a-C:H is to saturate the C=C bonds and convert  $sp^2$  C sites into  $sp^3 =CH_2$  and  $\equiv CH$  sites [96] and in the process stabilizing the  $sp^3$  fraction. The a-C: H has a large  $sp^2$  content [97] and thus a small band gap due to the presence of the  $\pi$  states. The  $sp^2$  sites in this type of material are therefore strongly arranged in aromatic rings thus causing the D peak to appear in the Raman spectra.

For the case where the a-C:H with maximum H content has a high  $sp^3$  content, the band gap will be very large and the D peak will be absent. This means that the  $sp^2$  sites will arrange in very small clusters. The H bonds which form bonding chains at olefinic sites start to become like polyacetylene. The Raman spectra of a-C:H are best understood in the following way:

- Some  $sp^3$  sites of a-C:H are arranged in form of aromatic rings
- while the other  $sp^3$  sites are in chains.

All these factors decrease the G peak with increasing  $sp^3$  content in a-C:H. Additionally, Tamor and Vassel [98] have established an empirical relation between the Raman parameters and optical band-gap of amorphous carbon thin films. This theory is also valuable in films fabricated using RF magnetron sputtering since the intensity dependence of the G peak scales with the increase in  $sp^3$  fraction, however there are exception to the rule particularly in the case where hydrogen does not stabilize the  $sp^3$  fraction [51].

### 2.6.3 Fourier Transform Infrared (FTIR) spectroscopy

FTIR spectroscopy is another widely used technique to characterise the bonding in a-C:H. The IR absorption consists of C-H stretching modes at  $2800-3300\text{ cm}^{-1}$  and C-C modes and C-H bending modes below  $2000\text{ cm}^{-1}$ . Generally, the C-H stretching modes can be broken down into three types [44];

- the  $sp^1 \equiv \text{C-H}$  modes centre on  $3300\text{ cm}^{-1}$ ,
- the  $sp^2 = \text{CH}_n$  modes detect from  $2975$  to  $3085\text{ cm}^{-1}$ ,
- $sp^3$ - C-H<sub>n</sub> modes locate from  $2850$  to  $2955\text{ cm}^{-1}$ .

The deconvolution of the C-H bands using Gaussian profiles has been widely used to estimate the fraction of  $sp^3$  bonds. The deconvolution process provides information on the broadening and shifting of the vibrational modes, so the decomposition of C-H stretching modes into the individual bands is not unique [40]. However, the variation of the oscillator strengths of different C-H stretching modes makes the determination of  $sp^3$  [40] to be inconsistent and unreliable despite its growing popularity, and thus in this thesis, complimentary approaches such as direct measurement

of the  $sp^3$  content using X-ray photoemission spectroscopy have been used and describes later in 2.6.6.

#### **2.6.4 Hydrogen content in disordered carbon**

The hydrogen fraction of a-C:H can also be obtained using the nuclear techniques such as, nuclear reaction analysis (NRA), nuclear magnetic resonance (NMR) and elastic recoil detection analysis (ERDA). There are also other methods such as combustion, hydrogen evolution or IR spectroscopy which have been used for determining the hydrogen content. The nuclear processes are largely used even though they require special facilities that are very expensive. Their advantage is that they can derive the H:C ratio without measuring the film thickness. The NMR requires the proton decoupling utilisation to derive H content by separating the bonds of carbon and hydrogen [99]. It is a unique process for determining the following;

- the fraction of each type of C
- the hybridisation of C
- the number of bonded hydrogen

The two other methods usually used to determine hydrogen for a-C:H are the thermal evolution and IR but they are not easy to process. In thermal evolution, the a-C:H is heated and the amount of  $H_2$  with some hydrocarbons such as  $CH_4$  and  $C_3H_8$  are released. This requires a complete mass spectrometer analysis for improved accuracy [100, 101]. In IR spectroscopy on the other hand, the spectrum of the C-H bonds stretching modes can be obtained in the measurement range of  $\sim 2900\text{ cm}^{-1}$  after background subtraction. The integrated weight under curve is derived and the number of H atoms per unit area is determined by multiplying by an absorption strength, A.

$$n_H = A \int \frac{\alpha(\omega)}{\omega} d\omega \quad (2.3)$$

The problem of this technique is that A is not a constant. Jacob and Unger [92] obtained a series of values of A after performing calibration experiments. This problem has been resolved by decomposing the IR band into its component absorption bands and the integrated intensity multiplied by the appropriate absorption strength  $A_j$ . Ristein *et al.*[90] reported in detail, using bond absorption strength scaled from molecules. They found the values of H content from IR to be approximately the same with those obtained by H evolution. However, the fundamental question of whether all hydrogen involved is bound at C-H bonds remains unanswered and controversial.

Some interstitial H<sub>2</sub> molecules have been observed by inelastic neutron scattering. Grill and Patel [102] argued that in extreme cases, 50% of the hydrogen could be unbound. However more recent NMR data by Donnet *et al.*[103] found a much lower H content and neutron scattering only found a small molecular hydrogen component. Thus, in general, this is a less critical issue.

### **2.6.5 Density determination by X-ray reflectivity (XRR)**

The mass density of diamond is 50% greater than graphite, because the inter-layer bonding of graphite takes considerable space. This difference carries over into the amorphous phase, and indeed a linear correlation of density and sp<sup>3</sup> fraction is expected for a mixed sp<sup>2</sup>- sp<sup>3</sup> network. Thus, the density is also a useful indicator of sp<sup>3</sup> fraction particularly in hydrogen-free carbons. The presence of hydrogen complicates the problem, as CH<sub>x</sub> groups also occupy a lot of space, so CH<sub>x</sub> groups reduce the density. The density can be measured by floatation techniques or by use of X-ray reflectivity (XRR) [92].

XRR is a technique widely used to determine the density, film thickness and surface roughness using a high resolution x-ray diffractometer based on symmetrical arrangement of incident and secondary beam optics. The angles of  $\omega$  and  $2\theta$  can be configured from sample alignment with scanning movement of speed 2:1. The scanning range is set to measure from the critical angle of  $\theta_c \sim 0.8^\circ$  to angle  $2\theta = 5^\circ$ , where the intensity diminishes to background levels. The XRR principle is based on total external reflection where the incident X-ray beam angle is equal to or less than the critical angle,  $\theta_c$ . Thus, the density of the surface film obtained from the critical angle for total reflection depicted in Figure 2.8 is obtained as;

$$\Theta_c = \lambda \sqrt{\frac{r_e \rho_e}{\pi}}, \text{ where } r_e \text{ is the Bohr atomic radius, } \rho_e \text{ is the electron density.}$$

The oscillations in the XRR spectrum are a function of the film thickness and refraction index of the film in which information about the film thickness is obtained. The film thickness can be given

$$\text{by } d = \frac{1}{2} m \lambda \frac{1}{\sqrt{\theta_m^2 - \theta_c^2}}$$

where  $m$ -th represents the interference maximum and  $d$  stands for thickness. Surface and interfacial roughness arising from the decay of the oscillation is extracted using the Fresnel reflection coefficient,  $\rho_{v,h} \exp\left(-\frac{d}{2\sigma^2}\right)$ . A typical X-ray reflectivity spectrum formed from the interference of the reflected X-rays at the film-substrate interfaces is shown in Figure 2.8. The X-ray reflectivity data in this work were fitted to the theoretical data using *Leptos* software from Bruker AXS [76].

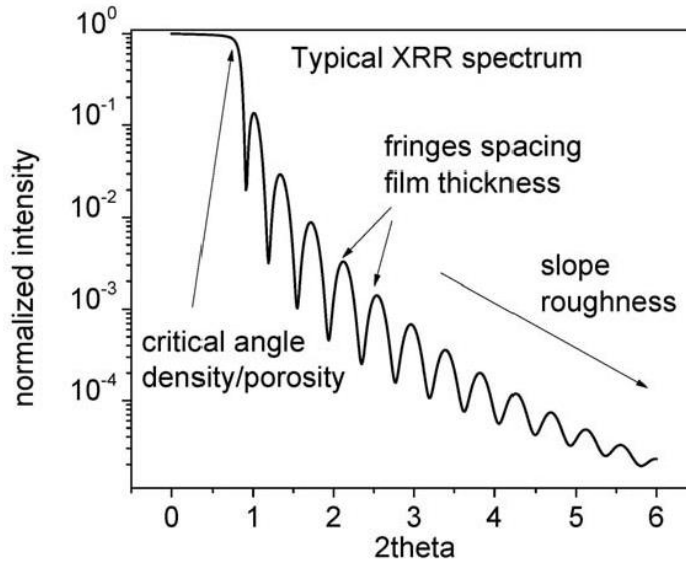


**Figure 2.8:** X-ray reflectivity pattern illustrating Kiessig oscillations of a thin film on a substrate system [104] .

### 2.6.6 X-ray photoemission spectroscopy (XPS)

XPS consists of measuring the shifts of the core levels which are associated with the chemical bonding of each site. The largest shifts are caused by the Coulombic potential from ionic charges on adjacent atoms. The Si-O band is polar, Si 2p level is shifted by 4 eV from its position in Si, whereas for carbon the bonding is homopolar and thus the shifts are small. The small shift of the carbon core level is of the order of 0.9 eV between diamond and graphite [105]. In the study of DLC films, XPS is mainly utilized to obtain the elemental composition and the quantitative characterization of the fraction of  $sp^3$  and  $sp^2$  carbons at the surface. Firstly, all elements except hydrogen or helium can be detected by XPS. Furthermore, by focusing on the carbon orbital C1s, detailed information about  $sp^3$  and  $sp^2$  carbon can be obtained. Due to the difference of the local environment, the binding energy of  $sp^3$  is slightly higher than that of  $sp^2$  carbon and so by using Gaussian-curve fitting procedure, it can be deconvoluted into two separate peaks with the higher

peak corresponding to  $sp^3$  carbon and lower peak due to  $sp^2$  carbon [105]. In the present study, the apparatus used could not fully distinguish the  $sp^2$  and  $sp^3$  fraction binding energy. Fortunately, that problem was solved by using Auger electron spectroscopy (AES) technique.

## **2.7 Electronic structure of disordered carbon**

### **2.7.1 The $\sigma$ and $\pi$ states**

Disordered carbons are composed of  $sp^2$  and  $sp^3$  sites. The  $sp^3$  form only the  $\sigma$  bonds in the  $\sigma^*$  states while the  $sp^2$  sites have the  $\pi$  states and the  $\pi^*$  states. All electronic properties are dependent [102] on the  $\pi$ - $\pi^*$  and  $\sigma$ - $\sigma^*$  states. They need to be treated separately because their associated bonds do not have similar characteristics. The  $\sigma$  bonds have two centre-bond orbitals between neighbouring atoms. The  $\pi$  band can form two-centre bonds such as ethylene and in general  $\pi$  orbital interacts with  $\pi$  states and form a conjugated system that can make a continuous linkage of  $\pi$  bonds as in polyacetylene or graphite. These bonds are termed conjugated bonds. It is impossible to separate conjugated bonds into two-centre bonds [106]. This situation creates wider range forces and larger range polarizabilities [106].

### **2.7.2 Cluster model**

The cluster model is the first useful model which explains in a simple way the electronic structure and bonding. This is done by taking the Huckel approximation of treating  $\sigma$  and  $\pi$  states separately [106]. The model describes the  $\sigma$ - and  $\pi$ - states at different energies with the  $\pi$  states located in a plane orthogonal to the  $\sigma$  bonds at  $sp^2$  sites. This configuration ensures that the interaction of the  $\pi$  states and  $\sigma$ -bonds are minimal [73, 77]. The principal effect postulated by this model is that  $\pi$  bonding promotes a clustering of  $sp^2$  sites, thus the binding energy of the occupied states is lowered if a half-filled band creates a gap in this band at the Fermi level,  $E_F$ . The model requires that the

$sp^2$  sites form planar clusters by maximising the  $\pi$  interaction. The  $\pi$  bonded clusters are controlled by a  $sp^3$  bonded matrix. The ordering of  $sp^2$  sites determines the electronic properties and the optical gap, as their  $\pi$  states locate nearest to the Fermi level, while the  $sp^3$  is correlated to the mechanical properties [107]. This model works well for micro-crystalline graphite as well as DLC thin films. However, as-deposited DLC's are more disordered to fit in the description of the cluster model. The band gap ( $E_g$ ) of aromatic clusters in graphite, have minimum band energies given by [78, 107].

$$E_g \approx \frac{2\gamma}{M^{1/2}} \approx \frac{2\gamma}{L_a} \quad (2.4)$$

Where  $\gamma$  is the nearest neighbour V(pp $\pi$ ) interaction, and M the number of six-fold rings in the cluster. M is related to the cluster diameter length  $L_a$  as  $M \approx L_a^2$ .

The problem with the cluster model is that the clusters must be sufficiently large for measurable band gaps. Such clusters are not found experimentally in as-deposited a-C and a-C:H. In the Raman spectroscopy, it was found that the  $sp^2$  sites were arranged principally in small olefinic rather in aromatic clusters. It is commonly known that the cluster model furnishes a reasonable description of micro-crystalline graphite and thermally annealed DLCs, but it greatly over-estimates degree of order in as-deposited DLCs [108].

### 2.7.3 Network calculations

Direct simulations of networks have produced the best theories of the electronic and atomic structure of amorphous carbons. The molecular dynamics simulations are carried out as function of density to determine how the  $sp^3$  fraction varies with density in carbon based materials.

Frauenhein *et al.* [109] used an empirical core-core repulsive term to give the correct bond length. This method provides a good level of approximation to retain sufficient accuracy, while

being able to expand enough networks. These calculations were the first to show that  $sp^2$  sites in ta-C and a-C:H were mainly organised in chains and not in rings, in contrast to the cluster model [109]. They also found band gaps comparable with experiment. These results emphasised that it was possible to have small gaps even for small clusters. The smaller gaps arise because they are controlled by the distortions of the  $\pi$  bonding from the aligned configuration. Simulations were carried out for networks wide range of densities and hydrogen contents. A recent simulation has now found aromatic rings in low density a-C: H [108]. There have been few simulations of the structure of a-C:H [110]. Bilek *et al.*[111] found a network with surprisingly graphite ordering of  $sp^2$  sites.

#### **2.7.4 Optical gap**

In the discussion of the cluster model on section 2.7.2, it is the orientation of  $\pi$  states on the  $sp^2$  sites that was observed to determine the band gap  $E_g$  according to eqn. (2.4) from [65] .

This cluster model does not give a good estimation of the size of the clusters. It was found that the distortions of the clusters determine and affect the size of the band gap. Thus it is not possible to provide a simple expression for the band gap, corresponding to eqn. (2.4). Researchers such as Frauenhiem and co-workers [108], Chen and Robertson [110] , and McCulloch *et al.*[112] have found the same result showing that the band gap increased with decreasing  $sp^2$  content. The presence of hydrogen has little direct effect as the C-H states locate well away from the band gap region. This theory gives the same trend with the variation of experimental values of Tauc gap against  $sp^2$  fraction for a-C:H, ta-C:H and ta-C films [112] . In an amorphous semiconductor where there is no true gap, an arbitrary definition must be used for the optical gap. Thus there are two most common concepts that are used to represent the band gap in disordered materials, namely;

- the  $E_{04}$  gap which is defined as the energy at which the optical absorption coefficient  $\alpha$  is  $10^{-4} \text{ cm}^{-1}$ ,
- the Tauc gap which is the intercept of energy in the expression;

$$\alpha E = \alpha (E - E_g)^2 \quad (2.5)$$

Tagliaferro and co-workers [113] carried out a simple model of the optical transitions which postulated that the increase of band gap with decreasing  $sp^2$  content [114] could be related to a decrease in the width of the  $\pi-\pi^*$  bands, with a constant  $\pi-\pi^*$  separation. The gap depends generally on the order of  $sp^2$ , which does not vary simply with  $sp^3$  fraction. It means therefore that the gap does not vary with  $sp^2$  content all the time. The cluster model does not give correct information but it can be useful in the case of a network of amorphous carbon. Since it consists of an inhomogeneous mixture of  $sp^2$  and  $sp^3$  sites when the local band gap in this network is regarded in term of distance between clusters [115], therefore each configuration of  $sp^2$  cluster forms a local band gap. The band gap of a sample is thus determined by the averaging of the local band gap of each of the clusters. The  $sp^3$  matrix has a much larger gap and behaves as a tunnel barrier between each  $sp^2$  cluster. The distribution of  $sp^2$  gaps forms inhomogeneous disorder [115]. In Raman spectroscopy, the Raman G width is a measure of the homogeneous disorder and bond angle distortions within the network. It has been known to vary linearly with compressive stress in as-deposited films. Thus the homogeneous disorder in a-C:H attains a maximum in the most diamond-like a-C:H at a band gap of around 1.4 eV, where the density, C-C bonding, mechanical hardness and stress all reach a maximum, whilst the homogeneous disorder in a-C:H polymeric decreases to very small values. On the other hand, the inhomogeneous disorder increases progressively with increasing the optical gap in a-C:H. This means that the cluster size becomes smaller as the gap becomes wider, but the range of cluster sizes stays large in the large gap of a-C:H [116].

## 2.8 The Doping of DLC

Generally, any semiconductor can be used as an electronic material upon doping to form either a p-type or n-type material. The challenge of DLC doping is due to its large-band gap. P-type doping has been found to be relatively easy since either the dopant levels is slightly deep or high dopant solubility, however n-type doping has proved to be a lot more complicated. P-type doping is usually realised with boron as a dopant [117] because boron acts as a good acceptor and it is well incorporated into the structure of DLC, analogous with the case in diamond. Further it has been established that ta-C is slightly p-type in character [118] . This behaviour is attributed to vacancy created defects. Again, like diamond the n-type doping of DLC is more difficult. There have been many studies of nitrogen as an n-type dopant [119-121]. Dopants must fulfil two conditions: moderate solubility and having a shallow energy level. DLC has a significantly smaller band gap than diamond (ta-C has a maximum band gap of around 5.4 eV). This means that the nitrogen donor level should lie closer to the conduction band. However, with nitrogen substitution the site undergoes a distortion which reduces the size of the band gap. Phosphorus was difficult to dope with but success has been reported with a level at about 0.55 eV below  $E_C$  [122]. Another problem in amorphous semiconductors is that the density of trap states must be low enough to ensure that  $E_F$  is shifted away from the gap states. DLC doped nitrogen changes some of the  $sp^3$  fraction to  $sp^2$  sites and increases the conductivity by the reducing the width of the band gap while pinning the Fermi level. Further nitrogen forms principally non-doping (compensated) sites. The poor doping efficiency of nitrogen is partially due to the fact that it can make so many bonding configurations in a carbon network [122] such as pyridine, pyrrole and nitrile. Capacitatively coupled radio frequency (RF) plasma deposition has been used to produce p-type doped DLC films using  $PH_3$  as a dopant gas, producing films with P content estimated to be 11% [123] . These films also showed

increases in room temperature conductivity of nearly five orders of magnitude for which Golzan *et al.*[124] showed that when films were doped with 3% P, the dopant stabilised the tetrahedral network in favour of a  $sp^2$  bonded network. The n-type doping of DLC with sulphur has started to be investigated [125], but to date no conclusive reports of a successful n-doping have been published.

## **2.9 Electrical properties**

The electrical properties of DLC thin films have assumed a band structure consisting of only a mobility gap, where carriers living in gap states are localized [126]. The semiconductor behaviour is strictly dependent on the mobility gap. But the high densities of localised gap states give rise to low carrier mobility that degrades the semiconducting properties of the materials. The room temperature mobility of DLC and ta-C was found to be in the range of  $10^{-11}$ - $10^{-12}$   $\text{cm}^2/\text{V}$  [127]. These films are characterised by a high resistivity with values varying in the range  $10^2$  -  $10^{16}$   $\Omega\text{cm}$ . The difference in these values is determined by the deposition conditions [128]. The resistivity of diamond-like carbon could be reduced by incorporating metals or nitrogen in the films structure [129], however the low doping efficiency prevents the formation of p-n junctions in these materials. Several experiments have confirmed that the decrease in resistivity can be achieved by the incorporation of dopants and the graphitization [130] of the films. Nitrogen was found to be a good n-type dopant in ta-C films, as it raised the Fermi level from 0.91 eV above the valence band to 0.65eV below the conduction band for various nitrogen concentrations [134]. Doping was emphasised by substitution in the  $sp^3$  coordination at low N concentrations and increase of  $sp^2$  bonding at high N concentrations over 10% [131]. Due to high intrinsic defect formation concentration in ta-C, the doping efficiency is low. The most probable site hosting an impurity atom is shown to be a graphite-like carbon atom site. The ratio of  $sp^2$  sites and  $sp^3$  sites increase

as the number of the impurity valence electrons increases. In this study it was observed that for DLC thin films the I-V curves exhibited a highly non-linear behavior (non-Ohmic) even with the biasing of the counter electrode with positive or negative polarity. Although DLC and /or ta-C are not established semiconducting materials but they could be used in field emission displays [132].

## **2.10 Surface Brillouin scattering**

### **2.10.1 Introduction**

Surface Brillouin scattering (SBS) is a non-contact technique for measuring the near-surface mechanical properties of solids and thin supported layers, achieved by optically probing the acoustic excitations within a micron of the surface. This technique is applicable to opaque or semi-opaque solids such as metals and semiconductors, but can also be applied to transparent solids where this has been achieved by depositing a thin (~20 nm) reflective coating on the surface. SBS allows small samples to be studied, and these can be studied as a function of temperature and pressure. SBS has found a wide range of applications, from measuring the bulk elastic properties of super-alloys and other hard materials, to probing the thin films used as protective coatings and in microprocessors and micro-mechanical devices. SBS is also one of the techniques that evaluates the effects of near-surface damage caused by polishing or ion-bombardment, and for investigating natural and chemically generated oxidation [133].

### **2.10.2 The Mechanisms for Brillouin Scattering**

For transparent solids, Brillouin scattering is dominated by elasto-optic scattering from bulk acoustic modes that generally occur at higher frequencies. On the other hand, for opaque or semi-opaque solids the scattering takes place at the surface itself or in the near-surface region that the

light is able to penetrate, and is referred to as surface Brillouin scattering (SBS). Because of the relatively small scattering volume involved in SBS, the intensity of SBS signals is generally much smaller than volume/bulk Brillouin scattering in transparent solids. In the following sections, we will focus more on kinematic conditions applicable to SBS and the complementary theoretical considerations.

### 2.10.2.1 Elasto-optic scattering in transparent media: Kinematic conditions

While the main idea of this section is on SBS, it is important to start with a brief discussion of Brillouin scattering in transparent media. The schematic in Figure 2.9 shows the scattering that takes place for a ray of light of angular frequency  $\omega_i$  and wave vector  $\mathbf{k}_i$  that is passing through a medium of refractive index  $n$ . The magnitude of  $\mathbf{k}_i$  is given by

$$k_i = \frac{2\pi}{\lambda_i} = \frac{n\omega_i}{c}, \quad (2.6)$$

where  $\lambda_i$  is the wavelength, and  $c$  is the velocity of light in vacuum.

At any finite temperature there are thermal fluctuations in all possible acoustic modes of vibration of the medium, accompanied by fluctuations in the elastic strain field  $\eta_{ij}$  and through the elasto-optic effect, small fluctuations  $\delta\epsilon_{jk} = P_{jklm}\eta_{lm}$  in the dielectric constant of the medium, where  $P_{jklm}$  are the Pockels elasto-optic coefficients. Generally, for Brillouin scattering the operative conditions are usually such that the acoustic vibrations which the light interacts with have frequencies  $f = \omega / 2\pi \ll k_B T / h$ , where  $k_B = 1.38 \times 10^{-23}$  J/K is Boltzmann's constant,  $T$  is the absolute temperature and  $h = 6.63 \times 10^{-34}$  J.s is Planck's constant.

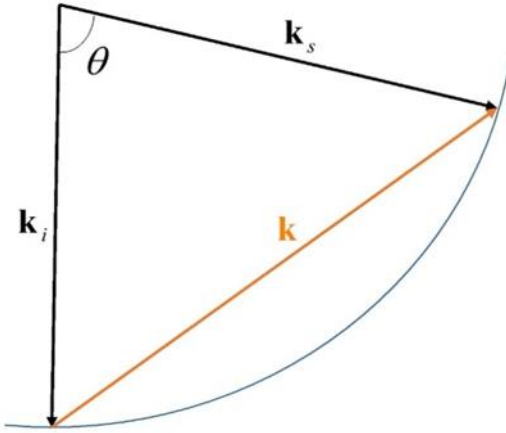


**Figure 2.9:** Kinematic condition for Brillouin scattering, Eq. (2.9).

Classical statistical mechanics dictates that for the conditions, where the average thermal energy per vibrational mode given by  $k_B T$ , which is much greater than the vibrational energy quantum  $hf$ , the scattering can be treated classically. At very low temperatures (liquid He temperatures) or the much higher frequencies encountered in Raman scattering, then  $hf \approx k_B T$ , and the scattering needs to be treated quantum mechanically and the quantum approach applied under the conditions of Brillouin scattering, yields essentially the same result as the classical approach [134].

A fluctuation in the dielectric constant associated with an acoustic mode of wave vector  $\mathbf{k}$  and angular frequency

$$\omega = vk \tag{2.7}$$

where  $v$  is the acoustic velocity, will result in a very small fraction, proportional to  $T$ , of the incident light being inelastically scattered with wave vector

$$\mathbf{k}_s = \mathbf{k}_i \pm \mathbf{k}, \tag{2.8}$$

and angular frequency

$$\omega_s = \omega_i \pm \omega . \quad (2.9)$$

The phonon vibrational frequency is much smaller than the optical frequency by a factor of the order  $v/c \approx 10^{-5}$ , so  $\omega_i$  and  $\omega_s$  differ only very slightly, and  $\mathbf{k}_i$  and  $\mathbf{k}_s$  figure 2.9 depicts the geometry of the scattering process where the tips of these two vectors lie on a circle, and are joined by the vector  $\mathbf{k}$ . The angle through which the light has been scattered has been labelled  $\theta$ . The scattering geometry of choice for our investigations was the back- scattering geometry, such that,  $\theta = \pi$ . It follows from Figure 2.10 that

$$2k_i \sin(\theta/2) = k . \quad (2.10)$$

Combining this with eqns. (2.6), (2.7) and (2.10) yields

$$v = \frac{\omega c}{2n\omega_i \sin(\theta/2)} . \quad (2.11)$$

Note that  $\theta$  refers to the angle between the incident and scattered wave vectors inside the transparent medium. Depending on the orientation of the surfaces through which the light enters and leaves the medium, because of refraction  $\theta$  may not be the same as the angle between the external beams. Using equation (2.11) allows one to calculate the acoustic velocity from the measured frequency shift. Generally there is also far more light which is elastically scattered at any angle due to in homogeneities in the medium and other causes, such that one observes at any scattering angle a very intense spectral line at frequency  $\omega_i$  and then much less intense lines at frequencies  $\omega_i \pm \omega$ . The frequency down-shifted line is known as the Stokes component and the up-shifted line as the anti-Stokes component. There could be more than one line in each sideband if there is scattering from both longitudinal (L) and transverse (T) modes of a solid.

### 2.10.2.2 Surface ripple-mediated Brillouin scattering from opaque solids: Kinematic conditions

In the case of metals and other opaque solids, incident light penetrates only a very short distance into the medium and there is small elasto-optic scattering, Hence one largely observes the inelastic scattering from dynamic rippling of the surface derived from thermal fluctuations in Rayleigh and other guided surface modes and from the continuum of bulk modes impinging on the surface. The spectrum of the scattered light conveys information about the near surface mechanical properties of the solid, to a depth of order the wavelength of the light. These may differ from the bulk properties because of surface treatment, oxidation, radiation damage, the presence of one or more thin over-layers of another substance or for other reasons.

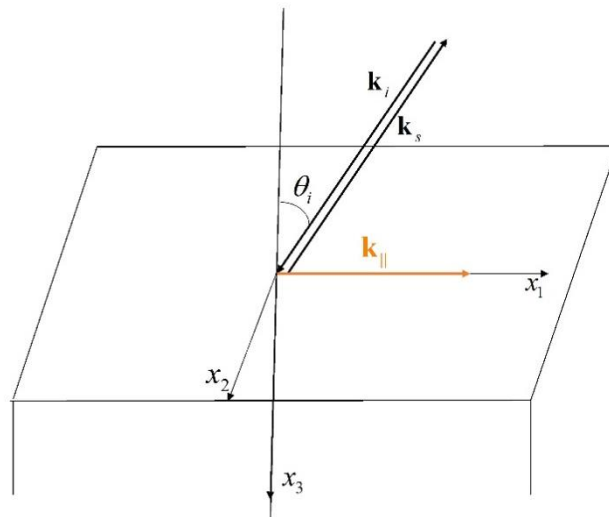


**Figure 2.10:** Backscattering geometry commonly utilised for SBS measurements [135].

Figure 2.10 shows the common back-scattering geometry that was employed to perform the SBS measurements. A laser beam of frequency  $\omega_i$  and wave vector  $\mathbf{k}_i$  is incident on the highly polished surface of a sample at an angle  $\theta_i$  to the surface normal. Notable, most of the light is

specularly reflected without change in frequency and only a small fraction of the light is inelastically scattered in all directions by the dynamic rippling of the surface. In the backscattering geometry used here, collection of scattered light, of frequency  $\omega_s$  and wave vector  $\mathbf{k}_s$  is carried out in the reverse direction. The spectrum of this scattered light generally consists of an intense central peak and then symmetrically disposed on either side of it much less intense Stokes and anti-Stokes sidebands. The central peak is comprised of diffusely scattered light of frequency  $\omega_i$ , and a slightly broadened component which is usually attributed to entropy fluctuations. The sidebands, which ideally are mirror images of each other about the central peak, display one or more sharp lines associated with Rayleigh, Sezawa and other guided surface modes, and a broad band known as the Lamb shoulder (see figure 2.14), given rise to by the continuum of bulk modes incident on the surface.

In SBS from an opaque solid the scattering takes place at the surface and is caused by dynamic rippling of the surface, which can be thought of as comprised of a multitude of ripples of different wave vectors  $k_{//}$  moving parallel to the surface, with frequency  $\omega$ , which act as moving diffraction gratings. The incident light is thus scattered in all directions and with Doppler changes in frequency determined by the ripples phase velocities. Because the velocities of these acoustic ripples is 5 orders of magnitude smaller than the velocity of light,  $c$ , the change in frequency of the scattered light is proportionately small, and the same goes for the magnitude of the wave vector, and so to a good approximation  $k_s \approx k_i$ . It follows from the diffraction grating principle that the ripples responsible for back scattering have  $k_{//}$  in the plane of incidence of the light, and of magnitude the component of  $\mathbf{k}_s - \mathbf{k}_i$  in the surface, i.e.

$$k_{//} = 2k_i \sin\theta_i \quad (2.12)$$

For a ripple travelling along the surface at the velocity  $v$ , its frequency is

$$\omega = v k_{//} \quad (2.13)$$

and this determines the change in frequency of the scattered light, i.e.

$$\omega_s - \omega_i = \pm 2k_i \sin \theta_i v = \pm 2\omega_i \frac{v}{c} \sin \theta_i \quad (2.14)$$

Guided surface modes such as Rayleigh and Sezawa waves have discrete velocities which are in most cases smaller than bulk wave velocities, and give rise to sharp lines in the SBS spectra at relatively small frequency shifts. Surface rippling is also caused by bulk longitudinal (L) and transverse (T) waves of velocities  $v_L$  and  $v_T$  respectively, being incident on and reflected from the surface at all angles. The phase velocity  $v$  of the surface ripple resulting from the incidence of a T wave at an angle  $\theta$  to the surface normal is

$$v = \frac{v_T}{\sin \theta}, \quad (2.15)$$

which ranges from  $v_T$  to  $\infty$ , depending on the angle. These ripples give rise to a broad band in the SBS spectrum, known as the Lamb shoulder, which for the anti-Stokes sideband extends from the T wave threshold at

$$\omega_s - \omega_i = 2\omega_i \frac{v_T}{c} \sin \theta_i, \quad (2.16)$$

to as far as the spectrum can be measured, with the Stokes sideband being the mirror image of this. The incidence of L waves adds a second broad band to the spectrum, extending from the L wave threshold at

$$\omega_s - \omega_i = 2\omega_i \frac{v_L}{c} \sin \theta_i, \quad (2.17)$$

to large frequencies. The abovementioned thresholds correspond to T and L waves respectively travelling parallel to the surface, which are known as transverse and longitudinal lateral waves.

The situation for anisotropic solids is somewhat more subtle in that the lateral waves and their thresholds correspond to bulk waves with energy flux vectors (group velocities) parallel to the surface, which in some cases may have associated wave vectors oblique to the surface.

For ripple scattering the L threshold, because of mode conversion effects, shows up as a sharp dip in the Lamb shoulder. It is useful, although not always possible, to be able to measure the position of this dip, since it yields the velocity of a bulk L waves travelling along the surface ( $\theta = 90^\circ$ ), known as a longitudinal lateral wave, or longitudinal guided mode (LGM). This velocity, together with the Rayleigh velocity is sufficient to determine the two independent elastic constants of an isotropic solid. The T threshold tends to be a little more difficult to measure because of its proximity to the much more intense Rayleigh peak.

### 2.10.2.3 Surface ripple scattering intensity and Green's function

It can be shown that in the classical regime the cross section for the scattering of light by the ripple mechanism with frequency change  $\omega$  and surface scattering wave vector  $k_{//}$  is proportional to the power spectrum  $\langle |u_3(k_{//}, \omega)|^2 \rangle$  of thermal fluctuations in the normal displacement of the surface profile [136]. The fluctuation dissipation theorem is then commonly invoked to express the power spectrum in terms of the imaginary  $\text{Im}G_{33}(k_{//}, \omega)$  part of the Fourier  $(k_{//}, \omega)$  elastodynamic surface response Green's function. The scattering cross section is thereby given by

$$\frac{d^2\sigma}{d\Omega d\omega} = \frac{AT}{\omega} \text{Im} G_{33}(k_{//}, \omega) \quad (2.18)$$

where  $A$  is a constant that depends on the scattering geometry, frequency and polarization of the incident light and optical properties of the medium, and  $T$  is the absolute temperature. Expressing the light scattering in terms of  $\text{Im} G_{33}(k_{//}, \omega)$  is simply a convenient computational

strategy, and it should not be inferred that the incident light is causing the fluctuations. The light is simply probing existing thermal fluctuations.

#### 2.10.2.4 Calculation of the surface Green's function $G_{33}(k_{//}, \omega)$

The SBS technique is generally used to study elastically anisotropic solids such as crystals and textured polycrystalline films, and so it is easy to implement computer coding for calculating  $G_{33}(k_{//}, \omega)$  for one or more anisotropic layers supported on an anisotropic substrate. Such coding is equally applicable to a homogeneous isotropic solid as a special case. It is briefly explained below how  $G_{33}(k_{//}, \omega)$  is calculated for a bare anisotropic substrate. More comprehensive discussions, including the effects of an over layer, can be found in Comins [137], Beghi *et al.* [138] and Zhang *et al.* [139].

For a spatially and temporarily periodic force acting in the  $x_j$  direction on the otherwise free surface of a solid occupying the half space  $x_3 > 0$ , the particle displacement field  $\mathbf{u}(\mathbf{x}, t)$  takes the form of a linear superposition of three phase matched (i.e. sharing a common value of  $k_{//}$  and  $\omega$ ) partial waves. These are plane wave solutions of the wave equation [178]

$$u_i = U_i \exp[i(\mathbf{k} \cdot \mathbf{x} - \omega t)], \quad (2.19)$$

$$\rho \frac{\partial^2 u_i}{\partial t^2} = c_{ijkl} \frac{\partial^2 u_k}{\partial x_j \partial x_l}, \quad (2.20)$$

where  $\rho$  is the density, and  $c_{ijkl}$  the elastic modulus tensor of the solid. The unit polarization vector,  $\mathbf{U}$ , wave vector,  $\mathbf{k} = (k_{//}, k_{\perp}) = (k_1, k_2, k_3)$ , and the angular frequency,  $\omega$ , are governed by the Christoffel equations

$$(c_{ijkl}k_jk_l - \rho\omega^2\delta_{ik})U_k = 0; i = 1, 2, 3. \quad (2.21)$$

The corresponding secular equation

$$D(\mathbf{k}, \omega) = |c_{ijkl}k_jk_l - \rho\omega^2\delta_{ik}| = 0, \quad (2.22)$$

represents the dispersion relation for the medium, and expresses the proportionality of  $\omega$  to  $k = |\mathbf{k}|$ . For given  $k_{//}$  and  $\omega$ , eqn.(2.18) is of degree 6 in  $k_{\perp} = k_3$  and yields 6 solutions. For given wave normal  $\mathbf{k}/k$  or wave vector direction, the phase velocity is  $v = \omega/k$  and the acoustic slowness vector is  $\mathbf{s} = \mathbf{k}/\omega$ . Only the three outgoing solutions of (2.22) are retained, i.e. either real solutions with associated group velocity (energy flux) vectors

$$\mathbf{V}_g = \nabla_{\mathbf{k}}\omega(\mathbf{k}), \quad (2.23)$$

directed away from the surface or complex solutions with positive imaginary part, corresponding to evanescent waves with amplitude falling off exponentially away from the surface.

The superposition takes the form

$$u_i^{(j)}(k_{//}, \omega; x_3) = \sum_{n=1}^3 A_j^{(n)} U_i^{(n)} \exp(ik_3^{(n)} x_3) \quad (2.24)$$

and is subject to the boundary conditions

$$\sigma_{i3}(k_{//}, \omega; x_3 = 0_+) = -\delta_{ij}. \quad (2.25)$$

From the stress-strain relationship

$$\sigma_{ij} = c_{ijkl}\eta_{kl}, \quad (2.26)$$

and the boundary conditions, the three partial wave amplitudes  $A_j^{(n)}$  are governed by a set of linear equations, having solution

$$A_j^{(n)} = \frac{i}{\omega} (\mathbf{B}^{-1})_j^{(n)} = \frac{i}{\omega} \frac{\text{adj}(\mathbf{B})_j^{(n)}}{\det|\mathbf{B}|}; B_l^{(n)} = c_{3lpq} U_p^{(n)} s_q^{(n)}. \quad (2.27)$$

The surface displacement response function or Green's function is obtained by taking the limit  $x_3 \rightarrow 0_+$  and set in

$$G_{33}(k_{//}, \omega) = \frac{i}{\omega} \sum_{n=1}^3 \frac{\text{adj}(\mathbf{B})_3^{(n)} U_3^{(n)}}{\det|\mathbf{B}|} \quad (2.28)$$

### 2.10.2.5 The surface Green's function $G_{33}(\mathbf{k}_{//}, \omega, d)$ for a coated solid

Considerable impetus was given to the study of the surface dynamics of coated solids by the review of Farnell and Adler [140]. One outcome is that SBS has become established as a valuable tool in the determination of the elastic properties of thin near-opaque sub-micron supported films that critically depend on the synthesis conditions. With the SBS frequency being in the range 1 to 50 GHz, and the wave field penetrating to about a wavelength below the surface, the SBS technique is ideal for studying such films. The evaluation of  $Im G_{33}(k_{//}, \omega, d)$  used in the interpretation of SBS spectra for a supported film of thickness  $d$ , takes into account also the 6 phase matched partial waves in the film, and there are the 6 additional boundary conditions of continuity of displacement field and traction force at the interface, see Zhang *et al.* [135]. The velocity dispersion curves of the surface excitations are measured as a function of  $k/d$ , and appropriate fitting routines are employed to extract the set of elastic constants (see below).

An open source program for calculating  $I = Im G_{33}(\mathbf{k}_{//}, \omega, d)$  as a function of  $v = \omega/k_{//}$  and  $k_{//}d$  is employed, generating an output that is 480x480 array of integer values, allowing  $I$  to be depicted as a gray scale representation of the surface wave dispersion relation, as shown in Figures 2.13(a) and (b) below, using ORIGIN or other suitable graphics software. Also generated

are files of  $I$  vs.  $\nu$  for a selection of values of  $k_{//}d$ . The main program requires insertion of the values of the materials constants of the layer and substrate, the crystallographic orientation of the surface and scattering plane to be specified and the range of  $k_{//}d$  and  $\nu$  to be provided.

It is well known from the review of Farnell and Adler [140] that film-substrate combinations can broadly be classified into two types, slow-on-fast and fast-on-slow. The slow on fast category comprises combinations for which the bulk transverse velocity of the film is smaller than the transverse velocity of the substrate, which of course depends on the elastic moduli and densities of both components. The fast-on-slow category comprises combinations for which the bulk transverse velocity of the film is greater than the transverse velocity of the substrate.

As an example of a slow-on-fast combination, Figure 2-11(a) shows the dispersion relation for an isotropic aluminum layer,  $\rho = 2.7\text{g/cm}^3$ ,  $\nu_L = 6.42\text{ km/s}$  on a fused quartz substrate,  $\rho = 2.2\text{ g/cm}^3$ ,  $\nu_L = 5.97\text{ km/s}$ ,  $\nu_T = 3.765\text{ km/s}$ . Below the T wave threshold of the substrate at  $V_T^s$ , the substrate partial waves for any  $k_{//}d$  are both evanescent, and the modes that exist there, which are conditioned by the vanishing of the boundary condition determinant, are guided surface modes, with the displacement large in the layer, and falling off exponentially in the substrate. Starting at  $k_{//}d=0$ , which corresponds to the condition of a bare substrate, there is only one guided mode, the Rayleigh wave of the substrate. With increasing  $k_{//}d$ , the Rayleigh wave falls off in velocity, ultimately for large  $k_{//}d$  asymptotically approaching [141] the Rayleigh velocity of the layer material. At a sequence of critical values of  $k_{//}d$ , additional guided modes, known as Sezawa modes and denoted  $S_1$  and  $S_2$  in Fig. 2-11(a), emerge from the T wave threshold and fall off in velocity. The lowest of these asymptotically approaches the T velocity of the layer material for large  $k_{//}d$ , becoming the new T wave threshold. The existence of all these modes and their dependence on  $k_{//}d$  allows for accurate determination of the properties of the layer. Above  $\nu_T^s =$

3.765 km/s the substrate T mode is a bulk mode and then above  $v_T^s = 5.97$  km/s the L mode of the substrate is also a bulk mode, allowing energy to be radiated away from the surface. The guided modes that exist here tend to be leaky PSAW, damped to a lesser or greater extent. For certain combinations the PSAW are recognizable as extensions of the Sezawa modes into the radiative domain, and can be regarded as pseudo-Sezawa modes.

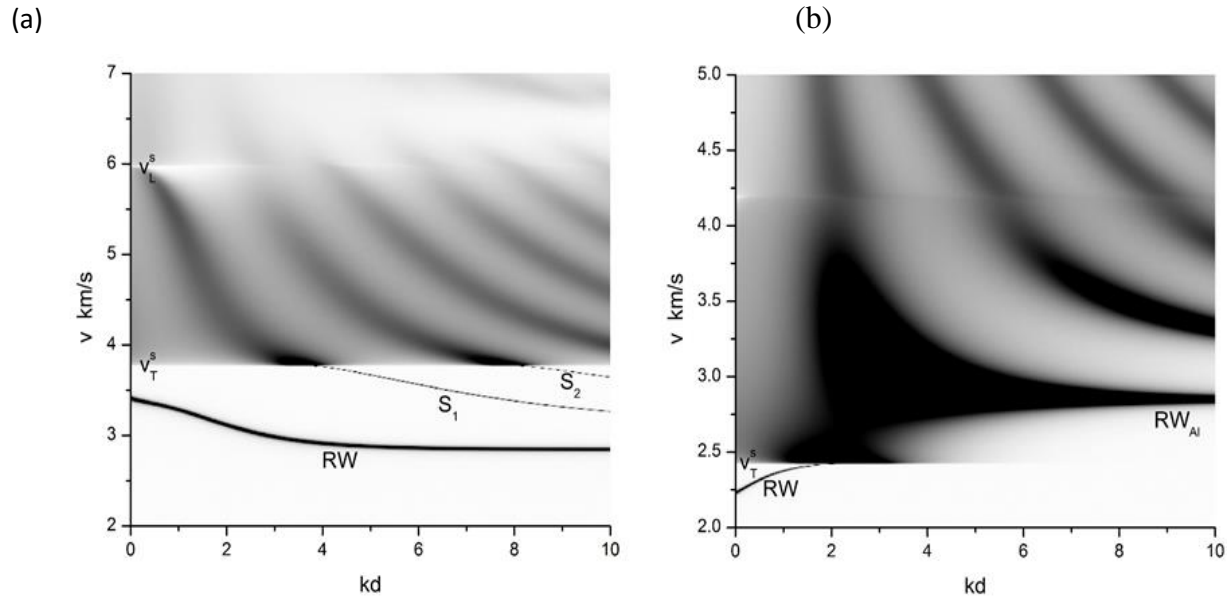


**Figure 2.11:** Dispersion relations for (a) an aluminium layer on a fused quartz substrate and (b) an aluminium layer on zinc. and denote the substrate T and L threshold velocities respectively [140].

### 2.10.2.6 SBS in semi-opaque solid

In semi-opaque materials such as semiconductors, the presence of both bulk and surface Brillouin scattering can often be observed. The less opaque the material the greater the penetration of the light into the medium, and the greater the proportion of bulk elasto-optically scattered light in the spectrum. However, the fact that there is some attenuation of light in the medium means that the wave vectors of the incident and scattered light in the medium,  $\mathbf{k}_i$  and  $\mathbf{k}_s$ , are both complex. As

a consequence, the scattered light is broadened in frequency. Figure 2.14 shows combined surface and bulk Brillouin spectra for various values of the complex dielectric constant  $\varepsilon = \varepsilon_1 + i\varepsilon_2$  of a solid calculated by Mills and Subbaswamy [142]. The attenuation is determined by the imaginary part of the dielectric constant  $\varepsilon_2$ . Where this is very small, as shown in Fig. 2.12(a), the bulk L and T scattering peaks are very sharp and there is little SBS. A slightly larger value of  $\varepsilon_2$  yields slightly broadened bulk L and T peaks and the trace of SBS Rayleigh peak. A still larger value of  $\varepsilon_2$  yield significantly more broadened bulk L and T peaks and now a clear SBS spectrum, including the Lamb shoulder. Finally, a very large value of  $\varepsilon_2$ , as shown in Fig. 2.12(d) yields a clear SBS spectrum and no trace of bulk scattering. From the point of view of determining materials properties, the intermediate situation of moderate  $\varepsilon_2$  and hence absorption offers some advantage since the data it yields on both bulk and surface velocities provides more handles on the materials properties. It can also expose any differences there may be between bulk and near-surface properties. In a recent development, Jiménez Riobóo *et al.*[143] have succeeded in measuring and interpreting the relatively weak SBS signals from transparent glasses and the crystals MgO and sapphire, without the aid of reflective coatings. These experiments clearly demonstrated the ability of SBS to collect SAW data from transparent bulk samples and thus extends this non-destructive and contactless method to a wider range of bulk materials.

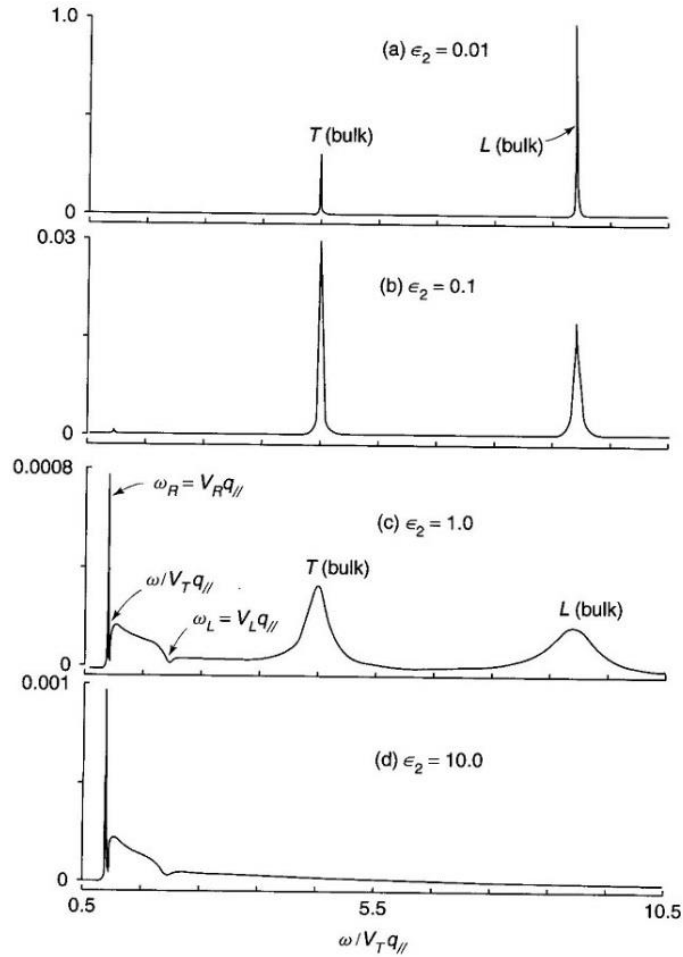


**Figure 2.12:** Calculated combined surface and bulk Brillouin spectra for various values of the complex dielectric constant and  $\epsilon = \epsilon_1 + \epsilon_2$  [142].

### 2.10.2.7 Determination of elastic moduli of thin supported films from SBS spectra

SBS has been widely used in the determination of the elastic moduli, and in some cases also the density, of thin supported films. The better and more extensive the observed data, the more accurate is the determination of elastic constants. The simplest case is to position a single isotropic layer of known density on a known substrate (similar to DLC films on c-Si substrate), in which case there are just two free parameters,  $C_{11}$  and  $C_{44}$  of the film, to consider. Often textured polycrystalline films are encountered which are transversely isotropic with symmetry axis normal

to the surface. Although transverse isotropy is characterized by 5 independent elastic moduli, only 4 of them are accessible through SBS, which probes sagittal plane vibrations. These are  $C_{11}$ ,  $C_{13}$ ,  $C_{33}$  and  $C_{55}$ . The density  $\rho$  is a possible fifth free parameter. SBS has been most successfully in its application to slow-on-fast combinations, with the film being opaque. Under favorable conditions one observes the  $k/d$  dependence of the Rayleigh wave and also one or more Sezawa's. With fast-on-slow combinations one is limited to the variation of the Rayleigh velocity before it merges into the substrate T threshold, and the appearance of pseudo-SAW resonances and their behavior for large  $k/d$ . The situation is further complicated for transparent films on an opaque substrate, in that interference effects between ripple scattering for the surface and interface and elasto-optic scattering in the film can tend to suppress some resonances. For a thick transparent film, scattering from an interfacial mode can be observed [144].

An example of a successful characterization of a film using SBS, homogeneous tungsten carbide films were grown using RF sputtering with steps of differing thickness (60-655 nm) on a silicon substrate by Wittkowski *et al.* [145]. With the high mass density of WC, the system falls into the slow-on-fast category, yielding the Rayleigh SAW and many Sezawa modes. Figure 2.13 shows the measured data and calculated phase velocity dispersion curves that were obtained by adjusting the elastic constants and density of the film to obtain a best fit to the velocities, which yielded  $C_{11} = 349 \pm 7$  GPa,  $C_{13} = 126 \pm 8$  GPa,  $C_{33} = 348 \pm 13$  GPa,  $C_{55} = 114 \pm 2$  GPa, and density  $\rho = 13.0 \pm 0.2$  /cm<sup>3</sup>. The proximity of  $C_{33}$  to  $C_{11}$  and of  $C_{55}$  to  $(C_{11} - C_{13})/2$  indicates that the film is very nearly isotropic.

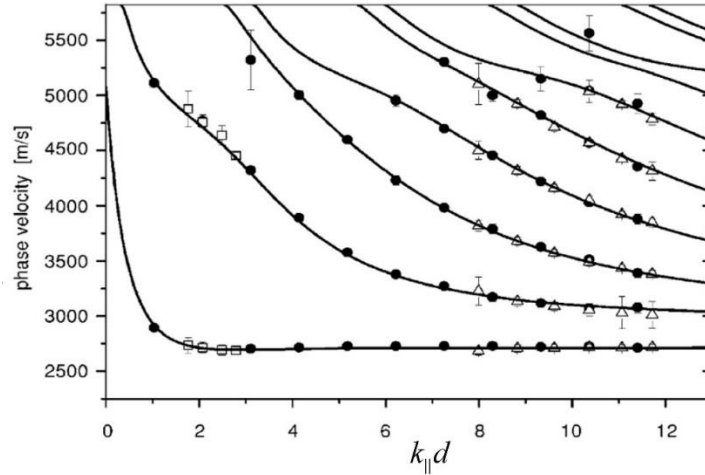


**Figure 2.13:** Phase velocity dispersion curves for tungsten carbide (WC) films on a silicon substrate, calculated using optimized values of elastic constants and density for the film [146].

### 2.10.2.8 Diamond-like carbon films and SBS

Diamond-like carbon (DLC) exists in various forms, most importantly as tetrahedrally amorphous carbon (ta-C). There is a fairly extensive literature on the use of SBS to investigate DLC synthesized under various conditions that admit different types of impurities and different ratios of tetrahedral carbon (where the tetrahedral coordination is maintained by four  $sp^3$  hybridized atomic orbitals on each carbon atom) to graphitic carbon (where three  $sp^2$  hybridized orbitals on each C atom are directed towards its three neighbors in the honeycomb graphene structure). In general, the greater the  $sp^3$  fraction, the larger the elastic constants, with diamond and its 100%  $sp^3$  fraction representing the upper limit.

Ferrari *et al.* [147] have used SBS measurements of the Rayleigh wave and LGM to determine the elastic constants of cathodic arc deposited ta-C with 88% of  $sp^3$ , and plasma deposited hydrogenated ta-C (ta-C:H) with 70% of  $sp^3$  and 30 at. % of H. Their measured values of Young's modulus  $E$  for ta-C and ta-C:H are respectively 757 and 300 GPa, while their measured values of the shear modulus  $G$  are respectively 337 and 115 GPa, showing the expected contrast. These

values may be compared with those for polycrystalline diamond, which are  $E = 1145$  GPa and  $G = 534$  GPa. Manghnani et al. [148] have synthesized ta-C from  $C_{60}$  fullerene powder at a pressure of 13 to 13.5 GPa. Their sample B, synthesized at  $900^{\circ}\text{C}$  yielded  $G = 375$  GPa, indicating a high proportion of  $sp^3$  carbon, while their sample A, synthesized at  $800^{\circ}\text{C}$ , displayed a smaller value of  $G$  and proportion of  $sp^3$  carbon. Berezina et al. [149] have used SBS and a laser-SAW technique to investigate a thick chromium containing DLC layer deposited by physical vapor deposition on steel. Measured value of  $E = 68.9$  GPa from this study is much smaller than other reported values for DLC. It appears that alloying DLC with certain other elements reduces internal stresses and elastic moduli, but the wear behavior is still sufficient for industrial applications.

## **Chapter 3: Thin Film Growth and characterisation**

### **Introduction**

In this chapter, the growth conditions of DLC thin films using plasma based RF and DC magnetron sputtering are presented and discussed. The growth of thin films has been carried out using a reactive and non-reactive plasma in which a mixture of argon and methane was used in the chamber under zero and negative substrate bias voltages. Substrate biasing was carried out using a floating DC voltage on the substrate in various voltage sweeps of interest.

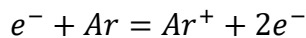
The determination of the film properties was carried out using the following techniques: Raman spectroscopy was applied to determine the microstructure and structure of the films, whilst electrical properties were obtained by use of 4-point probe of the I-V Characteristics. Optical emission spectroscopy (OES) used to monitor the plasma species in-situ during thin film growth, UV-vis spectroscopy used to determine the transmittance, absorption and the Tauc-gap, X-ray reflectivity (XRR) used to determine the densities, thicknesses and the roughness, Fourier transform infra-red spectroscopy (FTIR) was employed to investigate the chemical bonding and determine the fraction of hydrogen in the films. X-ray photoelectron spectroscopy (XPS), and X-ray induced Auger electron spectroscopy (AES) have the advantage of providing quantitatively determine the ratio of  $sp^2$  to  $sp^3$  fraction in the films. The correlation of the  $sp^3$  fractions and the mechanical properties was probed by using Surface Brillouin scattering (SBS) to determine the elastic properties of diamond like carbon films under various conditions of film growth.

### **3.1.1 Diamond like carbon thin film deposition**

The films have been prepared by DC and RF magnetron sputtering techniques. This is among the best techniques for the preparation of DLC thin films. The films were deposited under two conditions, in one instance thin DLC films were deposited in a pure argon gas plasma while in the

other instances a gaseous mixture of argon (Ar) and methane (CH<sub>4</sub>) was used to provide a reactive ambient. In RF magnetron sputtering, a radio frequency (RF) signals superimposed on a target self-bias, often negative is used to ionize the inert gas such as argon, xenon and so on. The RF power from the generator is applied onto the target to form the plasma and this will generate a self-sustained glow discharge constituting mainly of positive gas (argon) ions, radicals (CH<sub>x</sub>, x=1-3) and its ions.

The mechanism for plasma formation involves the production of electrons inside the chamber. Under acceleration of high voltage from the RF generator, these electrons move rapidly towards the inert gases such as Ar and transfer their energy and momentum to the neutral argon atoms. A portion of these argon atoms are ionized to Ar<sup>+</sup> with the release of two electrons in a cascade process. The process of ionization is illustrated by the expression;



The resulting electrons have the same energy as the parent electron and thus participate in the subsequent ionization of Ar atoms to produce Ar<sup>+</sup> ions and electron. This multiple process works very fast up to the breakdown or ignition region for which plasma is formed. The argon ions bombard the negatively biased graphite target to eject neutral C atoms away from the cathode. The carbon ad atoms move to the anode and finally condense on the substrate to form DLC films. The RF generator (13.56 MHz) is not enough to accelerate the heavy and positive ions, such as Ar<sup>+</sup>, towards the target. By consequent with zero bias, sputtering cannot take place. It is the DC self-bias voltage on the target induced by the RF generator coupled capacitatively to the sputtering system that makes it possible to maintain the RF plasma in an ambient Ar working gas. The schematic diagram of the entire sputtering process is shown in figure 3.1. The magnets located behind the targets are used to increase the percentage of electrons that take part in ionization

events. This will increase both the probability of electrons striking the argon atoms and the length of electron path and hence increase the ionizations efficiency significantly. The surface atoms of the target are ejected by momentum transfer and are deposited as thin films into the surface of the substrate.

Sputter yield,  $S$ , is defined as the mean number of atoms removed from the surface of solid per incident ion. The sputter yield is a process parameter that is influenced by the RF power, gas pressure and target material [150].

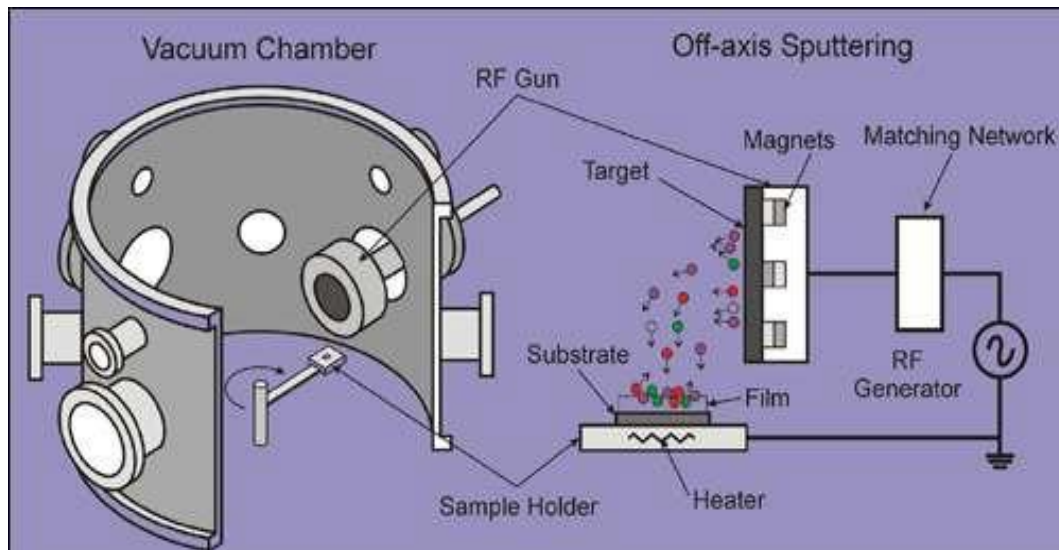


**Figure 3.1:** Schematic diagram of RF sputter system with sputtering process [150].

RF magnetron sputtering has no limitation regarding target materials as both pure metals and insulators can be sputter deposited as thin films on a substrate. However, the DC sputtering method is predicated towards the deposition of metallic targets only at appreciable voltages. The presence of the matching network between the RF generator and the target is necessary in order to optimize the power dissipation in the discharge [150].

For the DC magnetron sputtering, DLC thin films were prepared by using TruPlasma DC

3002 system. At the initial step, the power was set at 200 W for the initial RF sputtering run. Afterwards the power was varied from 200 W to 300 W using a step of 50 W. The discharge voltage was typically in the order of 413 V to 524 V and the current was in order of 402 mA to 972 mA. The base and working pressure was about  $3.6 \times 10^{-5}$  mbar and in order of  $2.0$  to  $6.0 \times 10^{-2}$  mbar, respectively. The substrate was biased negatively from -25 V to -100 V. Before deposition of each film, the graphite target was pre-sputtered in argon atmosphere for 5 minutes.

### 3.1.2 Experimental procedure

The DLC thin films were prepared either by DC or RF magnetron sputtering. All the DLC thin films on (001)Si and SiO<sub>2</sub> were deposited using the RF magnetron sputtering system shown in figure 3.2. The growth of these films were carried using argon and methane atmosphere, at room temperature.

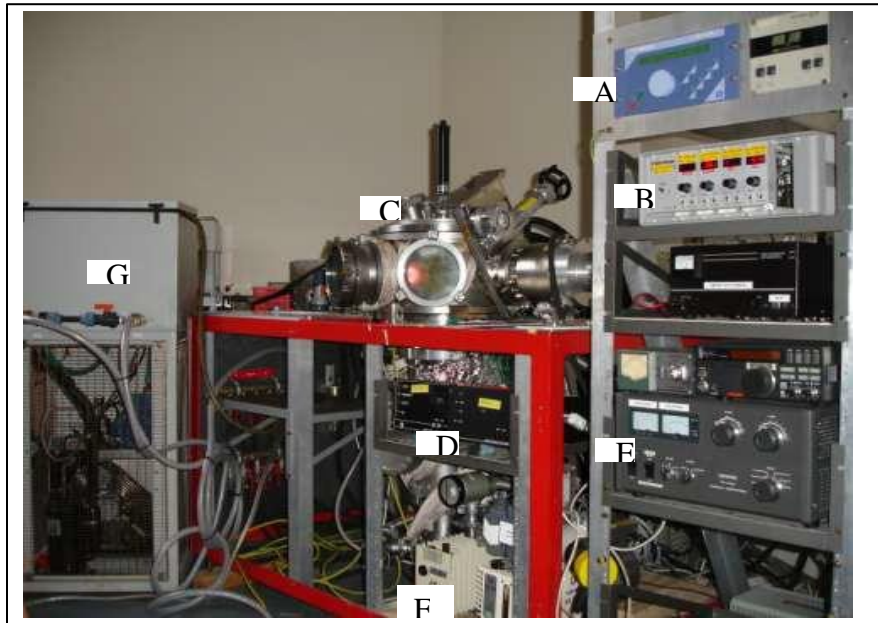


**Figure 3.2:** RF magnetron sputtering system and the related instruments. A– RF generator, PFG 300RF; B – gas control unit; C – vacuum chamber; D – turbo pump control unit, Turbotronik NT 150/360 VH; E – linear amplifier, Kenwood TL-922; F – fore pump; G – Compac cooling unit [151].

A vacuum system composed of a rotary vane (F) and a turbo-molecular pump (D) was used to evacuate down to a pressure around  $2.9 \times 10^{-5}$  mbar before the introduction of argon and methane to the chamber. The target to substrate distance was set constant to 6 cm. For DC and RF magnetron sputtering unbiased substrate input power densities (E) were kept constant at  $4.41 \text{ W/cm}^2$  and the target self - bias voltage varied from 360 V to 423 V. Argon and methane were introduced to the vacuum chamber at constant flow rates of 20 sccm and 13 sccm, respectively for the DC and RF sputter conditions, while varying the methane flow rates between 3.5-26 sccm. The pre-sputtering of the graphite target was done with argon at  $2.21 \text{ W/cm}^2$  for 5 minutes to remove the impurities present on the target. Pre-sputtering was performed through a shutter mechanism that involves the rotation of the substrate relative to a fixed mask thus preventing the exposure of the substrate to impurities. The film deposition was subsequently carried out after adjustment of the process conditions specific to the experiment. The substrate temperature measured to 60-70 °C for sputter powers below 350W, at fixed target-substrate distance (6 cm) and for argon flow rates used. Moreover, DLC thin films were prepared by DC and RF magnetron sputtering system employing a 13.56 MHz radio frequency at room temperature with DC substrate bias voltages between (-25V and -100V). The deposition of the films was done in argon and methane gas ambient on a glass and Si substrate. Table 3.1 shows the deposition parameters of the RF magnetron sputtering biased substrate on the glass. Table 3-2 shows parameters of the RF magnetron sputtering biased substrate (on the silicon) and the last table 3-3 shows parameters of DC magnetron sputtering biasing on silicon substrate.

**Table 3.1:** Growth conditions for RF sputtered films with biased SiO<sub>2</sub> substrate condition from -25 to -100V.

RF input power density (W/cm <sup>2</sup> )	4.4
CH <sub>4</sub> /Ar ratio	15/15
Base pressure (mbar)	3.7×10 <sup>-5</sup>
Working pressure (mbar)	2.8× 10 <sup>-2</sup>
Thickness (nm)	94 - 147
Self-bias voltage (V)	360 - 423
Deposition time (minutes)	5
Density (g/cm <sup>3</sup> )	2.10 - 2.59
Pre-sputtering Power (W/cm <sup>2</sup> ) in 5 min	2.2
Target distance (cm)	6

The films grown on glass substrates were used to conduct transmission measurements and enabled the determination of optical characteristics of the DLC films, discussed later in section 4.5.

**Table 3.2:** Growth conditions for RF magnetron sputtered films with biased silicon substrate from -25 to -100V.

RF input power density (W/cm <sup>2</sup> )	4.4
CH <sub>4</sub> /Ar ratio	13/13
Base pressure (mbar)	3.1×10 <sup>-5</sup>
Working pressure (mbar)	5.1-5.6 × 10 <sup>-3</sup>
Thickness (nm)	91 - 132
Self-bias voltage (V)	360-423
Deposition time (minutes)	5
Density (g/cm <sup>3</sup> )	2.2 - 2.4
Pre-sputtering Power (W/cm <sup>2</sup> ) in 5 min	2.2
Target distance (cm)	6

**Table 3.3:** DC magnetron sputtering biased silicon substrate from -25 to -100V

DC input power density (W/cm <sup>2</sup> )	4.4
CH <sub>4</sub> /Ar ratio	20/20
Base pressure (mbar)	4.0 × 10 <sup>-5</sup>
Working pressure (mbar)	5.2-5.8 × 10 <sup>-2</sup>
Thickness (nm)	52-73
Self-bias voltage (V)	360 - 423
Deposition time (minutes)	5
Density (g/cm <sup>3</sup> )	2.39 - 2.58
Pre-sputtering Power (W/cm <sup>2</sup> ) in 5 min	2.2
Target distance (cm)	6

## **3.2. Characterization technique**

### **3.2.1 Experimental setup of Raman spectroscopy**

#### **3.2.1.1 Introduction**

The phenomenon of Raman scattering was first observed in 1928 and it has since 1960 been used on a large scale to study the structural properties of materials. The Raman scattering effect is not very strong in intensity, only one in  $10^8$  photons incident on a material is subject to Raman scattering. Thus intense incident radiation and very sensitive apparatus are required. These problems have been solved by the advent of high power lasers and the production of very sensitive spectrometers. These developments have made Raman spectroscopy readily accessible as one of the most useful and most reliable techniques of studying and characterizing carbon based materials [152].

### **3.2.2 Experimental Apparatus**

#### **3.2.2.1 The Laser**

A laser is a source of intense, coherent monochromatic radiation. The only excitation wavelength used in this work, was namely the 514.5 nm line from an Innova coherent argon ion laser. This belongs to the set of noble gas lasers, where laser light is produced by the amplification of the electronic transitions of the ionised states of noble gas atoms.

The gas is enclosed in sealed ceramic cylinder, termed a plasma tube, at a low pressure. An intense electric discharge between two electrodes is used to generate plasma, comprising of ionised gas particles and electrons. The electrons collide with the neutral gas particles leading to their further ionization and excitation.

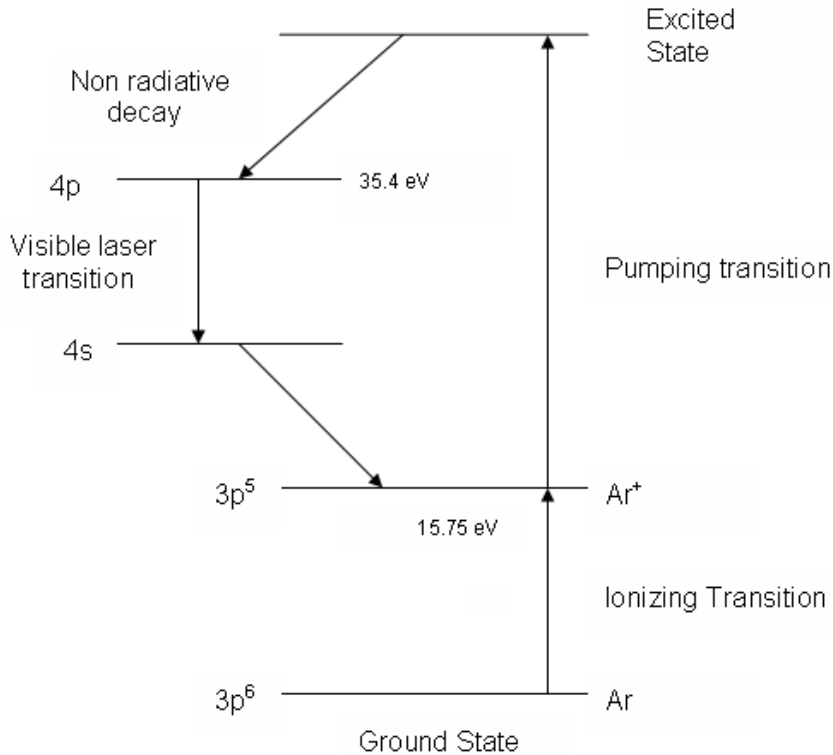


**Figure 3.3 :** A transition scheme for an Ar<sup>+</sup> laser. The first collision ionises the neutral argon and the next pumps it to an excited state (from the Operational Manual for the Spectra Physics 2020/2025 Ion Laser) .

In the Ar<sup>+</sup> laser, in the first collision the electron ionises the argon and the second collision pumps it to an excited state (Figure 3.3). The lifetime value is very short at that level and the ion decays to the 4p energy level without emitting any radiation. The 4p energy level has a relatively long lifetime value, allowing the population of a large number of ions in that level. This condition creates what is termed as population inversion, in which the density of ions in the higher energy levels surpasses that in the ground state. Population inversion is one of the required conditions for a laser to operate. The 4p ions then decay into the 4s level, either spontaneously or by activating a photon of equivalent energy. The transition is radiative and gives a photon of which the wavelength can be written as

$$\lambda = \frac{hc}{E}$$

where  $h$  is Planck's constant,  $c$  the speed of light in the vacuum and  $E$  the energy separation between two different states.

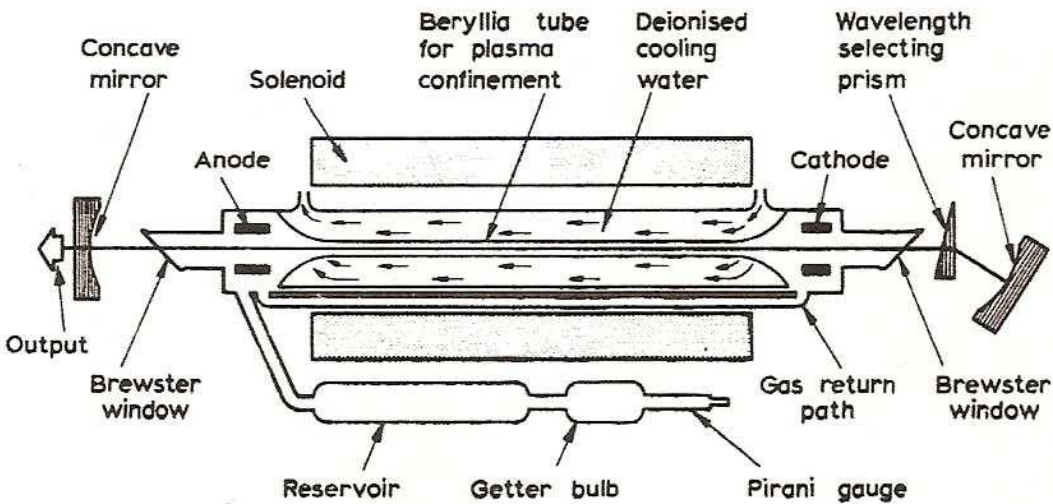


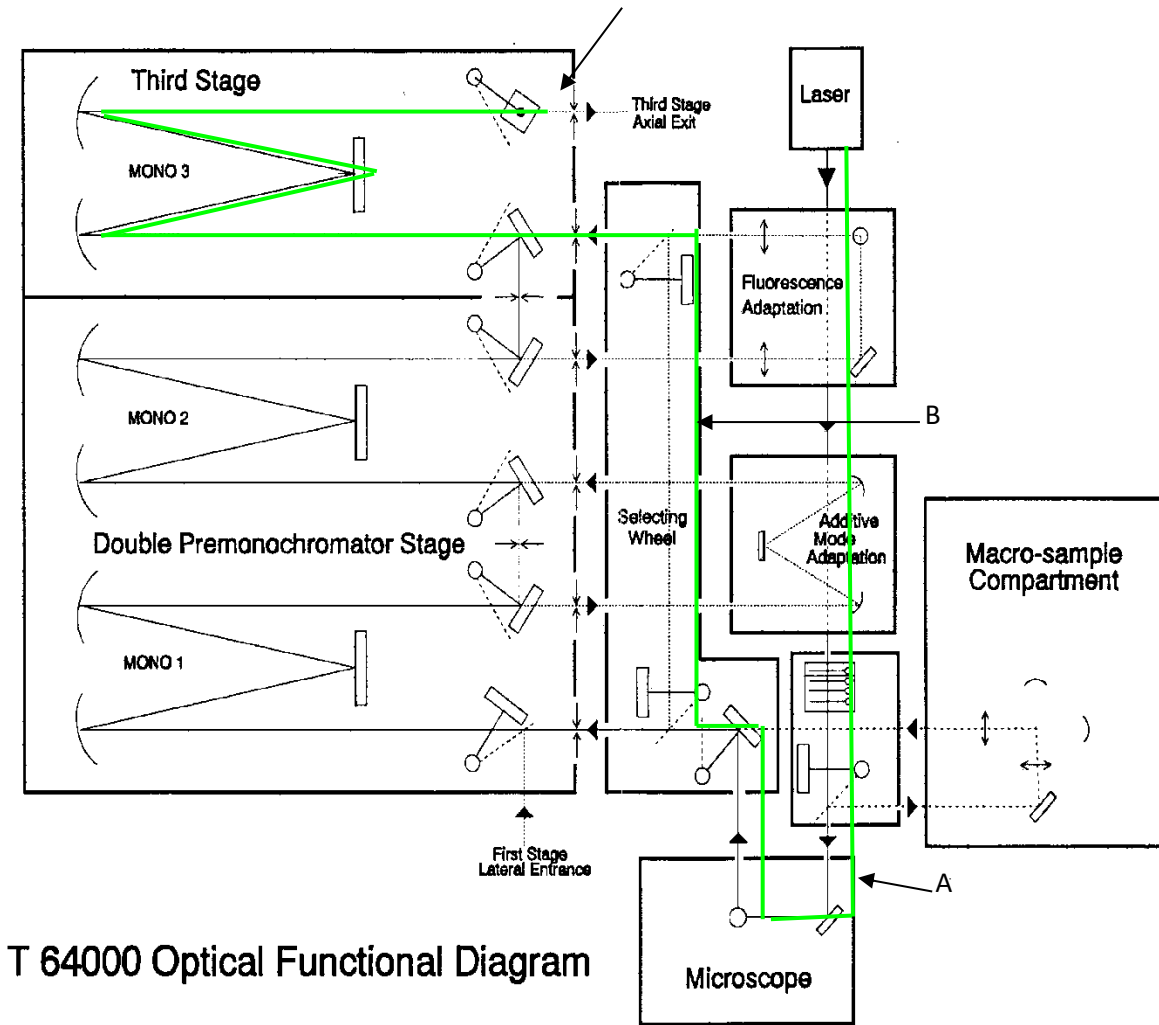
**Figure 3.4:** Schematic diagram of a gas laser [152].

The light energy sent through stimulated emission in the plasma tube is kept in the optical cavity of the ion laser. Figure 3.4 displays a schematic diagram of the laser optical cavity. At one site is a high reflector mirror with a reflectivity of 100%, and at the other site is an output mirror with a reflectivity of slightly less than 100%. The emitted photons move back and forth between these mirrors and in the process create more ions to produce photons. A small percentage of the photons can pass through the output mirror and these make up the output laser beam coming from the population inversion, photons emitted by the stimulated emission process are emitted coherently and greatly exceed those emitted spontaneously that are incoherent. The design of the long optical cavity ensures that the activated photons are sent out co-linearly with the cavity axis, whereas the spontaneous photons are arbitrarily

emitted and hence the relatively few on-axis photons result in a very weak incoherent noise overlaid on the beam [152].

### **3.2.2.2 The Raman Spectrograph**

Figure 3.5 displays the schematic diagram of the Jobin-Yvon T64000 Raman spectrometer used in School of Physics. Laser light is diffracted through the spectrometer by optical mirrors. Raman Spectra were obtained using an Olympus BX40 microscope attachment which focused the light on the sample. The Spectrometer was operated in single Spectrograph mode. At point “A” on the diagram is the location of the plasma line filter which takes out the laser plasma lines by narrow band pass filter and allows only the laser line to be transmitted into the microscope. Backscattered light returns from the sample through the microscope into the spectrometer, where it is processed in any one of the three configurations of the spectrograph. In the single spectrograph mode, the beam is directed to a holographic notch filter, at point “B” which strongly filters out the Rayleigh scattered light but allows the Raman scattered light to pass through. The transmitted light then passes through an entrance slit and falls on a grating where it is dispersed. Two different types of grating are available with the spectrometer and might be used interchangeably using the software. The choice of grating depends on the resolution and spectral range required. The 600 lines/mm grating gives a wide spectral range but at a lower resolution, whereas the 1800 lines/mm grating has a narrow spectral range but with improved resolution. The 600 lines/mm grating was used in this work.



T 64000 Optical Functional Diagram

**Figure 3.5:** Schematic diagram of the Raman Spectrograph showing the beam trajectory (From the Instruction Manual for the Jobin-Yvon T64000 Raman spectrograph).

The incident laser beam was focused onto the sample using a 100X objective, backscattered light dispersed by the grating falls on the charge coupled device (CCD) detector, which monitors the scattered light and produces a spectrum. The CCD detector is situated on top of the third (final) stage spectrograph as indicated on the diagram. The CCD is a rectangular chip consisting of 1024 x 256 pixels, where the light is dispersed along the 1024 pixels and binning of the measured photons takes place along the 256 pixels and each pixel being a silicon photo-

sensor. When scattered light falls on a pixel, photoelectrons are produced in numbers proportional to the intensity of the radiation. For optimum performance, the CCD is cooled to 140 K by liquid nitrogen. The spectra were acquired and displayed using Lab Spec V4 software. For the 514.5 nm measurements, the power at the sample was 1.3 mW. The spectral resolution was better than  $4\text{ cm}^{-1}$  for both wavelengths. The advantage of the single spectrograph mode is that it has a higher throughput and offers rapid analysis time. Its disadvantage is that it cannot be used for Raman bands of frequency in proximity of the laser line. The readout from the detector goes through the CCD controller to the computer, where the Labspec software captures the output and displays it for saving and processing [152].

Raman spectroscopy is probably the most common technique used for evaluation of carbon films because of its ability to distinguish between different forms of carbon. For diamond, the single phonon (first order) Raman spectra was produced using laser excitation in the visible range (e.g. 514.5 nm from the  $\text{Ar}^+$  ion lasers) gives a single band at  $1332\text{ cm}^{-1}$ . Generally, Raman scattering above the diamond one-phonon band is assigned to  $\text{sp}^2$  carbon containing materials. Three generally distinguishable types of  $\text{sp}^2$  carbon include: crystalline graphite (a single band at  $1580\text{ cm}^{-1}$ ), defective or microcrystalline graphite (two broad bands at  $1580$  and  $1350\text{ cm}^{-1}$ ), and amorphous carbon (a broad asymmetric band peak at around  $1500 \pm 40\text{ cm}^{-1}$ ).

For DLC films, although it contains  $\text{sp}^3$  and  $\text{sp}^2$  carbon, there is no  $1332\text{ cm}^{-1}$  band (associated with pure diamond) detected. This is due to the higher sensitivity (by a factor of 50) to visible light by  $\text{sp}^2$  bonding than in  $\text{sp}^3$  bonding. Overall, two typical Raman peaks are detected at around  $1350\text{ cm}^{-1}$  (called the D peak) and around  $1580\text{ cm}^{-1}$  (called the G peak) and they give us a range from graphite-like-diamond-like and polymer-like called hydrogenated

amorphous carbon [106] .

### **3.2.2 I-V characteristics by van der Pauw method**

Electrical properties of the films are a very important from the point of view of their electronic application. DLC thin films are generally characterized by high electrical resistivity ranging from  $10^7$  to  $10^{16}$   $\Omega\text{cm}$  depending on the deposition technique and the process conditions used. It was found that some DLC thin films had high electrical resistivity, large band gap and high thermal conductivity that can challenge the natural diamond in many of its applications. This combination of high thermal conductivity and high electrical resistivity makes DLC thin film more attractive as dielectric layer for high temperature device [153].

#### **3.2.2.1 Description of the instrument**

The HP Model 4140B pA Meter/DC Voltage Source shown in Figure 3.6 a high stability pA meter with  $10^{-15}\text{A}$  (max) resolution coupled with two programmable DC Voltage sources to secure usability in many application fields. The pA meter has a basic accuracy of 0.5% over wide measurement ranges ( $\pm 0.001 \times 10^{-12}$  -  $1.999 \times 10^{-2}$  A) allowing stable pA current measurement at  $10^{-15}\text{A}$  (1 count). This is accomplished by using a new unique, variable, digital, integration method. This stable and fast (less than 35 ms at 1 nA) measurement technique is very useful, not only for the measurement of the small outflow currents of semiconductor devices and the static characteristics of FET, but also for making insulation resistance/leakage, current/absorption measurements/analyses of capacitance and insulation materials. One of the programmable DC Voltage sources ( $V_A$ ) can work not only as a programmable DC voltage source, but also as a unique staircase and accurate ramp generator. The DC voltage source has an output range of  $\pm 100$  V in 100 mV steps or  $\pm 10$  V in 10 mV steps, and the ramp rate can be set from 0.001 V/s to 1 V/s at 0.001 V mode with a pause key and in the manual sweep mode with down and up keys. Each

programmable DC voltage source ( $V_A$  and  $V_B$ ) has a current limiter to avoid damaging the DUT by excessive current.



**Figure 3.6:** Model 4140B and supplied accessories (From manual HP 4140B pA Meter/D.C Voltage Source).

### 3.2.2.2 Measurement of I-V Characteristics

The 4140B pA Meter/ DC Voltage is connected with the 3488A Switch/Control unit plate via a BNC connector to the source voltage through selected relay configurations and simultaneously measure the current flowing in the sample through 4 probe geometry with 2 grounded contacts. The voltage from the HP 4140B was sourced from the  $V_A$  output via a female BNC connector to sweep voltage values to the sample through a selected relay configuration of the HP 3488A switch/control unit. Current measurement of the samples was carried out using a triaxial cable after grounding the chassis and the force pin of the cable. A HP 3456A Digital voltmeter was connected in series to read out the voltage output from the terminal  $V_A$  of the HP 4140B device. All these three apparatus were interfaced using home built Lab View via GPIB control for I-V characteristics measurements as shown in figure 3.7. The first sweep involved the variation of voltage values from +3V to -3V in steps of 0.1V; The voltage – current (I-V) characteristic was

carried out sequentially after sourcing voltage and simultaneously measuring the current through the sample using the Picoammeter (pA) HP 4140B module.

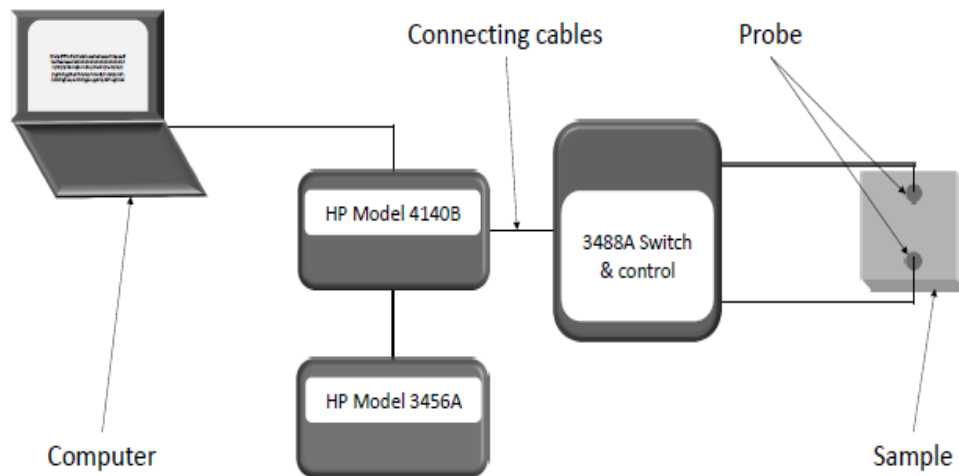


**Figure 3.7:** Schematic diagram of the Model 4140B and supplied accessories for I-V characteristics measurements

### 3.2.3 X-ray photoelectron spectroscopy and X-ray induced Auger spectroscopy

X-ray photoelectron spectroscopy, also called ESCA, was developed in the mid 1960 s by K. Siegbahn and his research group. K. Siegbahn was awarded the Nobel Prize for Physics in 1981 for his work in XPS. The phenomenon is based on the photoelectric effect outlined by Einstein where photons impinge upon the surface [154].

X-ray photoelectron spectroscopy is the technique used to irradiate a surface with X-ray to extract photo-electrons. By measuring the kinetic energy of the extracted electrons and knowing the energy of incident X-ray photons, the binding energy of the bonds in the solid can be determined. The method can detect all elements except hydrogen and helium and it is also suited for the determination of the bond levels of constituent elements in compounds, because the

binding energy of an element differs from compound to compound. It is basically the technique that enables studying the surface, as the depth of the photo-electrons ranges from 2 to 5 nm. The accuracy of XPS is approximately 0.1 at.% (from National Metrology Institute of South Africa). The XPS measurements were performed using the Thermo ESCIab 250Xi (similar to the one shown in figure 3.8) using monochromatic Al  $K\alpha$  (1486.7 eV) X-ray source. The chamber vacuum level was maintained beyond  $10^{-8}$  mbar. The X-ray power and spot size are 300 W and 900  $\mu\text{m}$  respectively. It is the lens/ analyser / detector combination in ESCALAB 250 that makes the instrument unique for both imaging and small area XPS as shown in figure 3.9. The XPS were used to determine the elemental composition on the surface of DLC thin film. Two samples prepared by RF magnetron sputtering unbiased substrate with different concentration (6.5 sccm and 13 sccm) were investigated. Thereafter two samples of RF and DC substrate bias voltage (-75V and -100V) were also analyzed using XPS equipment (ESCALab 250 Xi) at the National Metrology Institute of South Africa (NMISA), South Africa.



**Figure 3.8:** Picture of the Thermo ESCALab 250Xi X-Ray Monochromatic Al K $\alpha$  (1486.7 eV).

In the study of DLC films, XPS is mainly utilized to obtain the elemental composition and the quantitative determination of the fraction of  $sp^3$  and  $sp^2$  carbons at the DLC thin film surface. This is achieved through analysis of the C1s level. Due to the difference of the local environment, the binding energy of  $sp^3$  is slightly higher than that of  $sp^2$  carbon [154]. By using the Gaussian-curve deconvoluted fitting procedure, two separate peaks can be resolved. The peak with higher energy corresponds to the  $sp^3$  carbon while that of lower energy is attributed to the  $sp^2$  carbon [154]. Unfortunately, the XPS instrument used in this present study was unable to resolve the  $sp^3$  and the  $sp^2$  fractions due to its limited resolution. The X-ray induced C KLL Auger peak aids in distinction of these bonding states in a semi-quantitative manner for non-functionalized samples. The differentiated form of the C KLL spectrum allows measurement of the D-Parameter,

which gives an indication of the relative amounts of  $sp^2$  and  $sp^3$  carbon as shown in figure 3.9.

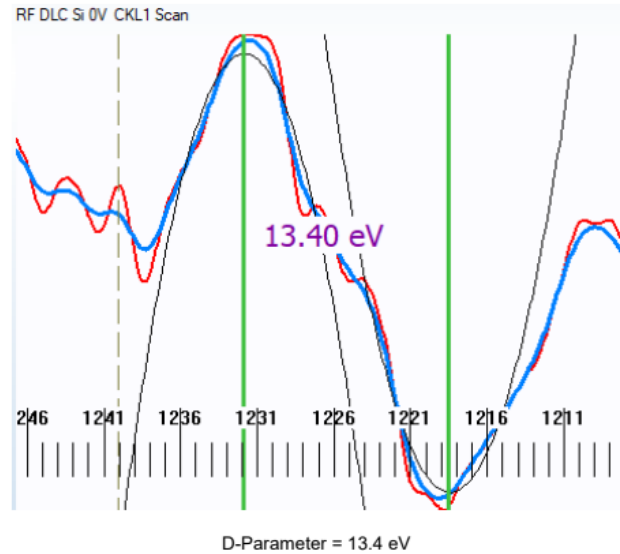


**Figure 3.9:** D-parameter of DLC thin prepared by RF magnetron sputtering Ar/CH<sub>4</sub>:13/6.

### 3.2.4 X-ray reflectometry (XRR)

XRR is a non-destructive technique used to determine the thickness, density and roughness of the films with high resolution. This technique involves monitoring the intensity of the X-ray beam reflected by the specimen at grazing angles usually varied from  $0.1^\circ$  to  $5.0^\circ$  in the incident angle. X-ray diffractometer (Bruker AXS D8 Discover) used is based on symmetrical arrangement of incident and secondary beam optics.

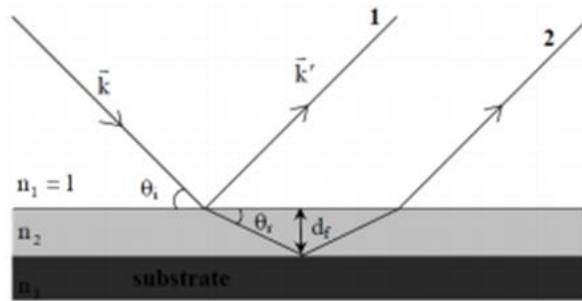


**Figure 3.10:** Schematic diagram depicting the X-ray total external reflection from a film substrate system [155].

In principle, a monochromatic X-ray beam of wavelength  $\lambda$  irradiates a sample at a grazing angle  $\theta_g$  and the intensity reflected at an angle  $2\theta_R$  is recorded by a detector. Total reflection will occur at a certain critical angle,  $\theta_c$ . The angle varies depending upon the electronic density of the material. For an ideal flat surface, the reflectivity decreases at angles above the critical angle in proportion to  $\theta_g^{-4}$ . If the material surface is rough, a more drastic decrease in reflectivity occurs. This is because roughness gives rise to diffuse scattering, resulting in less intensity in the specular reflected beam. Given a thin film evenly overlaid on the substrate with electronic density different from the substrate, the reflected X-rays from the interface and the thin film as well as from the free surface of the thin will interfere constructively and destructively as depicted in Figure 3.10. The period of the interference fringes and the decrease in the intensity are related to the thickness and the roughness of the layer. As a result, density ( $\rho$ ), film thickness ( $d$ ), and roughness (rms) may be extracted from the critical angle, interference spectra, and reflectivity.

The following discussion follows closely the treatment of [156]. At X-ray frequencies, the refractive index  $N$  can be expressed as

$$N=1 - \delta - i\beta \tag{3.1}$$

$$\delta = \frac{\rho_e r_e \lambda^2}{2\pi} \quad (3.2)$$

$$\beta = \frac{\mu \lambda}{4\pi} \quad (3.3)$$

Where  $\rho_e$  is the electron density,  $r_e$  is the classical electron radius equal to  $e^2/mc^2$ ,  $\lambda$  is the X-ray wavelength and  $\mu$  is the linear absorption coefficient for energies far from the X-ray threshold. From the measurement of the critical angle, the density of the films can be estimated by the formula.

$$\theta_c = \sqrt{2\delta} = \lambda \sqrt{\frac{r_e \rho_e}{\pi}} \quad (3.4)$$

For incident angles greater than  $\theta_c$  ( $\theta_R > \theta_c$ ) the X-ray beam penetrates inside the film. Reflection will therefore occur at the top and bottom surfaces of the film. The interference between the rays reflected from the top and the bottom of the film surfaces results in interference fringes, a typical fringe pattern for DLC films is shown in figure 4.2.

For intensity maxima, the path difference between the reflected waves should be an integral multiple of the incident wavelength.

$$m\lambda \approx 2d\sqrt{\sin^2\theta_m - \sin^2\theta_c} \quad (3.5)$$

Where  $m$  is an integer, since the angle is small, equation (3.5) can be expressed

$$m\lambda \approx 2d\sqrt{\theta_m^2 - \theta_c^2} \quad (3.6)$$

The layer thickness is therefore given by

$$d = \frac{1}{2} m \lambda \frac{1}{\sqrt{\theta_m^2 - \theta_c^2}} \quad (3.7)$$

For very small angles ( $\theta_R < 0.2^\circ$ ), the scattered X-ray intensity is almost constant, whereas above the critical angle the intensity rapidly drops by several orders of magnitude and oscillation appear in the spectrum [156] .

### 3.2.5 Infrared spectroscopy

Fourier Transform Infrared Spectroscopy (FTIR) is one of the widely used technique that provides information about the chemical bonding in a-C:H. The IR absorption composed of C-H stretching modes at 2800-3300  $\text{cm}^{-1}$ , C-C and C-H bending modes below 2000  $\text{cm}^{-1}$ , as illustrated in figure 3.11.

Fourier Transform IR operating in the range 650-4000  $\text{cm}^{-1}$  was used to collect the spectra in the transmission mode. The infrared radiation transmitted through the sample from the surface is detected and a plot of IR transmission versus wavelength is generated. The peak position is mostly used for qualitative identification of the chemical functional group present. The specificity of these bands allows computerized data searches to be performed against reference libraries to identify a material. To determine the identity of the material being analyzed, the unknown IR absorption spectrum is compared with standard spectra in computer databases or a spectrum to identify the unknown sample. In addition, FTIR can also be used to quantify a material. Quantitative concentration of a compound can be determined from the area under the curve in characteristic regions of the IR spectrum. Concentration calibration is obtained by establishing a standard curve from spectra for samples of known concentrations [157].

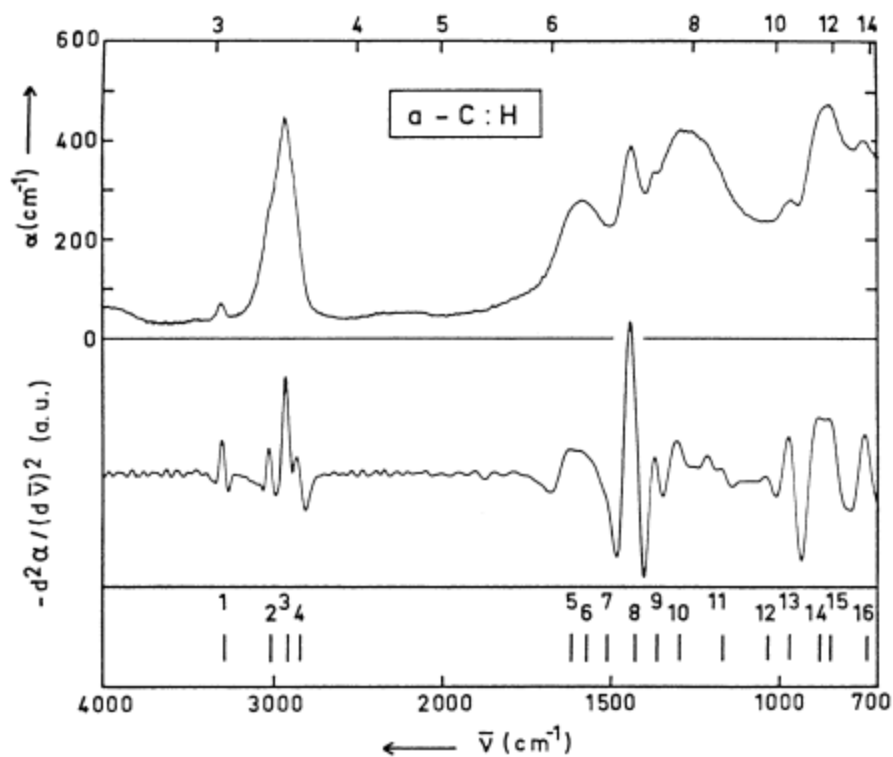


**Figure 3.11:** IR spectrum of a-C:H films [157].

As far as DLC films are concerned, FTIR is an effective tool in analyzing the hydrogen content and probing the different C-H configuration by using the optical mode of the microscope. As for aliphatic hydrocarbons, C-H stretching vibrations occur in the region  $2975\text{-}2840\text{ cm}^{-1}$  for hydrogenated DLC films [157]. It is well known that the  $\text{sp}^2\text{-C-H}_n$  and  $\text{sp}^3\text{-C-H}_n$  modes is located between  $2975$  and  $3085$ , and  $2850$  and  $2955\text{ cm}^{-1}$ , respectively [157].

FTIR was performed at NMISA. To eliminate the background of Si wafer, a spectrum was obtained with a blank Si wafer, which was used to deposit the DLC films. This Si spectrum was then subtracted from the spectra obtained for the DLC films.

### **3.2.6 Optical emission and UV-Vis spectroscopy**

#### **3.2.6.1 Optical emission spectroscopy**

Optical emission spectroscopy (OES) is the powerful tool to investigate the active species present in glow discharge plasma. A number of studies have reported the spectroscopic studies of the process of RF deposited amorphous carbon films involving OES on CH<sub>4</sub>, C<sub>2</sub>H<sub>2</sub>, and CH<sub>4</sub>-Ar plasma. Studies by C. Barholm-Hansen et al. [158] investigated plasma species during the growth of the DLC films from the methane plasma and the influence of flow rate. The plasma species produced by RF magnetron sputtering (13.56 MHz) was monitored *in situ* by means of OES technique. This method monitors the emitting species coming from Ar excitation/ionization and CH<sub>4</sub> dissociation and because the methane concentration was step-increased for a fixed concentration of argon, the intensity of the radical C-H was expected to show corresponding increase. The emissions of the excited species for the CH<sub>4</sub>-Ar plasmas in the spectral range of 200-850 nm were monitored using a fiber-coupling spectrometer through a quartz vacuum mounted on the top flange of the chamber.

#### **3.2.6.2 UV-visible spectroscopy**

Optical spectroscopy was conducted using the Varian Carry 500 spectrophotometer in the transmittance mode. A schematic of the spectrophotometer is shown in figure 3.12. The spectrometer uses two lamp sources and diffraction grating to produce a dispersive spectrum of light. The tungsten lamp source produces light in the visible region, whilst the deuterium lamp produces light across the ultra violet spectrum. Transmittance measurements were conducted in the wavelength range of 300-800 nm after zero baseline calibration. The spectrophotometer allows for a dual beam for transmittance to be measured relative to the control sample. The transmission of each sample was measured relative to air and a typical spectrum recorded for a DLC thin film

is shown in Figure 5.18, from which one could obtain the optical parameters of the thin films [155]

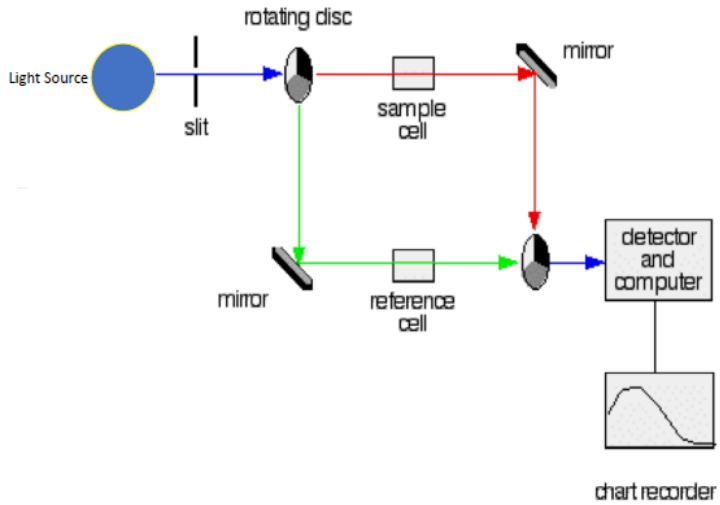


**Figure 3.12:** Schematic diagram of the Varian Cary 500 spectrophotometer.

### 3.2.7 Surface Brillouin scattering

#### 3.2.7.1 Introduction

Surface Brillouin scattering (SBS) is a technique using the light laser scattering to investigate the properties of near opaque materials [150]; it enables the probe of thermally induced surface acoustic waves at the surfaces of either homogenous solids or thin supported films [150]. Laser light is suitable for this experiment because it is intense, monochromatic, highly collimated and highly polarized. In this section the principle of a laser, and the theory behind the laser action and intra-cavity etalon are presented. The section follows closely the instruction manual for Spectra-Physics Model 2060/2080 Ion Laser. A detailed description of the Tandem Fabry-Pérot interferometer (TFPI) used for this study is given in Section 3.2.7.3 which is found in the user manual for JRS Scientific Instruments tandem Fabry-Pérot Interferometer[150]. The SBS experimental configuration using the backscattering geometry is shown in figure 3.13.

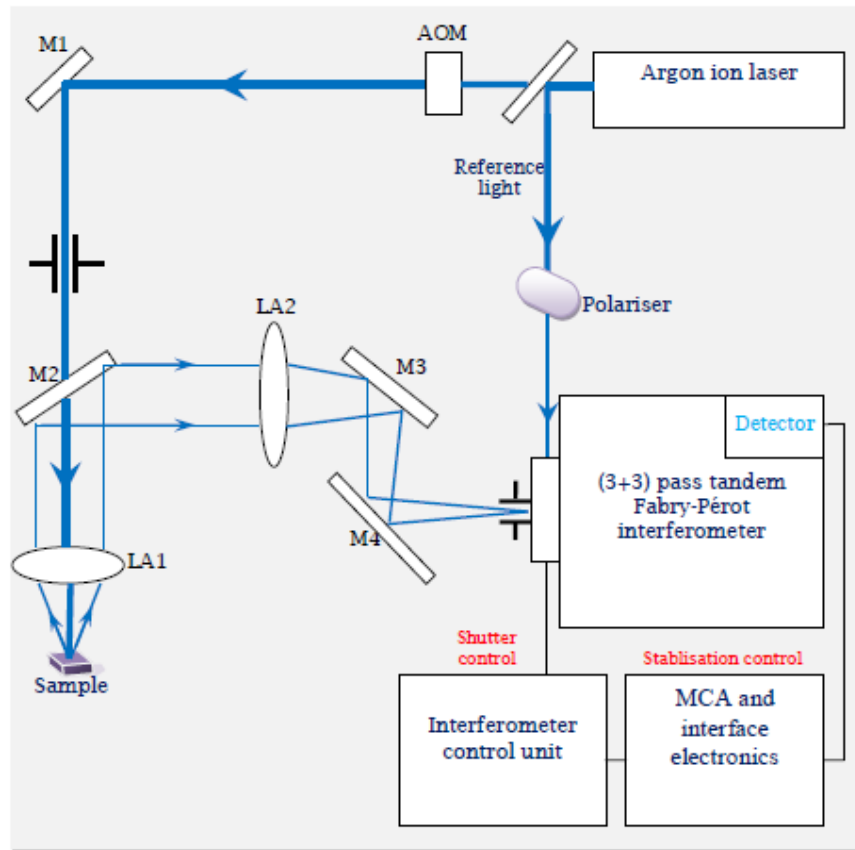


**Figure 3.13:** A schematic diagram of the external optics used for Brillouin light scattering in the backscattering geometry [150].

### 3.2.7.2 Laser and intra-cavity etalon

The green line of wavelength 514.5 nm, generated by an argon-ion laser operated with power of 200 mW in a single axial (longitudinal) mode was the source of the incident photons used in this study and the spectrum of the scattered light from the specimen was investigated. The frequency shifts of the scattered light were in the range of a few GHz (to about 150 GHz). From the broad gain profile of the laser as shown in the Figure 3.14, a single longitudinal mode was selected, with a very narrow laser line width suitable for SBS.

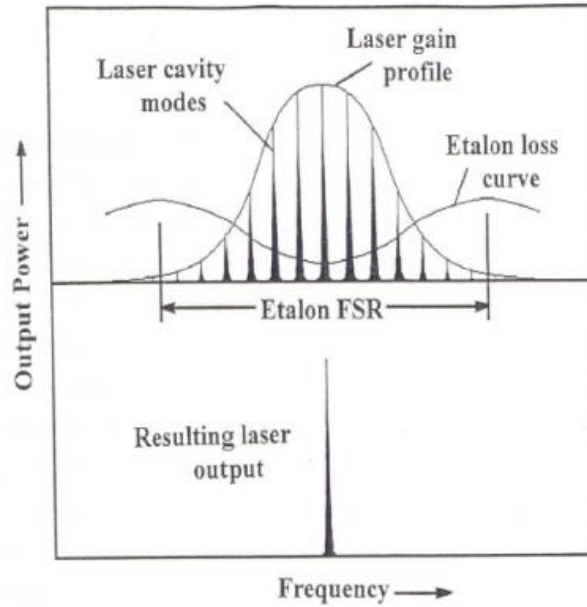


**Figure 3.14:** Selection of the single axial longitudinal mode from the intersection of the maximum of the laser gain profile and the minimum of the Etalon loss curve (From the instruction manual for the spectra-Physics Model2060/2080 Ion Laser).

### 3.2.7.2.1 Argon ion laser

The properties of the argon-ion ( $\text{Ar}^+$ ) laser are probably the most understood of all the ionized gas laser media and they have been presented previously in the section covering Raman Spectroscopy. For SBS experiments discharge currents of up to 30 A which yields laser output power of up to 600 mW are commonly used. Considerable higher output powers may be achieved with higher discharge currents.

### 3.2.7.2.2 The Fabry-Pérot interferometer

The French physicists Charles Fabry and Alfred Pérot first introduced the Fabry-Pérot interferometer (FP) in 1897. It is an optical instrument which uses multi-beam interference by utilizing the fringes produced in the transmitted light (Born and Wolf, 1975) [159].

The light is transmitted after multiple reflections in the air-film interface between two

plane mirrors mounted accurately parallel to one another as shown in figure 3.15. The two highly reflecting mirrors constitute an assembly referred to as an etalon. Due to the high reflectivity of the parallel mirrors, the successive multiple reflections of light (R) waves diminish very slowly in intensity and form very narrow sharp fringes which may be used to reveal hyperfine structures in the line spectra. The varying transmission function of an etalon is caused by the interference between the multiple reflections of light between the two reflecting surfaces. Constructive interference occurs if the transmitted beams (T) are in phase and destructive interference occurs when they are out of phase. Constructive interference corresponds to a high-transmission peak of the etalon whilst destructive interference corresponds to a transmission minimum.

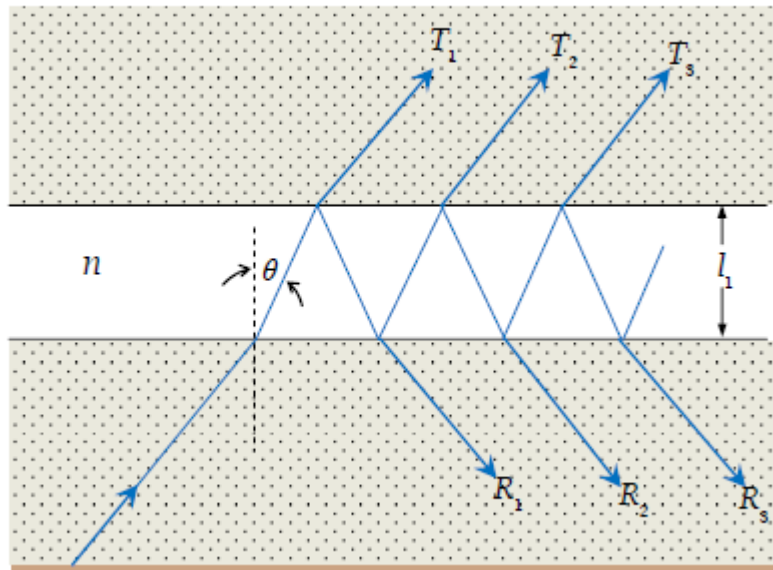


**Figure 3.15:** The reflection of a plane wave in a plane parallel plate, Fabry-Pérot [150] .

The frequency shift of the backscattering light is very small compared to the frequency of the laser. Hence, a high resolution and high contrast interferometer is used. Fabry-Pérot Interferometer is an

optical instrument that plays the role of band pass filter. As its pass frequency can be adjusted, it can be used to scan the full spectrum width to be measured. The most widely used interferometer is the Sandercock type (shown in Figure 3.16) and it is able to resolve the weak Brillouin doublets. Sandercock showed that the contrast can be significantly improved by multipassing the interferometer with three, five or even seven passes. In our laboratory, the Sandercock-type (3+3) multi pass tandem interferometer was used to attain a contrast of  $10^{11}$  required to distinguish the weak scattered light from the elastically scattered light.

This type of interferometer has the added advantage of using tandem FPs to enable the attainment of such high contrast. Two synchronized or coupled Fabry- Pérot interferometer are used in tandem to prevent the overlapping of different orders of interference fringes. A schematic of this arrangement is shown in Figure 3.17, where the spacing of the second FP,  $L_2$  is close to  $L_1$  but not equal to  $L_1$ , taking  $L_2$  and  $L_1$  as the mirror spacing. In general, a good practical value for  $L_2/L_1$  is 0.95. A plane view of two Fabry- Pérot Interferometers on a single translational stage is shown in figures 3.16 and 3.17.

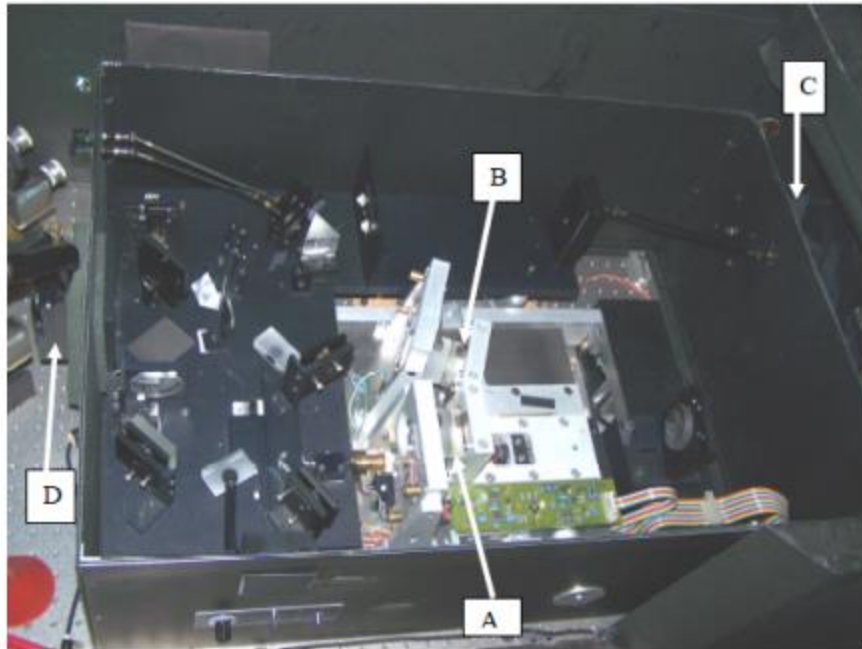


**Figure 3.16:** A photograph of (3+3) multipass Tandem interferometer, in which FP1 (A) and FP2 (B) are mounted in tandem on a translating stage. The detector (C) is mounted on the TFPI box and the shutter mechanism is labelled (D) [151].

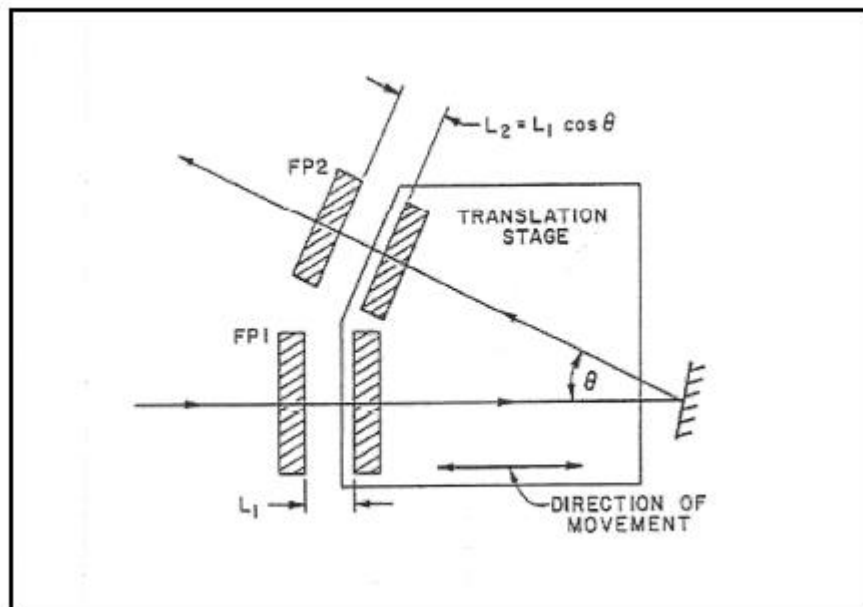


**Figure 3.17:** Translational stage of the two Fabry-Pérot, which are capable of scanning synchronously (From JRS Scientific Instruments, TFPI operator manual).

# **Chapter 4: Correlation of optoelectronic and mechanical properties of unbiased DLC thin films**

## **4.1 Introduction**

In this chapter, the results on the characterization of diamond like carbon thin films prepared by RF and DC magnetron sputtering on unbiased substrates are presented. Diamond-like carbon (DLC) thin film is a metastable allotrope of amorphous carbon containing  $sp^2$  clusters embedded in high fractions of  $sp^3$  bonded carbon. Their unique properties such as the  $sp^3$  fraction depend on the optical transmittance and the electrical resistivity which coexist with superior mechanical properties such as high hardness, low friction coefficient [160-168] have seen them being applied in diverse environments. These properties dictate numerous technological applications of diamond like carbon films spanning from protective coatings in optical windows, magnetic storage disks and cutting tools to be realized [168]. Furthermore, the tuning of the  $sp^2$  and  $sp^3$  fractions in DLC thin films has driven their applications as strain gauges in microelectromechanical systems (MEMS). Despite their extensive potential, the presence of high hydrogen content in DLC thin films continues to preclude their application due to the inherent inferior mechanical properties such as low shear modulus. This is evident particularly in DLC thin films fabricated by the conventional plasma enhanced chemical vapor deposition (PECVD) technique which often contains more hydrogen even at low temperatures (27 °C). The evolution of large fractions of hydrogen in these films has often been found to produce moderate fractions of  $sp^3$  bonding, leading to low hardness, weak adhesion, limited resistance to wear and tear. This chapter presents the results of DLC thin films fabricated using physical vapour deposition techniques. These PVD techniques include RF and DC magnetron sputtering and have been used due to their low hydrogen fractions, moderately high elastic constants and strong adhesion between the substrate and the

films. These films have been fabricated at room temperature with a pure graphite (99.99%) target under Ar and CH<sub>4</sub> atmosphere. The dependence of the optoelectronic and the mechanical properties of the DLC thin films based on the ratio of sp<sup>2</sup>/sp<sup>3</sup> coupled with the hydrogen content is presented in the following sections.

#### **4.2 Plasma species characterization by optical emission spectroscopy**

The nature and the properties of the film produced during growth are determined by the type of ions and their charge states in the plasma. Characterization of the plasma is enabled by two variables namely the electron temperature and the emission of the plasma species in the visible and ultraviolet range. In this work, the optical or luminous emission due to relaxation was used to identify the species in the plasma. The plasma species produced by RF magnetron sputtering (13.56 MHz) was monitored *in situ* by means of optical emission spectroscopy (OES) technique. Which measures the emitting species arising from Ar excitation/ionization and CH<sub>4</sub> dissociation. The main emission lines observed in Ar-CH<sub>4</sub> plasma were identified to be Ar\* at 750.39 nm, Ar<sup>+</sup>\* at 387.53, 387.21, 386.85 nm, atomic hydrogen lines of the Balmer series (H<sub>α</sub> at 656.28 nm, H<sub>β</sub> at 486.13 nm, H<sub>γ</sub> at 434.05 nm), H<sup>2</sup>\* at 602.80, 622.48 nm. The presence of CH\*(system A<sup>2</sup>Δ-X<sup>2</sup>Π at 431.42 and 432.4 nm) and C<sup>2</sup>\*(Swan system, A<sup>3</sup>Π<sub>g</sub>-X<sup>3</sup>Π<sub>u</sub> at 516.52 nm) [162, 169, 170] were also observed. In general, the CH<sub>4</sub> molecules are decomposed into some hydrocarbon neutral radicals (CH, CH<sub>2</sub>, CH<sub>3</sub>), ionic radicals (CH<sup>+</sup>, CH<sub>3</sub><sup>+</sup>, C<sub>2</sub>H<sub>5</sub><sup>+</sup>), and atomic or ionic hydrogen. While the typical Ar lines are to be expected in the plasma, of interest in the growth of diamond like carbon are plasma emissions due to CH radicals. This is confirmed in Figure 4.1 which shows an intense CH\* emission for a Ar:CH<sub>4</sub> gas ratio of 1.1. This emission line was attributed to the increased presence of CH<sub>4</sub> when contrasted with the Ar only spectra. Besides the intense argon

lines (from 419 to 738 nm), the emissions lines,  $H_{\alpha}$  (657.9 nm) and  $H_{\beta}$  (486.2 nm) corresponding to the Balmer series of atomic hydrogen were clearly present in the plasma.

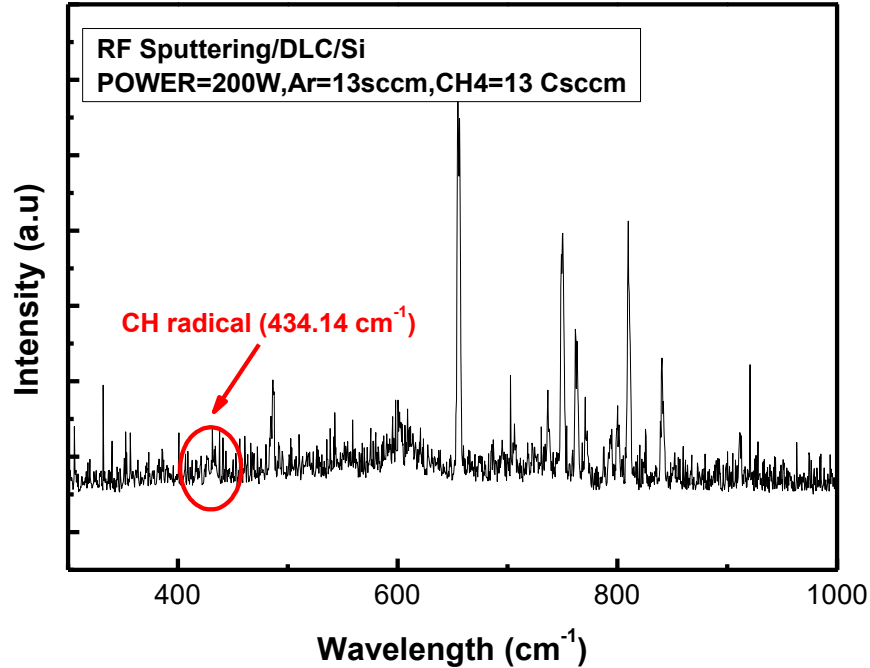


**Figure 4.1:** Optical emission spectroscopy of DLC film with the highest deposition rate occurs at 50 % methane and 50 % argon composition using RF magnetron sputtering.

The observed peak corresponds to the band head of the transition  $A2\Delta \rightarrow X2\Pi$  of the CH radical at  $\sim 434 \text{ cm}^{-1}$ . This corroborates literature reports which suggest that the neutral CH species in the plasma are associated with the deposition of the diamond-like films [162]. These conditions were subsequently optimised and used to fabricate diamond-like carbon thin films, at varied Ar/CH<sub>4</sub> ratios.

### 4.3 Thin film growth rate determination using X-ray reflectivity

X-ray reflectivity (XRR) is a non-intrusive and non-destructive method to measure the film thickness, density and interfacial roughness of thin films deposited on a substrate. A typical XRR spectrum of DLC on Si is presented in Figure 4.2 in which the black line represents the raw data

while the blue line represents the corresponding simulation assuming a layer stack of DLC/SiO<sub>2</sub>/Si. The thicknesses of several DLC films were measured in order to determine the deposition rates at various gas (Ar/ CH<sub>4</sub>) ratios.

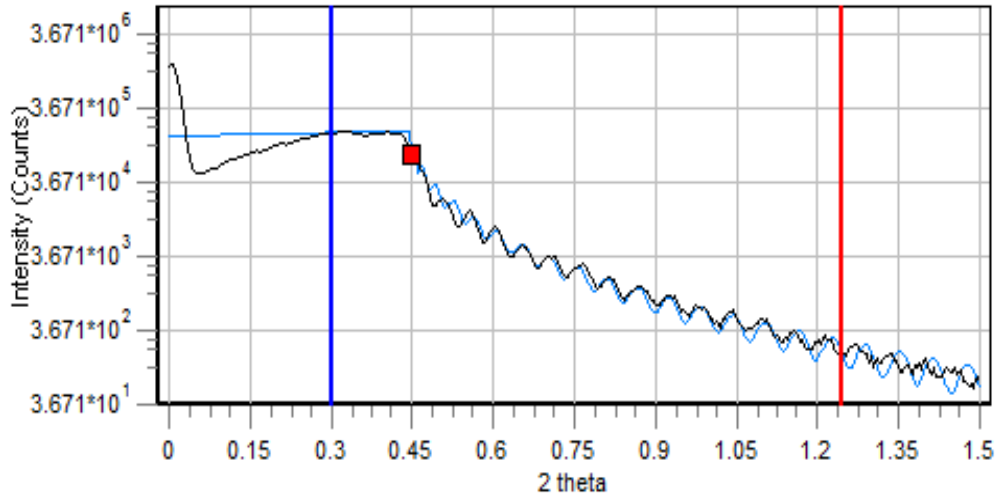


**Figure 4.2:** Typical XRR scan of DLC thin films deposited on silicon with a bias substrate at -100V, for a 50 % methane and argon composition and deposition power of 200W.

Figure 4.3 shows the deposition rate of the amorphous hydrogenated carbon as a function of CH<sub>4</sub> flow. The deposition rate increased from 19.84 to 27.99 nm/min with increasing CH<sub>4</sub> concentrations up to a maximum at 50 %. The increase in the deposition rate is indicative of the contribution of carbon atoms from the CH radical that is required in the fabrication of DLC thin films. The noticeable decrease to a value of 20.02 nm/min for the film deposited using 67% of methane in plasma could be associated with the competition between the working gas pressure and the reduced energy of the ad-atom species. According to literature, the density of DLC films have been reported to vary between 2.35 and 2.44 g cm<sup>-3</sup>. Using the physical property arguments it was established that the optimum condition for DLC film fabrication from the gas mixture was for Ar/CH<sub>4</sub> flow rate ratios of 1:1. During this study, additional confirmation was provided by Raman spectroscopy using the intensity ratio of the I<sub>D</sub>/I<sub>G</sub> values, which showed a maximum for the 1:1

plasma composition. At this composition, it is evident that a maximum deposition rate was attained (27.99 nm/min), this in turn corresponds to the optimum growth condition, and composition for the formation of DLC films ( $\text{CH}_4/\text{Ar}$  ratio of 1:1). The increase in the deposition rate at 50% of methane concentration in the mixture ( $\text{Ar} + \text{CH}_4$ ) is attributed to the increased dissociation and deposition of hydrocarbon ions and radicals onto the depositing films at the respective power. Additionally, corresponding to this optimal ( $\text{Ar} + \text{CH}_4$ ) composition is the higher film density of the film ( $2.49 \pm 0.02 \text{ g cm}^{-3}$ ) for RF sputtered films. There was no obvious correlation of the film roughness with the methane flow rates (Table 4.1), with the mean roughness relatively stable at about 1 nm.

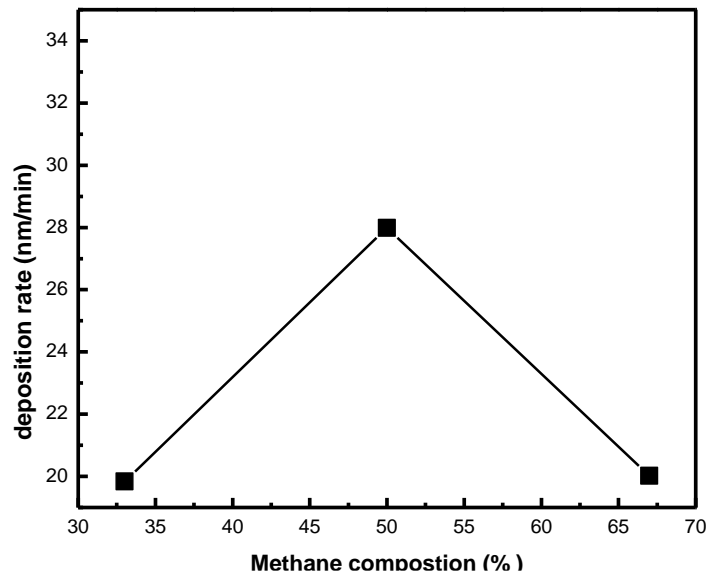


**Figure 4.3:** The deposition rate versus methane concentration, highest deposition rate occurs at 50 % methane composition of the (argon and methane) mixture.

**Table 4.1:** Physical properties of DLC thin films measured using X-ray reflectivity with varied Ar/CH<sub>4</sub> ratio.

% CH <sub>4</sub>	Roughness (nm) ± 0.20	Deposition rate (nm/min) ±0.05	Density (g/cm <sup>3</sup> ) ± 0.02	Thickness (nm) ±0.03
33	1.05	19.84	2.35	99.2
50	0.99	27.99	2.49	140.0
67	1.00	20.02	2.44	100.1

#### **4.4 Determination of sp<sup>3</sup> and sp<sup>2</sup> fractions and hydrogen content by Raman spectroscopy**

Raman spectroscopy is an excellent tool to characterize the structural properties of carbon based nanomaterials. As such it has been distinguished as the technique to identify the various allotropes of carbon and their bonding configurations in bulk and nanoscale regimes. Thus it has been used in this work to establish the nature and composition of sp<sup>2</sup> and sp<sup>3</sup> bonding configurations in diamond like carbon films. In figures 4.4 – 4.10, the Raman spectra of DLC films deposited on (001) Si substrate at varied (Ar and CH<sub>4</sub>) flow rates/ratios, using RF and DC sputtering at varied powers are shown. In disordered carbon-based material, the spectrum is composed of the two vibrational modes with distinct vibrational frequencies. In table 4.2, the complete list of DLC films deposited by RF and DC magnetron sputtering with unbiased substrate is given, together with the respective deposition parameters.

**Table 4.2:** DLC films deposited on unbiased substrate by (a) RF magnetron sputtering - and (b) DC magnetron sputtering - at different flow rate ratios and power ( $\text{CH}_4 = 20$  sccm,  $\text{Ar}^+ = 20$  sccm).

(a) RF magnetron sputtering on (001)Si at different (%) of $\text{CH}_4$ and fixed power (200W)		(b) DC magnetron sputtering on (001)Si at different (%) of $\text{CH}_4$ and power	
Type	(%) $\text{CH}_4$	Type	(%) $\text{CH}_4$
a-C:H	20	a-C:H	27 (200 W)
a-C:H	33	a-C:H	43 (200 W)
a-C:H	50	a-C:H	50 (200 W)
		a-C:H	50 (250 W)
a-C:H	67	a-C:H	50 (300 W)

#### 4.4.1 Raman spectroscopy of diamond like carbon using RF magnetron sputtering

The measured Raman spectra of DLC thin films are shown in Fig. 4.4 in the range of 800 - 1800  $\text{cm}^{-1}$ . These modes are primarily the D and the G band. In all the figures, these spectra have been obtained through deconvolution of two Gaussian peaks constituting the following:

- a broad peak centred at approximately  $1560 \text{ cm}^{-1}$ , this mode corresponds to the graphitic peaks (G bands)
- While the asymmetric shoulder at  $\sim 1370 \text{ cm}^{-1}$ , corresponds to the D (disordered) peaks, [79, 165, 171, 172] .

The G-peak and D-peak positions were obtained after deconvolution around  $1580\text{-}1600\text{ cm}^{-1}$  and around  $1350\text{ cm}^{-1}$ , respectively and as expected, there was also a corresponding increase in intensity with increased flow rate.

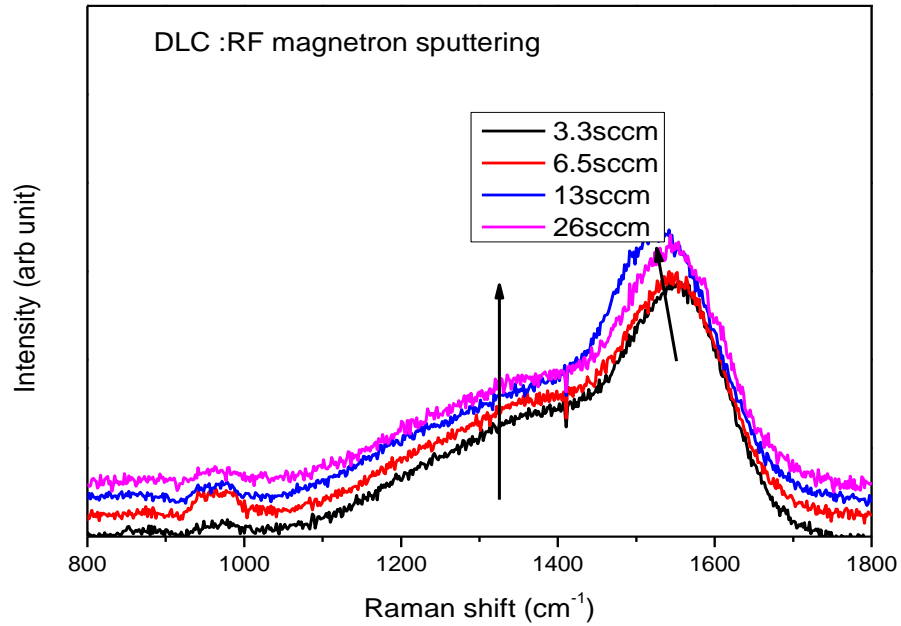


**Figure 4.4:** Raman Spectra of DLC films deposited at different (Ar and  $\text{CH}_4$ ) flow rate ratios using RF magnetron sputtering at 200 W.

These DLC films have shown characteristics consistent with spectral features observed from other literature [172-175] [176]. In Table 4.3, a summary of the D and G peak positions, their peak width ( $W_D$  and  $W_G$ ), and their corresponding  $I_D/I_G$  ratios obtained from the Figure 4.5 is tabulated for RF sputtered films.

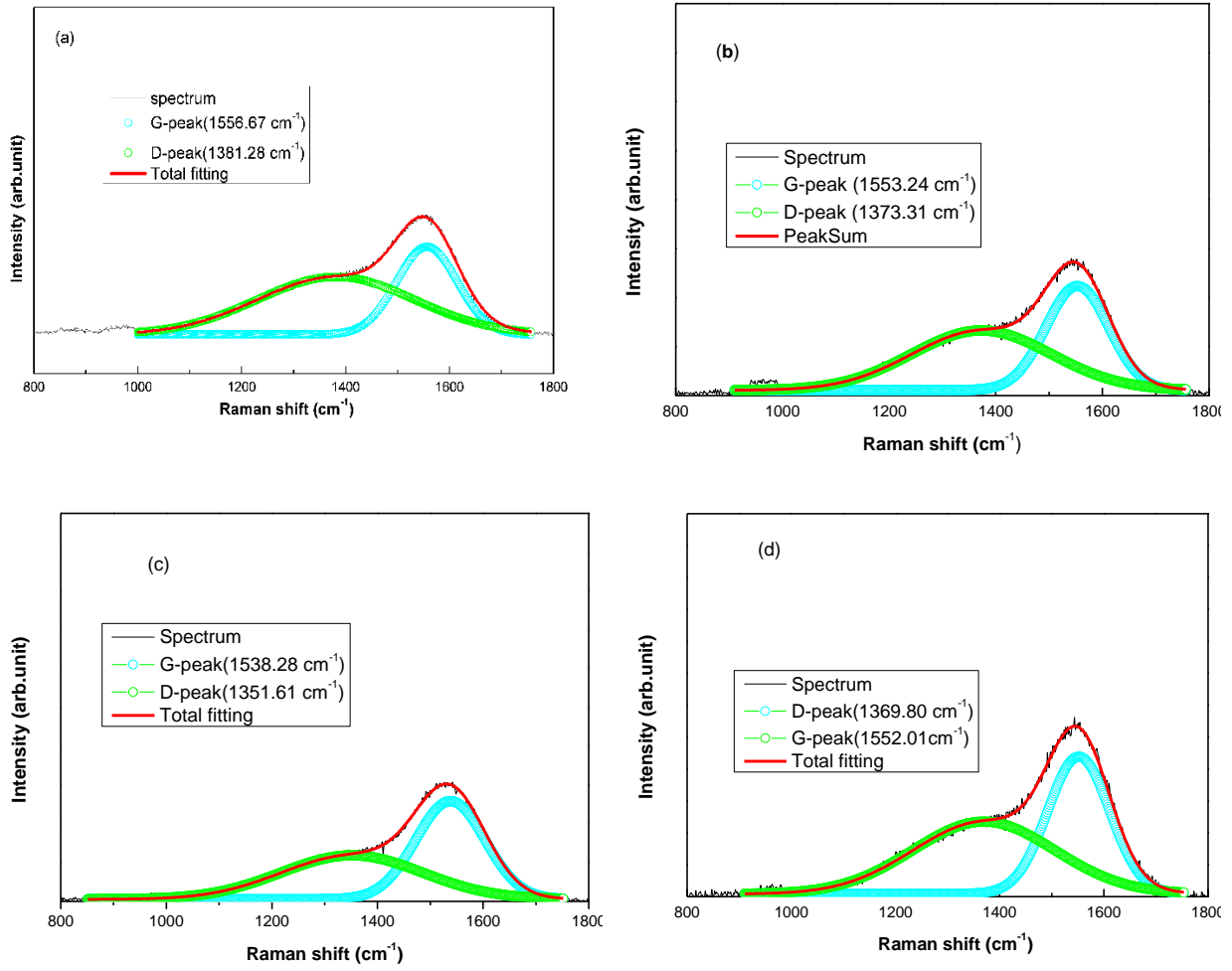


**Figure 4.5:** Raman Spectra of DLC films deposited at different (Ar and CH<sub>4</sub>) flow rate ratios: (a) 3.3/13, (b) 6.5/13, (c) 13/13 and (d) 26/13 using RF sputtering at 200W.

**Table 4.3:** Summary of spectral features of RF sputtered films at 200W

Methane composition (%) with Ar constant	Peak Position		Width		I <sub>D</sub> /I <sub>G</sub> ratio	
	D-Peak (cm <sup>-1</sup> )	G-Peak (cm <sup>-1</sup> )	W <sub>D</sub> (cm <sup>-1</sup> )	W <sub>G</sub> (cm <sup>-1</sup> )	From Area	From Height
DLC 20%	1382	1557	302	117	1.69	0.66
DLC 33 %	1373	1553	261	118	1.27	0.57
DLC 50%	1352	1538	268	131	0.92	0.45
DLC 67%	1370	1552	272	119	1.21	0.53

For these RF magnetron sputtered films, it was observed that FWHM of the (G) peak increases with methane concentration and reaches a maximum at 50% of methane and then decays monotonically at 67% CH<sub>4</sub> as shown in table 4.3. From the results in Table 4.3, the larger FWHM of (G) (~ 131 cm<sup>-1</sup>) is related to higher fractions of sp<sup>3</sup> bonds and higher structural disorder (poor electronic property). This in turn could suggest an expected large Tauc-gap, greater density and superior mechanical properties. From literature, it is also known that the methane has a broad range of hydrogen to carbon ratio that can easily dissociated in plasma to produce more hydrogen in the films and thus possibly affect their properties. It was said before that the high fraction of sp<sup>3</sup> was optimal for fabricating films with excellent tribological, mechanical properties, however this observation is inadequate as recent works have shown that sp<sup>2</sup>/sp<sup>3</sup> ratio alone does not provide a reliable estimate of the film structure or properties [176]. Therefore, it is imperative to determine the fraction of hydrogen in the films obtained under diverse conditions of growth. This is even more significant in the sputtering environment with carbon sources that have inherent hydrogen

such as methane. For films that have been grown under increasing methane flow rates and thus methane concentrations at constant argon compositions, it has been observed that the G-peak position decreases from  $1557\text{ cm}^{-1}$  at 20 % methane composition to a minimum value of  $1538\text{ cm}^{-1}$  corresponding to the Ar/CH<sub>4</sub> ratio of 1:1. At higher concentrations such as at 67 % methane the G-peak position was observed to increase. This increase in the G-peak position is attributed to the possible polymerization or termination of the sp<sup>3</sup> bonds with hydrogen of the films [Casiraghi *et al.*] [176]. The I<sub>D</sub>/I<sub>G</sub> ratios decrease in both height and area ratios of the corresponding D-peak and G-peak with the increased methane concentration. This increase again reaches a maximum at 50% of methane and then decays monotonically at 67% CH<sub>4</sub> that further confirms the formation of higher sp<sup>3</sup> fraction in the films structure, thus forming more and more diamond like carbon films. These observations are largely in agreement with the work done by Tamor and Vassel [116].

The fraction of hydrogen content in these films was again determined using Photoluminescence Raman of the sputtered films. This method provides semi-quantitative information about the H content of the a-C:H films and makes use of the slope (m) of photoluminescence (PL) background. The PL background was calculated as the ratio between the slope (m) of the spectral background and the maximum intensity (height) of the Raman G peak [I(G)]. The presence of hydrogen in hydrogenated DLC thin films modifies the C-C network. At optimum condition, the methane concentration was obtained at 50% with the average fraction of hydrogen of 31.61 at.% as shown in Figure 4.6, that enables the films to be more dense ( $2.44 - 2.49\text{ g/cm}^3$ ). The a-C:H film with dense structure and moderate sp<sup>3</sup>C-C/sp<sup>3</sup>C-H ratio may exhibit the best tribological properties [183]. The PL background plotted in logarithmic scale, measures linearly with hydrogen content and the H % can be deduced from the interpolation of elastic recoil detection data (ERDA) [177] equation (4.1).

$$[H]_{\text{Raman}} = 30 + 4.6 \log \left[ \frac{m}{I(G)} \right] \quad (4.1)$$

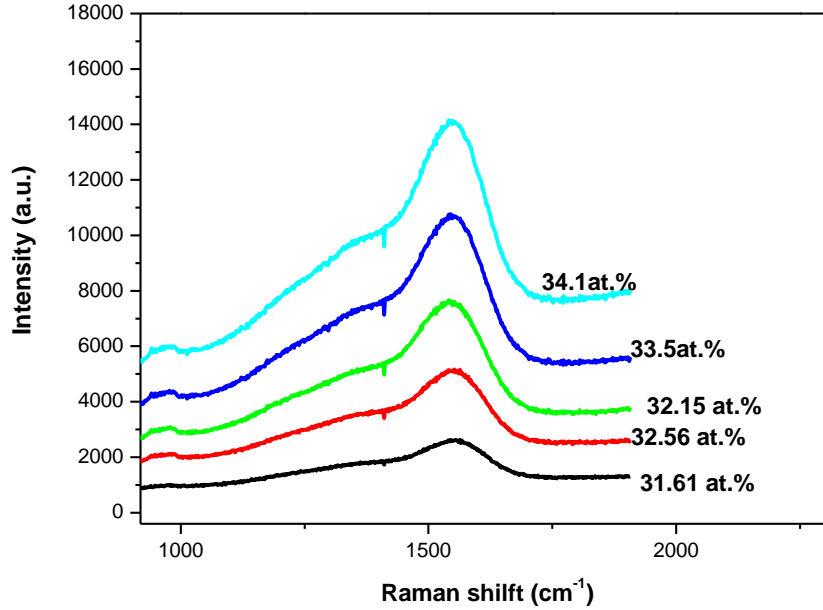


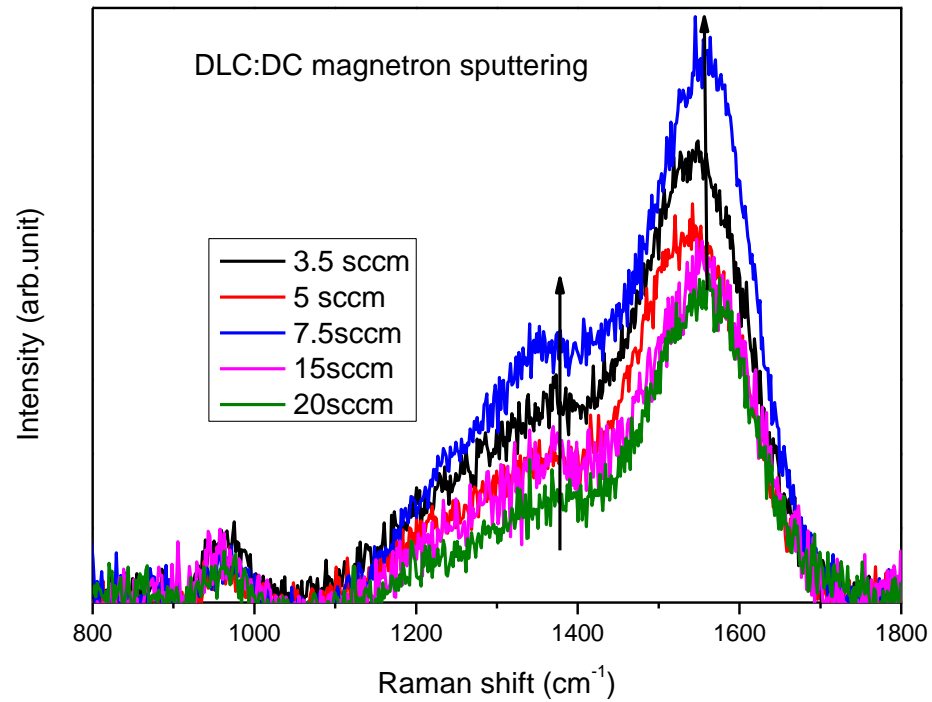
**Figure 4.6:** Raman spectra of DLC thin films prepared using RF magnetron sputtering unbiased on Si at 200W with different composition of Ar/CH<sub>4</sub> ratio.

Previous work on the growth of DLC thin films by RF magnetron sputtering and subsequent characterization using visible Raman have established an optimum methane concentration of (40%) [161]. The present results show an optimum closer to 50 % methane concentration, in agreement with the work done by Y. Wang *et al.* [178]. A more detailed analysis and discussion is presented in section 4.4.3, covering the microstructure, and optical properties summarized in the table 4.6.

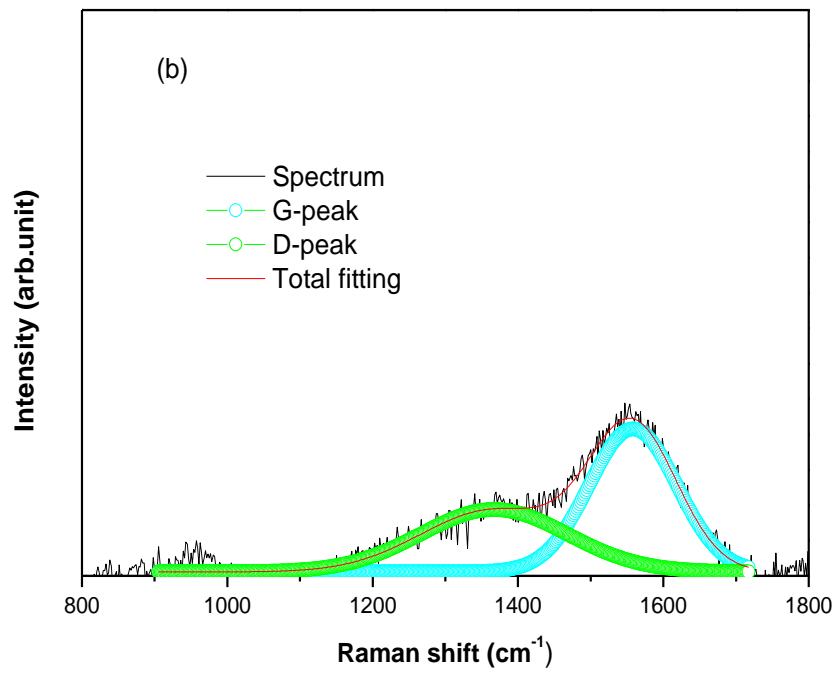
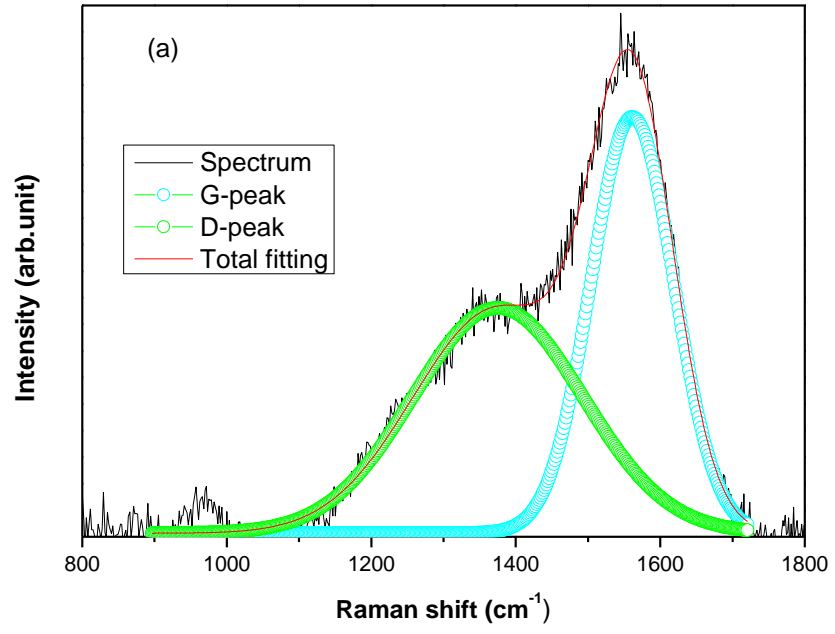
#### 4.4.2 Raman spectroscopy of DLC films grown using DC magnetron sputtering

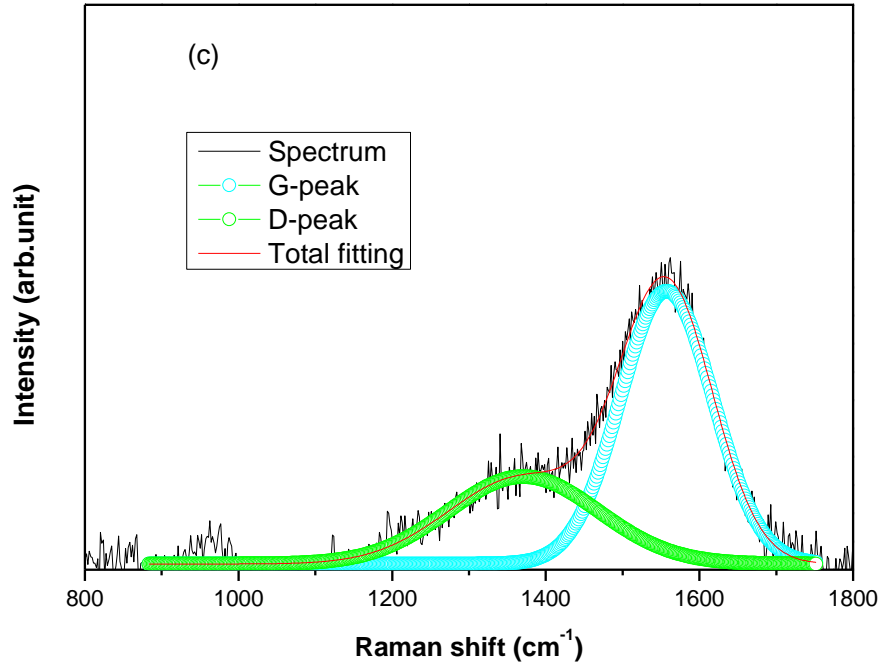
Following the same treatment applied to RF sputtered films in the preceding section, DC sputtered films were studied and representative Raman spectra were collected using an excitation wavelength of 514 nm, as shown in figure 4.7. After deconvolution of all Raman spectra into the

D-peak and G-peak, similar results were obtained as in RF sputtered films. This is confirmed in the schematic of figures 4.8(a-c,d) – 4.10, and Tables 4.4 and 4.5.

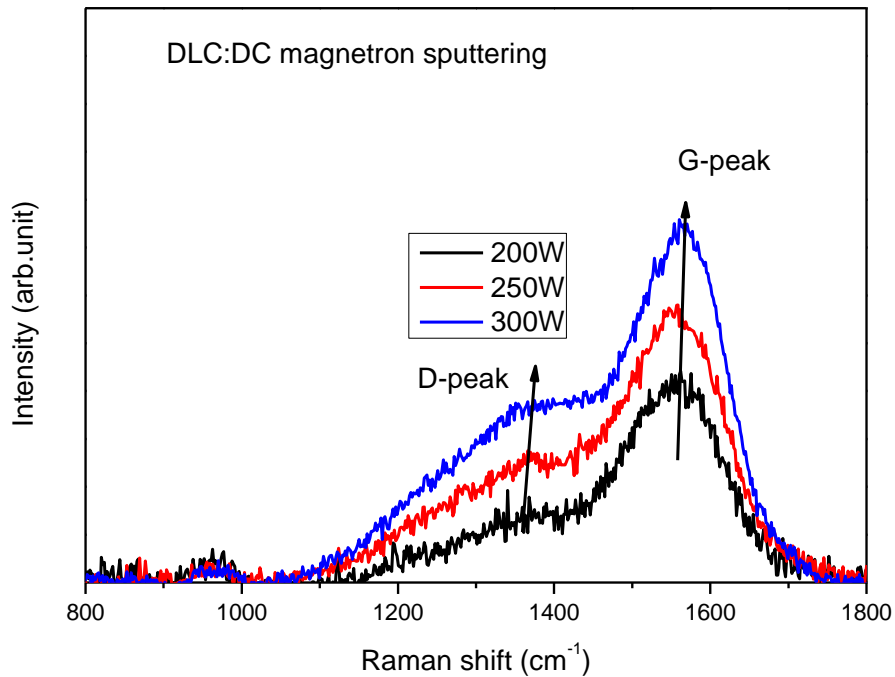


**Figure 4.7:** Raman Spectra of DLC films deposited at different (Ar and CH<sub>4</sub>) flow rate ratios using DC magnetron sputtering ( $\lambda_{exc} = 514$  nm).

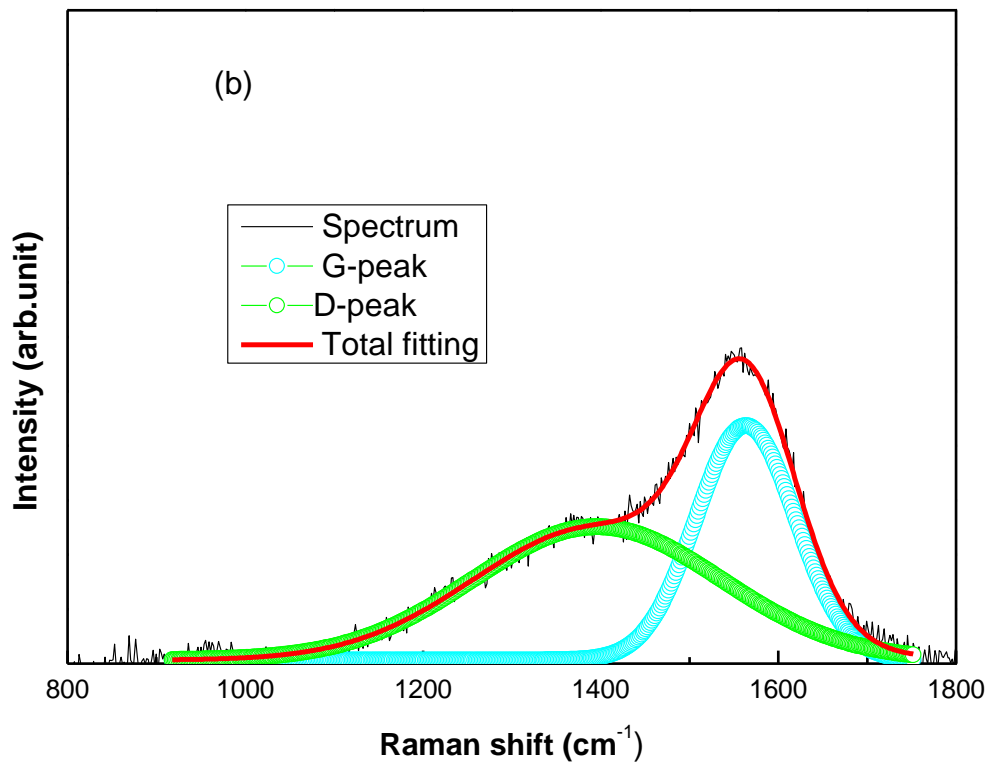
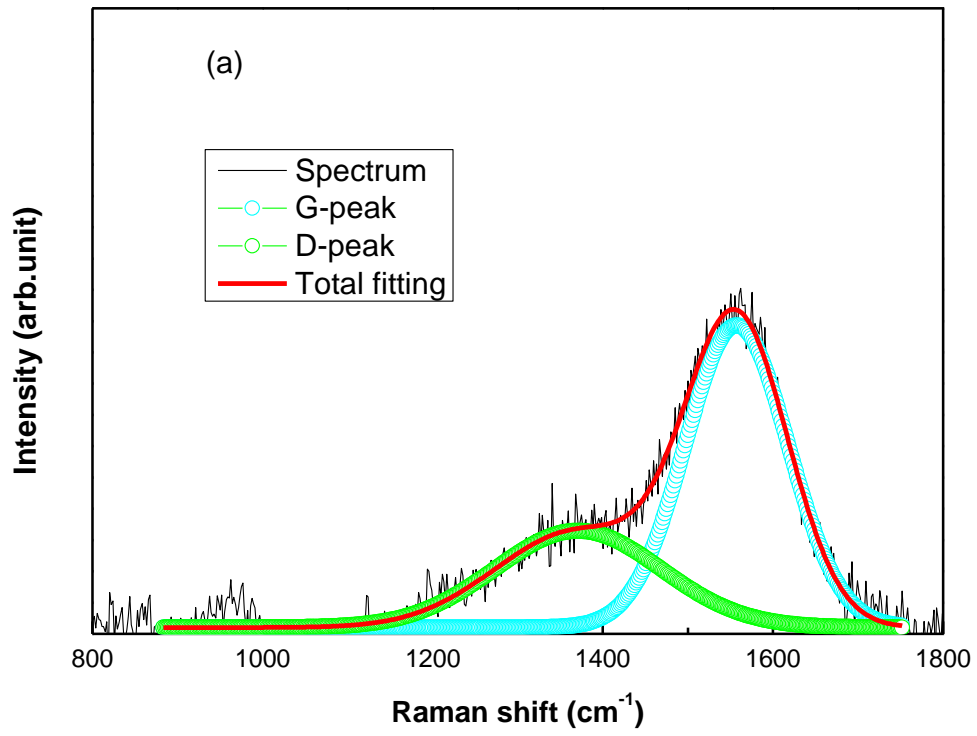




**Figure 4.8:** Raman Spectra of DLC films deposited at different (Ar and CH<sub>4</sub>) flow rate ratios: (a) 7.5/20, (b) 15/20 and (c) 20/20 using DC sputtering.



**Figure 4.8d:** Raman spectra of DLC films deposited at same (Ar and CH<sub>4</sub>) flow rate ratio: 20/20 using DC sputtering, for increasing power, showing a slight blue shift of the G peak.



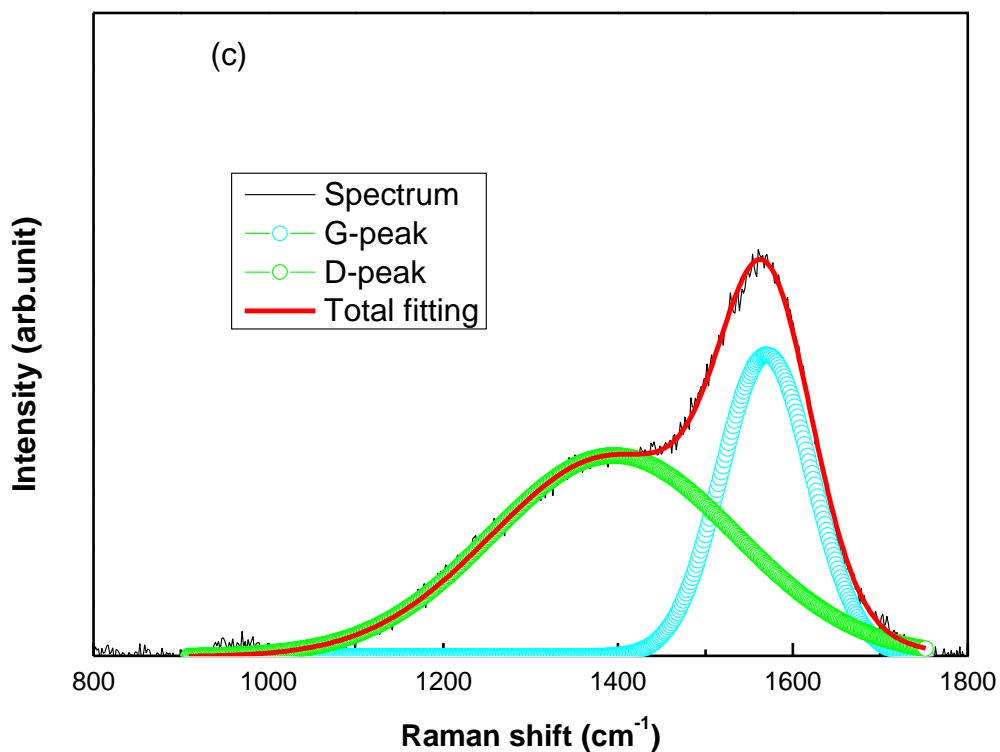


**Figure 4.9:** Raman spectra of DC sputtered DLC films deposited at constant ratio of Ar/CH<sub>4</sub>, 1:1 with different power: (a) 200W, (b) 250W and (c) 300W.

**Table 4.4:** Summary of spectral features of DC sputtered films grown at fixed power of 200W, obtained after deconvolution of the D and G-peaks.

% CH <sub>4</sub> composition in sputtered DLC thin films*	Peak Position		Width		I <sub>D</sub> /I <sub>G</sub> ratio	
	D-Peak (cm <sup>-1</sup> )	G-Peak (cm <sup>-1</sup> )	W <sub>D</sub> (cm <sup>-1</sup> )	W <sub>G</sub> (cm <sup>-1</sup> )	From Area	From Height
27	1376	1562	235	115	1.11	0.54
43	1367	1559	202	121	0.73	0.44
50	1371	1558	121	195	0.52	0.32

\* Ar flow rate was kept constant in all deposited films

**Table 4.5:** Summary of spectral features obtained after deconvolution of the D and G-peaks for DC sputtered films, using different powers.

DLC deposited at Ar / CH <sub>4</sub> : 20/20 with varying Sputter power (W)	Peak Position		Width		I <sub>D</sub> /I <sub>G</sub> ratio	
	D-Peak (cm <sup>-1</sup> )	G-Peak (cm <sup>-1</sup> )	W <sub>D</sub> (cm <sup>-1</sup> )	W <sub>G</sub> (cm <sup>-1</sup> )	From Area	From Height
200	1371	1558	121	195	0.52	0.32
250	1396	1563	279	112	1.42	0.57
300	1395	1570	280	104	1.80	0.67

For DC magnetron sputtering, all Raman spectra have been also deconvoluted into distinct the D-peak and G-peak with two Gaussian distributions leading to the determination of the variations in the G-peak positions (1558-1570 cm<sup>-1</sup>) and I<sub>D</sub>/I<sub>G</sub> ratios (0.32-0.67). The results show that the G-peak position and I<sub>D</sub>/I<sub>G</sub> ratio decrease with methane concentration of 20 sccm (at 50%) and the full width at half maximum (FWHM) of (104 - 195) also increases with methane concentration at the constant power (of 200W); that possibly indicates corresponding increase of sp<sup>3</sup> fraction in the dc sputtered films as shown in table 4.4.

Using the optimum condition at 50% of methane composition for the DC sputtered films, the sputtering power was varied from 200W to 300W to establish the effects of the ad atom energy on the sp<sup>2</sup>/sp<sup>3</sup> fractions and subsequently on the DLC film properties. The results of these experiments (spectra shown in fig 4.9) are summarized in Table 4.5. The ad atom energy was determined from the target self - bias and the plasma potential, and the energy ranges from 120 to 1000 eV. The results in Table 4.5 show that the G-peak position and I<sub>D</sub>/I<sub>G</sub> ratio decrease with the decreasing sputter power. Since the orientation of the sp<sup>2</sup> clustering of the sp<sup>2</sup> phases as well as the sp<sup>3</sup> content in the films determine the elastic, optical and electronic properties, then the addition of methane

gas in the Ar plasma can be used to establish whether the amorphous trajectory is followed in the deposited films. Previously it was widely believed that the high fraction of  $sp^3$  C-C bonds was the only critical parameter for the fabrication of DLC films with excellent tribological, and superior mechanical properties. However, recent results by numerous groups seem to indicate that the  $sp^2/sp^3$  carbon ratio alone is not a reliable determinant of the film's structural, optoelectronic and mechanical properties. It has been reported that other factors such as the amount of H and N present can immensely influence the properties of the DLC thin films [102]. For this reason the fraction of hydrogen content in the films was also determined using Photoluminescence Raman for DC sputtered films as shown in Figure 4.8.

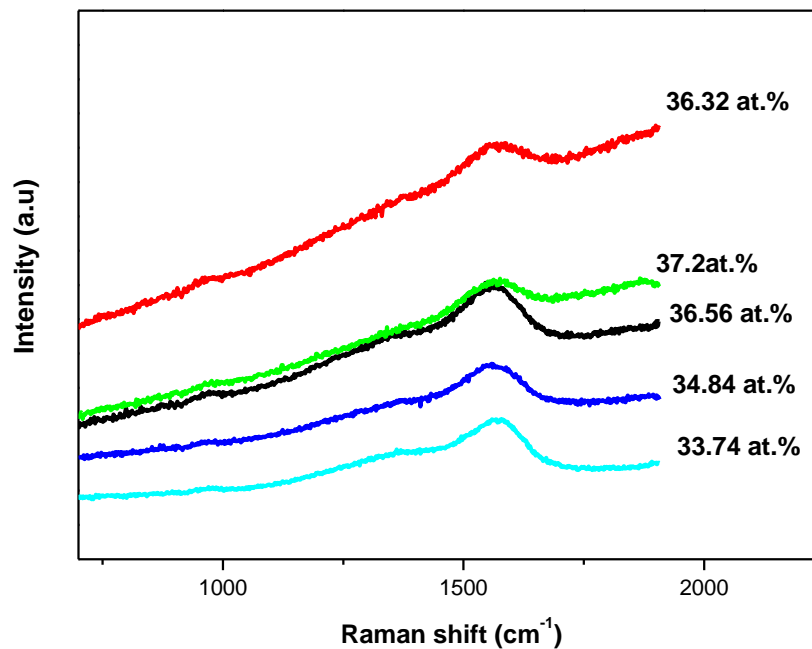


**Figure 4.8:** The Raman spectra of DC sputtered DLC thin films grown on unbiased (001) Si at 200 W with different composition of Ar/CH<sub>4</sub> ratio. Spectra have been vertically shifted for clarity.

This composition also enables the formation of different phases of DLC like films which conform to the three stage amorphous trajectory model [Casiraghi *et al.*] [176]. This is confirmed using a combination of Raman measurements on films deposited with high H content in which they

exhibited a polymer like structure, particularly for the DC sputtered thin films. The critical hydrogen concentration that separates the optimum DLC films from the polymerized amorphous carbon was determined to be 37 at.% as tabulated in table 4.7. It is evident from both deposition techniques that the optimum DLC films were obtained using a 1:1 composition ratio for the Ar:CH<sub>4</sub> gaseous mixture. By observing the fraction of hydrogen films, it can be concluded that DC magnetron sputtering likely leads to a polymer –like structure. These current observations are consistent with the work done by Marchon *et al.*[179]. Thus for both techniques, the optimum condition (at 50% CH<sub>4</sub>) for DLC film growth was obtained.

Semi-quantitative information about the H content of the a-C:H films deposited using DC sputtering was obtained from Raman spectra using the slope (m) of photoluminescence (PL) background. The present results for the DC sputtered thin films are in agreement with Joel W's work which prescribes the formation of a polymer-like composition for films containing minimum hydrogen of 34 at %. Notably, we have observed that DC-magnetron sputtered films exhibited strong photoluminescence activity than the RF grown films, suggesting higher H % levels in DC films, hence polymer-like composition is a reasonable conclusion.

#### **4.4.3 Raman parameters related to microstructure and optical property**

We have estimated the sp<sup>3</sup> fraction of all DLC films prepared by RF and DC sputtering using empirical curves and the statistical results of the I<sub>D</sub>/I<sub>G</sub> versus sp<sup>3</sup> curve in reference [116] . The sp<sup>3</sup> values can also be obtained from the G-Peak position. It is noted that the trends of both values are similar. Ferrari *et al.* [88] plotted the statistical Tauc- Gap (eV) versus I<sub>D</sub>/I<sub>G</sub> ratios in carbon materials. From the data curve (not shown here) the results of the Tauc Gap for our DLC thin films results have been obtained (E<sub>g</sub>) [115]. It is found that band gap (E<sub>g</sub>) increases with decrease of I<sub>D</sub>/I<sub>G</sub> ratio when CH<sub>4</sub>/Ar ratio increases in DLC thin films during the deposition process. This

confirms the formation of  $sp^3$  rich carbon film. From above the relationship, we derived the Tauc-gap versus  $sp^2$  fraction from which the  $sp^2$  fraction was estimated in the DLC film structure [115]; which enabled the calculation of the  $sp^3/sp^2$  ratios.

Raman spectra measured in this work was to obtain information on defects and the size of the graphite clusters. By extending the Tauc Lorentz optical model for semiconductors to the Raman data, the optical band gap,  $E_g$  was evaluated. This follows from the empirical relationship that prescribes the Tauc gap in amorphous carbon thin films to be inversely proportional to the graphite cluster size  $L_a$ . The graphite cluster size is extracted from the  $I_D/I_G$  ratio through the linear proportionality [175]. The  $I_D/I_G$  ratio in terms of height and area is a parameter which gives the amount of ring-like  $sp^2$  clusters and their disorder in a-C:H films. From the results obtained, it is observed that the decrease in the intensity ratio of heights and peak areas of D and G peaks is indicative that the decrease in the  $sp^2$  clusters size is attributed to the reduction of rings numbers. This further implies that the disorder in graphitic cluster increases. A summary of the  $I_D/I_G$  ratio and their respective graphite cluster size is presented in Tables 4.6 and 4.7.

It is seen that the  $I_D/I_G$  ratio scales inversely with the Tauc gap,  $E_g$  especially in the presence of D peak related vibration. It is thus expected that the bonding fractions of the DLC films fabricated in this work can be used to establish the high  $sp^3$  fraction DLC thin film, which possess multifunctional properties, namely;

- high transparency,
- excellent mechanical and
- reasonably high conductivity (electrical properties).

Furthermore, the full width at half maximum FWHM of the G peak has been used to derive information on the structural disorder and elastic strain in DLC films; The FWHM(G) gives

information on the structural disorder induced by variations of the bond angles (dihedral) and bond lengths (distortions) in amorphous carbon films. Therefore an increase in this parameter could plausibly lead to the enhancement of the mechanical properties. To estimate the Elastic properties of DLC films in this work, the fraction of the  $Csp^3$ - $Csp^3$  was established and implemented in the empirical formula of eqn. 4.2 (table 4.6).

$$E \text{ [GPa]} = -511 + 4.66 W \text{ [cm}^{-1}\text{]}, \quad (4.2)$$

where E is Young's modulus and W is the full width at half maximum [175]. The FWHM(G) is small ( $\sim 100 \text{ cm}^{-1}$ ) when  $sp^2$  clusters have less defects and are thus more ordered, whereas a higher FWHM(G) is indicative of an increase in structural disorder. This effect originates from the higher bond length and higher bond angle in more disordered materials. The FWHM (G) is in direct relation with the C–C  $sp^3$  bonding content.

**Table 4.6:** Microstructure and electronic properties of RF sputtered thin films.

Methane Content %	$I_D/I_G$ ratio	Cluster Size ( $L_a$ ) ( $\text{\AA}$ ) <sup>a</sup>	$sp^3/sp^2$ ( $\pm 0.05$ )	XRR Density ( $\text{g/cm}^3$ )	Tauc gap $E_g$ [115]	Young modulus $E$ (GPa) <sup>b</sup>	H content (at. %)
20	0.66	10.95	1.07		1.48	32.73	32.5
33	0.57	10.18	1.22	2.35	1.49	38.18	32.2
50	0.45	9.05	1.48	2.49	1.56	99.83	31.1
67	0.53	9.81	1.47	2.44	1.54	42.19	34.1

<sup>a</sup> [88] and <sup>b</sup> [175]

**Table 4.7:** Microstructure and electronic properties of DC sputtered thin films.

Methane Composition %	G-peak position (cm <sup>-1</sup> )	I <sub>D</sub> /I <sub>G</sub> Ratio	sp <sup>3</sup> /sp <sup>2</sup> (±0.05)	Cluster size (L <sub>a</sub> ) (Å) <sup>a</sup>	XRR Density (g.cm <sup>3</sup> )	Tauc gap (eV) <sup>b</sup> [± 0.5]	Young's modulus E(GPa) <sup>c</sup>	H content (at.%)
50% at 300W	1572	0.67	0.96	11.04	2.48	1.45	23.50	37.7
50% at 250W	1562	0.57	1.13	10.18	2.56	1.49	51.83	34.8
50% at 200W	1557	0.32	1.81	7.62	3.12	1.71	52.44	37.0
43% at 200W	1558	0.44	1.60	8.94	2.70	1.59	10.83	36.3
27% at 200W	1560	0.54	1.17	9.90	2.58	1.51	8.50	36.3

<sup>a</sup>[88], <sup>b</sup> [115] and <sup>c</sup> [175]

#### 4.5 Vibrational mode of DLC thin films by Fourier Transform Infrared

Figures 4.12 and 4.13, respectively show the typical Fourier transform infrared transmittance spectra of RF sputtered films with thickness in the range of 99.2 to 140 nm and DC sputtered DLC films with an average film thickness of 100 nm. The spectra comprises of typical broad bands in the range 2780 – 3050 cm<sup>-1</sup> due to the different C-H vibrational modes attributed to the sp<sup>3</sup> and sp<sup>2</sup> clusters in the films. At the optimum condition (50% methane) of DC magnetron sputtering sample, the sp<sup>3</sup> symmetric and asymmetric stretching peaks corresponding to = CH<sub>2</sub> and = C-H<sub>2</sub> at about 2850 and 2920 cm<sup>-1</sup>, respectively. The spectra also exhibit the sp<sup>3</sup> antisymmetric at about 2960 cm<sup>-1</sup>. However it is not possible to resolve the excitation for the sp<sup>2</sup>- CH<sub>2</sub> at about 2975 cm<sup>-1</sup> shown in

figure 4.12. Further analysis of the spectra indicates that the intensities of these peaks increasing with methane composition and also with hydrogen content. The presence of these vibrational bands is attributed to the formation of hydrogenated DLC thin films with the hydrogen being attached to the  $sp^3$  carbon in the film. The band corresponding to the  $sp^2$ -CH (olefinic) vibrations in the vicinity of the  $3000\text{ cm}^{-1}$ . The presence of  $CH_4$  in the Ar plasma leads to the increase in ratio the  $sp^3$  peak areas to the  $sp^2$  peak area with increasing the  $CH_4$  concentrations [162]. The RF sputtered films containing 50% methane also shows the  $sp^3$  symmetric and asymmetric stretching peaks corresponding to  $=CH_2$  and  $=C-H_2$  at about  $2850$  and  $2920\text{ cm}^{-1}$ , respectively. The spectra also exhibit the  $sp^3$  antisymmetric peak for  $CH_3$  at about  $2959\text{ cm}^{-1}$ . This indicates that the presence of  $CH_4$  promotes very strongly the formation of  $sp^3$ -type carbon bonds. The peaks described above have been reported for diamond samples deposited at high  $CH_4$  concentration and in DLC films [169], in agreement with our data. Moreover, the bond concentration of hydrogen estimated from the absorbance [169] shows that the amount of bound hydrogen is estimated to be proportional to the integrated intensity of a cluster of C-H stretch bands centered around  $2900\text{ cm}^{-1}$  [102]. Thus, the films are becoming more diamond-like with increasing H content. Hydrogen causes the character of the C-C bonds to shift from  $sp^2$  to  $sp^3$  giving rise to high optical transmittance in the films, but the rising number of C-H bonds ultimately relieves stress and produces a softer “polymer-like” material as observed for the DC films. The deposition of DLC thin films using low sputter power, such as  $200\text{ W}$ , appears to stabilize the formation of  $sp^3$ C-C bonds, accompanied by increased transparency and a large  $T_{auc}$  gap [102]. Our results have shown that the bonding structures between carbon and hydrogen in a-C:H films consist predominantly of  $sp^3$  bonds with a few  $sp^2$  bonds. However the role of hydrogen terminated in the films and its determination and

interpretation of the mechanical properties of DLC thin film. For this reason we converted the transmittance data to absorbance using the expression

$$\alpha = \frac{1}{d} \times \ln \frac{1}{T} \quad (4.3)$$

where  $\alpha$  is an absorption coefficient ( $\text{cm}^{-1}$ ),  $d$  is a thickness (nm) and  $T$  is a transmittance (%).

The IR spectrum of the C-H<sub>n</sub> bond stretching modes around 2900  $\text{cm}^{-1}$  is measured after background subtraction, and consists of many stretching modes originate from sp<sup>2</sup> or sp<sup>3</sup> C-H<sub>n</sub> (n=1,2,3) depending on the film preparation conditions. By deconvoluting these modes, the ratio of sp<sup>3</sup>/sp<sup>2</sup> can be estimated. Thus the integrated total C-H band intensity in the limit of 3000 -2800  $\text{cm}^{-1}$  is obtained by applying eqn. (4.3) in eqn. (4.4) to derive the number of H atoms per unit area  $n_H$ . This is determined by multiplying by the ratio of absorption strength,  $A_s$  by the wavenumber at 2900  $\text{cm}^{-1}$  hydrogen in the selected films;

$$n_H = \frac{A_s}{2900} \int_{2800}^{3000} \alpha(\nu) d\nu \quad (4.4)$$

In which the area under the absorbance curve has been approximated by the integration of absorbance. The coefficient,  $A_s = 0.85 \times 10^{21} \text{ cm}^{-2}$  in the integral was adopted from the average value of the paraffin standard due to Erz *et al.* [180] and that from Gheeraert *et al.* [181]. The sp<sup>3</sup> and sp<sup>2</sup> C-H<sub>n</sub> chemical bonds are presented in the table 4.8 obtained from the absorption bands obtained by Gaussian deconvolution as shown figures 4.14 and 4.15.

Similar bands have been reported for diamond samples prepared with high CH<sub>4</sub> concentrations and in DLC films [169]. The hydrogen concentration calculated by IR spectroscopy as shown in table 4.8 exhibits the same trends as observed for hydrogen percentage estimated using Raman spectroscopy technique.

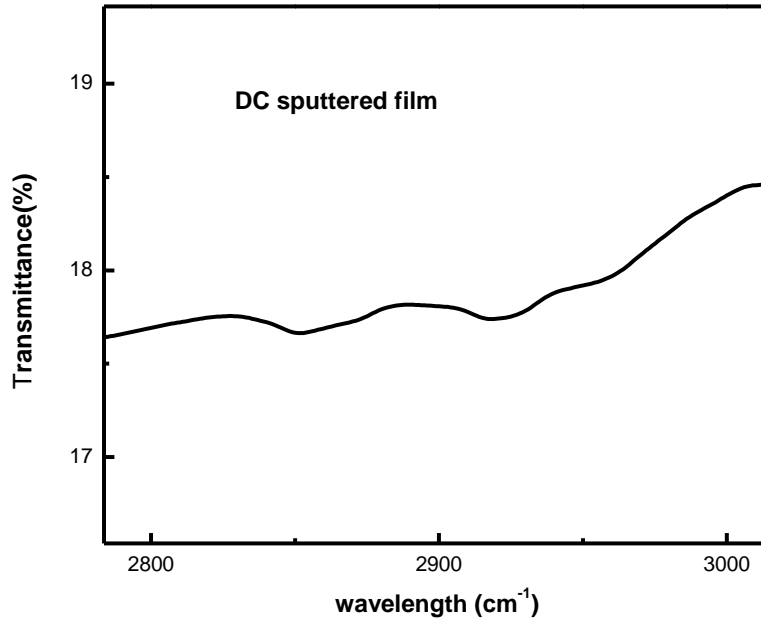


**Figure 4.9:** FTIR spectra for DC magnetron sputtering showing the CH<sub>2</sub> symmetric stretching peaks at ~ 2850 cm<sup>-1</sup>, characteristic of DLC films deposited at 50 at.% Ar/CH<sub>4</sub> concentrations.

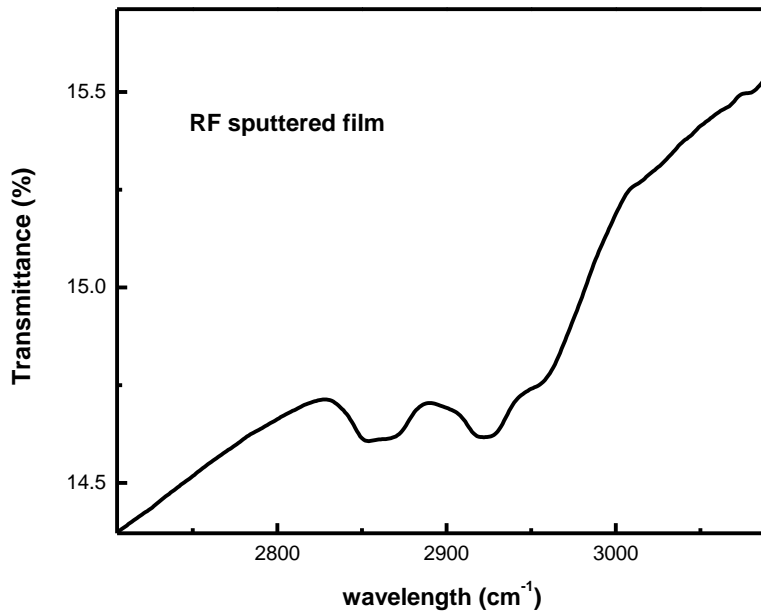


**Figure 4.10:** FTIR spectra RF magnetron sputtering showing the CH<sub>2</sub> symmetric stretching peaks at ~ 2850 cm<sup>-1</sup>, characteristic of DLC films deposited at 50 at.% Ar/CH<sub>4</sub> concentrations.

Using IR spectra enables the use of the C-H bond stretching modes to derive the fraction of  $sp^3$  to  $sp^2$  bonding [182, 183], however, the problem is that this technique does not detect sites not bonded to H. It is well-known that nearly all  $sp^3$  sites in normal DLC are hydrogenated, but many  $sp^2$  sites are not [184]. Thus the amount of  $sp^3$  fraction will be overestimated as the modes at 2970 and 2945  $cm^{-1}$  are reversed their in assignment [90], and all modes below 2960  $cm^{-1}$  are merely regarded as  $sp^3$  bonds.

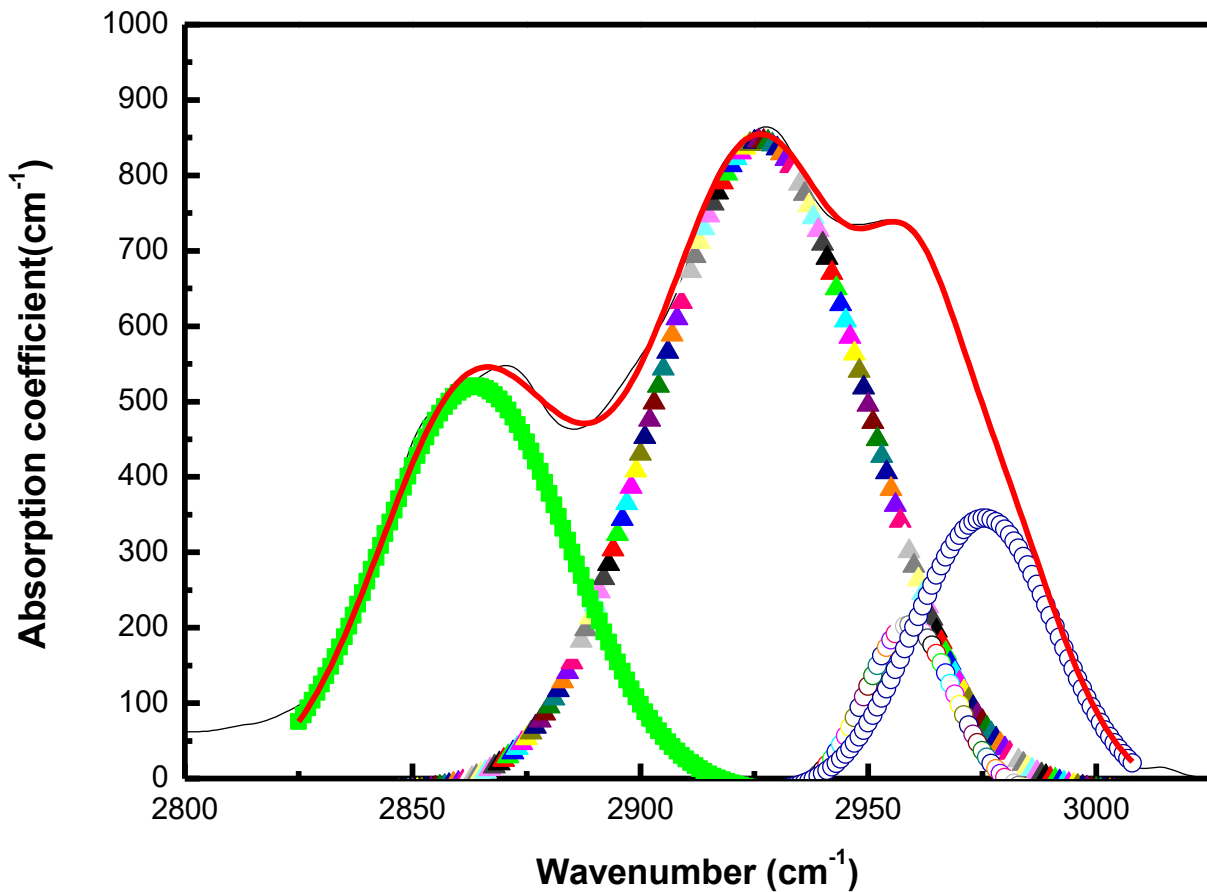


**Figure 4.11:** FTIR spectra of absorbance of RF magnetron sputtering showing the  $CH_2$  symmetric stretching peaks at  $\sim 2850\text{ cm}^{-1}$ , characteristic of DLC films deposited at 50 at.% Ar/ $CH_4$  concentrations.

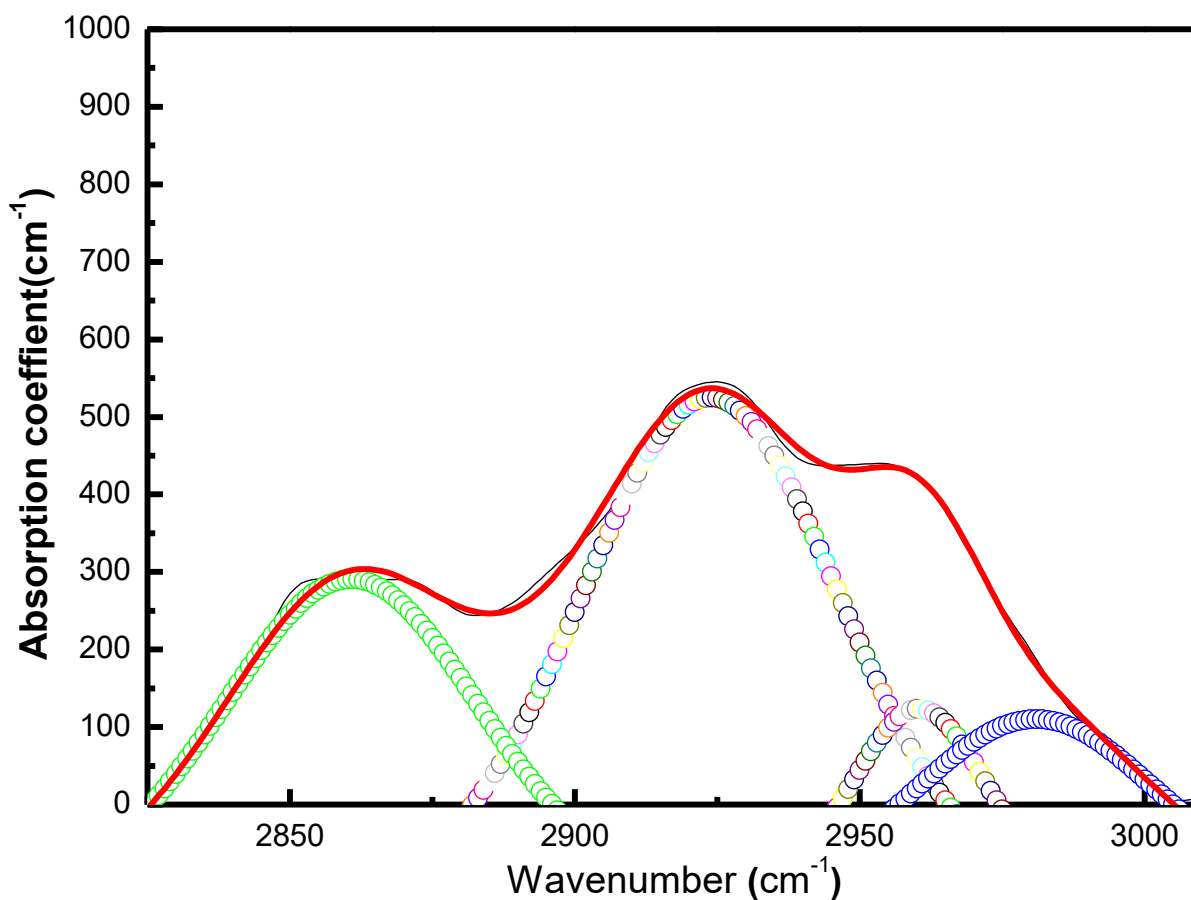


**Figure 4.12:** FTIR spectra of absorbance of DC magnetron sputtering showing the CH<sub>2</sub> symmetric stretching peaks at ~ 2850 cm<sup>-1</sup>, characteristic of DLC films deposited at 50 at.% Ar/CH<sub>4</sub> concentrations.

**Table 4.8:** C-H<sub>n</sub> bonds and hydrogen density at optimum condition of DLC films.

Sample (CH <sub>4</sub> /Ar)	sp <sup>3</sup> -CH <sub>2</sub> (cm <sup>-1</sup> )	sp <sup>3</sup> -CH <sub>2</sub> (cm <sup>-1</sup> )	sp <sup>3</sup> -CH <sub>3</sub> (cm <sup>-1</sup> )	sp <sup>2</sup> -CH <sub>3</sub> (cm <sup>-1</sup> )	Hydrogen density (10 <sup>21</sup> cm <sup>-2</sup> )
RF(13/13)	2863	2926	2959	2975	28.66
DC(20/20)	2861	2923	2960	2980	22.08

#### 4.6 I-V Characteristics of DLC thin films

In the previous sections, it has been demonstrated that the properties of DLC thin films are dependent on the relative fractions of the  $sp^3$  and  $sp^2$  bonds which are further dependent on the deposition conditions. Thus the variations in the type of deposition (DC/ RF power) and the process parameters (gas mixture concentration, substrate bias voltage and temperature, etc.) could plausibly lead to films with contrasting electronic transport properties. This can also be correlated to the resulting optical excitations in the films. In this section, the electronic properties of DLC thin films will be discussed, i.e. I-V characteristics of the films and consider the role of the  $sp^3$  and  $sp^2$  bonds. The current- voltage characteristics were measured in the van der Pauw configuration using a 4140B picoammeter /DC voltage source interfaced via lab view to a computer.

The results presented in Figures 4.16 and 4.17 show I-V characteristic of RF and DC sputtered DLC thin films deposited under various methane concentrations (33-67%) and (27-50%) respectively. The thicknesses of RF unbiased magnetron sputtering were increased from 99.2 to 140 nm whilst that of unbiased DC sputtered films averaged 100 nm. The Van der Pauw method of the determining the resistivity ( $\rho$ ) or the sheet resistance ( $R_s$ ) of materials in the form of thin films approximation ( $t \ll s$ ) where  $s$  is the distance between two contacts and  $t$  is the film thickness is described by the relation [186] ;

$$\rho = \frac{\pi}{\ln 2} t \frac{V}{I} = 4.523 t \frac{V}{I} \quad (4.5)$$

where  $t$  is the film thickness, while  $V$  and  $I$  are the voltage and current sourced and measured at the terminals of the sample.

In general, all presented I-V curves of the DLC films displayed non-Ohmic behavior. The sheet resistance of DLC films fabricated by RF and DC sputtering was obtained by measuring the slope of I-V curves as shown in Figures 4.16 and 4.17. The sheet resistivity of the film was obtained

from the product of sheet resistance and film thickness. The values of film thicknesses were obtained from X-ray reflectivity measurements. From figures 4.16 and 4.17, it can be seen that the resistivity increased strongly with methane concentration at 50% CH<sub>4</sub> composition. This observation was also observed for RF films, a high fraction of sp<sup>3</sup> bonds (0.80) with higher resistivity ( $36.89 \times 10^2 \Omega \text{ cm}$ ) resemble a more diamond-like structure. The high resistivity of the DLC films containing (50% CH<sub>4</sub>) correlates with the higher Tauc-gap value (1.56 eV) measured in this study. From this data, it has been noted that the resistivity (conductivity) and optical properties of the films depend on the sp<sup>2</sup> fraction and its cluster size [173]. Beyond 50% methane concentration, the resistivity was observed to decrease, and this was attributed to the presence of a higher hydrogen fraction in the films, (the presence of hydrogen promotes the conversion of sp<sup>3</sup> to sp<sup>2</sup> leading to the low resistivity values,  $2.62 \times 10^2 \Omega \text{ cm}$ ). This observation is in agreement with the IR spectra that showed clear evidence of C=C olefinic bonds in the more polymeric a-C:H films, whilst at 50% composition, the resistivity is the highest ( $36.89 \times 10^2 \Omega \text{ cm}$ ) for these films. Below 50% CH<sub>4</sub> composition, the resistivity is lower due to the higher fraction of sp<sup>2</sup>. These I-V characteristics results are in agreement with the present Raman results showed that the high resistivity of the films corresponded to high fractions of sp<sup>3</sup> bonding. In addition, similar trends for RF and DC sputtered films were observed as shown in Figures 4.16 and 4.17, and the results obtained as shown in tables 4.9 and 4.10 are also consistent with the work done D. Caschera et al. [185].

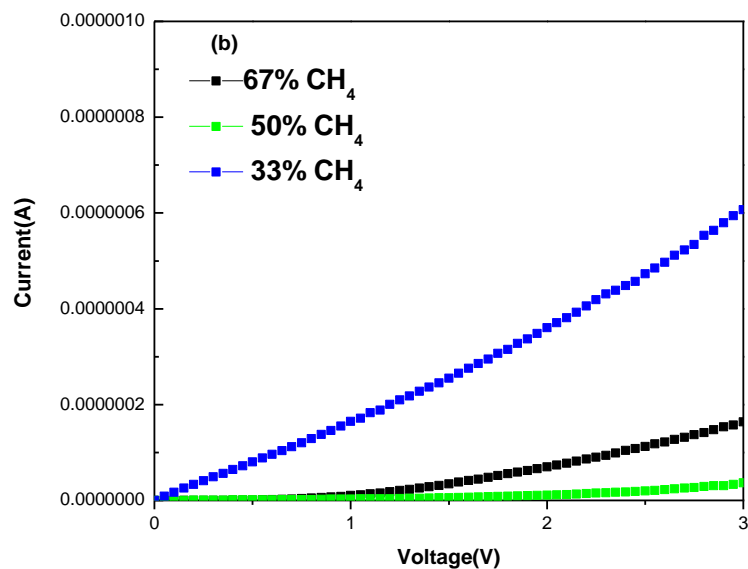


**Figure 4.13:** Current-Voltage characteristics for RF sputtered films at the optimum condition of 50% methane composition. The lower conductivity is attributed to the presence of a higher  $sp^3$  fraction in the films.

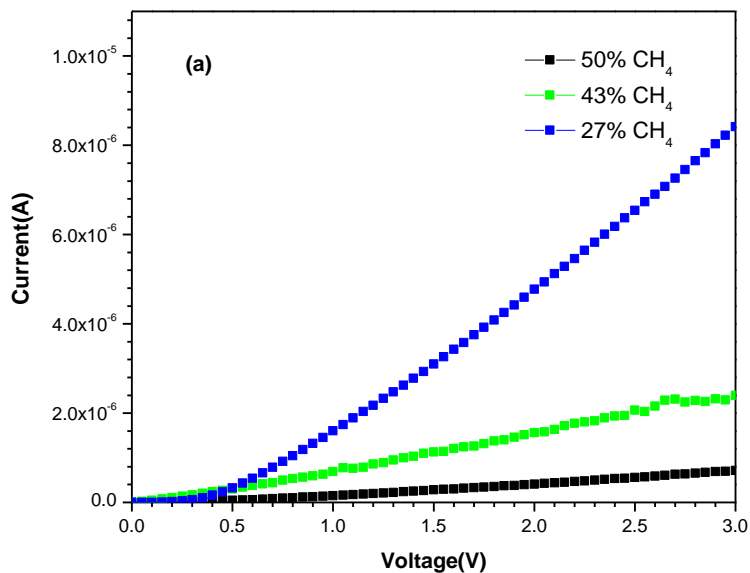


**Figure 4.14:** Current-Voltage characteristics for DC sputtered films showing increased conductivity below 50% methane composition, attributed to the presence of a higher  $sp^2$  fraction in the films.

**Table 4.9:** Electrical properties of DLC prepared by RF magnetron sputtering.

DLC/RF Methane (%)	Slope of V/I ( $10^7$ V/A)	Resistance ( $10^7 \Omega/\text{sq}$ )	Resistivity ( $10^2 \Omega \text{ cm}$ )
33	0.58	2.62	2.60
50	5.80	26.35	36.89
67	1.26	5.73	5.74

**Table 4.10:** Electrical properties of DLC prepared by DC magnetron sputtering.

DLC/DC Methane (%)	Slope of V/I ( $10^7$ V/A)	Resistance ( $10^7 \Omega/\text{sq}$ )	Resistivity ( $10^2 \Omega \text{ cm}$ )
27	0.03	0.14	0.14
43	0.12	0.54	0.54
50	0.46	2.07	2.07

#### 4.7 X-ray photoelectron and Auger electron spectroscopy analyses

The analysis of the XPS spectra can be used to determine the qualitative and quantitative composition of almost all chemical elements except hydrogen and helium. Additionally its versatility enables it to be used in the analysis of multi-element compounds from the determination of their elemental specific binding energy in the compound and structure. In the present work, XPS analysis of DLC was carried out using the Al  $K\alpha$ -line (1486.7eV), to analyse the surface sensitive composition within the depth resolution (2 to 10 nm) of the photoelectrons. The power used to generate the X-rays is 300 W and the X-ray beam was collimated and focussed to a spot size of 900  $\mu\text{m}$ . The precision of the XPS is approximately 0.1 at. %. The X-ray photoelectron was done for the films prepared by RF magnetron sputtering with different concentration of methane (50 % and 33 % of methane) mixture with constant Ar concentration to determine the composition and

the chemical bonding of the films. The results of these measurements are presented in Figures 4-18 and 4-20 for which the dominance of the carbon, C1s peak and oxygen, O1s are evident.

For DLC thin films with 50% of methane, the spectra consists of the peak C1s (88.1 atomic %), the peak O1s (9.9 atomic %) and the peak Si2p (2.0 atomic %). However DLC thin films with 33% of methane have shown the following peaks;

- peak C1s (86.3 atomic %),
- peak O1s (11.5 atomic %),
- peak N1s (0.6 atomic %),
- peak Si2p (1.6 atomic %).

DLC thin films with 50% of methane have been observed to contain more carbon- atom than those fabricated with 33% of methane. This is attributed to the high concentration of  $sp^3$  bonds in 50%  $CH_4$  fabricated DLC thin films as presented by Raman spectroscopy. The presence of oxygen, silicon and nitrogen in the spectra can be attributed to the edge/surface oxidation. The line shapes of the O1s and C1s peaks give information about the chemical bonding environment. The intense bonded peak in the spectrum of DLC thin film with 50% of methane corresponds to C-C  $sp^3$  with (91.1 atomic %) at binding energy of 284.8 eV and a full width at half maximum of 1.1 eV. The second peak is C-O at binding energy of 286.6 eV (FWHM=1.1 eV and 5.9 atomic %) and, the last bonding of carbon formed is O-C=O at 289.0 eV (FWHM=1.1 eV and atomic %= 3.0). The peak corresponding to the O1s bonding that are O-(C,H) at 532.2eV (FWHM=1.3 eV) and O-(C,H,Si) at 533.6 eV(FWHM=1.1 eV) was also observed.

For DLC with 33% of methane, the very important binding energy is for carbon C1s that consist of C-C  $sp^3$  at 285.0 eV (FWHM =1.3 eV and 82.9 at. %), the second peak is C1s (C-O) at 286.9 eV (FWHM=1.3 eV and 4.9 at. %), the third peak is C1s O-C=O at 288.7eV (FWHM =1.3

eV and 1.7 at. %). The Si2p (organic Si) at 102.4 eV (FWHM=1.4 eV, 1.6 at. %) was observed. The peak O1s is bonding with O-(C,H) and O-(C,H, Si) at 532.4 eV(FWHM=1.6 eV and atomic % of 7.6) and 533.8 eV (FWHM=1.3 eV and atomic % of 1.4), respectively. Evidently, the DLC thin films fabricated with a 50% CH<sub>4</sub> mixture have been observed to contain more carbon- carbon bonds than those made with 33% of methane, which again confirms that there is a higher fraction of sp<sup>3</sup> bonds in films deposited at 50% CH<sub>4</sub>. It is important to note that there is no way to distinguish the sp<sup>3</sup> and sp<sup>2</sup> bonds because of the symmetry of the peak C-C at peak binding energy of 284.8 eV and 285 eV, respectively as these are the peak positions of sp<sup>3</sup>-C of 50% and 33% methane, respectively as shown in Figures 4.19 and 4.21. The net result is that the technique will also cause an overestimation of the sp<sup>3</sup> fraction, and make it difficult to determine the ratio of sp<sup>3</sup>/sp<sup>2</sup>. This is also further compounded by the limited depth and lateral resolution of the technique which does not provide adequate sampling volume. Our results indicate that for DLC films prepared with 50% of methane contained about 91 atomic % of sp<sup>3</sup> fractions whereas films fabricated with 33% methane had much lower fraction of about 82.9 atomic % of sp<sup>3</sup> bonds as shown in the table 4.11.

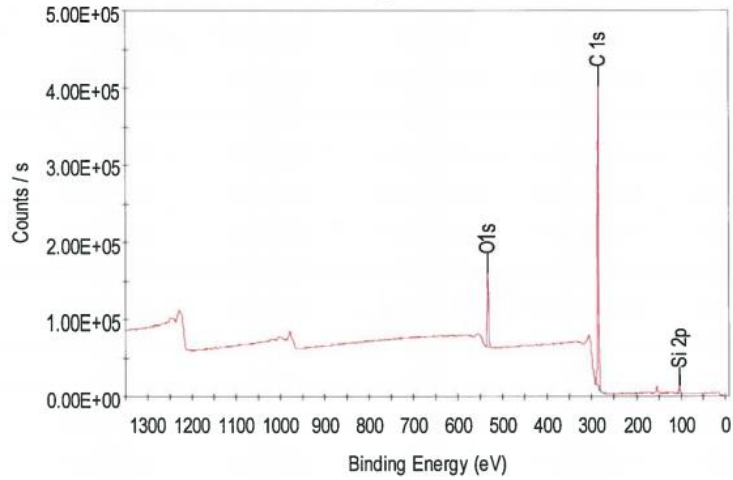


**Figure 4.15:** XPS survey scan spectrum of DLC thin film prepared with Ar/CH<sub>4</sub> 1:1 deposited on silicon substrate at 200W, unbiased substrate.

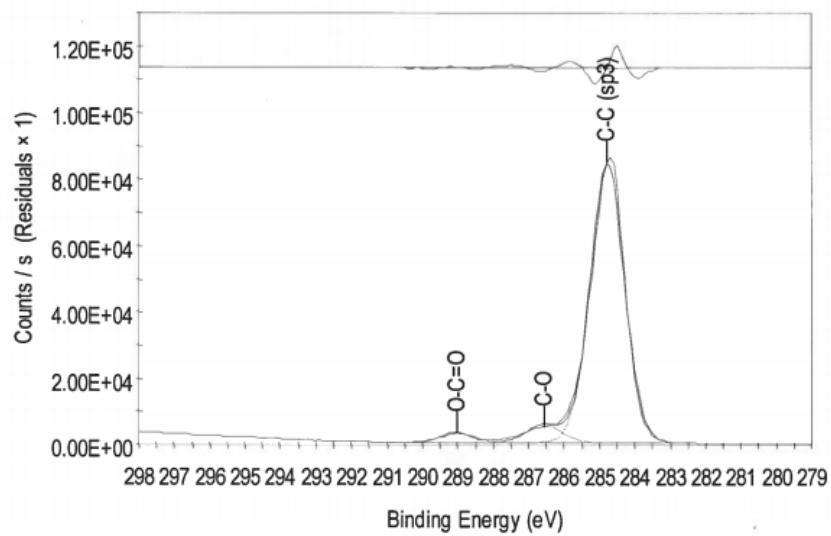


**Figure 4.16:** XPS survey C1s scan spectrum of DLC thin film prepared with Ar/CH<sub>4</sub> 1:1 deposited on silicon substrate at 200W, unbiased substrate.

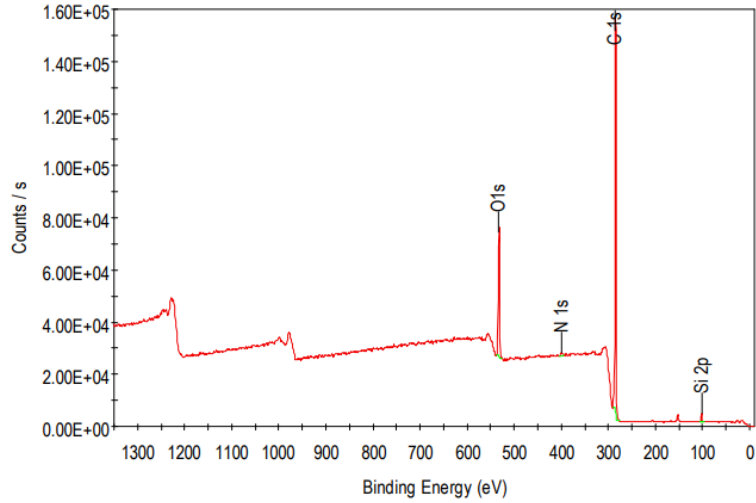


**Figure 4.17:** XPS survey scan spectrum of DLC thin film prepared with Ar/CH<sub>4</sub> 13:6 deposited on silicon substrate at 200W, unbiased substrate.

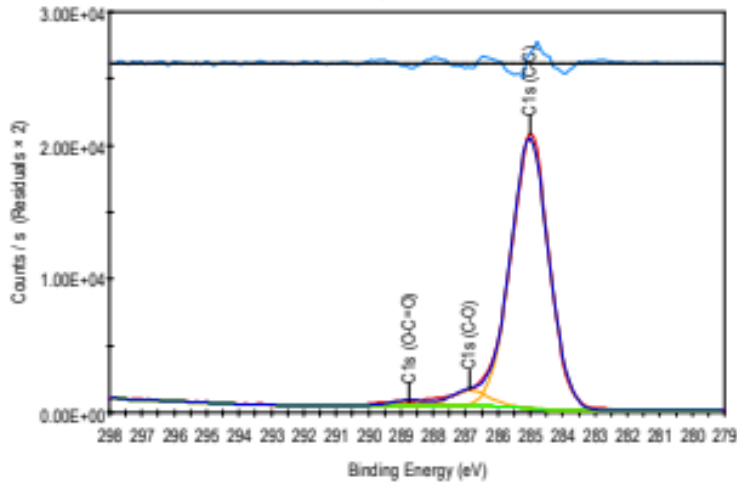


**Figure 4.18:** XPS survey C1s scan spectrum of thin film prepared with Ar/CH<sub>4</sub> 13:6 deposited on silicon substrate at 200W, unbiased substrate.

**Table 4.11:** Summary of the XPS results of DLC prepared by RF magnetron sputtering with Ar/CH<sub>4</sub> ratios of 13/13 and 13/6.

DLC	sp <sup>3</sup> C-C atomic %	Peak BE
50%	91.1	284.8
33%	82.9	285.0

#### 4.7.1 Determination of D-parameters of DLC thin films by Auger Emission

The method induced by XPS for peak of C1s, also called X-ray induced Auger peak of CKLL enables the determination of the ratio of  $sp^2/sp^3$  semi-quantitatively, using the first derivative of the X-ray Auger Emission Spectrum, (XAES) or from the (C KLL) spectrum.

The procedure involves the calculation of the width of the kinetic energy, D between the most positive maximum and the most negative minimum (the so-called D value) as shown in Figures 4.21-22. This method has been calibrated for graphite and diamond and then used to determine the D parameters of DLC thin films.

The values of the D parameter for graphite ( $D = 21$  eV) and diamond ( $D = 13$  eV) were determined by calibration and a linear approximation between these two points of  $D_g$  (100 %,21) and  $D_d$  (0%,13 ) was plotted which allowed for the extrapolation of the  $sp^2$  content from the measured D parameters of samples (energy difference between the two vertical green solid lines) shown in Figures 4.22 and 4.23. A summary of the results is tabulated in table 4. 12 together with the corresponding  $sp^2$  content of the DLC thin films.

It is defined from the table 4.12 that both films yield a very low fraction of  $sp^2$ . Nonetheless the XAES results are in agreement with XPS results because their value of D-parameters (13.5 and 13.4 eV) and binding energies (285.0 and 284.8 eV) are almost close to diamond (which has 100%  $sp^3$ ). Again, it is worth noting that the XPS and AES are much less sensitive to the  $sp^2$  bonded carbon, and this explains why the  $sp^3$  fraction is much higher by comparison with data obtained using Raman spectroscopy.

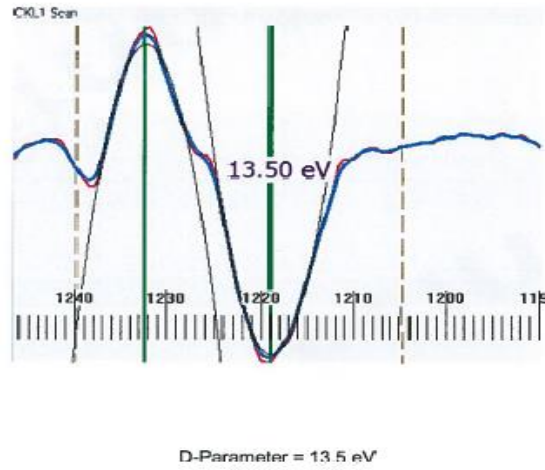


**Figure 4.19:** Auger spectra of DLC thin film prepared with Ar/CH<sub>4</sub> 1:1 deposited on silicon substrate at 200W, with D-Parameter, 13.50 eV.

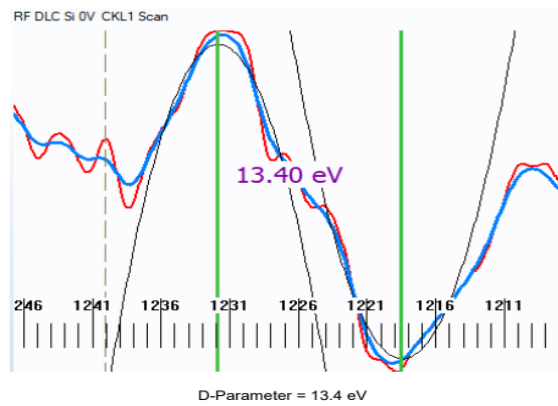


**Figure 4.20:** Auger spectra of DLC thin film prepared with Ar/CH<sub>4</sub> 13:6 deposited on silicon substrate at 200W with D-Parameter, 13.40 eV.

**Table 4.12:** Summary of the AES results and sp<sup>2</sup> fraction of DLC films.

DLC/CH <sub>4</sub>	D-parameter(eV)	sp <sup>2</sup> fraction (%)
33%	13.4	5.0
50%	13.5	6.3

#### **4. 8 Surface Brillouin scattering on DLC thin films**

Brillouin scattering is an excellent tool for the characterization of elastic properties of materials, especially of thin films, by measuring the frequency shift of light scattered inelastically from phonons in the GHz range. The measurement of small frequency shifts is made possible by the high contrast and high resolution that the tandem Fabry-Perot interferometer provides through the multi-pass technique. The propagation of the surface acoustic waves is dependent on the nature of the scattering geometry and the optical properties of the film. Thus two scattering mechanisms can be identified that determine the type of acoustic waves inherent in the material. For transparent materials, the elasto-optic mechanism is dominant and thus enables the coupling of light to the dynamic modulations of the dielectric constant of the materials leading to the observation of bulk modes. On the other hand ripple scattering mechanism is evident in near opaque materials and thin supported films. In a single inelastic scattering evident for opaque materials several modes can be localized on the surface, these include the true Rayleigh Surface Acoustic (RSAW) waves, the guide discrete modes comprising of the Sezawa waves amongst other. The velocity dispersion of the surface (Rayleigh) modes, localized (Sezawa) and lateral modes produces information about the elastic properties such as shear modulus of the films. Surface Brillouin scattering (SBS) have been successfully applied to investigate the elastic properties of hard films such as diamond-like carbon thin films [186]. In Figures 4.23 and 4.25, we show a sequence of Brillouin spectra of amorphous DLC films prepared at different CH<sub>4</sub> concentrations using RF sputtering. The surface Brillouin scattering spectra shows the characteristic frequency sidebands/doublets attributed to the Stokes – anti Stokes symmetry characteristic of phonon excitations. The DLC films produced here are amorphous and have thus a random orientation of the nanocrystallite grains subsequently making the propagation of the acoustics to be independent of the film orientation. In these circumstances the films are considered to be isotropic at the wavelength scale (hundreds of

nanometres for SBS). Therefore the full set of elastic constants can be completely determined by only two independent elements of the elastic tensor, usually,  $C_{11}$  and  $C_{44}$ , from which moduli such as Young's modulus (E), shear modulus (G) and Poisson ratio can be determined.

The measurement and knowledge of the density  $\rho$  allow of the elastic moduli for the determination. In practice though, while  $v_l$  can be determined from the guided mode (LGM), the dip in the Lamb shoulder at the L wave threshold, the Rayleigh wave velocity  $v_R$  is far easier to measure accurately than  $v_T$ , because of the prominence of the Rayleigh wave peak in SBS spectra. In this case, with  $C_{11}$  can be determined from the longitudinal velocity  $v_L$ , it remains to determine  $C_{44}$  from the Rayleigh velocity  $V_R$ , through a correction term for bulk thin films, since the Rayleigh velocity in this case is proportional to the transverse velocity ( $k_z/d \gg 0$ ).

In this work the backscattering geometry was chosen to investigate acoustic modes with their acoustic wave-vector component parallel to the surface. The phonon velocities are obtained by dividing the measured mode frequencies by the component  $q_{\parallel}$  of wave-vector parallel to the surface,

$$V_R = \frac{2\pi\Delta f}{q_{\parallel}} \quad (4.2)$$

where  $q_{\parallel}$  is determined by the scattering geometry, as  $q_{\parallel} = \left(\frac{4\pi}{\lambda_i}\right) \sin \theta_i$ , where  $\lambda_i$  and  $\theta_i$ , represent the wavelength of the incident light and the angle of incidence, respectively.

In Figures 4.24 - 4.26 two peaks are observed, the Rayleigh mode (RW) with lower frequency and the longitudinal guide mode (LGM) occurring at higher frequency [187], which appears as a sharp resonance in the Brillouin spectrum, indicative of the localization of the LGM within the DLC thin film. Acoustic excitations in thin supported films display characteristically

different velocity propagations which depend on the relative magnitudes of the longitudinal and transverse velocities in the film and substrate. At higher velocities, in the range bounded by longitudinal sound velocity of the film ( $V_L^{film}$ ) and substrate ( $V_L^{sub}$ ), the LGM exists when  $V_L^{film} < V_L^{sub}$ , and is characterised by mode displacements primarily the film plane and close to the  $V_L^{film}$  [188]. The phonon velocities were determined as shown in table 4.13 taking a mass density of  $\rho = 2.49 \text{ g/cm}^3$  for the DLC films, the corresponding elastic constant can be assessed ( $C_{11} = \rho v_{LGM}^2$ ,  $C_{44} = \rho \beta v_{RW}^2$ ): This quasi-bulk approach approximates the elastic constants of the isotropic thin DLC films to within 8%. In this case,  $v_{LGM}$  is detected by the spectra and the elastic constant  $C_{11}$  is directly obtained by  $C_{11} = \rho v_{LGM}^2$ . Moreover, in an isotropic sample it is possible to estimate the value of the transverse acoustic phonon velocity from the SAW velocity [188, 189] (where the  $v_{RW}$  obtained from the dispersion curve when  $q/h$  tend towards infinity is closed to  $v_t$ ). In this case the shear modulus  $G$  coincides with  $C_{44}$  is also determined by  $C_{44} = \rho \beta v_{RW}^2$ , while Young modulus  $E$ , Bulk modulus  $B$  and Poison ratio  $\nu$  is given by the following relations [133]

$$E = \frac{C_{44}(3C_{11}-4C_{44})}{C_{11}-C_{44}} \quad (4.7)$$

$$B = C_{11} - \frac{4}{3}C_{44} \quad (4.8)$$

$$C_{11} = \frac{2(1-\nu)}{(1-2\nu)}C_{44} \quad (4.9)$$

**Table 4.13:** Elastic constants and related mechanical moduli of RF magnetron sputtered films

DLC films CH <sub>4</sub> (%)	Rayleigh velocity (m/s)	LGM Velocity (m/s)	C <sub>44</sub> (= G) (GPa)	C <sub>11</sub> (GPa)	E (GPa)	B (GPa)
33	3084	4346	20.8	47.0	46.0	19.2
50	3298	4533	23.6	51.2	50.6	19.7
67	3294	4556	23.0	51.7	51.4	19.7

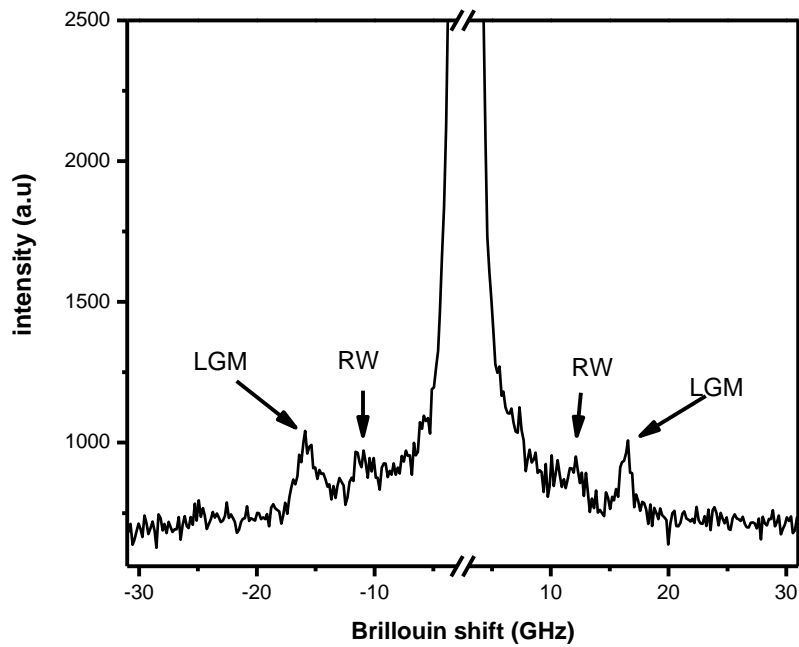


**Figure 4.21:** Surface Brillouin scattering spectrum of RF sputtered films measured at 70° incidence, showing the two phonon modes, Rayleigh and Longitudinal guided modes; a) Ar (13 sccm), CH<sub>4</sub> (6.5 sccm).

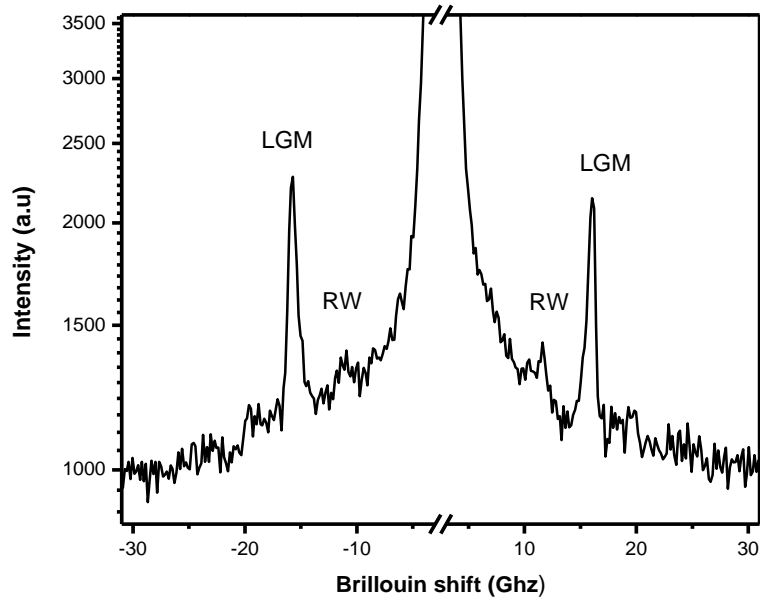


**Figure 4.22:** Surface Brillouin scattering spectrum of RF sputtered films measured at  $70^\circ$  incidence, showing the two phonon modes, Rayleigh and Longitudinal guided mode; b) Ar (13 sccm), CH<sub>4</sub> (13 sccm).

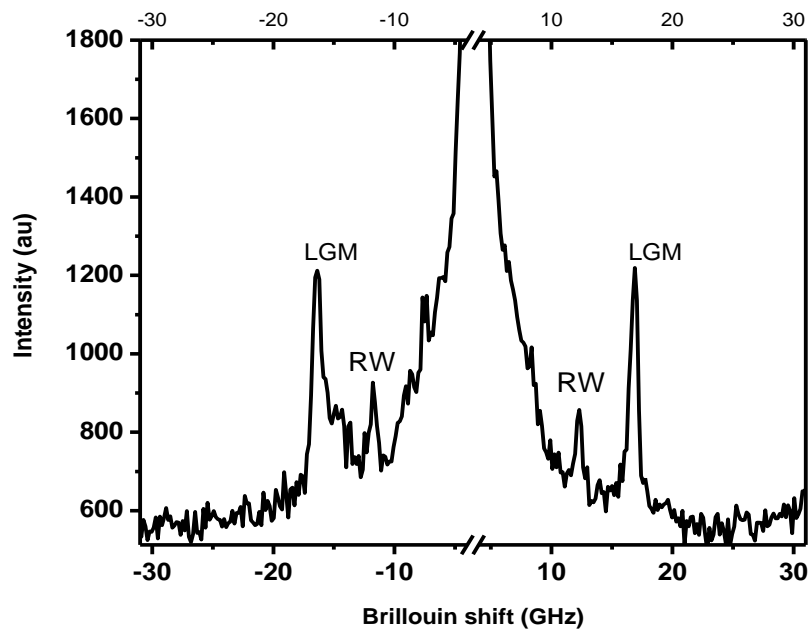


**Figure 4.23:** Surface Brillouin scattering spectrum of RF sputtered films measured at  $70^\circ$  incidence, showing the two phonon modes, Rayleigh and Longitudinal guided mode; c) Ar (13 sccm), CH<sub>4</sub> (26 sccm).

The changes of the phonon frequency and phase velocity are certainly a result of microstructural changes which are related to the fraction of the  $sp^2$  and  $sp^3$  bonds present in the films. Depending on the deposition techniques and conditions used for the preparation of the DLC films, the films are either graphite-like (RW  $\sim 2765$  m/s) i.e. consisting more of  $sp^2$  – bonded carbon, or contain both  $sp^3$  – and  $sp^2$  hybridized carbon with more hydrogen passivation dangling bonds. The latter films may be mechanically soft with a relatively large optical band gap in range of 2 -3 eV, known as polymer-like films, or hard and dense with an optical band gap of 1 – 1.5 eV. The Rayleigh mode of diamond-like amorphous, hydrogenated DLC films studied here is  $\sim 3300$  m/s, which is higher than that reported for graphite-like DLC films, however, this velocity is still lower than that reported for hydrogenated DLC films ( $\sim 4600$  m/s) prepared by plasma decomposition of methane at a frequency of 13.56 MHz with an active bias and or annealing, as expected. Diamond has a uniquely low Poisson's ratio (0.07), and the value obtained for the optimum DLC films studied here is similar ( $\nu \sim 0.1$ ), presumably due to the same high bond angle rigidity of carbon's  $sp^3$  bonds and or small thickness of the films ( $< 200$  nm). This is even supported by the low fraction of Hydrogen in the optimized DLC film. However, the modulus of these thin films is expected to be smaller than those of thicker ( $\sim 500$  nm) films. The reason for this uncertainty seems to be associated with the different film properties caused by the significant effect of the initial transient period of the film deposition. In this study, the DLC film properties have no dependence on the ion energy normally required by the condensing carbon atoms, hence a gradual optimization of the elastic moduli is observed at about 50 %  $CH_4$  content, directly relatable only to the moderate  $sp^3/sp^2$  ratio of the sputtered films. The statistical error of the Rayleigh and LGM mode measurements is about 1-2%.

#### 4.8.1 Theoretical considerations: Phonon Dispersion curves

In this section Green's elastodynamic function was specifically used to determine elastic constants by comparing the theoretical and experimental values of phase velocities of the Rayleigh and Sezawa modes in the phonon velocity dispersion curves. From SBS measurements, elastic stiffness of the film are extracted by the simultaneous fitting of the dispersion curves (surface waves velocities as a function of  $k/h$ ) for the observed modes. The process of fitting the dispersion curves is one of inversion. The best fit is obtained by a least-squares minimization procedure. Dispersion curves of DLC film on (001) Si was used for this purpose. These phonon dispersion curves were obtained by:

- varying the angle of incidence at a constant film thickness constant
- increasing the parameter space in the dimensionless  $k/d$  product through film thickness variations.

The simulation using the Green's function method must have the elastic properties of the substrates as well as the film thickness and the mass density of the DLC film. The parameters used for the crystalline Si substrate (100) were;

$$C_{11}= 165.7 \text{ GPa}, C_{12}= 63.9 \text{ GPa}, C_{44}=79.6 \text{ GPa and } \rho = 2.32 \text{ g cm}^{-3}.$$

The DLC films prepared with  $\text{CH}_4/\text{Ar}$  (1:1) over 5 minutes had a measured thickness of 139.99 nm and density of  $2.49 \text{ g/cm}^3$  when deposited on a silicon substrate. The incident angle was varied in the range of  $50$  to  $80^\circ$ . The thicknesses were varied by changing the time of deposition of the films by 3, 5 and 8 minutes at a deposition rate of  $28 \text{ nm /min}$ . These variations lead to  $k_{||}d$  values that span from 2.4 to 5.5.

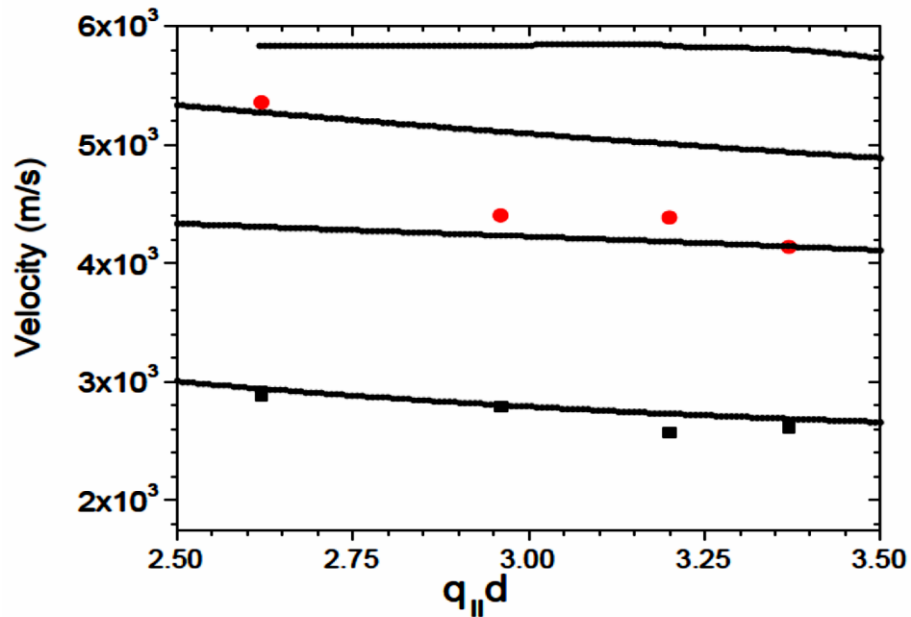


**Figure 4.24:** Dispersion plot of experimental data measured from 50 to 70° incidence, with deposition times 3, 5 and 8 minutes and the  $q_{||}d$  was varied from 2.5 to 3.5; and velocity dispersion simulations by elastodynamic Green’s function (continuous line).

Fig. 4.24 depicts the fitted phonon dispersion relations for an isotropic DLC film on a (001)Si substrate. Generally, below the T wave threshold of the substrate (5843 m/s), the substrate partial waves for any  $k_{||}d$  are both evanescent, and the modes that exist are the guided surface modes. The displacements of these modes are large in the layer and fall off exponentially in the substrate. Starting at  $k_{||}d = 0$ , which corresponds to the condition of a bare substrate, there is only one guided mode, the Rayleigh wave of the substrate. With increasing  $k_{||}d$ , the Rayleigh wave falls off in velocity, ultimately for large  $k_{||}d$  asymptotically approaching the Rayleigh velocity of the layer material, at 3079 m/s. At a sequence of critical values of  $k_{||}d$ , additional higher order guided modes, known as Sezawa modes are observed, (red dots), that emerge from the T wave threshold and fall off in velocity. Adjusting the elastic constants yield the calculated phase velocity dispersion curves which are superimposed on the measured data (red and black dots) for the best

fit elastic constants of  $C_{11} = 62$  GPa and  $C_{44} = 19$  GPa. The difference in the values of the elastic constants determined from the method of bulk determination of the elastic constants and the elastodynamic Green function's approach is 14% and 40% for  $C_{11}$  and  $C_{44}$ , respectively.

To determine the uncertainty in the elastic constant values the least square fitting procedure was applied to the linearized expression of the phase velocities of the RSAW and SW, using Mathematica software. The procedure for optimization uses an expression for the linearized surface phonon velocity as a function of the elastic constants based on a Taylor series expansion for the velocity as shown:

$$V_j(C_{11}, C_{44}) = V_j^0 + \frac{\partial V_j^0}{\partial C_{11}} (C_{11} - C_{11}^0) + \frac{\partial V_j^0}{\partial C_{44}} (C_{44} - C_{44}^0) \quad (4.10)$$

the coefficients  $\frac{\partial V_j^0}{\partial C_j}$  are the calculated derivatives corresponding to each data point in the velocity dispersion curve at the respective  $k/d$ . The formalism for the determination of the elastic constant values and their uncertainty is based on the method due to Every *et al.* which has also been applied for anisotropic cubic material systems. In the present work, the method has been have modified and applied to two independent elastic constants, namely  $C_{11}$  and  $C_{44}$  using the values of the Rayleigh surface acoustic and Sezawa wave velocities at various  $k/d$  directions in the respective phonon velocity dispersion curves to minimize the  $\chi^2$  in the form using least squares fitting;

$$\chi^2(C_{11}, C_{44}) = \sum_{RSAW_j} (V_j^{meas.} - V_j^{calc.})^2 + \sum_{SW_j} (V_j^{meas.} - V_j^{calc.})^2 \quad (4.11)$$

The minimization of the  $\chi^2$  results in a set of elastic constants whose boundary give the uncertainty in the elastic constants. This is depicted as covariance in the fits of Figure 4.25 by

displaying projections on two parameter planes of the sets of  $C_{ii}$  that yield values of  $\Delta\chi^2 = \chi^2 - \chi^2_{\text{min}}$  minimum at different intervals.

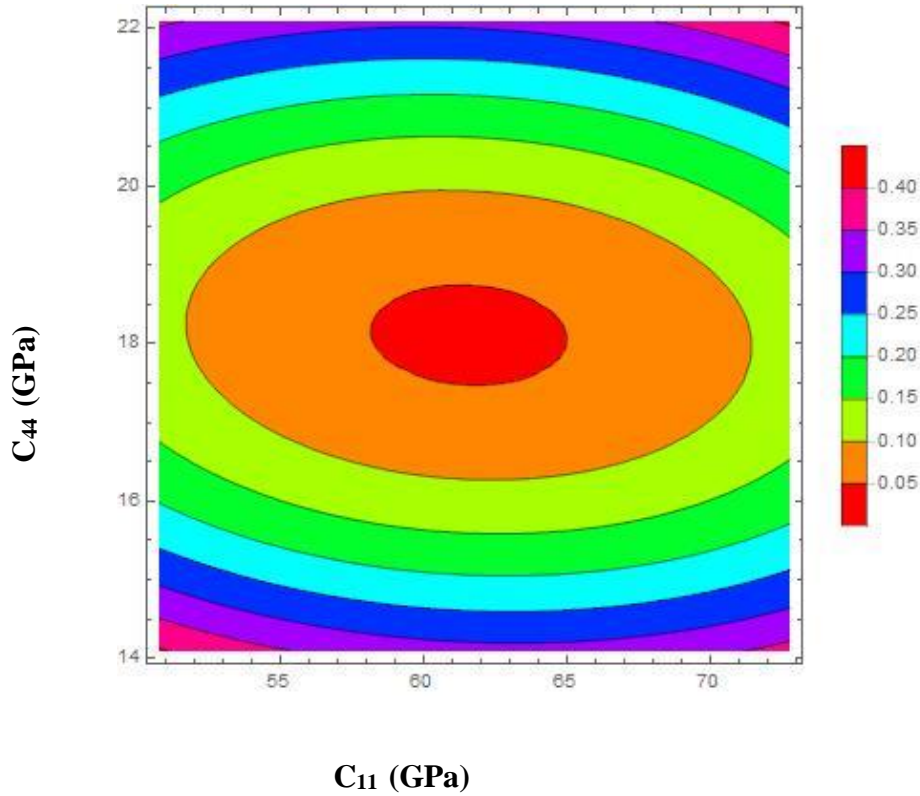


**Figure 4.25** Elliptical plots to determine the error of the elastic constants, as  $C_{44} = 19 \pm 2.0$  GPa and  $C_{11} = 62 \pm 7.0$  GPa, respectively.

The evaluation of the Surface Brillouin scattering spectra of DLC thin films fabricated by DC magnetron sputtering is not reported in this work due to attenuation of the SBS spectra by the high surface roughness. There were no acoustic excitations observed under these conditions in all the samples.

## 4.9 Conclusion

The results show that the optimum condition of 50% of CH<sub>4</sub>-Ar concentration for these room-temperature sputtered films was achieved. The amorphous hydrogenated carbon films exhibit more diamond-like features at this composition, characterized by moderately high fraction of sp<sup>3</sup> bonds, coupled with higher Tauc band gap, (1 -1.5 eV). There is also a notable increase in density (~ 2.5 g/cm<sup>-3</sup>) and mechanical strength (E ~ 51 GPa), of which this E-modulus value is ~18 % lower than reported for amorphous DLC films prepared with active negative substrate bias (< -100 V) [190]. The mechanical and structural properties of the film depend on the degree of dilution, due to a different chemistry occurring in the plasma. When the amount of methane increases, XRR results show structural changes from a more disordered polymer-like structure to a less disordered graphitic arrangement. The FWHM (G) gives information on the structural disorder in DLC films and the measured data correlates with the mechanical properties of the films.

At the optimum condition, the film has a high resistivity owing to the increased proportion of sp<sup>3</sup> bonds as evidenced by the increased presence of CH<sub>n</sub> (n=1-3) radicals. The changes of the phonon phase velocity are related to the microstructural changes of the films, and it is demonstrated in the study that the mechanical strength of the *as-deposited* films flattens out at 50 % composition, thus necessitating either an active biasing of the substrate or annealing of the films in order to further improve the mechanical strength. In the next chapter, the bias substrate will be used to ameliorate the physical properties. The elastic constants of the amorphous carbon films prepared for this study have been evaluated using surface Brillouin scattering technique and provide the baseline data for further work to improve the elasticity of DLC films.

# Chapter 5: Bias enhanced nucleation and growth for improving DLC quality

## 5.1 Introduction

This chapter follows up on additional methods to enhance the  $sp^3$  fraction in the optimized DLC thin films fabricated using two distinct PVD techniques, namely RF and DC magnetron sputtering. The growth condition of thin films using RF and DC sputtering entail a non-equilibrium process and thus factors such as gas flow rates, substrate temperature and substrate bias and its polarity, can influence the microstructure and the film properties in general. In the present chapter, the dominant role of substrate bias in the nucleation and growth of DLC thin films on the opto-mechanical properties are examined. Thus the dependence of the elastic properties, structural and opto-electrical properties of DLC thin films on the substrate bias voltage forms the basis of this chapter. The substrate is biased negatively to extract the radicals and ions that enhance the  $sp^3$  fractions thus leading to films with more diamond-like carbon properties. The basis on this work follows from previous studies that have been carried on films deposited in a CVD reactor on grounded substrates. The films produced in this study at -25V bias had polymeric characteristics [191], however at higher impacting energies (100 eV) the  $sp^3$  fraction in the DLC films was observed to reach a maximum value thus inferring on the role of substrate bias in the modulation of  $sp^3$  bond and formation of DLC thin films [192].

The quality and fraction of the  $sp^3$  bonds in the films needed to enhance the opto-mechanical properties of DLC films is investigated after applying an *in situ* DC substrate bias voltage during film growth. This procedure further seeks to establish the correlation between microstructure and physical properties of DLC thin films.

Besides the formation of  $sp^3$  bonds in DLC thin films it is also expected that the film microstructure is sensitive to the energetics and kinetics of the film growth processes. These conditions are subject to the amount of ion species, their charge states, the mass and ion energy [192]. Studies by the Thornton *et al.* [193] and more recently by Petrov *et al.* [194] have shown that the energy of the ad atoms and the presence of impurities can lead to a variety of growth zones having unique grain sizes and orientations. Factors such as the working pressure of argon (Ar) can affect the  $T_S/T_M$  ratios through changes in the ad atom energy thus predominantly influencing the ejection of sputtered carbon, its transport and arrival onto the substrate. The condensation rate of these ad atoms onto the growing film surface is also subject to the sputter energy and pressure [195].

The polarity and the magnitude of substrate bias voltage directly influence the energy of the ion species in the plasma and their selectivity. Besides the ad atom energy, a biased substrate can extract ions in the plasma and dissipate their kinetic energy to the film surface thereby raising the substrate temperature,  $T_S$  or enhance the diffusivity of the ad atoms. This is the fundamental basis of the Thornton model of film growth which prescribes the microstructure dependence on the ion energy (substrate bias, substrate temperature and working gas pressure) scaled to the melting temperature,  $T_M$  of the deposited film. Studies on the microstructure of sputtered DLC thin films using Raman spectroscopy have shown the sensitivity of  $sp^2$  phases or clusters to the working gas pressure [169].

The dependence of the  $sp^3/sp^2$  ratio on the substrate bias voltage is studied in the present chapter for DLC films prepared by RF and DC magnetron sputtering. This ratio is determined through analysis of the vibrational spectrum of DLC thin films by visible Raman spectroscopy. A typical DLC vibration spectrum comprises of the D and G bands. The ratio of their areal and peak intensities at various substrate bias voltages are investigated in detail to establish the nature of the

configurations of the C-C bond. While it is noted that the substrate bias provides ad atom energies or kinetic energies to the selected ion, the deposition of these energies through knock effects can change the microstructure, the bonding configurations can also be affected through ion bombardment through the substrate bias route. Thus, changes not only to the morphology of the DLC films are probable but the  $sp^3/sp^2$  ratio can be modified through variation of the combined process parameters such as the gas pressure and the substrate bias voltage. In this chapter the establishment of the critical bias voltage to form DLC thin films with optimum opto-mechanical properties is of fundamental interest. Linked to this aspect are the resultant properties of the optimized DLC thin films. While the concentration of the  $sp^3$  bonds is determined using empirical methods that are based on the  $I_D/I_G$  ratio, X-ray photoemission spectroscopy and Auger electron spectroscopy techniques are used to quantify the amount of  $sp^3$  bond in the biased DLC films.

## **5.2 Growth rate, thickness and density determination using X-ray reflectivity**

In the present work, DC and RF magnetron sputtering (13.56 MHz) techniques are used to fabricate DLC thin films at various substrate bias voltages. The films have been deposited on (001) Si and  $SiO_2$  at substrate bias voltages from -25 to -100V with the step-size of 25V. The determination of the optimized film growth conditions under the substrate bias voltages enabled the subsequent growth of thin DLC films for investigation of their structural properties. Thus the films were deposited for 5 min at the various substrate bias voltages of interest and characterized for thickness determination using X-ray reflectivity. Subsequently the extraction of the respective deposition rates for DC and RF fabricated DLC thin films was carried out. As a consequence, the maximum deposition rate were observed in films deposited on (001) Si biased at -100 V, these values have been determined to be  $(14.67 \pm 0.20 \text{ nm/min})$  and  $(26.49 \pm 0.20 \text{ nm/min})$ , respectively for the DC and RF magnetron sputtering methods. On the other hand, our results have shown a much higher

deposition rate of 25.90 nm/min for films deposited by RF magnetron sputtering on a glass substrate biased at -75 V. The increase in the deposition rate at -100 V (-75V on the glass) under Ar/CH<sub>4</sub> gaseous mixture is attributed to the increased dissociation and deposition of hydrocarbon ions, radicals and the particle density of the sputtered C species onto the depositing films. Therefore the sputtered C species increases whenever the bias voltage is increased due of the augmentation of both the excess dissociation energy and the plasma density. The increase in the sp<sup>3</sup>-C fraction results in more densification of DLC films corresponding to the optimal (Ar /CH<sub>4</sub>) methane composition (50:50) at -100 V. This observation is supported from the X-ray reflectivity measured mass density values of  $2.58 \pm 0.05 \text{ g cm}^{-3}$  and  $2.35 \pm 0.05 \text{ g cm}^{-3}$  for DC and RF sputtered DLC films on (001) Si, respectively. A summary of the measured physical properties at various substrate bias voltages for DLC films fabricated on Si and glass substrates using DC and RF magnetron sputtering is presented in Tables 5.1-5.3. It is defined from the tables that the deposition rate and the film density increases with the substrate bias voltage, however, there is no clear correlation between the film roughness and the substrate bias voltage. This could be indicative that bias voltage does not provide the ad atoms with sufficient energies through the knock effect to promote surface diffusion within the DLC film. These results are in general agreement with those published in [192, 196], in which the densification of the DLC films at -100 V substrate bias provides an ion energy of 100 eV as the threshold energy for sp<sup>3</sup> bond formation. This observation is further supported by the sub-plantation model [192] and computer simulation [106], which have established 100 eV as the critical ion energy value for creating sp<sup>3</sup> C bond through ion bombardment.

**Table 5.1:** Physical properties of biased DC sputtered DLC thin films on (001) Si.

DLC	Roughness (nm) $\pm 0.20$	Deposition rate (nm/min) $\pm 0.05$	Density (gcm <sup>-3</sup> ) $\pm 0.02$	Thickness (nm) $\pm 0.03$
-25 V	2.11	9.67	2.01	49.65
-50 V	2.05	10.38	2.39	51.88
-75 V	1.97	13.66	2.50	68.30
-100 V	1.72	14.67	2.58	73.37

**Table 5.2:** Physical properties of biased RF sputtered DLC thin films on (001) Si.

DLC	Roughness (nm) $\pm 0.20$	Deposition rate (nm/min) $\pm 0.05$	Density (gcm <sup>-3</sup> ) $\pm 0.02$	Thickness (nm) $\pm 0.03$
-25 V	1.07	18.17	2.20	90.84
-50 V	1.59	26.32	2.28	131.60
-75 V	1.21	23.41	2.32	117.07
-100V	0.77	26.49	2.35	132.48

**Table 5.3:** Physical properties of RF sputtered DLC thin films on SiO<sub>2</sub> substrate.

DLC	Roughness (nm) $\pm 0.20$	Deposition rate (nm/min) $\pm 0.05$	Density (gcm <sup>-3</sup> ) $\pm 0.02$	Thickness (nm) $\pm 0.03$
-50 V	1.01	21.40	2.22	107.00
-75 V	2.70	29.30	2.24	146.46
-100 V	2.51	22.10	2.38	110.49

### 5.3. Raman spectroscopy analysis of $sp^3$ , $sp^2$ and hydrogen- contents

Raman spectroscopy's sensitivity to the translational symmetry of materials is a suitable technique in the determination of the allotropes of carbon. It can be used to determine the quality of the DLC films by distinguishing the different bonding types and domain sizes during diverse processes of film growth. Raman spectroscopy measurements of DLC thin films prepared at different bias voltages and PVD methods have been carried out to establish the effect of substrate bias on the  $sp^2$  and  $sp^3$  bonding configurations. Two unresolved broad peaks consisting of the disordered bands and graphite-bands have been observed in the range of 800 - 2000  $cm^{-1}$ . The disordered band appears at approximately 1560  $cm^{-1}$  while the graphite band is present at 1580  $cm^{-1}$ , as shown in Figures 5.1 and 5.3.

It is well known that these peaks are the D and G peak, respectively, and their intensity ratio, namely the ( $I_D/I_G$ ) ratio can be used to determine the fraction of the  $sp^2$  clusters and  $sp^3$  bonding fractions in the film. Our results have shown that this ratio decreases when the bias voltage reaches -100 V and -75 V for RF magnetron sputtering deposited on (001) Si and glass substrates, respectively. However, for DC magnetron sputtering the intensity ratio increases with substrate bias voltage and peaks at -100 V. The divergence in the trends of the intensity ratio for the RF and DC magnetron sputtering is unexpected and it could be attributed to the variations in the energy of the arriving ad atoms. This is supported by the differences in the DC self-bias voltage and the DC voltage of the RF and DC magnetron sputtering for the same deposition power. Besides the intensity ratio, the FWHM and the peak positions for the D and G peaks are suitable indicators on the cluster size and the nature of the disorder, this aspect is also examined in detail in this chapter especially in instances for which the surface energy is changed (different substrates used) as well as at various substrate bias voltages. The dissociation of  $CH_4$  to produce hydrogen in the plasma

presents the possible formation of hydrogen terminated  $sp^3$  bonds. This bonding configuration affects the mechanical properties of DLC thin films and therefore the correlation of this property with the substrate bias voltages may be exigent. The amount of hydrogen in the fabricated films is determined from the empirical approach that uses the background photoluminescence of Raman spectroscopy. It is found that there is correlation between the intensity ratio ( $I_D/I_G$ ), the G peak's position and the FWHM of the G-peak and  $sp^3/sp^2$  ratio. In addition, the intensity ratio ( $I_D/I_G$ ) is related to the cluster size of  $sp^2$  bonds.

### **5.3.1 RF magnetron sputtering with substrate bias voltage on SiO<sub>2</sub> (glass substrate)**

Figure 5.1 shows the Raman spectra obtained using a 514.5 nm laser excitation energy in the scanning range of 800 to 1800  $cm^{-1}$  for biased DLC thin films on glass substrate. The spectra resemble that of disordered graphite constituting of two vibrational modes, namely;

- the G-peak around 1580-1600  $cm^{-1}$
- the D-peak around 1350  $cm^{-1}$ .

These modes are assigned to the zone centre phonons of  $E_{2g}$  symmetry and K-point phonons of symmetry, respectively [79]. The spectra of the DLC films were de-convoluted into distinct D- and G peaks using two Gaussian functions as shown in Figures 5.1. The broad peak near 950  $cm^{-1}$  represents the second – order Raman peak of the silicon substrate, providing an indication of the high transparency of the films to the 514.5 nm light source.

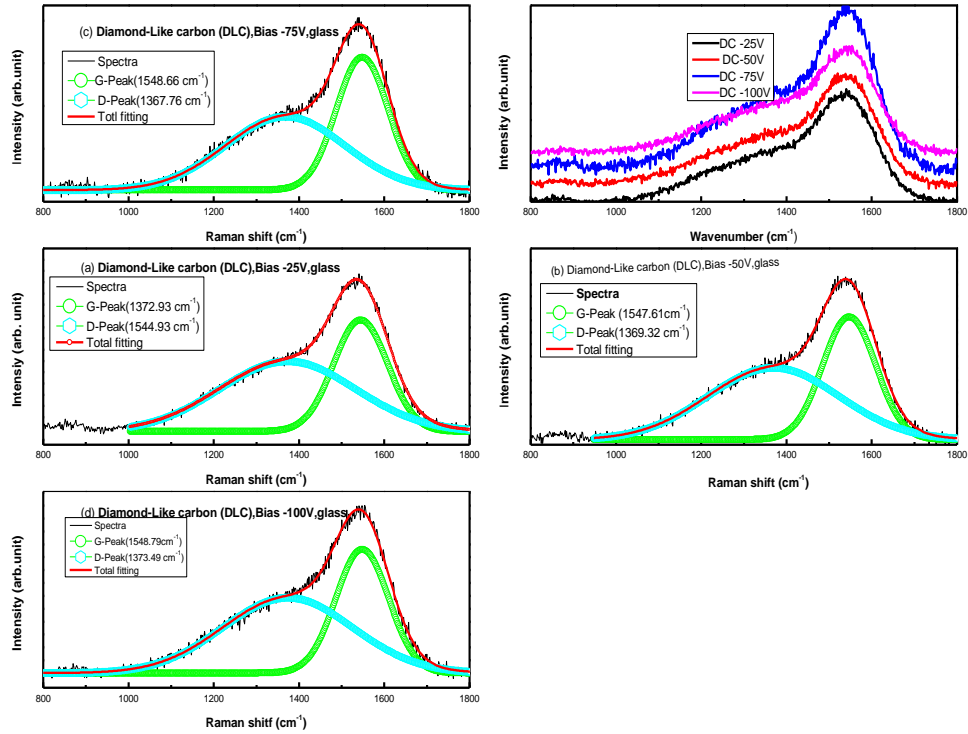


**Figure 5.1:** Raman spectra of RF sputtered films, showing D- and G-peaks of films deposited at different bias voltage: (a) -25 V, (b) -50 V, (c) -75 V and (d) -100 V on SiO<sub>2</sub>.

The present results indicate that the centroid of the D-peak occurs in the vicinity of (1374 - 1369 cm<sup>-1</sup>) and the I<sub>D</sub>/I<sub>G</sub> ratio decreases in terms of both the height (0.63-0.55) and area intensities (1.59-1.28) of the corresponding D- and G-peaks, with the increased substrate bias voltage. This further confirms the formation of higher sp<sup>3</sup>- content in the DLC films leading to the more diamond like carbon films. Additionally, the results have shown a decrease in the D-peak position and an increase in the FWHM which is indicative of enhanced disorder of the DLC films on SiO<sub>2</sub> with increasing substrate bias voltage. Corresponding to this trend is the increase in sp<sup>3</sup>/sp<sup>2</sup> fraction (1.07-1.33) in the films, and it represents the bonding configuration responsible for the formation of more diamond-like carbon films as shown in Table 5.4. The relationship between I<sub>D</sub>/I<sub>G</sub> and cluster size defined by eqn. (5.1) is an appropriate indication on the formation of DLC thin films;

$$I_D/I_G = C(\lambda)L_a^2 \quad (5.1)$$

where  $C(\lambda)$  is a wavelength-dependent constant (0.0055 for 514.5 nm) and  $L_a$  is cluster diameter or in-plane correlation length, Thus, it is evident that the  $I_D/I_G$  ratio decreases with decreasing cluster ( $L_a$ ) size of the  $sp^2$  bonds (9.05 - 10.95 Å).

The growth mechanisms of DLC thin films grown on Si were compared to those of  $SiO_2$  substrates. Applying bias on (001)Si in  $CH_4/Ar$  ambient optimizes DLC nucleation resulting in the highest fraction of  $sp^3$  bonds at -100 V, however nucleation can also be determined by the space charge effects which leads to a higher  $sp^3$  fraction at lower bias voltage (-75 V) [197]. In this study,  $CH_4$  is used as a precursor gas in the growth of DLC thin films due to its higher H/C ratio which contributes more hydrogen to the films.

A typical signature of hydrogenated samples is the increasing photoluminescence background with increasing H - content. Generally, this background overshadows the Raman signal of a-C:H with 40- 45 at.% of H. The ratio between the slope  $m$  of the linear background and the fitted intensity of the G-peak  $I(G)$ , is used as a measure of the bonded  $H$  content as shown in Figure 5.2. This expression is valid for  $H > 20$  at.% [177].

$$H[at. \%] = 21.7 + 16.6\{\log m/I(G)[\mu m]\} \quad (5.2)$$

Table 5.4 shows the results obtained using Raman spectra at the excitation wavelength 514.5 nm of DLC films deposited on a glass substrate in a methane and argon gas mixture ( $CH_4 = 15$  sccm and  $Ar = 15$  sccm). It is observed that substrate biasing increases the hydrogen content in the DLC films on  $SiO_2$  up to -75 V. Above -100 V, a reduction in the amount of hydrogen in the film is observed. This decrease is possibly due to re-sputtering effects arising from plasma etching. Indeed

the thickness of the DLC thin films deposited at -100 V is 110.49 nm compared to 146.46 nm for films deposited at -75 V. This implies that the films deposited on glass can be classified as hydrogenated diamond-like carbon a-C:H (DLC-H) since the hydrogen composition is in the range 20-40% [172, 176]. These observations are further supported by FTIR data that shows increased bias voltage leads to an increase in carbon coordination number [182].

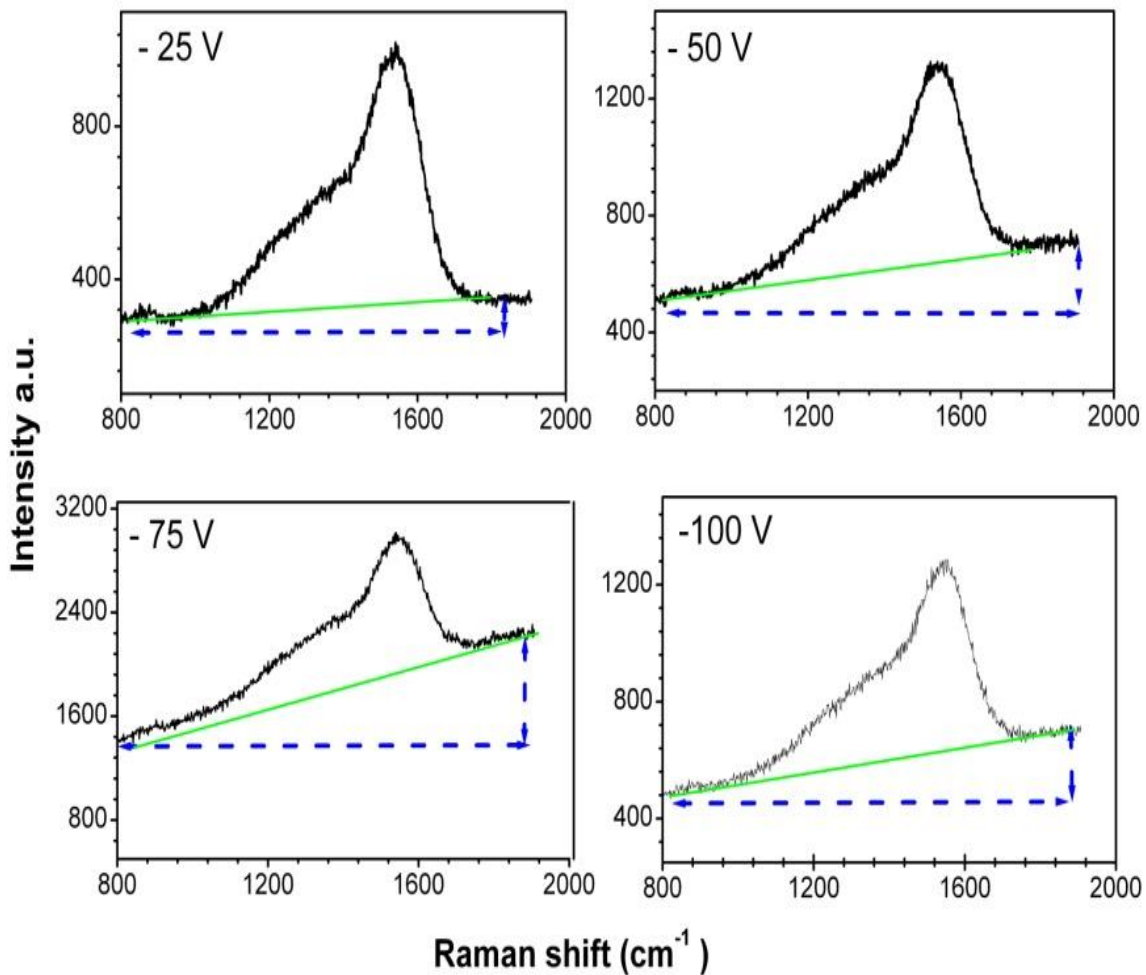


**Figure 5.2:** DLC thin film spectra showing influence of hydrogen on background photoluminescence at varying bias voltages, from -25 V to -100 V.

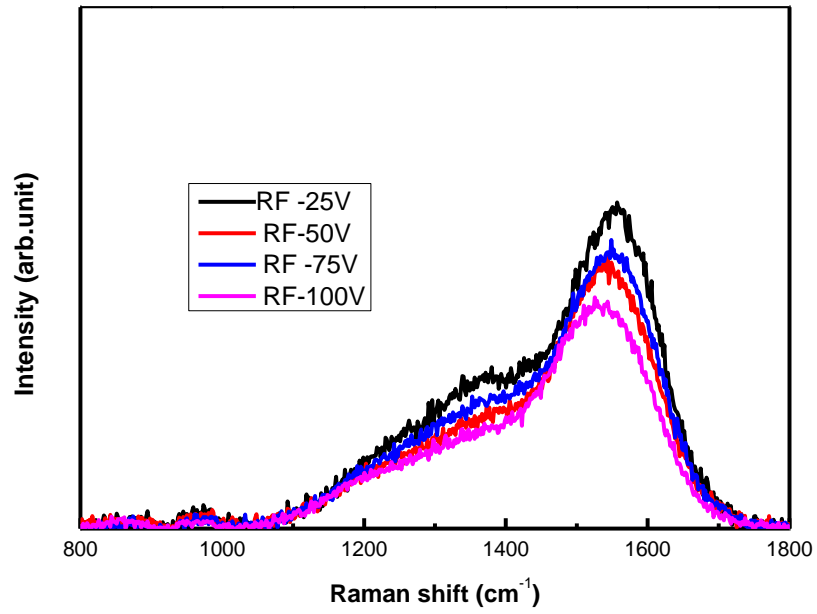
**Table 5.4:** Structural parameters of RF sputtered DLC thin films deposited on biased glass substrates.

Substrate bias voltage (V)	D-peak position (cm <sup>-1</sup> )	Area ratio (I <sub>D</sub> /I <sub>G</sub> )	Height ratio (I <sub>D</sub> /I <sub>G</sub> )	sp <sup>3</sup> /sp <sup>2</sup> (±0.05)	Hydrogen (at. %)
-25	1373	1.59	0.63	1.07	22.15
-50	1369	1.45	0.59	1.21	31.27
-75	1368	1.28	0.55	1.33	38.19
-100	1374	1.51	0.61	1.13	32.52

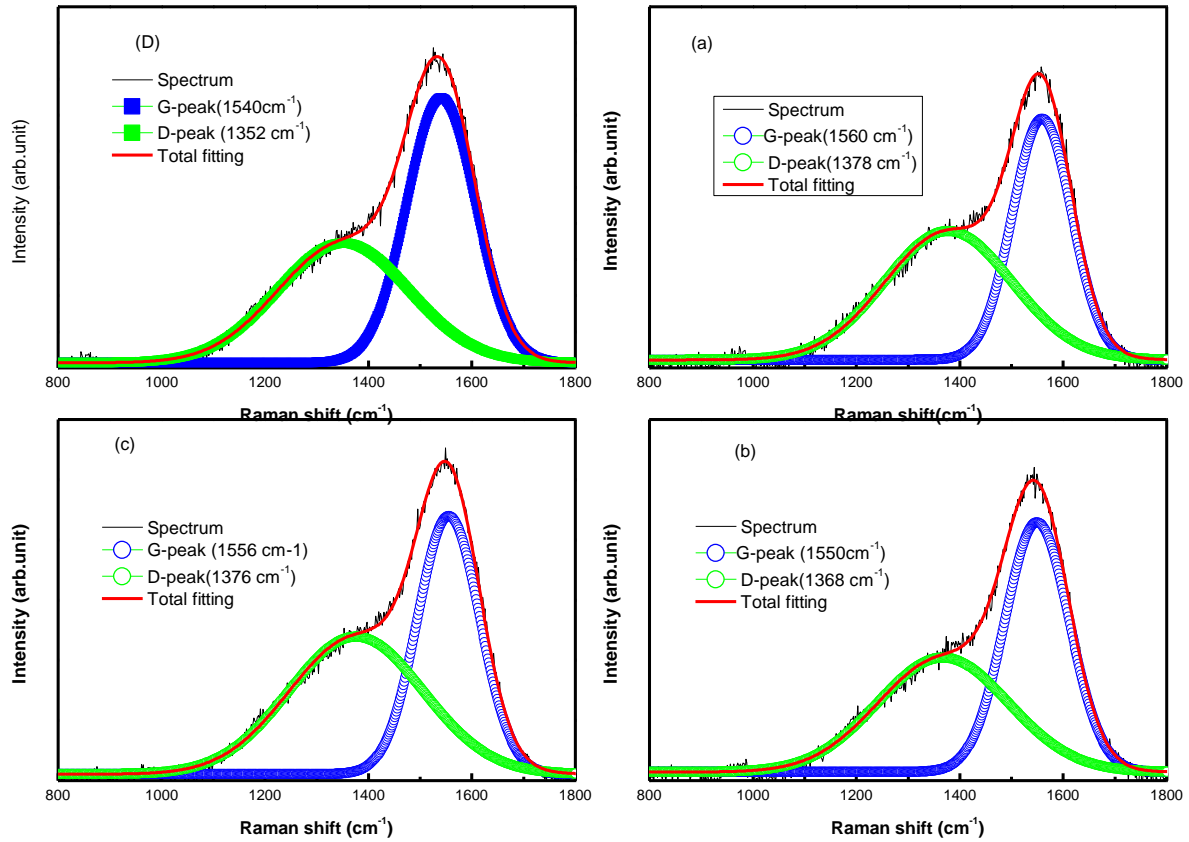
### 5.3.2 DLC thin films fabricated by RF magnetron on (001) Silicon at varying bias voltages

Figure 5.3 shows a summary of the Raman spectra of DLC thin films grown using RF magnetron sputtering on (001) Si with varying substrate bias voltages (from -25 V to -100 V with step of 25 V). The G- and D- modes of visible Raman are again observed in the range 1547 - 1555 cm<sup>-1</sup> and around 1345 - 1368 cm<sup>-1</sup> respectively. Furthermore, in Figure 5.3, it is evident that the increase in the substrate bias voltage leads to a shift in the D and G vibrational modes. For the case of the D band, a green shift is evident while a blue shift is observed for the G band as shown in figure 5.4. These observations are consistent with the work of Ferrari *et al.* [79, 198] who attributed the changes in the I<sub>D</sub>/I<sub>G</sub> ratios, the shift in the position and FWHM of the G peak with disordered sp<sup>2</sup> phase. The sp<sup>2</sup> phase is related to the amount of the sp<sup>3</sup> carbon in DLC films.

The spectra in Figure 5.3 is de-convoluted for quantitative determination of the structural properties and the subsequent results presented in Figures 5.4 (a)-(d) for the corresponding substrate bias voltages.



**Figure 5.3:** Raman spectra of DLC films deposited by RF magnetron sputtering on a Si substrate biased from -25 V to -100 V.



**Figure 5.4:** Fitted Raman spectrum of DLC films deposited by RF magnetron sputtering with different bias substrate voltage (a) -25 V, (b) -50V, (c) -75V and (d) -100V.

After background subtraction, the spectra were de-convoluted using two Gaussian peaks to determine the contributions of the D- and G-peaks from the resulting spectrum. The extracted structural parameters of Raman spectroscopy are tabulated in Table 5.5 for comparison.

The results of Table 5.5 show that the G-peak position decreases from 1560 to 1541  $\text{cm}^{-1}$  with increasing substrate bias voltage. This indicates an increase in  $\text{sp}^3$  fraction in the DLC films structure. The decrease in the intensity and area ratios from 0.54 to 0.45 and from 1.15 to 0.87, respectively is associated with increase in the  $\text{sp}^3$  fraction. Corresponding to the high  $\text{sp}^3$  content is the reduction in the cluster size of  $\text{sp}^2$  phases (from 9.90 to 9.04 Å) and subsequent increase of

$sp^2$  carbon in chains. As discussed earlier, the precursor gas  $CH_4$  used in this RF magnetron sputtering process has a significant effect for the formation of DLC thin films as well as their properties owing to its high H/C ratio. This means that the ratio of  $sp^3/sp^2$  is not a sufficient parameter to identify the structure and the properties of thin films. There is great need to know the fraction of hydrogen content in the films and this was again determined using the formalism of equation 4.1.

**Table 5.5:** DLC thin films on (001) Si substrate by RF magnetron sputtering at various substrate bias voltages.

Sample description	Peak Position		Width		$I_D/I_G$ ratio	
	D-Peak ( $cm^{-1}$ )	G-Peak ( $cm^{-1}$ )	$W_D$ ( $cm^{-1}$ )	$W_G$ ( $cm^{-1}$ )	From Area	From Height
-25 V	1378	1560	246	115	1.15	0.54
-50 V	1367	1550	251	124	0.92	0.46
-75 V	1376	1556	259	120	1.15	0.53
-100 V	1352	1541	254	133	0.87	0.45

In this expression, the background of the visible Raman photoluminescence obtained by ratio of the slope,  $m$ , of the linear background photoluminescence to the intensity of the G-Peak,  $m/I(G)$  can be empirically used as a measure of bonded H content (Marchon *et al.* 1997; Casiraghi *et al.* 2004b) [179, 199]. In Table 5.6, it is observed that the hydrogen content decreases with substrate bias voltage (31.85 - 18 at. %).

The full width at half maximum (FWHM) has been used to estimate the degree of structural disorder caused by variations of the bond (dihedral) angles and bond lengths in amorphous carbon films. The results in Table 5.5 show that the FWHM (G) increases (from 115 to 133  $cm^{-1}$ ) with the

increase of the bias voltage to the substrate (from -25 V to -100 V) for DLC films deposited on silicon substrate. The results show that a more elastically harder DLC film is possibly formed using a substrate bias voltage of -100 V. This assertion is further supported by the observed highest fraction of  $sp^3$  bonds and lowest fraction of hydrogen in the deposited films. To confirm this argument, surface Brillouin scattering measurements were performed and the results are presented in the subsequent sections.

**Table 5.6:** Dependence of Hydrogen content in DLC films with substrate bias.

Substrate bias voltage V	Hydrogen fraction (at.%); ( $\pm 2$ at.%)
-25	33.15
-50	31.85
-75	24.00
-100	18.00

An empirical approach to estimate the  $sp^3$  fraction based on the direct measurement of  $sp^3$  bonds by EELS, NMR has been applied to extract the bonding fractions in all DLC thin films in this work, using data obtained from the intensity ratios  $I_D/I_G$  from visible Raman spectroscopy [116]. Besides the  $sp^3$  concentration, the work done by Ferrari *et al.* [79] based on the statistical curve of intensity ratio values versus  $T_{auc}$ - gap (eV) of carbon based materials presents an alternative approach to determine the dependence of the optical properties on the  $sp^3$  bonding fractions. Thus in this study, the  $T_{auc}$  - gap for all the films deposited have been derived using this extrapolation. Generally, the results show that the  $T_{auc}$ -gap ( $E_g$ ) increases with decreasing of intensity ratio for increasing substrate bias voltage. This observation is adduced for the silicon substrates. Obviously, it is expected that as films become more diamond - like, their degree of transparency increases and

thus a higher Tauc gap is anticipated. This is confirmed in films with the highest of  $sp^3$  carbon concentrations as shown in the summary of Table 5.7.

**Table 5.7 : Parameters of DLC thin films by Raman Spectroscopy ( $\lambda_{exc} = 514.5$  nm)**

DLC films	G-peak FWHM $cm^{-1}$	$I_D/I_G$ ratio	$sp^3/sp^2$	$sp^3$ ( $\pm 0.05$ )	$sp^2$ ( $\pm 0.05$ )	Hydrogen fraction (at.%)	Tauc gap (eV)
-25V	115	0.54	1.18	0.56	0.44	33.15	1.51
-50 V	124	0.46	1.30	0.68	0.42	31.85	1.55
-75 V	120	0.53	1.26	0.57	0.43	24.00	1.53
-100 V	133	0.45	1.33	0.70	0.42	18.00	1.57

### 5.3.3 Structural properties of DLC films prepared by DC Magnetron sputtering on DC biased (001) Si

DLC thin films obtained at laser excitation of 514.5 nm are shown in Fig. 5.5 in the range of 800 - 1800  $cm^{-1}$ . Again the G- and D-peaks of visible Raman are observed around 1580-1600  $cm^{-1}$  and at 1350  $cm^{-1}$ , respectively. Table 5.8 shows the collated results obtained from Raman spectra of DLC films deposited in methane ( $CH_4 = 20$  sccm) and (Ar = 20 sccm) ambient at different substrate bias voltages. The increase in the  $I_D/I_G$  ratios determined from either the height (0.23 - 0.31) or area (0.22 - 0.40) of the corresponding D- and G-peaks is attributed to the apparition of aromatic  $sp^2$  with increase of substrate bias voltage. The data also shows that the G peak positions of DLC films are gradually shifted to lower energy level (from 1555  $cm^{-1}$  to 1545  $cm^{-1}$ ), when the substrate bias voltage ( $V_B$ ) increases gradually, and this reveals the formation of higher  $sp^3$ -content. Additionally, the  $I_D/I_G$  ratio gives an indication of the amount of ring-like  $sp^2$  carbon. The results in Table 5.8 suggest that the amount of  $sp^3$ -C is increased at the substrate bias voltage of -100 V, thus forming more diamond like carbon films, which is further confirmed by the results of I-V

characteristics and XPS analysis. The  $I_D/I_G$  ratio increases with increasing bias voltage as shown in Table 5.8. These ratios are related to the  $sp^2$  sites configuration i.e. topological disorder. Thus, the ring-like  $sp^2$  transforms to  $sp^3$  chains and increases the amount of  $sp^3$ - chains. The increased  $sp^3$ -content correlates with the hardness of the films, in agreement with the work done by Tamor and Vassel [116] by using Raman spectroscopy with visible excitation wavelength 514 nm of a-C

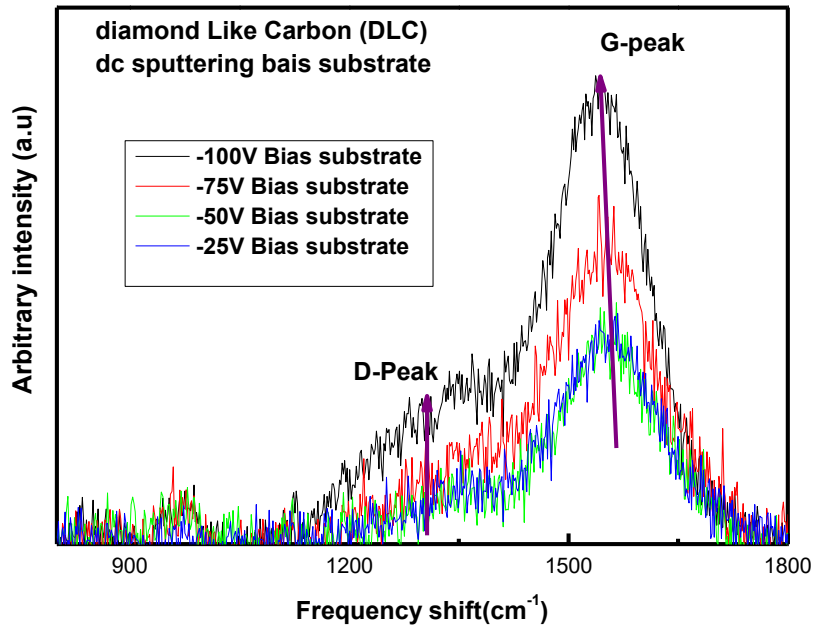


**Figure 5.5:** Raman spectra of DC magnetron sputtered DLC films with substrate bias variations in the range -25 V to -100 V.

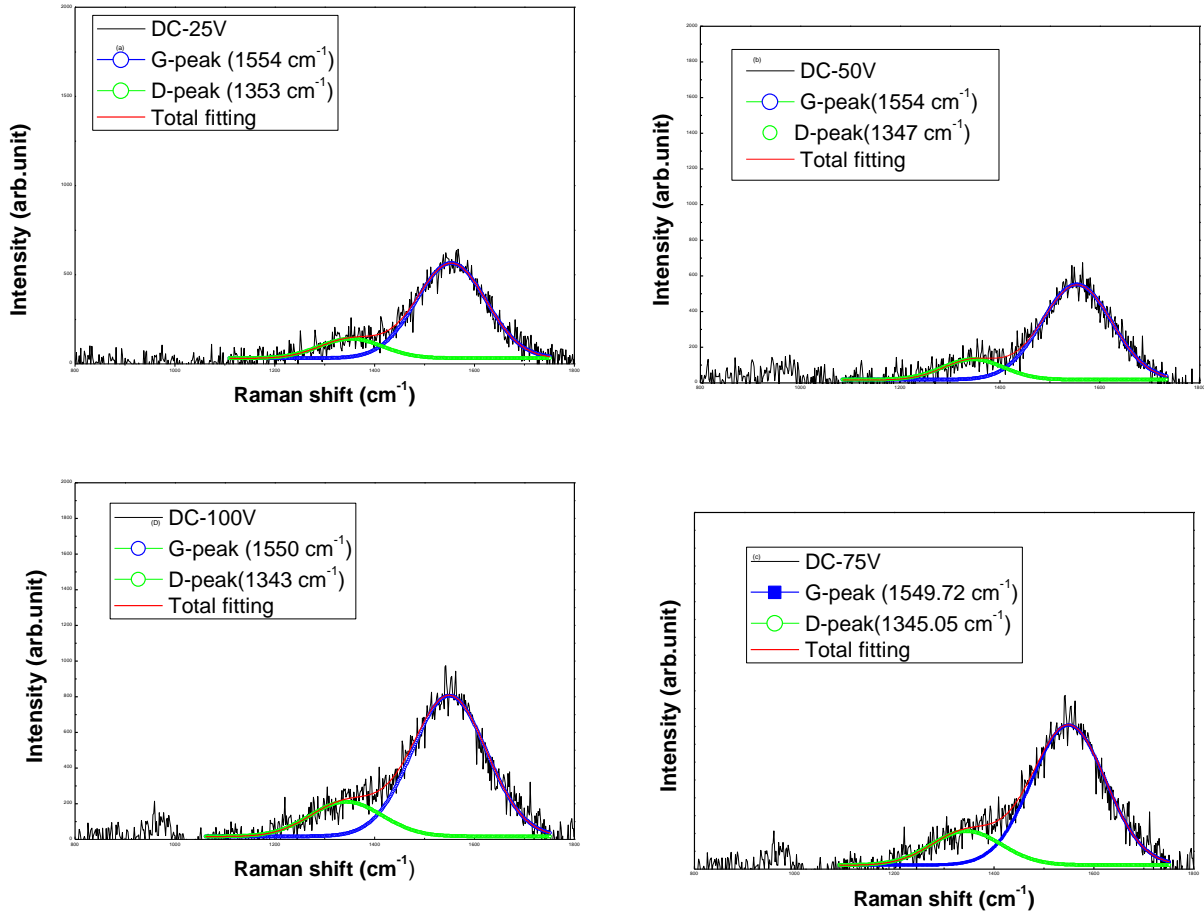


**Figure 5.6:** Raman spectra of DC magnetron sputtered DLC films with substrate bias voltage variations in the range -25 V to -100 V.

The bonded hydrogen in the DLC films was estimated using equation (4.1). Figure 5.7 shows that the hydrogen content decreases with substrate bias voltage. It can be due to the sputter-etching of C-H on the surface of the films.

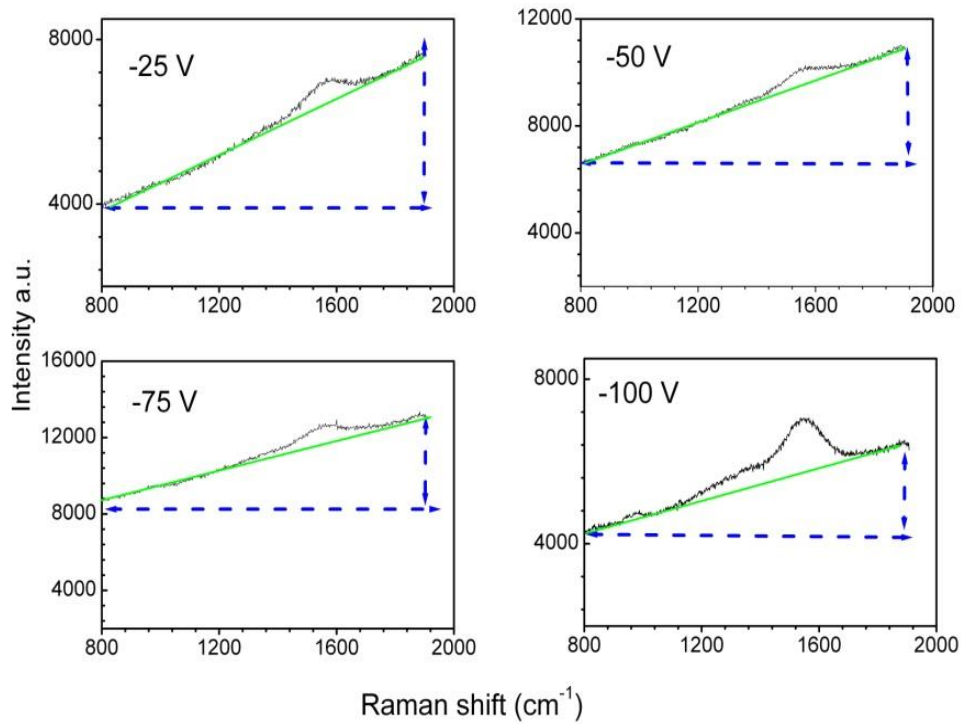


**Figure 5.7:** Schematic representation for hydrogen estimation in the films for DC magnetron sputtered with substrate bias varied in the range -25V to -100V.

**Table 5.8:** Parameters of DC magnetron sputtered DLC thin films for substrate bias voltages.

Sample description	Peak Position		Width		I <sub>D</sub> /I <sub>G</sub> ratio	
	D-Peak (cm <sup>-1</sup> )	G-Peak (cm <sup>-1</sup> )	W <sub>D</sub> (cm <sup>-1</sup> )	W <sub>G</sub> (cm <sup>-1</sup> )	From Area	From Height
-25 V	1345	1555	142.09	148.97	0.22	0.23
-50 V	1366	1555	85.47	113.23	0.21	0.28
-75 V	1367	1552	143.21	143.21	0.28	0.29
-100 V	1354	1545	169.48	132.37	0.40	0.31
Diamond	1332		1.2			
Graphite		1580		13		

## **5.4. Electrical properties of DLC thin films**

### **5.4.1. Current –Voltage (I-V) Characteristics**

Hydrogenated amorphous carbon (a-C:H) also called diamond-like carbon (DLC) thin films have many interesting combination of properties such as high thermal conductivity, tunable band gap over wide range (1 - 4 eV), variable electrical conductivity and high wear resistance (>10000 times greater than a-Si:H) [200-202] . These properties are dependent not only on the method of deposition, but also on the deposition conditions. The conditions for film growth can vary from the concentration of the gaseous mixture in the plasma to substrate bias voltage and temperature. Therefore the electrical properties of DLC films prepared by RF and DC magnetron sputtering with DC substrate bias voltage are also subject to the process conditions of thin film growth. This implies that the conductance of DLC films will greatly depend on the presence of the  $sp^3$ ,  $sp^2$  and Hydrogen terminated clusters in the film. The results on the electrical properties of DLC thin films prepared by RF and DC magnetron sputtering with a floating DC substrate bias voltage are described and discussed in this and subsequent sections.

### **5.4.2. Current-Voltage (I-V) characteristics of DLC thin films**

The conductivity of DLC films is predominantly dependent on the process parameters such as; deposition process, rf. power, substrate temperature and bias voltage. In this study, the DLC films deposited under different substrate bias voltage, starting from -25 V to -100 V in steps of 25 V by RF and DC magnetron sputtering technique are investigated for electrical property variations with respect to the  $sp^3$ ,  $sp^2$  and H compositions present in the film.

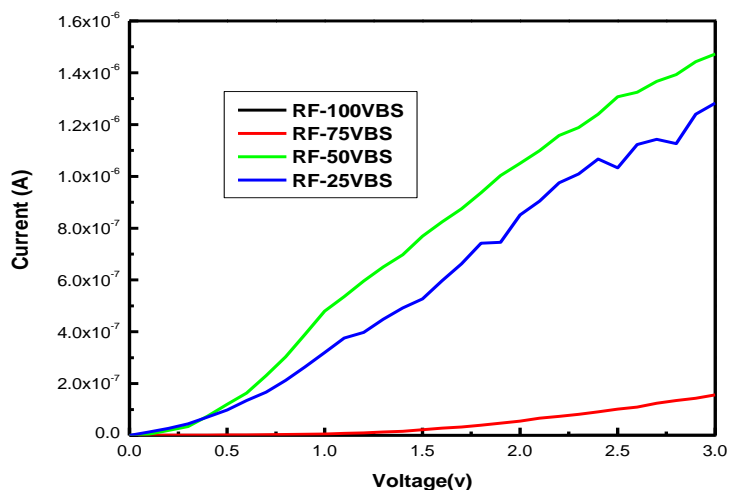


**Figure 5.8:** Current-Voltage characteristics of RF magnetron sputtering for various substrate bias voltages deposited DLC thin films (from -25 V to -100 V).

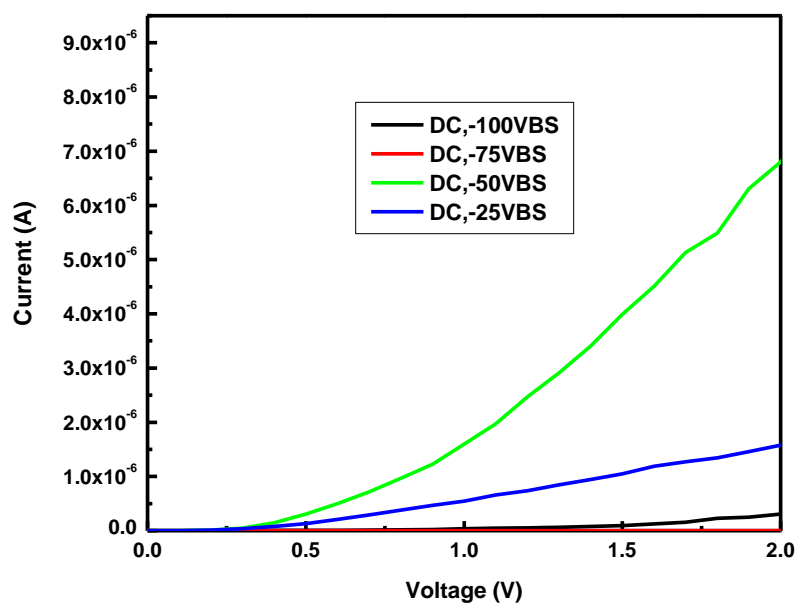


**Figure 5.9:** Current-Voltage characteristics of DC magnetron sputtering for various substrate bias voltages deposited DLC thin films (from -25 V to -100 V).

The current-voltage relationships of DLC thin films presented above show a similar trend for RF and DC magnetron sputtered films at various substrate bias voltages (Figures 5.8-5.9). In

general, all the I-V curves exhibit a non-Ohmic feature, which can be explained by tunnelling between conducting graphitic clusters in the film. The conductance decreases strongly when the substrate bias voltage increases. Therefore this clearly indicates that the DLC films become more  $sp^3$ -rich films with increasing substrate bias voltage. Despite the numerous excellent properties, the low conductance is not attractive for electronic applications. Moreover, DLC films show high residual stress that leads to poor adhesion to the substrate. The resistivity of a-C:H films is mainly dependent also on hydrogen content and the percentage of  $sp^3$  and  $sp^2$  bonds [153, 203]. The resistivity will increase with hydrogen content and the fraction of  $sp^3$  bonds [185]. Hydrogen plays an important role in the stabilization of C=C bonds from  $sp^2$  to  $sp^3$  due to the missing delocalized pi-electrons which are essential for high electrical conductivity. It is evident that a higher  $sp^2$ -content is responsible for the excellent conductivity. Raman spectroscopy has shown that the  $I_D/I_G$  ratio decreases with increasing substrate bias voltage, thus providing correlation between structural and electrical properties. This implied that the simultaneous increase in  $sp^3$ -content and  $T_{auc}$  gap correlates with the decrease of the conductivity. Furthermore DLC films deposited in a  $CH_4$ -Ar mixture have exhibited a Poole - Frenkel type conduction mechanism. This means that conduction occurs due to the thermal excitation of electron for traps into the conduction band of the insulator. By using the expression of the Van der Pauw method, the conductivity of DC and RF magnetron sputtered films grown on silicon substrate with average thicknesses of 61 nm and 117 nm, respectively was determined. The thicknesses were determined by X-ray reflectivity whilst the resistivity and the resistance were measured using the Van der Pauw technique, yielding results shown in the tables 5.9 and 5.10. From this data, it is evident that the sheet resistivity (resistance) increase strongly with the substrate bias voltage. Furthermore it is evident that RF sputtered films deposited at highest bias (-100 V), exhibit the highest sheet resistivity ( $131.43 \times 10^2 \Omega \text{ cm}$ ). This

is therefore indicative that the DLC film tends to be more diamond-like. The large value of sheet resistivity of the DLC film grown at -100V also correlates with the observed higher fraction of  $sp^3$  bonds from Raman data, which provides further evidence that the optical properties depend on the  $sp^2$  fraction and its clusters size [70].

Similar trends were also observed for DC sputtered films, however, the measured resistivity is less than the one obtained in RF sputtered films. Additionally, DC sputtered films tend to show more polymer-like carbon characteristics and there is a clear presence of more  $sp^2$  olefinic bonds.

**Table 5.9:** Electrical properties of RF sputtered DLC films at biased substrate voltage

DLC at biased substrate voltage, (V)	Slope of V/I ( $10^7$ V/A)	Sheet resistance ( $10^7$ $\Omega$ /sq.)	Resistivity ( $10^2$ $\Omega$ cm)
-25	0.23	1.04	0.95
-50	0.19	0.86	1.13
-75	3.24	14.68	17.18
-100	21.89	99.21	131.43

**Table 5.10:** Electrical properties of DLC prepared by DC magnetron sputtering biased substrate

DLC at Biased substrate voltage, (V)	Slope of V/I ( $10^7$ V/A)	Sheet resistance ( $10^7$ $\Omega$ /sq.)	Resistivity ( $10^2$ $\Omega$ cm)
-25	0.09	0.42	0.21
-50	0.23	1.04	0.54
-75	0.78	3.53	2.41
-100	2.90	13.14	9.64

### 5.5. X-ray photoelectron and Auger electron spectroscopy

X-ray photoelectron spectroscopy was carried out for the DLC thin films deposited at substrate bias voltages of -75 and -100 V since these films were more diamond-like carbon due to their high  $sp^3$  fractions.

For the DLC thin films prepared using RF magnetron sputtering at bias substrate voltages of -75 V and -100 V, the spectra were dominated by C1s peak at approximately 284.8 and 284.9 eV, respectively. In the spectra it is evident that there trace amounts of oxygen, nitrogen, sulphur and silicon corresponding to the surface impurities and also substrate contributions as shown in Figure 5.10 and 5.11. The most intense peak was carbon with 74.3 and 78.8 at. %, the next intense peak was oxygen with 13.7 and 11.6 atomic %, the third peak was silicon with 1.7 and 2.6 at. %, then nitrogen peak both are the same with 0.4 atomic % for -75 and -100V ,respectively. More C-C  $sp^3$  was observed in -100V than -75V that can be due to the dissociation hydrocarbon and ionization of argon.

The sulphur peak with 0.2 at. % was seen only in -75V shown in figure 5.10. The most intense peak constitutes C-C bonds at 284.8 and 284.9 eV corresponding to the  $sp^3$  fraction [204], the C-O bonds at 286.7 and 286.6 eV and the O-C=O at 288.8 and 288.9 eV, respectively. The second intense peak, oxygen and its bonds were O-(C, H) at 532.2 and 533.5 eV and O-(C, H, Si) at 533.6 and 533.5 eV respectively for -75 and -100V. The C-C bond represents completely the  $sp^3$  fraction as verified by the symmetry of the peak; this arises due to the limitation of the XPS resolution thus making the measurement insensitive to the  $sp^2$  bonds leading to an overestimated  $sp^3$  fraction as shown previously. Although the technique does not allow us to distinguish  $sp^2$  and  $sp^3$ , in this study, this was overcome by using the results of the D parameter obtained by XAES. The interpolation of parameter D for diamond C( $sp^3$ ) and graphite C( $sp^2$ ) enables for the

determination of the fraction of  $C(sp^3)/C(sp^2)$  content from the measured D parameter for any carbon material.

X-ray Photoelectron Spectroscopy was carried out for DLC thin films deposited at substrate bias voltages of -75 and -100V since these films were more diamond-like carbon due to their high  $sp^3$  fractions.

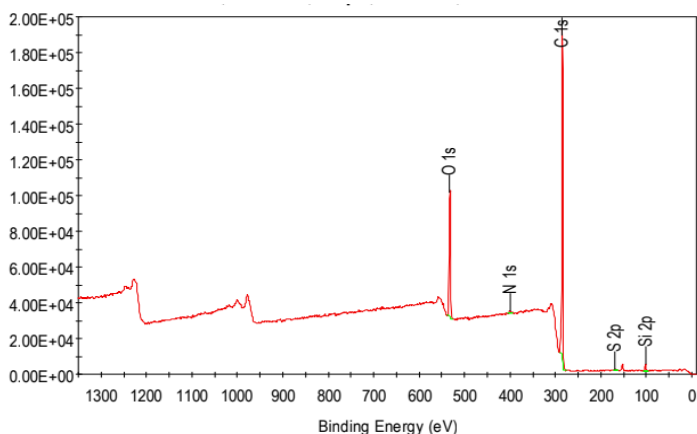


**Figure 5.10:** XPS survey spectrum of RF magnetron sputtering of DLC deposited on silicon with a bias -75V and power 200W.

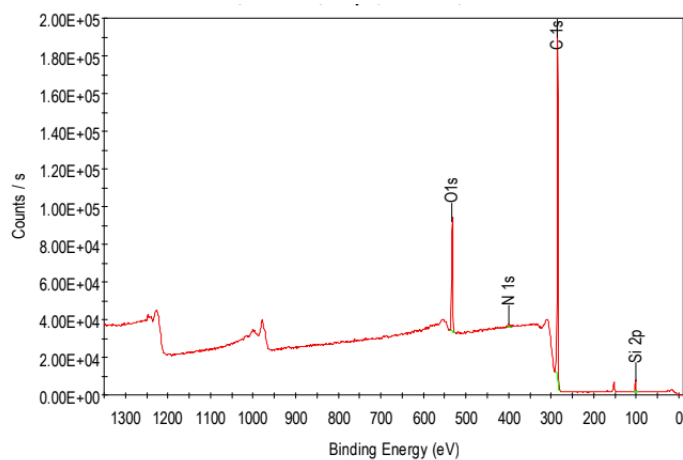


**Figure 5.11:** XPS survey spectrum of RF magnetron sputtering of DLC deposited on silicon bias -100 V and power 200W.

**Table 5.11:** XPS data showing composition and concentration of RF magnetron sputtering of DLC deposited on silicon bias -100 V and power 200W.

DLC	Peak BE	Atomic (%)
-75V	284.8	84.0
-100V	284.9	85.4

The analysis of the XPS induced CKLL Auger peak provides the resolution necessary to distinguish these bonding states in a semi-quantitative manner. The first derivative of CKLL spectra allow measurements of the D parameter obtained by measuring energy separation between maximum and minimum in the differential CKLL shown in Figure 5.12 and 5.13.

The  $sp^2$  fraction is related to the D-parameter. Thus the  $sp^3/sp^2$  ratio is obtained from the extrapolation of the straight line determined by two points such the position of diamond, D(0 %, 13) and the graphite G (100 %, 21) for a given D parameter.

The  $sp^2$ ,  $sp^3$  fractions and the ratio of  $sp^2/sp^3$  are obtained from the linear graph obtained by the reference values of the D parameters of diamond and graphite as shown in figure 5.12-13. Noting that the values of the D parameters in this present work is also overestimated as XAES is induced by XPS, thus the  $sp^2/sp^3$  ratios are significantly underestimated.

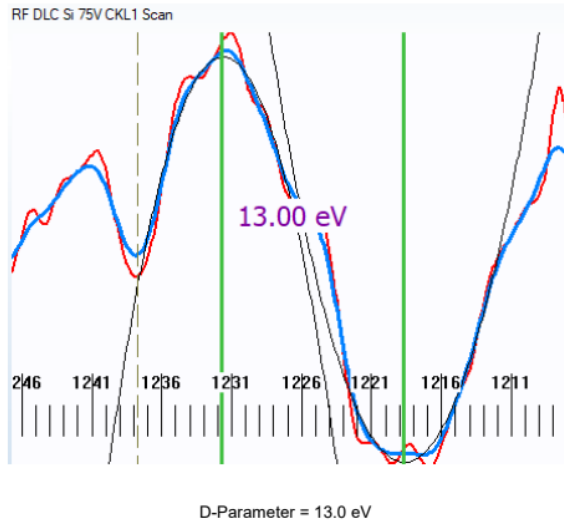


**Figure 5.12:** X-ray induced C KLL Auger peak of RF magnetron sputtering of DLC deposited on silicon bias -75 V and power 200W.

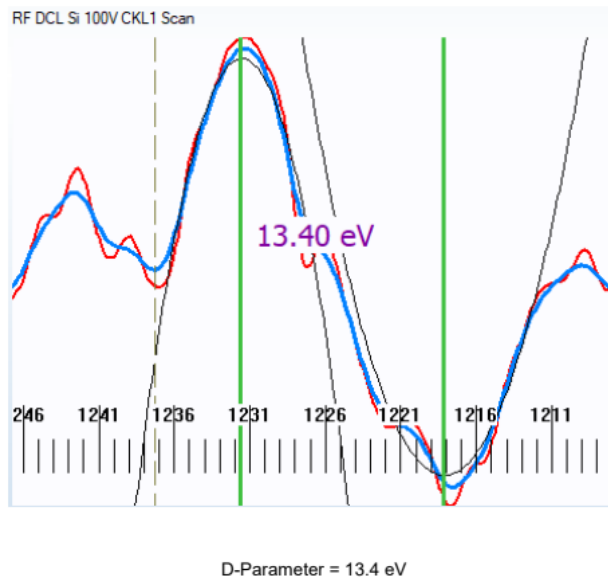


**Figure 5.13:** X-ray induced C KLL Auger peak of RF magnetron sputtering of DLC deposited on silicon bias -100 V and power 200W.

**Table 5.12:** Summary of the AES results of DLC films prepared by RF magnetron sputtering at bias voltages of -75 and -100V.

DLC/CH <sub>4</sub> /Ar	D-parameter(eV)	sp <sup>2</sup> fraction (%)
RF/DLC/Si/-75V	13.0	0
RF/DLC/Si/-100V	13.4	5

Similarly, for DC magnetron sputtering bias substrate for -75 and -100V, the spectra were also dominated by C1s peak at approximately 284.8 and 284.9 eV for the film deposited with bias voltages -75V and -100V, respectively. Also the presence of oxygen, nitrogen, sulphur and silicon has been observed on the surface of the films shown in Figures 5.14 and 5.15. The most intense peak observed was carbon with 83.5 and 80.9 atomic %, the third peak was silicon with 2.6 and 1.6 at. %, then nitrogen peak with 0.5 and 0.4 at. % for -75 and -100 V respectively. The sulphur peak with 0.1 at. % was seen only in -100 V shown in Figure 5.15. The most intense peak was carbon and its bonds were C-C sp<sup>3</sup> at 284.7 (FWHM=1.3 eV) and 284.7 eV (FWHM=1.2 eV), C-O at 286.6 and 286.6 eV, O-C=O at 288.7 and 288.9 eV respectively, for -75 and -100V. The second intense peak was oxygen and its bonds were O-(C, H) at 532.1 and 532.2 eV and O-(C,H,Si) at 533.3 and 533.5eV, respectively for -75 and -100V. The last one was organic silicon at 102 and 101.9 eV with concentrations of 2.6 and 1.7 atomic %, respectively for -75 and -100V. The presence of oxygen, sulphur and nitrogen can be due to the source contamination or air atmosphere in the chamber. The silicon seen in XPS is due the substrate uncovered at the edge.

The main challenge of the XPS technique in relation to DLC films was that it cannot detect the sp<sup>2</sup> bonds with sufficient sensitivity, thus the value of the sp<sup>3</sup> fraction will be overestimated as shown in table 5.13. The analysis of the XPS induced CKLL Auger peak can help distinguish

these bonding states in a semi-quantitative manner. The first derivative of CKLL spectra allows measurements of the D parameter obtained by measuring energy separation between maximum and minimum in the differential CKLL shown in Figure 5.16 and 5.17. The  $sp^2$ ,  $sp^3$  fraction and the ratio of  $sp^2/sp^3$  can be found by plotting a linear graph obtained by measuring the D parameter of diamond and graphite as references and the D parameter of the material locates between them. The lower extreme is diamond (100% of  $sp^3$ ) and higher extreme is graphite (100% of  $sp^2$ ). The  $sp^2$ ,  $sp^3$  fractions and the ratio of  $sp^2/sp^3$  are obtained from linear straight line [205, 206]. The XAES results show in table 5.14 that the  $sp^2$  fraction is underestimated and the ratio  $sp^3/sp^2$  is not reliable.

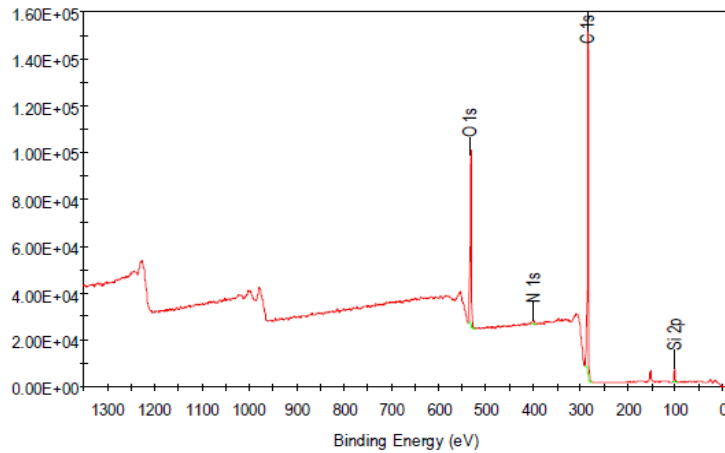


**Figure 5.14:** XPS survey spectrum of DC magnetron sputtering of DLC deposited on silicon bias -75V and power 200W.

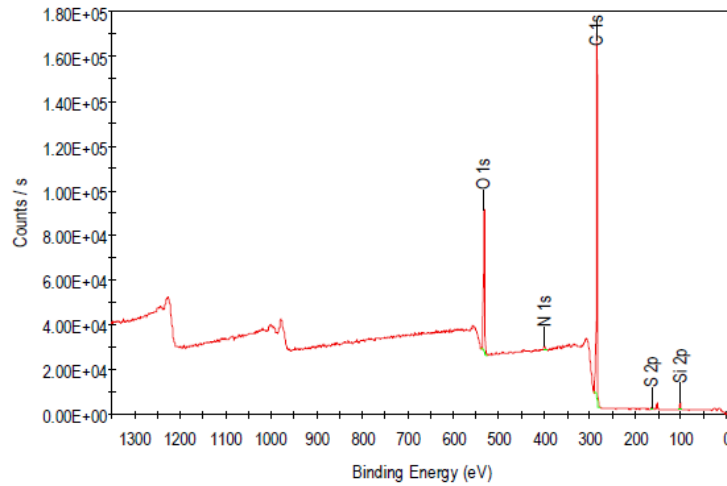


**Figure 5.15:** XPS survey spectrum of DC magnetron sputtering of DLC deposited on silicon at -100V and power 200W.

**Table 5.13:** XPS data on DC magnetron sputtered DLC on (001) Si at -100 V and 200W.

DLC	Peak BE	Atomic %
-75V	284.8	80.9
-100V	284.9	83.5

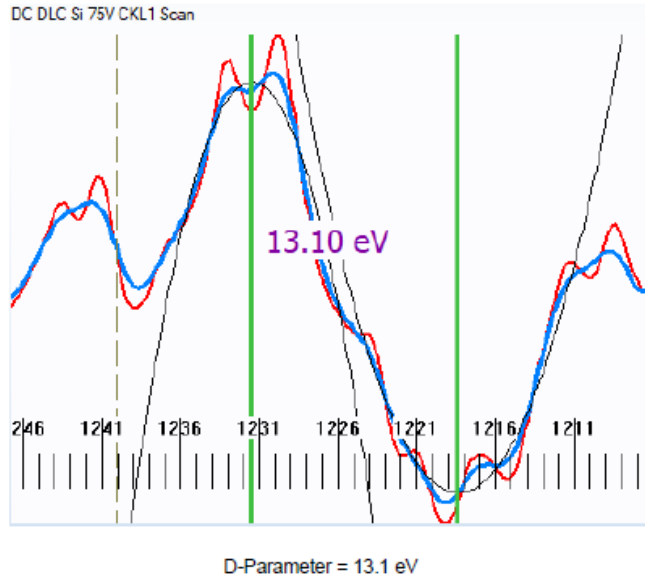


**Figure 5.16:** X-ray induced C KLL Auger peak of RF magnetron sputtering of DLC deposited on Si at -75 V and power 200W.

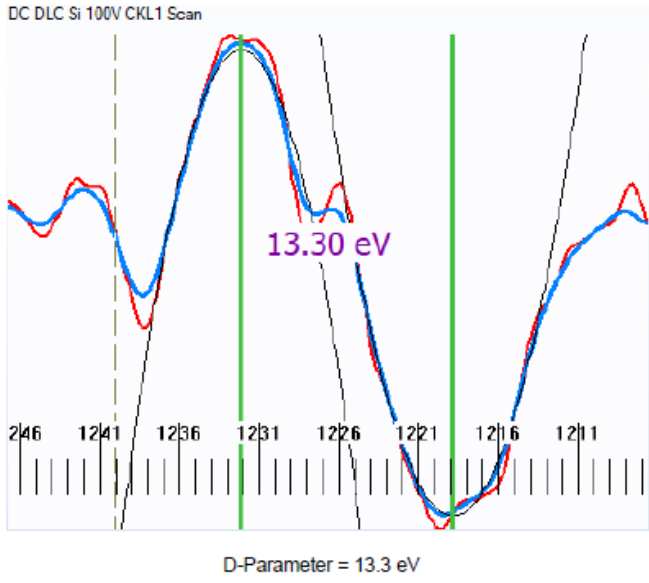


**Figure 5.17:** X-ray induced C KLL Auger peak of RF magnetron sputtering of DLC deposited on silicon bias -100V and power 200W.

**Table 5.14:** Summary of AES results of DC magnetron sputtered DLC: Si substrate biased at -75 V and -100 V.

DLC/CH <sub>4</sub> /Ar	D-parameter (eV)	sp <sup>2</sup> fraction (%)
DC/DLC/Si/-75V	13.10	1
DC/DLC/Si/-100V	13.30	4

## 5.6 Optical spectroscopy in the visible range

### 5.6.1 UV-Vis transmittance of biased DLC thin films on glass

The UV-Vis transmission spectra of DLC thin films on SiO<sub>2</sub> at various substrate bias voltages (-25 to -100 V) are shown in Figure 5.18. The dependence of transmittance on the optical constants of the glass substrates is decoupled by the use a blank glass substrate on the reference beam optical path. Additionally the films thickness has been determined for all to decouple the optical constants from the optical density. Thus the transmittance (%) is attributed solely to the intrinsic properties of the DLC film deposited at various substrate bias voltages. The highest transmittance is observed for films deposited with a bias voltage of -75V, and this is in agreement with the XAES data which confirm the presence of more sp<sup>3</sup> fractions in the films. The dispersion in the absorption coefficient is extracted using Beer's law and Fermi-golden rules for Interband transitions as shown in Figure 5.19. This figure is a plot of  $(\alpha h\nu)^{1/2}$  versus  $(h\nu)$  of DLC films prepared at different bias voltages and it is extrapolated to give the respective Tauc gaps. Additionally the presence of trap states due to the amorphous nature of DLC are observed as the non- zero absorption at cut-off energy of the Tauc gap.

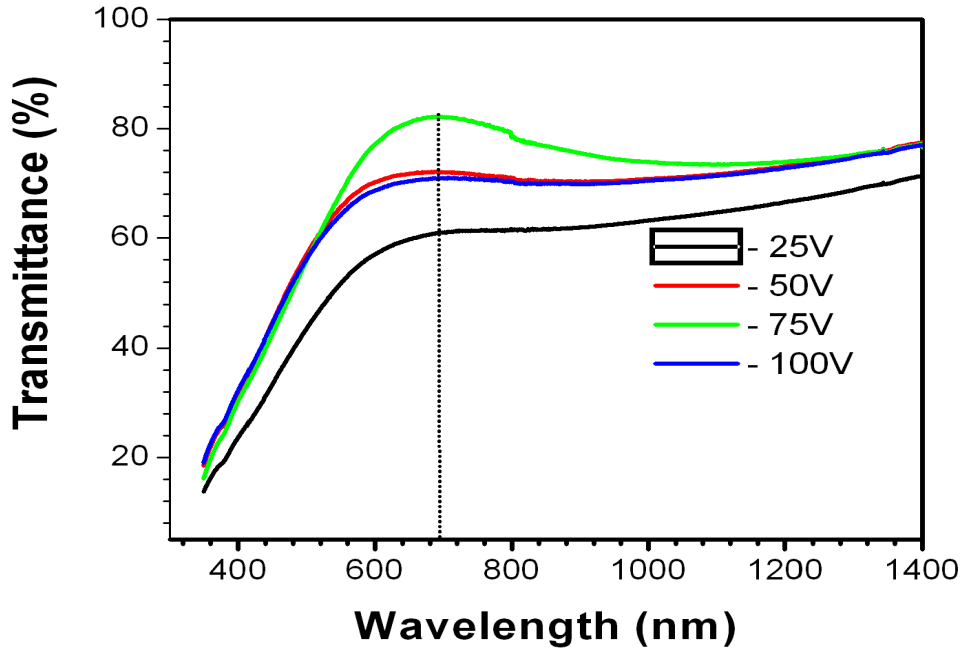


**Figure 5.18:** Transmittance spectrum of biased DLC thin films on glass.

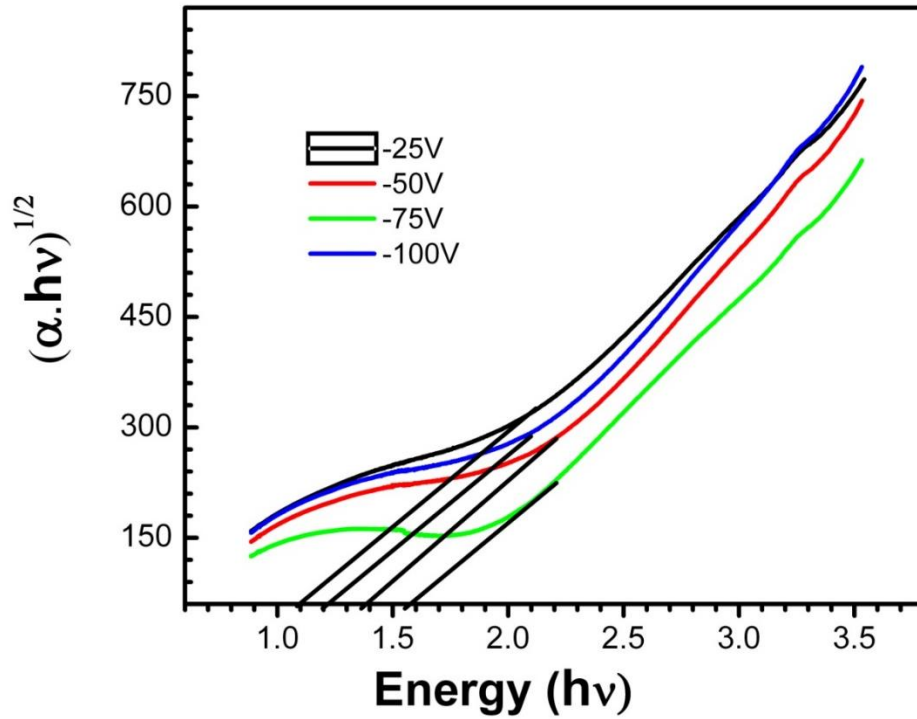


**Figure 5.19:** The plot of  $(\alpha h\nu)^{1/2}$  versus  $h\nu$  for DLC thin films on glass.

**Table 5.15:** Optical and structural properties of DLC thin films.

DLC films	Transmission (%)	Tauc gap PL (eV)	Cluster size (Å)
-25V	58	1.10	10.95
-50 V	69	1.37	10.18
-75V	80	1.56	9.05
-100 V	66	1.20	9.81

The linear extrapolation from the straight line to the energy axis has given the following Tauc gaps ( $E_g$ ) of 1.10, 1.37, 1.56 and 1.20 eV corresponding to substrate bias voltages of -25 V, -50 V, -75 V and -100 V, respectively as shown in figure 5.19. It is evident from the correlation between substrate bias voltage to the  $I_D/I_G$  ratios and the fraction of the  $sp^3$  bonds that the Tauc-gap increases with increasing  $sp^3$  fractions corresponding to more diamond - like films. This is plausible since more diamond like carbon films tend to be optically transparent and have larger Tauc gaps. Furthermore, the cluster sizes of these films are usually less than 20 Å corroborating the values appearing in Table 5.15. On the basis of these results, it can be postulated that the properties of the DLC films fabricated in this work correspond to those of diamond-like carbon a-C:H (DLCH) whose optical gaps appear in the range 1- 2 eV [207]. The Tauc gap is mainly determined by the C  $sp^2$  hybridization clusters embedded in the amorphous carbon medium [176]. Thus the increase in the Tauc gap is expected for decreased fraction of  $sp^2$  cluster sizes as shown in Table 5.15.

### **5.6.2 Fourier Transform Infrared spectroscopy of DLC films: Transmission mode**

The infrared spectra (IR) of DLC films deposited by RF and DC magnetron sputtering are shown in Figures 5.20 - 5.21 for the range of excitation of 2800 to 3000  $cm^{-1}$ . These transmittance spectra

represent DLC films grown under diverse bias voltages (-25 V, -50 V, -75 V, -100 V). In Figure 5.20, we determined the following vibration frequencies: the band between 2800  $\text{cm}^{-1}$  and 3000  $\text{cm}^{-1}$  was attributed to stretching vibration of  $\text{CH}_n$  groups; all the samples showed the  $\text{sp}^3$  symmetric and asymmetric stretching peaks corresponding to  $\text{CH}_2$  at about 2850 and 2920  $\text{cm}^{-1}$ . The spectra also exhibited the  $\text{sp}^3$  symmetric and antisymmetric small peaks for  $\text{CH}_3$  at about 2870 and 2960  $\text{cm}^{-1}$ . These peaks have been reported for diamond samples deposited at high  $\text{CH}_4$  concentration and in DLC films[169] in agreement with our data. The transmission (%) was also observe to increase with the substrate bias voltage for both DC and RF sputtered films. It is not obvious that the intensities of absorption of C-H vibrations varied with the negative bias potential from -25V to -100 V.

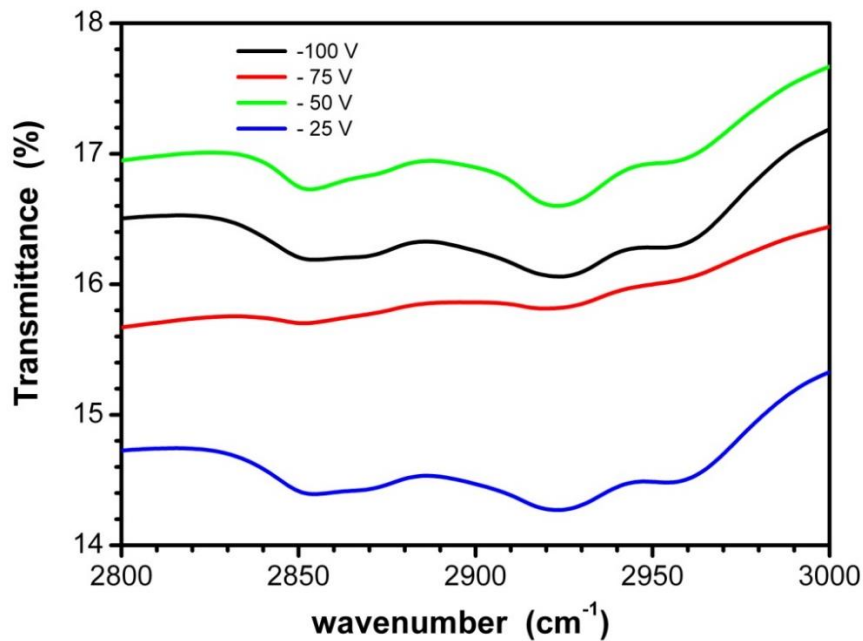


**Figure 5.20:** Transmittance spectrum of biased DC sputtered DLC thin films.

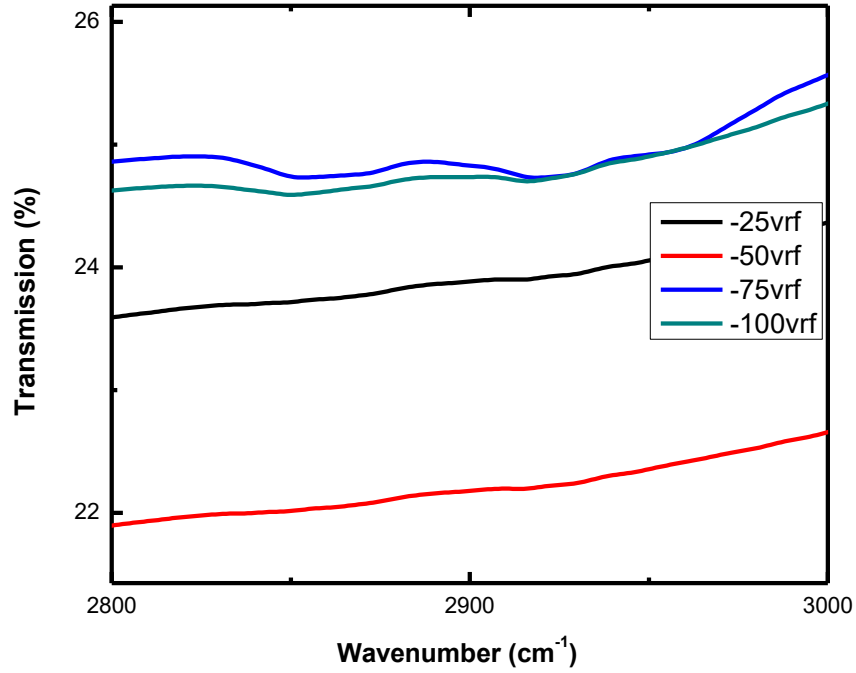


**Figure 5.21:** Transmission versus wavenumber for RF magnetron sputtering in between (2800-3000  $\text{cm}^{-1}$ )

In the FTIR spectra of both figures above, the  $\text{sp}^2$   $\text{CH}_2$  modes are not clearly evident, or at the very least, are weakly showing. Hence, our results have shown that the bonding structures between carbon and hydrogen in a-C:H films consist predominantly of  $\text{sp}^3$  bonds below  $2960 \text{ cm}^{-1}$ . However the role of hydrogen terminated in the films and its concentration cannot be ruled out in the determination and their subsequent modification of the mechanical properties of DLC thin film. For this reason we converted the transmittance (T) data in absorbance coefficient ( $\alpha$ ) using the expression

$$\alpha = \frac{1}{d} \ln \frac{1}{T} \quad (5.3)$$

where  $d$  is a thickness of the DLC thin films expressed in nm.

In IR, the spectrum of the C-H bond stretching modes around  $2900\text{ cm}^{-1}$  is measured after background subtraction. At the vicinity of the  $2900\text{ cm}^{-1}$  band are many stretching modes that originate from  $\text{sp}^2$  or  $\text{sp}^3$  C-H<sub>n</sub> (n = 1, 2, 3) depending on the film preparation conditions. By deconvoluting these modes, the ratio of  $\text{sp}^2/\text{sp}^3$  can be obtained. Additionally, the number of H atoms per unit area  $n_H$  can be determined from the product of the ratio of absorption strength,  $A_s$  and the integrated C-H band intensity in the limit of  $3000 - 2800\text{ cm}^{-1}$ . This product is normalized by  $2900\text{ cm}^{-1}$ . Thus the density of hydrogen in the select films was determined in the form

$$n_H = \frac{A_s}{2900} \int_{2800}^{3000} \alpha(\nu) d\nu \quad (5.4)$$

The coefficient,  $A_s = 0.85 \times 10^{21}\text{ cm}^{-2}$  in the integral was adopted from the average value of the paraffin standard due to Erz *et al.* [180] and that from Gheeraert *et al.* [181]. The CH band consists of four peaks. The  $\text{sp}^3$  symmetric and asymmetric stretching peaks corresponding to  $\text{CH}_2$  at about  $2850$  and  $2920\text{ cm}^{-1}$ . The spectra also exhibit the  $\text{sp}^3$  antisymmetric for  $\text{CH}_3$  at about  $2960\text{ cm}^{-1}$  and the  $\text{sp}^2$  olefinic at about  $2980\text{ cm}^{-1}$  as shown in the tables 5.16 and 5.17. All these peaks are obtained by fitting the absorbance spectra as shown in figure 5.22-27 with four Gaussians. The hydrogen concentration values calculated by eqn. (5.4) show similar trends as those determined by Raman spectroscopy.

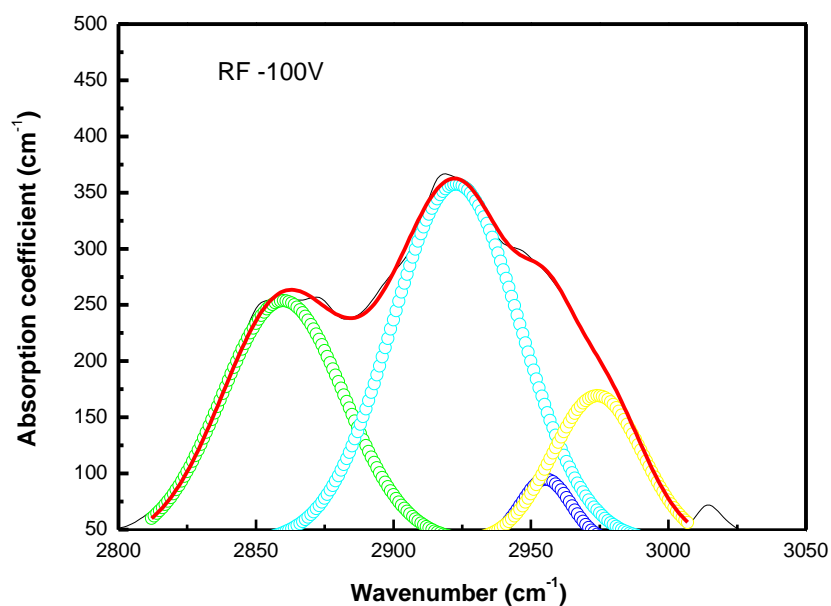


**Figure 5.22:** FTIR spectrum of RF sputtered DLC films showing the CH<sub>2</sub> symmetric stretching peaks at ~ 2850 cm<sup>-1</sup>. These films are deposited at -100V bias substrate.

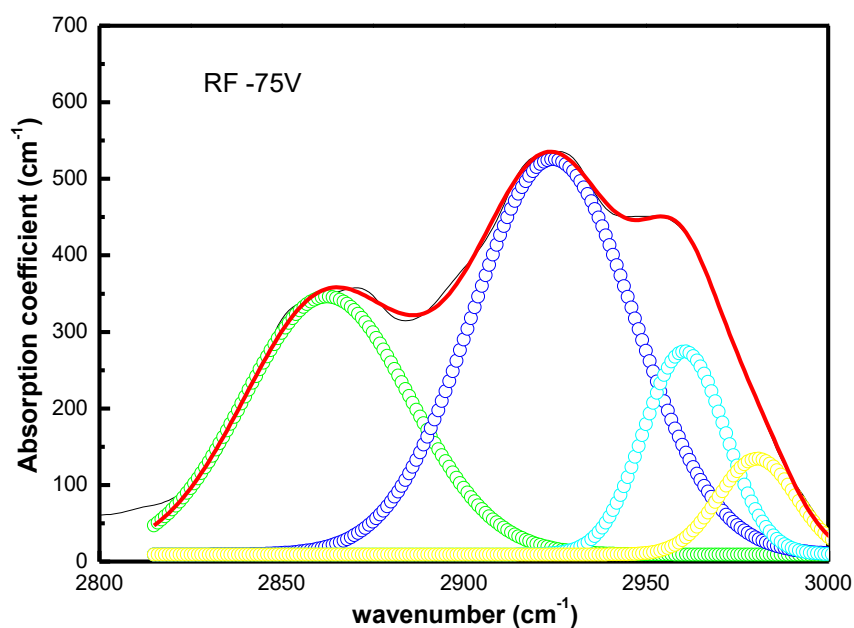


**Figure 5.23:** FTIR spectrum showing the CH<sub>2</sub> symmetric stretching peaks at ~ 2850 cm<sup>-1</sup>, characteristic of DLC films deposited at -75 V using RF magnetron sputtering.

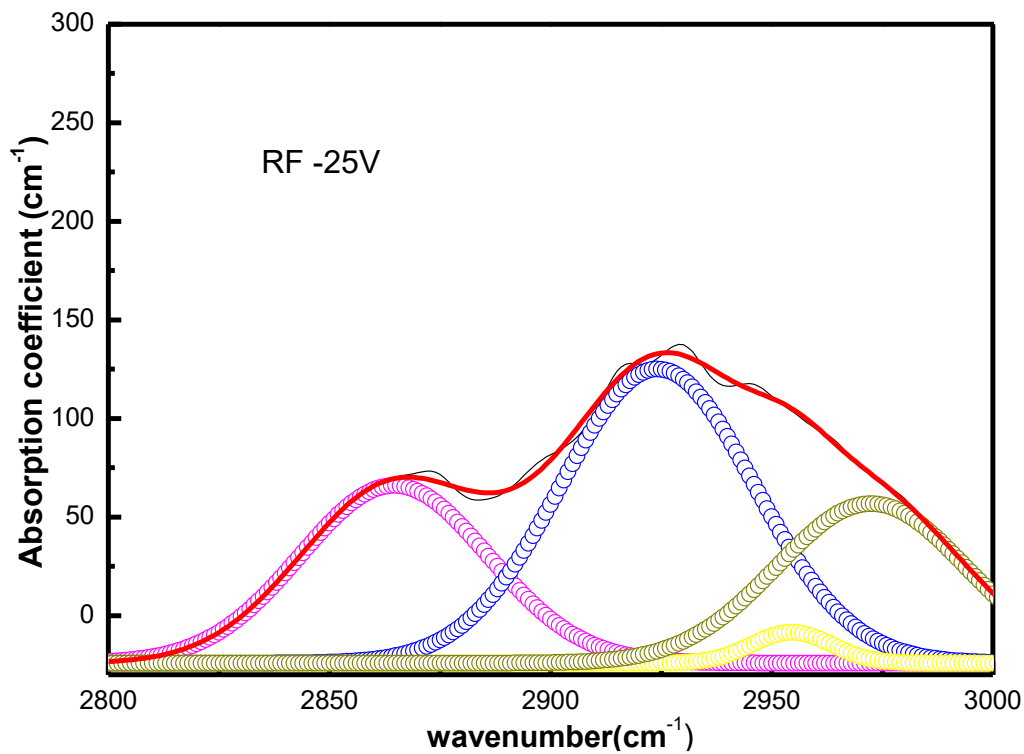


**Figure 5.24:** FTIR spectrum showing the CH<sub>2</sub> symmetric stretching peaks at ~ 2850 cm<sup>-1</sup>, characteristic of DLC films deposited at -25 V.

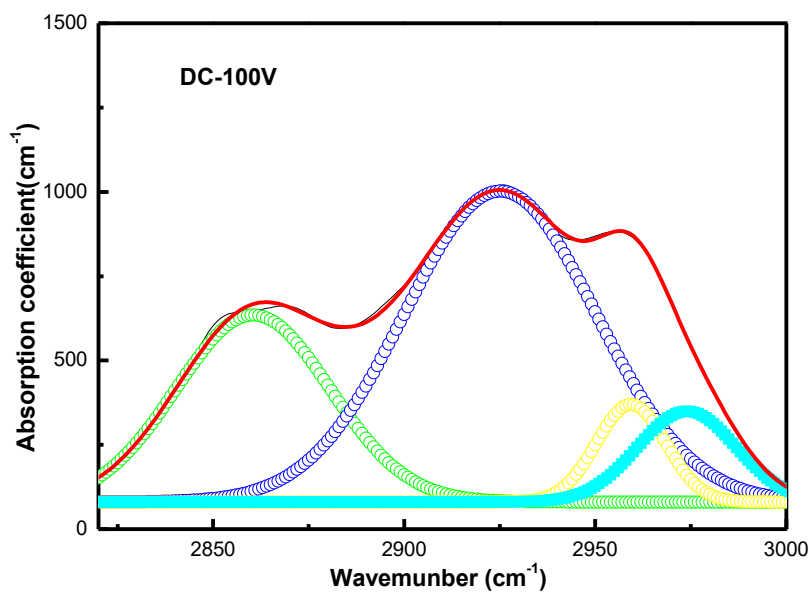


**Figure 5.25:** FTIR absorbance spectrum exhibiting the CH<sub>2</sub> symmetric stretching peaks at ~ 2850 cm<sup>-1</sup>, characteristic of DC magnetron sputtered DLC films deposited at -100 V bias voltage.

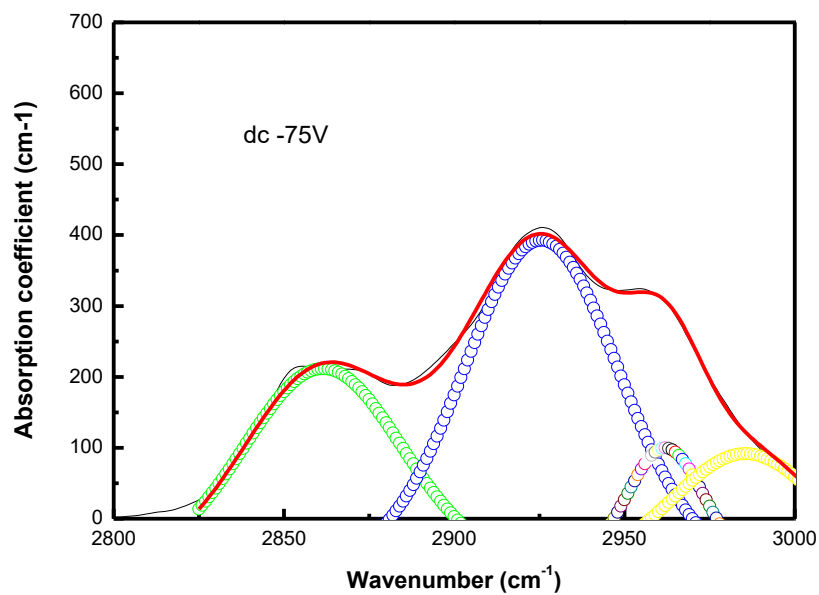


**Figure 5.26:** FTIR spectra of absorbance of DC magnetron sputtering showing the CH<sub>2</sub> symmetric stretching peaks at ~ 2850 cm<sup>-1</sup>, characteristic of DLC films deposited at -75V.

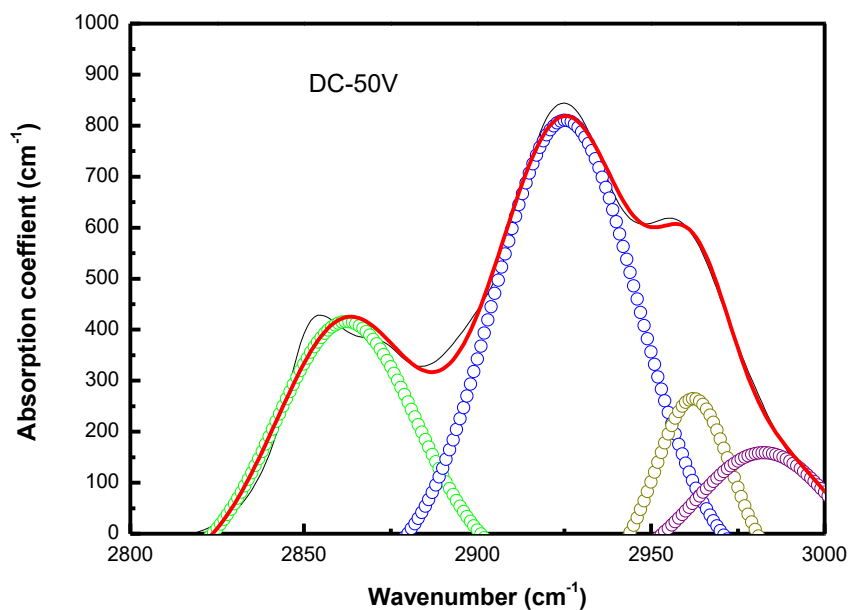


**Figure 5.27:** FTIR spectra of absorbance of DC magnetron sputtering showing the CH<sub>2</sub> symmetric stretching peaks at ~ 2850 cm<sup>-1</sup>, characteristic of DLC films deposited at -50V biased substrate.

**Table 5.16:** C-H bonds and hydrogen density of RF sputtered DLC films on biased substrate.

bias substrate, (V)	sp <sup>3</sup> -CH <sub>2</sub> (cm <sup>-1</sup> )	sp <sup>3</sup> -CH <sub>3</sub> (cm <sup>-1</sup> )	sp <sup>3</sup> -CH <sub>2</sub> (cm <sup>-1</sup> )	sp <sup>2</sup> -CH <sub>2</sub> (cm <sup>-1</sup> )	Hydrogen density (10 <sup>21</sup> cm <sup>-2</sup> )
-25	2864.66	2924.25	2954.51	2972.54	30.32
-75	2862.54	2924.48	2960.58	2980.61	27.32
-100	2859.88	2922.76	2955.42	2974.27	17.32

**Table 5.17:** C-H bonds, hydrogen density and the ratio of  $sp^3/sp^2$  for DC sputtered DLC films on biased substrate.

bias substrate (V)	$sp^3$ -CH <sub>2</sub> (cm <sup>-1</sup> )	$sp^3$ -CH <sub>3</sub> (cm <sup>-1</sup> )	$sp^3$ -CH <sub>2</sub> (cm <sup>-1</sup> )	$sp^2$ -CH <sub>2</sub> (cm <sup>-1</sup> )	Hydrogen density (10 <sup>21</sup> cm <sup>-2</sup> )
-50	2862.29	2925.29	2962.21	2982.51	43.18
-75	2861.50	2925.59	2962.00	2985.60	25.46
-100	2860.51	2925.17	2959.41	2973.98	20.31

### 5.7 Surface Brillouin scattering

Surface Brillouin scattering is an excellent tool for probing the dynamics of surface acoustic excitations in thin film materials. The analysis of the propagations of the acoustic waves enable the determination of the elastic properties of materials. Surface Brillouin scattering is based on the inelastic scattering of light by dynamic corrugations (acoustic phonons) on the surface leading to the measurement of the frequency shift of incident light. This is the ripple mechanism of inelastic scattering. In the case of thin films, the nature of the acoustic propagations is dependent on the elastic and physical properties of the film and the substrate. Thus dependent on the contrast of the elastic constants and mass density of the film and the substrate, two configurations of acoustic propagations can be encountered. Thus for the slow- on- fast film substrate configuration, numerous acoustic propagations are present in the film namely the true surface acoustic wave, Rayleigh Wave and the guided modes also called Sezawa waves. These discrete modes propagate in the transonic region. On the other hand, a fast- on- slow configuration is characterized by the propagation of the Rayleigh wave. Typical spectra of a slow- on- fast configuration measured at a fixed incidence angle using backscattering geometry is presented in Figure 5.7.3 It is evident that the scattering intensities show the frequency doublets, namely the Stokes – anti Stokes symmetry characteristic of phonon excitations. In the present work thin films of thickness in the range of 117

nm corresponding to  $k/d$  in the range of 2 to 5 have been investigated for elastic constant determination.

The surface Brillouin scattering (SBS) spectra for DLC thin films grown at various substrate bias voltages are presented in Figure 5.28 and 5.29 for the DC and RF magnetron sputtering methods, respectively.

The backscattering geometry was used in the present work to investigate modes with their acoustic wave-vector component parallel to the surface. The phonon velocities are obtained by dividing the measured mode frequencies by the component  $q_{\parallel}$  of wave-vector parallel to the surface using the expression of the equation (4.2).

The variation of the phase velocity of the acoustic phonons with the non-dimensionless parameter has yielded the phonon velocity dispersion for films deposited by RF magnetron sputtering as shown in Figure 5.30.

The extraction of the elastic constants has been solved from the inverse problem using the Elastodynamic Greens function approach, in which the following mass densities  $\rho = 2.35 \text{ g/cm}^3$  has been used for the DLC films on (001) Si prepared by RF magnetron sputtering. Such thin films are isotropic at wavelength scale (hundreds of nanometres for SBS) and thus the elastic constants can be completely determined by only independent elastic constants (e.g. Young's modulus  $E$  and shear modulus  $G$ ).

Since the film is amorphous and hence isotropic only two independent elements of the elastic tensor, usually,  $C_{11}$  and  $C_{44}$ , can be determined by the equations in the section (4.8).

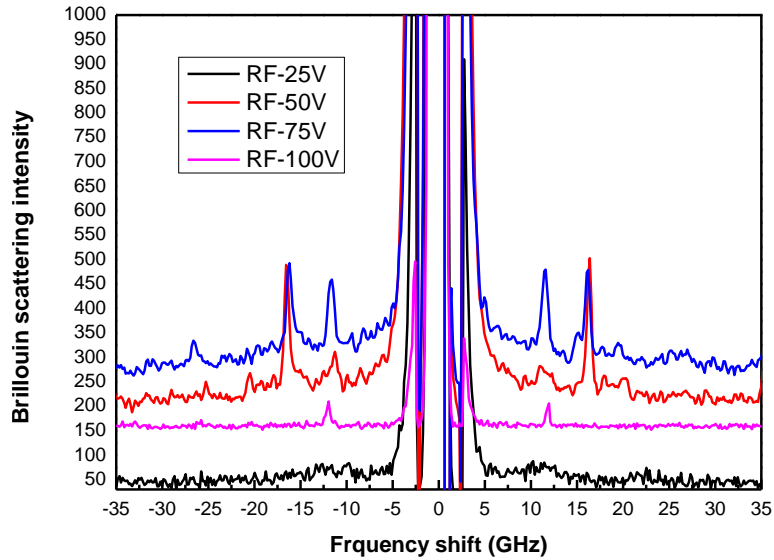


**Figure 5.28:** Surface Brillouin scattering spectra of RF sputtered films measured at 70° incidence.

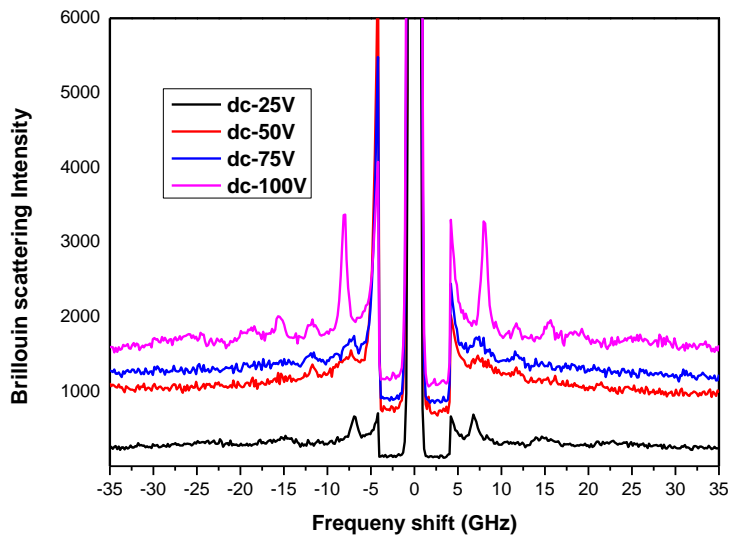


**Figure 5.29:** Surface Brillouin scattering spectra of DC sputtered films measured at 70° incidence.

The SBS spectra of the RF sputtered DLC thin films exhibit the loading of the film with increasing substrate bias due to the increase in the Rayleigh Velocity. This trend is also observed for DC sputtered films and it could be attributed to the increased fraction of the  $sp^3$  bonding fractions.

**Table 5.18:** Rayleigh velocities of biased RF and DC sputtered films.

Substrate Bias (V)	RF Magnetron Sputtered DLC	DC Magnetron Sputtered DLC
	Rayleigh velocity (m/s)	Rayleigh velocity (m/s)
-25	3070	1860
-50	3084	2012
-75	3170	1968
-100	3283	2275

Thus subsequent measurements of SBS spectra with varying incident angles and film thickness were carried out on RF and DC magnetron sputtered samples that exhibited the highest Rayleigh velocity with varying substrate bias voltage. From the spectra of figs. 5.28 and 5.29 this was observed for DLC films fabricated at -100V substrate bias.

The backscattering geometry was used in the present work to investigate the dispersion curves of the phonon modes with acoustic wave-vector component parallel to the surface. The variation of the phase velocity of the acoustic phonons with the non-dimensionless parameter  $k_{||}d$  yields the phonon velocity dispersion for films deposited by RF and DC magnetron sputtering. The extraction of the elastic constants has been solved using the inverse problem on the phonon dispersion curves by invoking the Elastodynamic Greens function approach, in which the following mass densities;  $\rho = 2.35 \text{ g/cm}^3$  and  $2.55 \text{ g/cm}^3$  have been used for the DLC films on (001)Si prepared by RF magnetron sputtering.

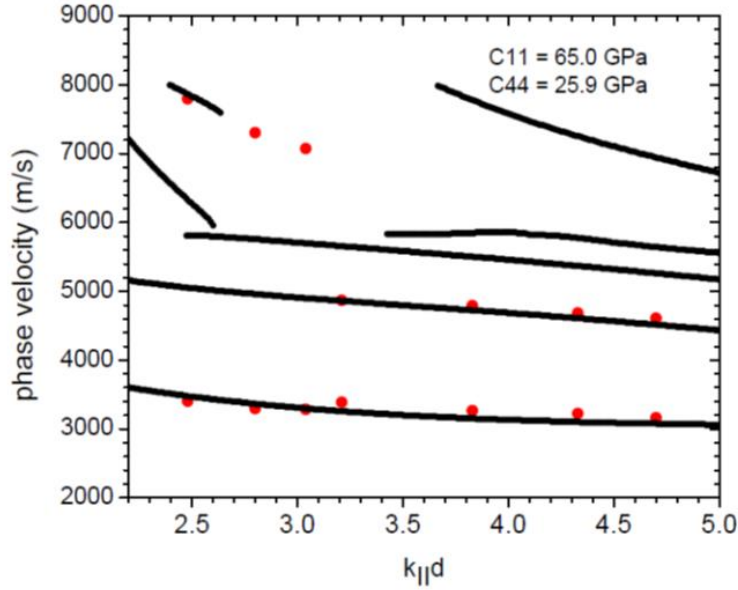


**Figure 5.30:** Dispersion curve for RF- sputtered DLC films grown on Si substrate bias at -100V.

Such thin films are isotropic at wavelength scale (hundreds of nanometres for SBS) and thus the elastic constants can be completely determined by only two independent elastic constants (e.g. Young's modulus  $E$  and shear modulus  $G$ ). Since the film is amorphous and hence isotropic only two independent elements of the elastic tensor, usually,  $C_{11}$  and  $C_{44}$ , can be determined.

**Table 5.19:** Elastic constants and mechanical moduli of DLC films.

Bias voltage (V)	Rayleigh velocity (m/s)	$C_{44}$ (= $G$ ) (GPa)	$C_{11}$ (GPa)	$E$ (GPa)	$B$ (GPa)
RF Magnetron Sputtered DLC films					
-100	3283	25.9	65.0	62	33
DC Magnetron Sputtered DLC films					
-100	2274.46	11.47	26	20.4	15.3

The determination of the uncertainty of the elastic constants is been performed using the formalism discussed in chapter 4. The elliptical plots of fig. 5.31 determine the uncertainty in the elastic constants to within 7.7 and 1.2 % for  $C_{11}$  and  $C_{44}$ , respectively.

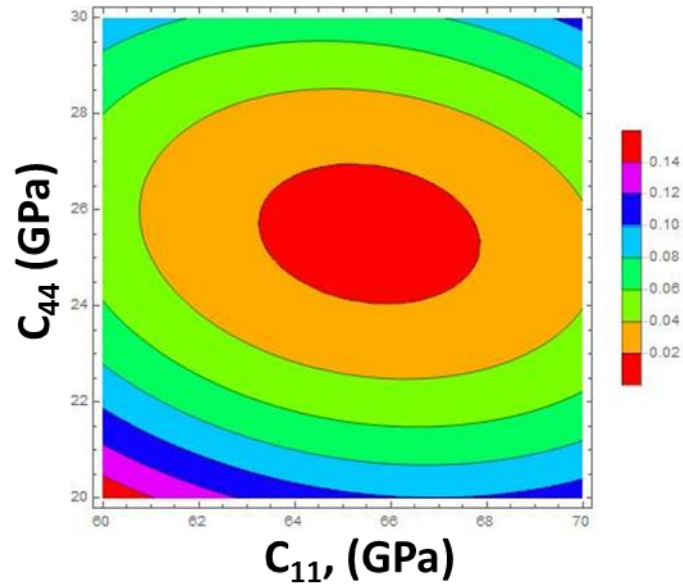


**Figure 5.31** Elliptical plots to determine the best fit elastic constants and associated error estimates for RF sputtered DLC thin films grown on (001)Si at -100 V. The elastic constants have been refined to  $C_{11} = 65.0 \pm 5.0$  GPa and  $C_{44} = 25.9 \pm 3.0$  GPa.

The fitting of the dispersion spectra (not shown here) of the DC sputtered DLC films did not yield a suitable fit for the two sets of the elastic constants, thus the determination of the elastic constants have been carried out using approximation transverse and longitudinal velocities of bulk.

## Results and Discussion

The phonon frequency and phase velocity are exhibiting changes certainly a result of microstructural changes of the films. Depending on the deposition techniques and conditions used for the preparation of the DLC films, the films are either graphite-like ( $RW \sim 2765$  m/s) i.e. consisting more  $sp^2$  – bonded carbon, or contain both  $sp^3$  – and  $sp^2$  hybridised carbon with more hydrogen passivating dangling bonds. The latter films may be mechanically soft with a relatively large optical band gap of 2 -3 eV, known as polymer-like films, or hard and dense with an optical band gap of 1 – 1.5 eV. The Rayleigh mode of diamond-like amorphous, hydrogenated DLC films prepared by RF magnetron sputtering bias voltage at -100V is  $\sim 3300$  m/s, while hydrogenated

DLC films prepared by DC magnetron sputtering bias voltage at -100V is ~2275 m/s .This observation suggests that the Rayleigh velocity for RF magnetron sputtering is higher than that one obtained for the DC magnetron sputtered films for the same substrate bias voltage. In this study, the biased DLC thin film properties have dependence on the ion energy normally required by condensing carbon atoms, hence a gradual optimisation of elastic moduli was observed at -100V directly relatable to the maximum  $sp^3/sp^2$  ratio and lowest hydrogen content of the RF magnetron sputtered films. The bias voltage of the substrate has the same effect on the mobility and adsorption of the atoms as an increase in the substrate temperature, so when the bias voltage is increased (or temperature increased), according to the SZM model, it would result in denser thin films with a high degree of crystallinity. In addition, the bias voltage also influences the mechanical properties of thin films; for example, with a voltage ( $\geq 100V$ ) applied to the substrate, the deformation of the lattice increases, causing high residual effects and low adherence between the substrate and the film.

As indicated in section 5.4, the substrate biasing also increases the hydrogen content in the DLC films up to -75 V, thus the increase of polymeric carbon content film beyond which (at -100 V) a decrease in the amount of hydrogen occurs. The elastic moduli presents a similar result in that there is no significant change for Young's moduli when the bias is ranged from -50 V to -100 V, even though the thickness of the DLC thin films deposited at -100V is about 110 nm compared to 146 nm for films deposited at -75 V. It is likely the main reason for the lower elastic moduli (~ 17 GPa - 20 GPa) compared to that of RF sputtered films (~ 47 - 62 GPa) in Table 5.18, is directly linked to the increase of polymeric carbon content in the DC films as evidenced by the Rayleigh velocities ranging between 1860 and 2274 m/s, characteristic of polymer-like films. Additionally, it is evident from the correlation between the substrate bias voltage to the  $I_D/I_G$  ratios

and the fraction of the  $sp^3$  bonds that the Tauc - gap increases with increasing  $sp^3$  fractions corresponding to more diamond - like films.

## 5.8 Conclusion

The initial work resulted in establishing the optimum condition of 50% composition of  $CH_4$ -Ar concentration for the room temperature sputtered films, a condition that was observed for both the RF and DC sputtered films. In this study, DLC films have been successfully deposited onto silicon and glass substrates at room temperature via a graphite using DC and the radio frequency (RF) magnetron sputtering. The structural evolution of DLC films as a function of the deposition conditions (such the substrate bias voltage, the pressure, power etc.) was also studied using Raman and UV-Visible spectra where it was observed that increasing substrate bias voltage leads to the reduction of the cluster size of  $sp^2$  rings, whilst increasing the  $sp^2$  chains and the  $sp^3$  bonds. The optical performance of the coatings, characterised by transmittance could be further improved by optimizing deposition conditions of the DLC thin films. The results of Raman analysis suggested that the  $sp^3$  phase that is related to the disordered  $sp^2$  phase may attain its maximum content at a bias voltage of -100 V and -75 V on films grown silicon and glass substrate, respectively. In addition, the results of electrical conductance, FTIR and XPS analyses have revealed that a bias voltage of -100V is more favourable to  $sp^3$  phase formation under the current experimental conditions. The FTIR spectra results confirmed that the films are indeed diamond-like carbon by the virtue of the presence of absorption bands such as  $sp^3$  C-H<sub>2</sub> symmetry and asymmetry ( 2850 and 2920  $cm^{-1}$  ) and  $sp^3$  C-H<sub>3</sub> asymmetry (at 2950  $cm^{-1}$ ). The investigations reported here show the importance of the substrate bias in changing the properties of the films. In addition, the results of X-ray photoemission spectroscopy and its induced X-ray Auger electron spectroscopy analyses

reveal that a bias voltage of -75V and -100V are more favourable to  $sp^3$  phase formation under the present conditions. In addition, there is significant agreement between these results and results obtained with other techniques such as Raman spectroscopy, I-V characteristics, Surface Brillouin scattering and UV-Visible spectroscopy. These results are explained in terms of the sub-plantation model for DLC growth, wherein the consistency of the results indicate the importance of ion energy and hence negative bias voltage in controlling the properties of coatings. At the end, the substrate bias improved the mechanical and optical properties of the RF sputtered films, whilst the DC sputtered films were negatively affected by the increased amount of hydrogen. The correlation between the microstructure and physical properties has thus been established.

## **Chapter 6: Conclusion and future work**

Hard diamond like carbon films have been deposited by RF magnetron sputtering using the optimum condition of 50% of CH<sub>4</sub>-Ar concentration at room temperature. In addition, the silicon substrate was biased from -25 to -100 V with the step of 25V. Structural investigations reported here indicate that the bonding characteristics, electrical and mechanical properties are strongly dependent on the substrate bias during deposition. The characterization results show that for the DLC film deposited at a substrate bias of -100 V for RF, the resistivity, the elastic constants and band gap reach maximum values. The investigations reported here show the importance of the substrate bias and the technique used in tuning the properties of the films. The RF magnetron sputtering bias voltage with respect to DC is the best technique for good quality diamond-like carbon films. The changes of the phonon phase velocity are related to the microstructural changes of the films, and it is demonstrated in the study that the mechanical strength of the *as-deposited* films flattens an active biasing the substrate necessity of the films in order to further improve the mechanical strength. The elastic constants of the amorphous carbon films prepared for this study have been evaluated using surface Brillouin scattering technique and provide the baseline data for further work to improve the elasticity of DLC films. This study clearly shows the significance of substrate bias in controlling the opto- mechanical properties of DLC films.

### **Suggestions for future work**

Doping can be a further possibility to improve the quality of DLC thin films.

Doping of DLC thin films with transition metals or single group IV elements has been posited as a possible approach towards the enhancement of the sp<sup>3</sup> fraction. However there has been no detailed study on the subsequent modifications in the mechanical properties of DLC thin films.

Additionally the effect of substrate temperature on the nucleation and formation of  $sp^3$  bonding fractions in DLC thin films should be investigated with the attendant property correlation.

Lastly the disparity between the Raman spectroscopy data and the XPS results requires detailed investigation through lateral XPS mapping of select DLC thin films having varying fractions of the  $sp^2$  and  $sp^3$  bonds. This investigation should further provide depth information to the lateral mapping of the DLC films with XPS technique.

## REFERENCES

1. Field, J. and M. Swain, *A simple predictive model for spherical indentation*. Journal of Materials Research, 1993. **8**(2): p. 297-306.
2. Clark, D., et al., *The Properties of Natural and Synthetic Diamond*. 1993, Academic Press, London, United Kingdom.
3. Dresselhaus, M.S., G. Dresselhaus, and P.C. Eklund, *Science of fullerenes and carbon nanotubes: their properties and applications*. 1996: Elsevier.
4. Green, D., D.R. McKenzie, and P. Lukins. *The microstructure of carbon thin films*. in *Materials Science Forum*. 1990. Trans Tech Publ.
5. Enke, K., *Some new results on the fabrication of and the mechanical, electrical and optical properties of i-carbon layers*. Thin Solid Films, 1981. **80**(1-3): p. 227-234.
6. Jacob, W. and W. Möller, *On the structure of thin hydrocarbon films*. Applied Physics Letters, 1993. **63**(13): p. 1771-1773.
7. McKenzie, D., *Tetrahedral bonding in amorphous carbon*. Reports on Progress in Physics, 1996. **59**(12): p. 1611.
8. Koidl, P., et al. *Plasma deposition, properties and structure of amorphous hydrogenated carbon films*. in *Materials Science Forum*. 1990. Trans Tech Publ.
9. Weiler, M., et al., *Highly tetrahedral, diamond-like amorphous hydrogenated carbon prepared from a plasma beam source*. Applied Physics Letters, 1994. **64**(21): p. 2797-2799.
10. Fanchini, G., S. Ray, and A. Tagliaferro, *Optical properties of disordered carbon-based materials*. Surface and Coatings Technology, 2002. **151**: p. 233-241.

11. Aisenberg, S. and R. Chabot, *Ion-beam deposition of thin films of diamondlike carbon*. Journal of applied physics, 1971. **42**(7): p. 2953-2958.
12. Davrs, C., et al., *Properties of tetrahedral amorphous carbon films deposited in a filtered cathodic arc in the presence of hydrogen*. Philosophical Magazine B, 1994. **69**(6): p. 1121-1131.
13. Rengan, A., et al., *Characteristics of diamond-like carbon films formed by a hybrid laser-plasma ablation of graphite*. Materials Science and Engineering: B, 1992. **15**(1): p. 15-24.
14. Godet, C., et al., *Structural and electronic properties of electron cyclotron resonance plasma deposited hydrogenated amorphous carbon and carbon nitride films*. Journal of applied physics, 2002. **91**(7): p. 4154-4162.
15. Whitmell, D. and R. Williamson, *The deposition of hard surface layers by hydrocarbon cracking in a glow discharge*. Thin Solid Films, 1976. **35**(2): p. 255-261.
16. Holland, L. and S. Ojha, *The growth of carbon films with random atomic structure from ion impact damage in a hydrocarbon plasma*. Thin Solid Films, 1979. **58**(1): p. 107-116.
17. Mort, J. and F. Jansen, *Plasma-deposited thin films*. 1986.
18. Wei, Q. and J. Narayan, *Superhard diamondlike carbon: preparation, theory, and properties*. International materials reviews, 2000. **45**(4): p. 133-164.
19. Lifshitz, Y., et al., *Subplantation model for film growth from hyperthermal species*. Physical Review B, 1990. **41**(15): p. 10468.
20. Lifshitz, Y., G. Lempert, and E. Grossman, *Substantiation of subplantation model for diamondlike film growth by atomic force microscopy*. Physical review letters, 1994. **72**(17): p. 2753.

21. Hofsäss, H., et al., *Doping and growth of diamond-like carbon films by ion beam deposition*. Diamond and Related Materials, 1994. **3**(1-2): p. 137-142.
22. Jansen, F., et al., *The effects of hydrogenation on the properties of ion beam sputter deposited amorphous carbon*. Journal of Vacuum Science & Technology A: Vacuum, Surfaces, and Films, 1985. **3**(3): p. 605-609.
23. Rubin, M., et al., *Optical and mechanical properties of dc sputtered carbon films*. Journal of materials Research, 1990. **5**(11): p. 2538-2542.
24. Kelly, P.J. and R.D. Arnell, *Magnetron sputtering: a review of recent developments and applications*. Vacuum, 2000. **56**(3): p. 159-172.
25. Lieberman, M.A. and A.J. Lichtenberg, *Principles of plasma discharges and materials processing*. MRS Bulletin, 1994. **30**(2): p. 899-901.
26. Müller-Sebert, W., et al., *Nitrogen induced increase of growth rate in chemical vapor deposition of diamond*. Applied Physics Letters, 1996. **68**(6): p. 759-760.
27. Wild, C. and P. Koidl, *Ion and electron dynamics in the sheath of radio-frequency glow discharges*. Journal of applied physics, 1991. **69**(5): p. 2909-2922.
28. Weiler, M., et al., *Preparation and properties of highly tetrahedral hydrogenated amorphous carbon*. Physical Review B, 1996. **53**(3): p. 1594.
29. Martinu, L., et al., *Properties and stability of diamond-like carbon films related to bonded and unbonded hydrogen*. Diamond and Related Materials, 1993. **2**(5-7): p. 673-677.
30. Zarrabian, M., et al., *Observation of nanocrystalline diamond in diamondlike carbon films deposited at room temperature in electron cyclotron resonance plasma*. Applied physics letters, 1997. **70**(19): p. 2535-2537.

31. He, X.-M., et al., *Characterization and optical properties of diamondlike carbon prepared by electron cyclotron resonance plasma*. Journal of materials research, 1999. **14**(3): p. 1055-1061.
32. Weiler, M., et al., *Deposition of tetrahedral hydrogenated amorphous carbon using a novel electron cyclotron wave resonance reactor*. Applied physics letters, 1998. **72**(11): p. 1314-1316.
33. Voevodin, A. and M. Donley, *Preparation of amorphous diamond-like carbon by pulsed laser deposition: a critical review*. Surface and Coatings Technology, 1996. **82**(3): p. 199-213.
34. Davanloo, F., et al., *Amorphic diamond films produced by a laser plasma source*. Journal of Applied Physics, 1990. **67**(4): p. 2081-2087.
35. Lossy, R., et al., *Filtered arc deposition of amorphous diamond*. Applied physics letters, 1992. **61**(2): p. 171-173.
36. Xiong, F., Y. Wang, and R. Chang, *Complex dielectric function of amorphous diamond films deposited by pulsed-excimer-laser ablation of graphite*. Physical Review B, 1993. **48**(11): p. 8016.
37. Kovarik, P., E. Bourdon, and R. Prince, *Electron-energy-loss characterization of laser-deposited a-C, a-C: H, and diamond films*. Physical Review B, 1993. **48**(16): p. 12123.
38. Huai, Y., et al., *Study of density in pulsed-laser deposited amorphous carbon films using x-ray reflectivity*. Applied physics letters, 1994. **65**(7): p. 830-832.
39. Merkulov, V.I., et al., *Structure and optical properties of amorphous diamond films prepared by ArF laser ablation as a function of carbon ion kinetic energy*. Applied physics letters, 1998. **73**(18): p. 2591-2593.

40. Robertson, J., *Diamond-like carbon*. Pure and applied chemistry, 1994. **66**(9): p. 1789-1796.
41. Spencer, E., et al., *Ion-beam-deposited polycrystalline diamondlike films*. Applied physics letters, 1976. **29**(2): p. 118-120.
42. Möller, W., *Modeling of the sp<sup>3</sup>/sp<sup>2</sup> ratio in ion beam and plasma-deposited carbon films*. Applied physics letters, 1991. **59**(19): p. 2391-2393.
43. Banhart, F., *Irradiation effects in carbon nanostructures*. Reports on progress in physics, 1999. **62**(8): p. 1181.
44. McKenzie, D., D. Muller, and B. Pailthorpe, *Compressive-stress-induced formation of thin-film tetrahedral amorphous carbon*. Physical review letters, 1991. **67**(6): p. 773.
45. McKenzie, D., *Generation and applications of compressive stress induced by low energy ion beam bombardment*. Journal of Vacuum Science & Technology B: Microelectronics and Nanometer Structures Processing, Measurement, and Phenomena, 1993. **11**(5): p. 1928-1935.
46. Xu, S., et al., *Properties of carbon ion deposited tetrahedral amorphous carbon films as a function of ion energy*. Journal of applied physics, 1996. **79**(9): p. 7234-7240.
47. Shi, X., et al., *Simulation of plasma flow in toroidal solenoid filters*. IEEE transactions on plasma science, 1996. **24**(6): p. 1309-1318.
48. Tay, B., et al., *Plasma flow simulation in an off-plane double bend magnetic filter*. Surface and Coatings Technology, 2000. **133**: p. 593-597.
49. Chhowalla, M., et al., *Influence of ion energy and substrate temperature on the optical and electronic properties of tetrahedral amorphous carbon (ta-C) films*. Journal of applied physics, 1997. **81**(1): p. 139-145.

50. Xu, S., et al., *Mechanical properties and Raman spectra of tetrahedral amorphous carbon films with high  $sp^3$  fraction deposited using a filtered cathodic arc*. Philosophical Magazine B, 1997. **76**(3): p. 351-361.
51. Shi, X., B. Tay, and S. Lau, *The double bend filtered cathodic arc technology and its applications*. International Journal of Modern Physics B, 2000. **14**(02n03): p. 136-153.
52. Möller, W., et al., *Mechanisms of the deposition of hydrogenated carbon films*. Japanese journal of applied physics, 1995. **34**(4S): p. 2163.
53. Mantzaris, N.V., et al., *Surface and plasma simulation of deposition processes:  $CH_4$  plasmas for the growth of diamondlike carbon*. Journal of applied physics, 1996. **79**(7): p. 3718-3729.
54. Perrin, J., et al., *Surface reaction probabilities and kinetics of H,  $SiH_3$ ,  $Si_2H_5$ ,  $CH_3$ , and  $C_2H_5$  during deposition of  $\alpha$ -Si: H and  $\alpha$ -C: H from  $H_2$ ,  $SiH_4$ , and  $CH_4$  discharges*. Journal of Vacuum Science & Technology A: Vacuum, Surfaces, and Films, 1998. **16**(1): p. 278-289.
55. Schwarz-Selinger, T., A. Von Keudell, and W. Jacob, *Plasma chemical vapor deposition of hydrocarbon films: The influence of hydrocarbon source gas on the film properties*. Journal of Applied Physics, 1999. **86**(7): p. 3988-3996.
56. Von Keudell, A. and W. Jacob, *Growth and erosion of hydrocarbon films investigated by in situ ellipsometry*. Journal of applied physics, 1996. **79**(2): p. 1092-1098.
57. Von Keudell, A. and W. Jacob, *Surface relaxation during plasma-enhanced chemical vapor deposition of hydrocarbon films, investigated by in situ ellipsometry*. Journal of applied physics, 1997. **81**(3): p. 1531-1535.

58. Kessels, W., et al., *A model for the deposition of aC: H using an expanding thermal arc*. Surface and Coatings Technology, 1998. **98**(1-3): p. 1584-1589.
59. Boutard, D., W. Möller, and B. Scherzer, *Influence of H-C bonds on the stopping power of hard and soft carbonized layers*. Physical Review B, 1988. **38**(5): p. 2988.
60. Hopf, C., et al., *Surface loss probabilities of hydrocarbon radicals on amorphous hydrogenated carbon film surfaces*. Journal of Applied Physics, 2000. **87**(6): p. 2719-2725.
61. Von Keudell, A., T. Schwarz-Selinger, and W. Jacob, *Simultaneous interaction of methyl radicals and atomic hydrogen with amorphous hydrogenated carbon films*. Journal of Applied Physics, 2001. **89**(5): p. 2979-2986.
62. Schwarz-Selinger, T., A. Von Keudell, and W. Jacob, *Novel method for absolute quantification of the flux and angular distribution of a radical source for atomic hydrogen*. Journal of Vacuum Science & Technology A: Vacuum, Surfaces, and Films, 2000. **18**(3): p. 995-1001.
63. Küppers, J., *The hydrogen surface chemistry of carbon as a plasma facing material*. Surface Science Reports, 1995. **22**(7-8): p. 249-321.
64. Knotek, O., F. Löffler, and J. Brand, *Hydrogen-free amorphous carbon coatings deposited by the arc ion-plating process*. Diamond and Related Materials, 1993. **2**(2-4): p. 243-245.
65. Robertson, J. and E. O'reilly, *Electronic and atomic structure of amorphous carbon*. Physical Review B, 1987. **35**(6): p. 2946.
66. Wu, W.-J., T.-M. Pai, and M.-H. Hon, *Wear behavior of silicon-containing diamond-like carbon coatings*. Diamond and Related Materials, 1998. **7**(10): p. 1478-1484.
67. Robertson, J., *Hard amorphous (diamond-like) carbons*. Progress in Solid State Chemistry, 1991. **21**(4): p. 199-333.

68. Wei, Q., et al., *Atomic structure, electrical properties, and infrared range optical properties of diamondlike carbon films containing foreign atoms prepared by pulsed laser deposition*. Journal of Materials Research, 2000. **15**(3): p. 633-641.
69. Lee, C.H., et al., *Electronic structure of dense amorphous carbon*. Physical Review B, 1994. **49**(16): p. 11448.
70. Robertson, J., *Structural models of aC and aC: H*. Diamond and related materials, 1995. **4**(4): p. 297-301.
71. Robertson, J., *Hard amorphous (Diamond-like) carbon*. Phys. Rev. B, 1996. **53**: p. 1594.
72. Bewilogua, K., et al., *Structure of amorphous carbon films*. physica status solidi (a), 1982. **71**(1): p. K57-K59.
73. Knight, D.S. and W.B. White, *Characterization of diamond films by Raman spectroscopy*. Journal of Materials Research, 1989. **4**(2): p. 385-393.
74. Visinoiu, A.M., *Growth mechanism and structure of epitaxial perovskite thin films and superlattices*. 2003.
75. Thornton, J.A., *High rate thick film growth*. Annual review of materials science, 1977. **7**(1): p. 239-260.
76. Merle, B., *Mechanical properties of thin films studied by bulge testing*. 2013.
77. Elman, B., et al., *Structural characterization of ion-implanted graphite*. Physical Review B, 1982. **25**(6): p. 4142.
78. Tuinstra, F. and J.L. Koenig, *Raman spectrum of graphite*. The Journal of Chemical Physics, 1970. **53**(3): p. 1126-1130.
79. Ferrari, A.C. and J. Robertson, *Interpretation of Raman spectra of disordered and amorphous carbon*. Physical review B, 2000. **61**(20): p. 14095.

80. Yu, P.Y. and M. Cardona, *Fundamentals of semiconductors: physics and materials properties*. 1996: Springer.
81. Alben, R., et al., *Vibrational properties of amorphous Si and Ge*. Physical Review B, 1975. **11**(6): p. 2271.
82. Beeman, D. and R. Alben, *Vibrational properties of elemental amorphous semiconductors*. Advances in Physics, 1977. **26**(3): p. 339-361.
83. Maley, N. and J. Lannin, *Raman coupling-parameter variation in amorphous germanium*. Physical Review B, 1987. **35**(5): p. 2456.
84. Shroder, R., R. Nemanich, and J. Glass, *Analysis of the composite structures in diamond thin films by Raman spectroscopy*. Physical Review B, 1990. **41**(6): p. 3738.
85. Field, J.E. and J.E. Field, *The properties of diamond*. 1979: Academic Press.
86. Al-Jishi, R. and G. Dresselhaus, *Lattice-dynamical model for alkali-metal—graphite intercalation compounds*. Physical Review B, 1982. **26**(8): p. 4523.
87. Mapelli, C., et al., *Common force field for graphite and polycyclic aromatic hydrocarbons*. Physical Review B, 1999. **60**(18): p. 12710.
88. Ferrari, A. and J. Robertson, *Resonant Raman spectroscopy of disordered, amorphous, and diamondlike carbon*. Physical Review B, 2001. **64**(7): p. 075414.
89. Chhowalla, M., et al., *Evolution of sp<sup>2</sup> bonding with deposition temperature in tetrahedral amorphous carbon studied by Raman spectroscopy*. Applied Physics Letters, 2000. **76**(11): p. 1419-1421.
90. Ristein, J., et al., *A comparative analysis of a-C:H by infrared spectroscopy and mass selected thermal effusion*. Journal of Applied Physics, 1998. **84**(7): p. 3836-3847.

91. Jiang, X., W. Beyer, and K. Reichelt, *Gas evolution from hydrogenated amorphous carbon films*. Journal of applied physics, 1990. **68**(3): p. 1378-1380.
92. Jacob, W. and M. Unger, *Experimental determination of the absorption strength of C–H vibrations for infrared analysis of hydrogenated carbon films*. Applied physics letters, 1996. **68**(4): p. 475-477.
93. Harrison, W.A., *Bond-orbital model and the properties of tetrahedrally coordinated solids*. Physical Review B, 1973. **8**(10): p. 4487.
94. Coulson, C.A. and H.C. Longuet-Higgins, *The electronic structure of conjugated systems I. General theory*. Proc. R. Soc. Lond. A, 1947. **191**(1024): p. 39-60.
95. Stillinger, F.H. and T.A. Weber, *Computer simulation of local order in condensed phases of silicon*. Physical review B, 1985. **31**(8): p. 5262.
96. Tamor, M., W. Vassell, and K. Carduner, *Atomic constraint in hydrogenated ‘‘diamond-like’’ carbon*. Applied Physics Letters, 1991. **58**(6): p. 592-594.
97. Murata, H., *Synthesis of Durable Poly (aminiumradical) s and Their Spin Alignment at Room Temperature*. 2005.
98. Tamor, M.A. and W. Vassell, *Raman ‘‘fingerprinting’’ of amorphous carbon films*. Journal of Applied Physics, 1994. **76**(6): p. 3823-3830.
99. Tersoff, J., *Structural properties of sp<sup>3</sup>-bonded hydrogenated amorphous carbon*. Physical Review B, 1991. **44**(21): p. 12039.
100. Brenner, D., *The art and science of an analytic potential*. physica status solidi (b), 2000. **217**(1): p. 23-40.
101. Heggie, M., *Semiclassical interatomic potential for carbon and its application to the self-interstitial in graphite*. Journal of Physics: Condensed Matter, 1991. **3**(18): p. 3065.

102. Grill, A. and V. Patel, *Characterization of diamondlike carbon by infrared spectroscopy?* Applied physics letters, 1992. **60**(17): p. 2089-2091.
103. Donnet, C. and A. Erdemir, *Tribology of diamond-like carbon films: fundamentals and applications*. 2007: Springer Science & Business Media.
104. Ulyanekov, A. *LEPTOS: a universal software for x-ray reflectivity and diffraction*. in *Advances in Computational Methods for X-Ray and Neutron Optics*. 2004. International Society for Optics and Photonics.
105. Haerle, R., et al., *sp<sup>2</sup>/sp<sup>3</sup> hybridization ratio in amorphous carbon from C 1 s core-level shifts: X-ray photoelectron spectroscopy and first-principles calculation*. Physical Review B, 2001. **65**(4): p. 045101.
106. Robertson, J., *Diamond-like amorphous carbon*. Materials Science and Engineering: R: Reports, 2002. **37**(4-6): p. 129-281.
107. Llamas-Jansa, I., et al., *Far-ultraviolet to near-infrared optical properties of carbon nanoparticles produced by pulsed-laser pyrolysis of hydrocarbons and their relation with structural variations*. Carbon, 2007. **45**(7): p. 1542-1557.
108. Frauenheim, T., et al., *Atomic-scale structure and electronic properties of highly tetrahedral hydrogenated amorphous carbon*. Physical Review B, 1994. **50**(11): p. 7940.
109. Frauenheim, T., et al., *Atomic structure and physical properties of amorphous carbon and its hydrogenated analogs*. Physical Review B, 1993. **48**(7): p. 4823.
110. Chen, C. and J. Robertson, *Nature of disorder and localization in amorphous carbon*. Journal of non-crystalline solids, 1998. **227**: p. 602-606.
111. Bilek, M., et al., *Ab initio simulation of structure in amorphous hydrogenated carbon*. Physical Review B, 2000. **62**(5): p. 3071.

112. McCulloch, D., D. McKenzie, and C. Goringe, *Ab initio simulations of the structure of amorphous carbon*. Physical Review B, 2000. **61**(3): p. 2349.
113. Oppedisano, C. and A. Tagliaferro, *Relationship between sp<sup>2</sup> carbon content and E<sub>04</sub> optical gap in amorphous carbon-based materials*. Applied Physics Letters, 1999. **75**(23): p. 3650-3652.
114. Conway, N., et al., *Defect and disorder reduction by annealing in hydrogenated tetrahedral amorphous carbon*. Diamond and Related Materials, 2000. **9**(3-6): p. 765-770.
115. Robertson, J.,  *$\pi$ -bonded clusters in amorphous carbon materials*. Philosophical magazine B, 1992. **66**(2): p. 199-209.
116. Tamor, M. and W. Vassell, *Raman "fingerprinting" of amorphous carbon films*. Journal of Applied Physics, 1994. **76**(6): p. 3823-3830.
117. Cheng, H.-F., et al., *Boron-doping effect on the field emission behavior of pulse laser deposited diamond-like carbon films*. Applied surface science, 1999. **142**(1-4): p. 504-509.
118. Clough, F., et al., *Tetrahedrally bonded amorphous carbon (ta-C) thin film transistors*. Electronics Letters, 1996. **32**(5): p. 498.
119. Clay, K., et al., *Characterization of a-C:H:N deposition from CH<sub>4</sub>/N<sub>2</sub> rf plasmas using optical emission spectroscopy*. Journal of applied physics, 1996. **79**(9): p. 7227-7233.
120. Robertson, J. and C. Davis, *Nitrogen doping of tetrahedral amorphous carbon*. Diamond and Related Materials, 1995. **4**(4): p. 441-444.
121. Chen, M.Y. and P.T. Murray, *Carbon nitride thin-film growth by pulsed laser deposition*. Journal of Vacuum Science & Technology A: Vacuum, Surfaces, and Films, 1998. **16**(4): p. 2093-2098.

122. Koizumi, S., et al., *Growth and characterization of phosphorous doped {111} homoepitaxial diamond thin films*. Applied physics letters, 1997. **71**(8): p. 1065-1067.
123. Helmbold, A., et al., *Electrical conductivity of amorphous hydrogenated carbon*. Philosophical Magazine B, 1995. **72**(3): p. 335-350.
124. Golzan, M., et al., *Magnetic and spin properties of tetrahedral amorphous carbon*. Diamond and related materials, 1995. **4**(7): p. 912-916.
125. Yamada, H., et al., *Study on improvements of tribological properties of magnesium alloys: Diamond-like carbon film coating with the interface layer of carbonaceous film containing silicon*. Japanese journal of tribology, 2003. **48**(4): p. 397-404.
126. Robertson, J., *Gap states in diamond-like amorphous carbon*. Philosophical Magazine B, 1997. **76**(3): p. 335-350.
127. Hie, A., et al., *Photoconductivity of diamond-like carbon*. MRS Online Proceedings Library Archive, 1997. **498**.
128. Spear, K.E. and J.P. Dismukes, *Synthetic diamond: emerging CVD science and technology*. Vol. 25. 1994: John Wiley & Sons.
129. Dimigen, H., H. Hübsch, and R. Memming, *Tribological and electrical properties of metal-containing hydrogenated carbon films*. Applied Physics Letters, 1987. **50**(16): p. 1056-1058.
130. Chen, C. and J. Robertson, *Doping mechanism in tetrahedral amorphous carbon*. Carbon, 1999. **37**(5): p. 839-842.
131. Cheah, L., et al., *Electron field emission properties of tetrahedral amorphous carbon films*. Journal of applied physics, 1999. **85**(9): p. 6816-6821.

132. Robertson, J., *Self-compensation and the absence of doping in amorphous GaAs*. Physical Review B, 1986. **33**(6): p. 4399.
133. Every, A., *The elastic properties of solids: Static and dynamic principles*. Handbook of Elastic Properties of Solids, Liquids and Gases, 2001. **1**: p. 3.
134. Comins, J., et al., *Surface Brillouin scattering of opaque solids and thin supported films*. Ultrasonics, 2000. **38**(1-8): p. 450-458.
135. Zhang, X., et al., *Surface Brillouin scattering studies on vanadium carbide*. International Journal of Refractory Metals and Hard Materials, 1998. **16**(4-6): p. 303-308.
136. Loudon, R. and J. Sandercock, *Analysis of the light-scattering cross section for surface ripples on solids*. Journal of Physics C: Solid State Physics, 1980. **13**(13): p. 2609.
137. Levy, M., et al., *Handbook of Elastic Properties of Solids, Liquids, and Gases: Elastic properties of solids: theory, elements and compounds, novel materials, technological materials, alloys, and building materials*. Vol. 2. 2001: Academic Press.
138. Beghi, M., et al., *Measurement of the elastic properties of solids by Brillouin spectroscopy*. 2012.
139. Zhang, X., et al., *Surface Brillouin scattering study of the surface excitations in amorphous silicon layers produced by ion bombardment*. Physical Review B, 1998. **58**(20): p. 13677.
140. Farnell, G. and E. Adler, *Elastic wave propagation in thin layers*. Physical acoustics, 2012. **9**: p. 35-127.
141. Shuvalov, A. and A. Every, *Characteristic features of the velocity dispersion of surface acoustic waves in anisotropic coated solids*. Ultrasonics, 2002. **40**(1-8): p. 939-942.
142. Mills, D. and K. Subbaswamy, *II Surface and Size Effects on the Light Scattering Spectra of Solids*, in *Progress in optics*. 1981, Elsevier. p. 45-137.

143. Riobóo, R.J.J., A. Sánchez-Sánchez, and C. Prieto, *Optical find of hypersonic surface acoustic waves in bulk transparent materials*. Physical Review B, 2016. **94**(1): p. 014313.
144. Zinin, P., et al., *Brillouin spectroscopy of surface modes in thin-film Si<sub>3</sub>N<sub>4</sub> on GaAs*. Physical Review B, 1999. **60**(4): p. 2844.
145. Wittkowski, T., et al., *Structural and chemical phase transitions in tungsten carbide films evidenced by the analysis of their stiffness tensors*. Journal of applied physics, 2006. **100**(7): p. 073513.
146. Wittkowski, T., et al., *General methods for the determination of the stiffness tensor and mass density of thin films using Brillouin light scattering: Study of tungsten carbide films*. Physical Review B, 2004. **69**(20): p. 205401.
147. Ferrari, A., et al., *Elastic constants of tetrahedral amorphous carbon films by surface Brillouin scattering*. Applied physics letters, 1999. **75**(13): p. 1893-1895.
148. Manghnani, M., et al., *Elastic properties of superhard amorphous carbon pressure-synthesized from C<sub>60</sub> by surface Brillouin scattering*. Physical Review B, 2001. **64**(12): p. 121403.
149. Berezina, S., et al., *Combining Brillouin spectroscopy and laser-SAW technique for elastic property characterization of thick DLC films*. Ultrasonics, 2004. **43**(2): p. 87-93.
150. Sumanya, C., J. Comins, and A. Every. *Surface brillouin scattering in opaque thin films*. in *Journal of Physics: Conference Series*. 2007. IOP Publishing.
151. Kotane, L.M., *Study of elastic properties of semiconductors by surface Brillouin scattering*. 2010.
152. Mpingi, W.M., *Structural, electrical and electronic properties of diamond like carbon (DLC) and carbon-based materials*. 2014.

153. Grill, A., *Electrical and optical properties of diamond-like carbon*. Thin solid films, 1999. **355**: p. 189-193.
154. Roberston, J., *Properties of diamond-like carbon films*. Surf. Coat. Technol, 1992. **50**(18): p. 5-203.
155. Karimi, P.M., *Atomic mechanisms of stress formation of group IVB-VIB transition metal nitrides deposited by DC magnetron sputtering*. 2007, Citeseer.
156. Bergese, P., E. Bontempi, and L. Depero, *A simple solution to systematic errors in density determination by X-ray reflectivity: The XRR-density evaluation (XRR-DE) method*. Applied surface science, 2006. **253**(1): p. 28-32.
157. Roberston, J., *Diamond-like amorphous carbon [J]*. Materials Science and Engineering R, 2002. **37**(4/6): p. 129-281.
158. Barholm-Hansen, C., M. Bentzon, and J.B. Hansen, *Optical emission spectroscopy during growth of diamond-like carbon from a methane plasma*. Diamond and Related Materials, 1994. **3**(4-6): p. 564-568.
159. Born, M. and E. Wolf, *Principles of optics: electromagnetic theory of propagation, interference and diffraction of light*. 2013: Elsevier.
160. Chowdhury, S., M. Laugier, and I. Rahman, *Characterization of DLC coatings deposited by rf magnetron sputtering*. Journal of Materials Processing Technology, 2004. **153**: p. 804-810.
161. Alba, N., et al., *Characterization of diamond-like carbon (DLC) thin films prepared by rf magnetron sputtering*. Superficies y vacío, 1999. **9**: p. 267-270.
162. Kim, J. and C. Lee, *Dependence of the Physical Properties DLC Films by PECVD on the Ar gas Addition*. Journal of the Korean Physical Society, 2003. **42**: p. S956-S960.

163. Gotzmann, G., *Long-term stable surface modification of DLC coatings*. Current Directions in Biomedical Engineering. **3**(2): p. 351-354.
164. Mednikarov, B., et al., *Optical properties of diamond-like carbon and nanocrystalline diamond films*. Journal of Optoelectronics and Advanced Materials, 2005. **7**(3): p. 1407-1413.
165. Coşkun, Ö.D. and T. Zerrin, *Optical, structural and bonding properties of diamond-like amorphous carbon films deposited by DC magnetron sputtering*. Diamond and Related Materials, 2015. **56**: p. 29-35.
166. Jiang, M. and Z. Ning, *Influence of deposition pressure on the structure and properties of fluorinated diamond-like carbon films prepared by RF reactive magnetron sputtering*. Surface and Coatings Technology, 2006. **200**(12-13): p. 3682-3686.
167. Ting, J.-M. and H. Lee, *DLC composite thin films by sputter deposition*. Diamond and related materials, 2002. **11**(3-6): p. 1119-1123.
168. Bewilogua, K., et al., *DLC based coatings prepared by reactive dc magnetron sputtering*. Thin Solid Films, 2004. **447**: p. 142-147.
169. Sanchez, N., et al., *Characterization of diamond-like carbon (DLC) thin films prepared by rf magnetron sputtering*. Thin Solid Films, 2000. **373**(1-2): p. 247-250.
170. Cicala, G., et al., *Plasma deposition of hydrogenated diamond-like carbon films from CH<sub>4</sub>-Ar mixtures*. Surface and Coatings Technology, 2004. **180**: p. 222-226.
171. Praver, S., et al., *Systematic variation of the Raman spectra of DLC films as a function of sp<sup>2</sup>: sp<sup>3</sup> composition*. Diamond and related materials, 1996. **5**(3-5): p. 433-438.
172. Singha, A., et al., *Quantitative analysis of hydrogenated diamondlike carbon films by visible Raman spectroscopy*. Journal of applied physics, 2006. **100**(4): p. 044910.

173. Casiraghi, C., et al., *Bonding in hydrogenated diamond-like carbon by Raman spectroscopy*. Diamond and Related Materials, 2005. **14**(3-7): p. 1098-1102.
174. Corbella Roca, C., *Thin film structures of diamond-like carbon prepared by pulsed plasma techniques*. 2006: Universitat de Barcelona.
175. Irmer, G. and A. Dorner-Reisel, *Micro-Raman Studies on DLC coatings*. Advanced Engineering Materials, 2005. **7**(8): p. 694-705.
176. Casiraghi, C., A. Ferrari, and J. Robertson, *Raman spectroscopy of hydrogenated amorphous carbons*. Physical Review B, 2005. **72**(8): p. 085401.
177. Buijnsters, J.G., et al., *Hydrogen quantification in hydrogenated amorphous carbon films by infrared, Raman, and x-ray absorption near edge spectroscopies*. Journal of Applied Physics, 2009. **105**(9): p. 093510.
178. Wang, H., et al., *Deposition of diamond-like carbon films by electrolysis of methanol solution*. Applied physics letters, 1996. **69**(8): p. 1074-1076.
179. Marchon, B., et al., *Photoluminescence and Raman spectroscopy in hydrogenated carbon films*. IEEE Transactions on Magnetics, 1997. **33**(5): p. 3148-3150.
180. Erz, R., et al., *Investigation of boron and hydrogen concentrations in p-type diamond films by infrared spectroscopy*. Diamond and related materials, 1995. **4**(4): p. 469-472.
181. Gheeraert, E. and A. Deneuville, *IR characterization of diamond films on Si substrates*. Diamond and Related Materials, 1992. **1**(5-6): p. 584-587.
182. Dischler, B., A. Bubenzer, and P. Koidl, *Bonding in hydrogenated hard carbon studied by optical spectroscopy*. Solid State Communications, 1983. **48**(2): p. 105-108.

183. Bubbenzer, A., et al., *rf-plasma deposited amorphous hydrogenated hard carbon thin films: Preparation, properties, and applications*. Journal of applied physics, 1983. **54**(8): p. 4590-4595.
184. Donnet, C., et al., *Solid state  $^{13}\text{C}$  and  $^1\text{H}$  nuclear magnetic resonance investigations of hydrogenated amorphous carbon*. Journal of applied physics, 1999. **85**(6): p. 3264-3270.
185. Caschera, D., et al., *Influence of PECVD parameters on the properties of diamond-like carbon films*. Thin Solid Films, 2011. **519**(12): p. 4087-4091.
186. Sooryakumar, R., *Elastic Properties of Hard Coatings, Films and Polymeric Composites via Light Scattering*. 2000, OHIO STATE UNIV COLUMBUS.
187. Ferrari, A., et al., *Elastic constants of diamond-like carbon films by surface Brillouin scattering*. MRS Online Proceedings Library Archive, 1999. **593**.
188. Farnell, G., *Properties of elastic surface waves*. Physical acoustics, 1970. **6**: p. 109-166.
189. Djemia, P., et al., *Brillouin scattering investigation of elastic properties of Cu–Mo solid solution thin films*. Journal of Applied Physics, 2001. **90**(2): p. 756-762.
190. Jiang, X., *Rayleigh mode in amorphous hydrogenated carbon films*. Physical Review B, 1991. **43**(3): p. 2372.
191. Lung, B., M.-J. Chiang, and M.-H. Hon, *Growth characterization and properties of diamond-like carbon films by electron cyclotron resonance chemical vapor deposition*. Thin Solid Films, 2001. **392**(1): p. 16-21.
192. Dey, R., et al., *Substrate bias effects during diamond like carbon film deposition by microwave ECR plasma CVD*. Current Applied Physics, 2008. **8**(1): p. 6-12.

193. Thornton, J.A., *Influence of apparatus geometry and deposition conditions on the structure and topography of thick sputtered coatings*. Journal of Vacuum Science and Technology, 1974. **11**(4): p. 666-670.
194. Petrov, I., et al., *Comparison of magnetron sputter deposition conditions in neon, argon, krypton, and xenon discharges*. Journal of Vacuum Science & Technology A: Vacuum, Surfaces, and Films, 1993. **11**(5): p. 2733-2741.
195. Kluth, O., et al., *Modified Thornton model for magnetron sputtered zinc oxide: film structure and etching behaviour*. Thin solid films, 2003. **442**(1-2): p. 80-85.
196. Singh, S., et al., *Optical and mechanical properties of diamond like carbon films deposited by microwave ECR plasma CVD*. Bulletin of Materials Science, 2008. **31**(5): p. 813-818.
197. Li, S., et al., *Photocatalytic and magnetic behaviors observed in nanostructured BiFeO<sub>3</sub> particles*. 2009, AIP.
198. Ferrari, A.C., *A model to interpret the Raman spectra of disordered, amorphous and nanostructured carbons*. MRS Online Proceedings Library Archive, 2001. **675**.
199. Ferrari, A.C. and J. Robertson, *Raman spectroscopy of amorphous, nanostructured, diamond-like carbon, and nanodiamond*. Philosophical Transactions of the Royal Society of London A: Mathematical, Physical and Engineering Sciences, 2004. **362**(1824): p. 2477-2512.
200. Brassard, D. and M. El Khakani, *Dielectric properties of amorphous hydrogenated silicon carbide thin films grown by plasma-enhanced chemical vapor deposition*. Journal of applied physics, 2003. **93**(7): p. 4066-4071.
201. Demichelis, F., et al., *Optical properties of hydrogenated amorphous silicon*. Journal of applied physics, 1986. **59**(2): p. 611-618.

202. Murri, R., et al., *Electrical resistivity of a-SiC: H as a function of temperature: evidence for discontinuities*. Physical Review B, 2000. **62**(3): p. 1801.
203. Staryga, E. and G.W. Bąk, *Relation between physical structure and electrical properties of diamond-like carbon thin films*. Diamond and related Materials, 2005. **14**(1): p. 23-34.
204. Filik, J., et al., *XPS and laser Raman analysis of hydrogenated amorphous carbon films*. Diamond and related Materials, 2003. **12**(3-7): p. 974-978.
205. Popov, C., et al., *Characterization of the bonding structure of nanocrystalline diamond and amorphous carbon films prepared by plasma assisted techniques*. Applied Physics A, 2007. **89**(1): p. 209-212.
206. Mezzi, A. and S. Kaciulis, *Surface investigation of carbon films: from diamond to graphite*. Surface and Interface Analysis, 2010. **42**(6-7): p. 1082-1084.
207. Lubwama, M., et al., *Flexibility and frictional behaviour of DLC and Si-DLC films deposited on nitrile rubber*. Surface and Coatings Technology, 2014. **239**: p. 84-94.

## Papers published

- W. M. Mbiombi, B.A. Mathe, D.M. Wamwangi, R.M. Erasmus, A. G. Every, D. G. Billing, Optoelectronic and mechanical properties of PVD diamond-like carbon films, *Material Today, Proceedings 5 (2018) 27307–27315*.
- W.M. Mbiombi, B.A. Mathe, D.Wamwangi, R. Erasmus, D. G. Billing, Bias enhanced nucleation and growth for improving the Opto-mechanical properties of diamond-like carbon films, *Proceedings of SAIP 2017, S A Institute of physics ISBN978-0-620-82077-6, 77*.